A UNITED STATES DEPARTMENT OF COMMERCE PUBLICATION

SECTION A

JOURNAL OF RESEARCH

of the NATIONAL BUREAU OF STANDARDS

Volume 74A, Number 2 March-April 1970

Physics and Chemistry

U.S. DEPARTMENT OF COMMERCE National Bureau of Standards

Journal of Research

of the

National Bureau of Standards

A. Physics and Chemistry

Mar.–Apr. • 1970

VOLUME • 74A

NUMBER • 2

Editor: C. W. Beckett

Associate Editor: D. D. Wagman

Publication dates:
Feb. 1, Apr. 1, June 1, Aug. 1, Oct. 1, Dec. 1, 1970

J. Res. Nat. Bur. Stand. (U.S.), A
CODEN: JNBAA 74A (2) 141–305 (1970)

JOURNAL OF RESEARCH

The National Bureau of Standards Journal of Research reports research and development in the fields of activity shown at right. Also included from time to time are survey articles on topics closely related to the Bureau's scientific and technical program.

The Journal is published in three separate sections as follows:

A. Physics and Chemistry

Contains papers of interest primarily to scientists working in these fields. Issued six times a year. Annual subscription: domestic, $9.50; foreign, $11.75. Single copy, varies.

B. Mathematical Sciences

Presents studies and compilations designed mainly for the mathematician and the theoretical physicist. Issued quarterly. Annual subscription: domestic, $5.00; foreign, $6.25. Single copy, $1.25.

C. Engineering and Instrumentation

Reports research and development results of interest chiefly to the engineer and the applied scientist. Issued quarterly. Annual subscription: domestic, $5.00 foreign, $6.25. Single copy, $1.25.

The National Bureau of Standards[1] was established by an act of Congress March 3, 1901. Today, in addition to serving as the Nation's central measurement laboratory, the Bureau is a principal focal point in the Federal Government for assuring maximum application of the physical and engineering sciences to the advancement of technology in industry and commerce. To this end the Bureau conducts research and provides central national services in four broad program areas. These are: (1) basic measurements and standards, (2) materials measurements and standards, (3) technological measurements and standards, and (4) transfer of technology.

The Bureau comprises the Institute for Basic Standards, the Institute for Materials Research, the Institute for Applied Technology, the Center for Radiation Research, the Center for Computer Sciences and Technology, and the Office for Information Programs.

THE INSTITUTE FOR BASIC STANDARDS provides the central basis within the United States of a complete and consistent system of physical measurement; coordinates that system with measurement systems of other nations; and furnishes essential services leading to accurate and uniform physical measurements throughout the Nation's scientific community, industry, and commerce. The Institute consists of an Office of Measurement Services and the following technical divisions:

Applied Mathematics — Electricity — Metrology — Mechanics — Heat — Atomic and Molecular Physics — Radio Physics[2] — Radio Engineering[2] — Time and Frequency[2] — Astrophysics[2] — Cryogenics.[2]

THE INSTITUTE FOR MATERIALS RESEARCH conducts materials research leading to improved methods of measurement standards, and data on the properties of well-characterized materials needed by industry, commerce, educational institutions, and Government; develops, produces, and distributes standard reference materials; relates the physical and chemical properties of materials to their behavior and their interaction with their environments; and provides advisory and research services to other Government agencies. The Institute consists of an Office of Standard Reference Materials and the following divisions:

Analytical Chemistry—Polymers—Metallurgy—Inorganic Materials—Physical Chemistry.

THE INSTITUTE FOR APPLIED TECHNOLOGY provides technical services to promote the use of available technology and to facilitate technological innovation in industry and Government; cooperates with public and private organizations in the development of technological standards, and test methodologies; and provides advisory and research services for Federal, state, and local government agencies. The Institute consists of the following technical divisions and offices:

Engineering Standards—Weights and Measures—Invention and Innovation—Vehicle Systems Research—Product Evaluation—Building Research—Instrument Shops—Measurement Engineering—Electronic Technology—Technical Analysis.

THE CENTER FOR RADIATION RESEARCH engages in research, measurement, and application of radiation to the solution of Bureau mission problems and the problems of other agencies and institutions. The Center consists of the following divisions:

Reactor Radiation—Linac Radiation—Nuclear Radiation—Applied Radiation.

THE CENTER FOR COMPUTER SCIENCES AND TECHNOLOGY conducts research and provides technical services designed to aid Government agencies in the selection, acquisition, and effective use of automatic data processing equipment; and serves as the principal focus for the development of Federal standards for automatic data processing equipment, techniques, and computer languages. The Center consists of the following offices and divisions:

Information Processing Standards—Computer Information—Computer Services—Systems Development—Information Processing Technology.

THE OFFICE FOR INFORMATION PROGRAMS promotes optimum dissemination and accessibility of scientific information generated within NBS and other agencies of the Federal Government; promotes the development of the National Standard Reference Data System and a system of information analysis centers dealing with the broader aspects of the National Measurement System, and provides appropriate services to ensure that the NBS staff has optimum accessibility to the scientific information of the world. The Office consists of the following organizational units:

Office of Standard Reference Data—Clearinghouse for Federal Scientific and Technical Information[3]—Office of Technical Information and Publications—Library—Office of Public Information—Office of International Relations.

[1] Headquarters and Laboratories at Gaithersburg, Maryland, unless otherwise noted; mailing address Washington, D.C. 20234.
[2] Located at Boulder, Colorado 80302.
[3] Located at 5285 Port Royal Road, Springfield, Virginia 22151.

U.S. DEPARTMENT OF COMMERCE
Maurice H. Stans, Secretary
NATIONAL BUREAU OF STANDARDS
Lewis M. Branscomb, Director

Order all publications from the Superintendent of Documents
U.S. Government Printing Office, Washington, D.C. 20402
Use of funds for printing this publication approved by the Director of the Bureau of the Budget (June 22, 1966).

JOURNAL OF RESEARCH of the National Bureau of Standards—A. Physics and Chemistry
Vol. 74A, No. 2, March–April 1970

A Theoretical Investigation of the Configurations $(3d+4s)^4 4p$ in Neutral Vanadium (V I)

C. Roth*

(October 13, 1969)

Experimental levels of the configurations $(3d+4s)^4 4p$ in V I were compared with corresponding calculated values. On fitting 228 experimental levels by means of 20 free parameters an rms error in the calculated values of 216 cm^{-1} was obtained. All the 438 theoretically predicted levels and g-factors were calculated.

Key words: Configurations in V I; configurations $(3d+4s)^4 4p$ in V I; configuration interaction; energy levels of V I; first spectrum; g-values V I; parameters; theory; vanadium; V I; Zeeman effect.

1. Introduction

Racah and Shadmi [1, 2][1] investigated theoretically the configurations $(3d+4s)^n$ in the second and third spectra of the iron group. The configurations $3d^n 4p$ in the second and third spectra of the iron group, the configurations $(3d+4s)^n 4p$ for Sc II, Ti II, V II, Ca I, Sc I and Ti I, as well as the odd configurations of Cu II were investigated by the author [3–7].[2]

The configurations $(d+s)^4 p$ comprise 165 theoretical terms splitting into 438 levels. In AEL [8], 74 terms splitting into 223 levels are assigned to the configurations $3d^4 4p + 3d^3 4s 4p$. In addition, 44 odd terms splitting into 119 levels are given without any configuration designation and an additional 36 odd levels are given with no term designations.

The initial values for the interaction parameters[3] were taken from the final results of Ti I, [6]:

$$\begin{aligned} B &= 560 \\ B' &= 660 \\ C &= 1{,}630 \\ C' &= 2{,}310 \\ G'_{ds} &= 1{,}650 \\ F_2 &= 150 \\ F'_2 &= 280 \end{aligned} \qquad (1)$$

$$\begin{aligned} G_1 = G'_1 &= 280 \\ G_3 = G'_3 &= 20 \\ G'_{ps} &= 5{,}800 \\ \alpha = \alpha' &= 50 \\ H &= 180 \\ J &= 1{,}500 \\ K &= 3{,}000 \\ \zeta_d = \zeta'_d &= 100 \\ \zeta_p = \zeta'_p &= 110 \end{aligned}$$

The initial values of A and A' were calculated from the electrostatic interaction matrices of ^{6}G, ^{6}F, and ^{6}P. These are given by:

^{4}F(^{3}P)^{6}G: $A' - 15B' - 3G'_{ds} - F'_2 - G'_{ps} - 10G'_1 - 10G'_3 + 12\alpha'$

$$\begin{array}{c} \\ (^5D)^6\mathrm{F} \\ \\ {}^4\mathrm{F}(^3\mathrm{P})^6\mathrm{F} \end{array} \left[\begin{array}{c|c} A - 21B - 2F_2 - 10G_1 - 20G_3 + 6\alpha & \\ & \frac{2\sqrt{5}}{5}(K-J) \\ \frac{2\sqrt{5}}{5}(K-J) & A' - 15B' - 3G'_{ds} \\ & + 3F'_2 - G'_{ps} - 6G'_1 - 26G'_3 + 12\alpha \end{array}\right]$$

*An invited paper. Present address: McGill University, Montreal, Canada.

[1] Figures in brackets indicate the literature references at the end of this paper.

[2] The reader is referred to these papers for an explanation of the method used, notation and significance of the various parameters.

[3] Unprimed quantities refer to the configuration $3d^4 4p$, primed quantities to $3d^3 4s 4p$ and doubly-primed quantities to $3d^2 4s^2 4p$. The numerical values of the parameters and levels are in cm^{-1}.

$$
\begin{array}{l|cc}
 & ({}^5\mathrm{D})\,{}^6\mathrm{P} & {}^4\mathrm{P}({}^3\mathrm{P})\,{}^6\mathrm{P} \\
\hline
({}^5\mathrm{D})\,{}^6\mathrm{P} & A-21B-7F_2-35G_3+6\alpha & \frac{3\sqrt{5}}{5}(K-J) \\
{}^4\mathrm{P}({}^3\mathrm{P})\,{}^6\mathrm{P} & \frac{3\sqrt{5}}{5}(K-J) & A'-3G'_{ds}-7F'_2-G'_{ps}-G'_1-21G'_3+2\alpha'
\end{array}
$$

By using the values of the parameters in (1) and the fact that the trace of a matrix equals the sum of its eigenvalues, we obtain:

$$
\begin{aligned}
A' &= 23{,}330 + z^6\,\mathrm{G}_{\mathrm{C.G.}} \\
A + A' &= 36{,}370 + z^6\,\mathrm{F}_{\mathrm{C.G.}} + y^6\,\mathrm{F}_{\mathrm{C.G.}} \\
A + A' &= 26{,}520 + z^6\,\mathrm{P}_{\mathrm{C.G.}} + y^6\,\mathrm{P}_{\mathrm{C.G.}}
\end{aligned} \qquad (2)
$$

By using the values for the centers of gravity of z^6G, z^6F, y^6F, z^6P and y^6P from AEL [8], and averaging, we obtain:

$$
\begin{aligned}
A &= 40{,}185 \\
A' &= 40{,}050.
\end{aligned} \qquad (3)
$$

2. Results

After three iterations, the differences between the values of the parameters obtained in the least-squares calculation and the corresponding values in the diagonalization were very small.

The final values of the parameters obtained are given in table 1 together with their standard errors.

The rather high value of 345 for the rms error can be partly attributed to the fact that the interactions with the configuration $3d^24s^24p$ were not considered, as there are no experimental levels assigned to that configuration. An approximate value for the height of $3d^24s^24p$ can be obtained as follows.

Racah and Shadmi, [1, 9], have shown that if $M(d^n)$, $M'(d^{n-1}s)$ and $M''(d^{n-2}s^2)$ are the centers of gravity of d^n, $d^{n-1}s$ and $d^{n-2}s^2$ respectively, i.e., the weighted averages of the terms of these configurations, then the parameters

$$D' = M'(d^{n-1}s) - M(d^n)$$

and

$$D'' = M''(d^{n-2}s^2) - M'(d^{n-1}s)$$

are linear functions of n with small quadratic corrections for the configurations $(3d+4s)^n$ in the second spectra of the iron group.

TABLE 1. *Final parameters for* V I $(3d+4s)^4 4p$

Parameter	$3d^4 4p + 3d^3 4s 4p$	$3d^4 4p + 3d^3 4s 4p + 3d^2 4s^2 4p$
A	39,052 ± 250	39,458 ± 259
A'	40,666 ± 283	41,022 ± 272
A''	.....	54,416 ± 757
B	555 ± 10	579 ± 12
B'	750 ± 6	730 ± 5
B''	.....	881 (Arith. Progress.)
C	2,008 ± 26	2,084 ± 23
C'	2,540 ± 25	2,587 ± 19
C''	.....	3,090 (Arith. Progress.)
G'_{ds}	1,495 ± 48	1,584 ± 33
$G = G'_{ds}$	.....	1,584 (Equal)
F_2	194 ± 9	160 ± 8
F'_2	275 ± 7	282 ± 6
F''_2	.....	404 (Arith. Progress.)
G'_{ps}	5,836 ± 76	6,022 ± 80
G_1	281 ± 10	229 ± 8
G'_1	296 ± 11	281 ± 8
G''_1	.....	333 (Arith. Progress.)
G_3	9 ± 3	13 ± 2
G'_3	23 ± 4	13 (Equal)
$G''_3 = G'_3$	.....	13
α	70 ± 3	54 ± 2
α'	70 (Equal)	54 (Equal)
$\alpha'' = \alpha'$	.....	54
H	172 ± 8	150 ± 6
$H' = H$	.....	150
J	1,088 ± 48	972 ± 48
$J' = J$	.....	972
K	2,492 ± 42	2,468
K'	.....	3,104 (Fixed Diff.)
$\zeta_d = \zeta'_d$	146 ± 29	141 ± 22
$\zeta''_d = \zeta'_d$	.....	141
$\zeta_p = \zeta'_p$	124 ± 77	140 ± 78
$\zeta''_p = \zeta'_p$	.....	140
rms error	345.3	215.8

Now, in d^np we must consider n interactions $d-p$, $n(n-1)/2$ interactions $d-d$ and the $L(L+1)$ correction. From p. 200 TAS [10], the center of gravity of dp is

$$M(dp) = F_0(dp) - (G_1 + 7/2\,G_3) \qquad (4)$$

From eq (78) RII [11], and by taking into account α, the center of gravity of d^2 is

$$M(d^2) = A + 7/9\ (\mathrm{C} - 2B) + 32/3\alpha. \qquad (5)$$

The $L(L+1)$ correction has to be considered as the combination of two-particle interactions, $[L(L+1) - 6n]\alpha$, and an additive constant $6n\alpha$, [12].

Then by writing

$$M(d^2) = A + 7/9(\mathrm{C} - 2B) + 12\alpha - 4/3\alpha \qquad (6)$$

we have

$$M(d^n p) = [A + 7/9(C-2B) - 4/3\alpha]n(n-1)/2 + 6n\alpha + n[F_0(dp) - (G_1 + 7/2G_3)]$$
$$= A + (7n/18)(n-1)(C-2B) + (2n/3)(10-n)\alpha - n(G_1 + 7/2G_3), \quad (7)$$

where we have replaced $[n(n-1)/2]A + nF_0(dp)$ by A.

In the configuration $d^{n-1}sp$, we have in addition $(n-1)$ interactions $d-s$ and the interaction $s-p$.

Then, since

$$M(ds) = F_0(ds) - G'_{ds}/2$$

and

$$M(ps) = F_0(ps) - G'_{ps}/2$$

we obtain, from (7)

$$M'(d^{n-1}sp) = A' + 7/18(n-1)(n-2)(C'-2B') + (2/3)(n-1)(11-n)\alpha' - (n-1)(G'_1 + 7/2G'_3 + G'_{ds}/2) - G'_{ps}/2. \quad (8)$$

Since for $d^{n-2}s^2p$ the interactions $d-s$ and $s-p$ are constant and can thus be incorporated into the height of the configuration, we have from (7)

$$M''(d^{n-2}s^2p) = A'' + (7/18)(n-2)(n-3)(C''-2B'') - (2/3)(n-2)(12-n)\alpha'' - (n-2)(G''_1 + 7/2G''_3) \quad (9)$$

Now, by using (1) for the final parameters of Ti I, we obtain from (8) and (9)

$$M'(d^2sp) = A' - 3{,}950$$

$M''(ds^2p) = A'' - 350$, as A'' incorporates $6\alpha''$.

Since the final values, before the uniform treatment (see ref. [6]) of A' and A'' for Ti I were

$$A' = 32{,}260 \text{ and } A'' = 40{,}240$$

then

$$D''(\mathrm{Ti}) = 11{,}580. \quad (11)$$

For Sc I, in the final results before the uniform treatment:

$$\begin{aligned} A' &= 24{,}920 \\ A'' &= 25{,}790 \\ G'_1 &= 330 \\ G'_3 &= 6 \\ G'_{ds} &= 1{,}930 \\ G'_{ps} &= 5{,}940. \end{aligned} \quad (12)$$

Then, since A' incorporates $6\alpha'$, we obtain from (8) and (9)

$$M'(dsp) = 20{,}634$$

$$M''(s^2p) = 25{,}790. \quad (13)$$

Thus,

$$D''(\mathrm{Sc}) = 5{,}156. \quad (14)$$

By assuming that D'' is a linear function of n, we would expect from (11) and (14)

$$D''(\mathrm{V}) = 18{,}000. \quad (15)$$

Now, from (8) and the values of the parameters in table 1

$$M'(d^3sp) = 37{,}780. \quad (16)$$

Then, from (15)

$$M''(d^2s^2p) = 55{,}780. \quad (17)$$

Assuming that the parameters of d^4p, d^3sp and d^2s^2p are in arithmetic progression, we finally obtain

$$A'' = 54{,}990. \quad (18)$$

Then, a new diagonalization was performed using the values of table 1 for the parameters of $d^4p + d^3sp$. The parameters pertaining to d^2s^2p had the following initial values:

$$\begin{aligned} A'' &= 54{,}990 \\ B'' &= 945 \\ C'' &= 3{,}072 \\ F''_2 &= 356 \\ G''_1 &= 311 \\ G''_3 &= 37 \\ \alpha'' &= 70 \\ J'(d^3sp - d^2s^2p) &= 1{,}088 \\ K'(d^3sp - d^2s^2p) &= 2{,}492 \\ H'(d^3sp - d^2s^2p) &= 172 \\ \zeta''_d = \zeta'_d &= \zeta_d = 146 \\ \zeta''_p = \zeta'_p &= \zeta_p = 124. \end{aligned} \quad (19)$$

A least-squares adjustment of the parameters was carried out in which A'' was fixed, the parameters, B, C, F_2, G_1, and G_3 were held in arithmetic progression, α, ζ_d, and ζ_p were made equal for the three configurations and the parameters H', J', K', and G were held equal to H, J, K, and G'_{ds}, respectively. The rms error was thus reduced from 345 to 249. In the least squares calculation of the next iteration, all levels inserted were below 43,000 cm^{-1}. Although all the experimental levels inserted into the least squares were assigned to the configurations $d^4p + d^3sp$, the eigenfunctions of some high levels inserted had contributions of up to 20 percent of d^2s^2p. Thus, a variation was attempted in which A'' was left to vary freely. The rms error was reduced from 236 to 231, with A'' assuming the very reasonable value of $54{,}424 \pm 741$.

In the least squares calculation of the final iteration of the uniform treatment 77 experimental terms splitting into 228 levels were inserted to yield an rms error

of only 216. Levels above 43,000 were not included, as many of them would show very high deviations if inserted into the least-squares. These high deviations are due to the fact that many of the terms above 43,000 either belong to, or are strongly perturbed by the configurations $(3d+4s)^4 5p$. In table 2, the experimental and calculated values of the levels and g-factors obtained from the least-squares calculation of the final iteration in the uniform treatment, are compared. The calculated values, percentage compositions and g-factors for all the 438 theoretically predicted levels are given. (The 45 levels assigned to $3d^2 4s^2 4p$ are included, since A'' was permitted to vary freely). Since G'_{ps} is much larger than G'_{ds} the $p-s$ interaction is stronger than the $d-s$ interaction. Consequently, the terms of d^3sp are coupled as $d^3(v_1 S_1 L_1)sp(^{1,3}\mathrm{P})SL$ and not $d^3s(S_2 L_1)pSL$ as given in AEL.

The final values of the parameters in the uniform treatment (see ref. [6]) are given in table 1.

The main reasons for fixing $\zeta_d = \zeta'_d$ and $\zeta_p = \zeta'_p$ are that the fitted values of the parameters are reasonable, and only small differences occur between ζ_d and ζ'_d as well as ζ_p and ζ'_p, but *very* large standard errors are associated with them. In fact, the latter two parameters had standard errors larger than the actual parameter values. Furthermore, as the results are from a uniform treatment, consideration was also given to the results of keeping ζ'_p and ζ'_d free in Sc I and Ti I. There, the above mentioned effects are even more pronounced.

Below the cutoff height of 43,000 there are 243 odd experimental levels in AEL. The following 15 levels were rejected from the final least squares:

1. The level $z\,^4\mathrm{S}$ at 28621.
2. The two levels of $w\,^2\mathrm{G}$ at 36629 and 36828.
3. The four levels of $3d^3 4s(b^3\mathrm{H})p\ y^4\mathrm{H}$ at 37481, 37517, 37566, and 37626.
4. The level $x\,^2\mathrm{S}$ at 40300.
5. The level $w\,^2\mathrm{P}_{3/2}$ at 40694.
6. The two levels of $3d^3 4s(b\,^1\mathrm{G})4pu\,^2\mathrm{H}$ at 42079 and 42221.
7. The level 2^e at 42237.
8. The three levels $w\,^6\mathrm{D}_{5/2,\,7/2,\,9/2}$ at 42480, 42587, and 42725.

3. Discussion

From the experimental results of Meggers and Russell [13], we note that the term $z\,^4\mathrm{S}$ is based only on combinations with the term $b\,^4\mathrm{P}$. Furthermore, as the lowest predicted term $^4\mathrm{S}$, i.e., $^2\mathrm{P}(^3\mathrm{P})\,^4\mathrm{S}$ is at 34065 and since for all the predicted levels in the neighborhood of 28,600 suitable experimental levels are known, the term $z\,^4\mathrm{S}$ was rejected.

In the range 33,500 to 38,500 two terms $^2\mathrm{G}$ are predicted. For the first term the main contribution is $(b\,^3\mathrm{F})\,^2\mathrm{G}$, whereas the second term is mostly $(^3\mathrm{H})\,^2\mathrm{G}$. However, in the narrower range of 36,600 to 37,300 there are the three experimental terms $d^4(b^3\mathrm{F})px^2\mathrm{G}$, $w\,^2\mathrm{G}$, and $d^4(a\,^3\mathrm{H})pv\,^2\mathrm{G}$. The experimental term $v\,^2\mathrm{G}$ was fitted to the theoretical term with the same assignment. The experimental term $x\,^2\mathrm{G}$ was then assigned to the other predicted term $^2\mathrm{G}$, since the experimental assignment $(b^3\mathrm{F})\,^2\mathrm{G}$ coincides with the major contribution of the predicted term, and also because $x\,^2\mathrm{G}$ is based on combinations with 7 even terms $a\,^2\mathrm{F}$, $a\,^2\mathrm{G}$, $b\,^2\mathrm{G}$, $a\,^2\mathrm{H}$, $b\,^2\mathrm{H}$, $a\,^4\mathrm{F}$, and $b\,^4\mathrm{F}$, whereas $w\,^2\mathrm{G}$ has combinations only with $a\,^2\mathrm{G}$ and $a\,^2\mathrm{H}$, [13]. Since there is no other predicted term to which the levels of $w\,^2\mathrm{G}$ could be assigned, $w\,^2\mathrm{G}$ was rejected.

In AEL, four experimental terms $z^4\mathrm{H}$, $y^4\mathrm{H}$, $x^4\mathrm{H}$, and $w^4\mathrm{H}$ are given, which should hopefully correspond to the four terms $^4\mathrm{H}$ which are predicted for the configurations $(d+s)^4\mathrm{p}$. Unfortunately, however, this correspondence is not feasible since the lowest predicted term $^4\mathrm{H}$, $^2\mathrm{G}(^3\mathrm{P})^4\mathrm{H}_{\mathrm{C.G.}}$ is at 29,750, whereas $z^4\mathrm{H}_{\mathrm{C.G.}}$ is at 32,856. In an earlier iteration, a variation was performed in which the four experimental terms $^4\mathrm{H}$ were assigned to the four theoretically predicted terms $^4\mathrm{H}$ with the same designations. Then, in the last-squares calculation the average deviations for the levels $^2\mathrm{G}(^3\mathrm{P})^4\mathrm{H}$ and $^2\mathrm{H}(^3\mathrm{P})^3\mathrm{H}$ were 2,269 and 3,244 respectively, and the rms error was 714. Subsequently, no experimental levels were assigned to $^2\mathrm{G}(^3\mathrm{P})^4\mathrm{H}$, the experimental levels $d^3s(b^3\mathrm{G})pz\,^4\mathrm{H}$ were assigned to $^2\mathrm{H}(^3\mathrm{P})\,^4\mathrm{H}$ and to the term $(^3\mathrm{G})\,^4\mathrm{H}$ was assigned the experimental term of the same designation. This left either $y^4\mathrm{H}$ or $x^4\mathrm{H}$ to assign to the theoretical term $(^3\mathrm{H})^4\mathrm{H}$. The term $x^4\mathrm{H}$ was chosen because:

1. it had the same designation as the theoretical term, whereas the designation of $y^4\mathrm{H}$ is given with a question mark in AEL,
2. the theoretical term $(^3\mathrm{H})^4\mathrm{H}$ is much closer to $x^4\mathrm{H}$ than to $y^4\mathrm{H}$,
3. the term $x^4\mathrm{H}$ is based on combinations with 5 even terms, whereas $y^4\mathrm{H}$ has combinations with 3 even terms.

Since there are no other terms of $(3d+4s)^4 4p$ to which the levels of $y^4\mathrm{H}$ could conceivably be assigned they were rejected.

In the range 36,000 to 43,000, suitable experimental levels correspond to *all* the predicted levels. The term $x\,^2\mathrm{S}$ is based only on three weak combinations [13], and so it was rejected.

To the theoretical term at 40,000, whose major contribution is $^2\mathrm{P}(^3\mathrm{P})^2\mathrm{P}$, is assigned the term $x\,^2\mathrm{P}$ rather than $w\,^2\mathrm{P}$ as for the former term both experimental levels are given, whereas the level $w\,^2\mathrm{P}_{1/2}$ is missing. It should be noted also that the deviation for $x\,^2\mathrm{P}_{3/2}$ is smaller by about 250 cm^{-1} than if $w\,^2\mathrm{P}_{3/2}$ were inserted.

Below 44,000 cm^{-1}, there are 5 predicted terms $^2\mathrm{H}$ to which the experimental terms $z\,^2\mathrm{H}$, $y\,^2\mathrm{H}$, $x\,^2\mathrm{H}$, $w\,^2\mathrm{H}$, and $v\,^2\mathrm{H}$ correspond. Although the levels of $u\,^2\mathrm{H}$ are based on 11 combinations with the 5 even terms $a\,^4\mathrm{F}$, $a\,^2\mathrm{G}$, $a\,^2\mathrm{H}$, $b\,^2\mathrm{H}$, and $b\,^2\mathrm{G}$ [13], this term is superfluous for $(3d+4s)^4 4p$ (it should be noted that it is not possible to reject $v\,^2\mathrm{H}$ and retain $u\,^2\mathrm{H}$, since the former is based upon more combinations with even terms than the latter, [13]).

From table 2, it is evident that there is no theoretical level of $(3d+4s)^4 4p$ to which the experimental level 2° at 42,237 could be assigned.

The three levels $w\ ^6D_{5/2,\ 7/2,\ 9/2}$ most probably should be assigned to $^4F(^3P)5pw\ ^6D$.

The following changes in designation were performed:

1. AEL $z\ ^2S_{1/2} \longrightarrow\ ^2P(^3P)^4P_{1/2}$
2. AEL $d\ ^3s(b\ ^3G)pz\ ^4H \longrightarrow\ ^2H(^3P)z\ ^4H$
3. $^2P(^3P)^2D \longleftrightarrow A^2D(^3P)^4F_{3/2,\ 5/2}$
4. $(A^3P)^4S \longleftrightarrow\ ^4P(^3P)^4S$
5. AEL $d^4(a\ ^3P)px\ ^4P \longrightarrow A^2D(^3P)x\ ^4P$
6. AEL $d^4(b\ ^3F)pw\ ^2F \longleftrightarrow A^2D(^3P)w\ ^2F$
7. $(A^3P)\ ^4D \longleftrightarrow (A^3F)\ ^4D$
8. AEL $d^3s(a\ ^5P)pw\ ^4P \longrightarrow (A^3P)w\ ^4P$
9. $A\ ^2D(^3P)u\ ^2D_{5/2} \longleftrightarrow (^3G)v\ ^2F_{5/2}$
10. AEL $d^3s(b\ ^1G)pt\ ^2G \longrightarrow (A^3F)t\ ^2G$
11. AEL $d^3s(a\ ^1H)pv\ ^2H \longrightarrow\ ^2G(^1P)v\ ^2H$
12. AEL $d^3s(b\ ^1D)pu\ ^2F \longrightarrow (^3D)u\ ^2F$
13. AEL $d^3s(a\ ^1P)pv\ ^2P \longrightarrow (^3D)v\ ^2P$

The lowest theoretically predicted term ^2S is at 32,342. Thus, only one of the two experimental terms $z\ ^2S$ or $y\ ^2S$ can be assigned to it. The term $y\ ^2S$ was chosen because:

1. its deviation is smaller by about 170 than if $z\ ^2S$ were chosen,
2. the combinations of $y\ ^2S$ are only with doublets, whereas $z\ ^2S$ is based on combinations also with $a\ ^4D$ and $a\ ^6D$,
3. the experimental g-factor of $y\ ^2S$ fits better to the theoretical g-factor of the lowest predicted term ^2S.

In the range 31,000 to 33,000 there is now left vacant the theoretical term ^4P whose main contribution is $^2P(^3P)^4P$, and the sole unassigned term is $z\ ^2S$. Since $z\ ^2S$ is based on combinations with $a\ ^2P$, $b\ ^2P$, $a\ ^4D$, and $a\ ^6D$, and since it fits quite well in value and g-factor to the theoretical level $^2P(^3P)^4P_{1/2}$, we performed the first change above.

The reasons for changing the assignment of $z\ ^4H$ were considered previously.

As mentioned already by Meggers and Russell [13], the configuration assignments of many odd doublets and quartets are doubtful. The exchanges 4–8 and 10–12 illustrate this point, as in all cases the contributions in the eigenfunctions of the experimental assignments are very small.

By means of the exchange 9, the calculated splittings of the terms $v\ ^2F$ and $u\ ^2D$ correspond more closely to the experimental splittings for these two terms.

With regard to the change 13, it should be noted that there is strong mixing between the eigenfunctions of the terms $(^3D)^2P$ and $^2P(^3P)^2P$.

Although the number of changes in assignment performed is not as large as may be expected on the basis of the complexity of this spectrum and the difficulties involved in determining the configuration assignments prior to a theoretical investigation, below 43,000 there are *22* experimental terms in AEL without configuration designations. Of these, the terms $z\ ^2S$, $w\ ^2G$, and $w\ ^2P$ were rejected, whereas for the other 19 terms the calculated configuration assignments are specified in table 2.

The level 1^0 has combinations with $a\ ^4P$, $a\ ^4D$, $b\ ^4D$, $a\ ^4F$, and $f\ ^6P$ with J equal to 1/2, 3/2, and 5/2. The theoretical terms $^2P(^3P)^4S$ and $^2P(^3P)^2S$ are predicted at around 34,000 and neither term has as yet any assigned corresponding experimental term. Since the deviation obtained on fitting the level 1^0 to $^2P(^3P)^4S$ is only -46 (for $^2P(^3P)^2S$ it would be about -450) and since the level 1^0 has combinations with even levels of J equal to 5/2 and the sextet $f\ ^6P$, we assigned it to the theoretical term $^2P(^3P)^4S$.

Below 43,000 cm^{-1} the following theoretical terms had no experimental counterparts:

1.	$^2G(^3P)^4H$	29,583 – 29,942
2.	$^2P(^3P)^4P$	31,467 – 31,669
3.	$^2P(^3P)^2S$	34,476
4.	$^2H(^3P)^4I$	34,950 – 35,223
5.	$A^2D(^3P)^2P + ^2P(^3P)^2P$	35,484 – 35,749.

Most of the experimental and calculated g-factors correspond quite closely. However, there are some exceptions due to unsuitably calculated eigenvectors. For example, the experimental g-factor of $u\ ^4F_{3/2}$ is 0.54. However, as the theoretical eigenfunction contains 13 percent of ^4S with g-factor of 2.00, the calculated g-factor is 0.803. Similarly, the experimental g-factor of $x\ ^4S$ is 2.00, but as the theoretical eigenfunction contains contributions of $^2D_{3/2}$ and $^4D_{3/2}$ with g-factors of 0.800 and 1.200, respectively, the calculated g-factor of $x\ ^4S$ is 1.539. On the other hand, since the theoretical g-factors for $^2S_{1/2}$ and $^2P_{1/2}$ are 2.000 and 0.667 respectively, and the experimental g-factors for $w\ ^2S_{1/2}$ and $w\ ^2P_{1/2}$ are 1.50 and 1.14, it is evident that the experimental mixing between these two levels is very strong. However, the theoretical eigenfunctions are almost pure ^2S and ^2P and hence the calculated g-factors are 2.020 and 0.672, respectively.

4. Table Entries

In the column "NAME" the calculated designation of the term is given. Whenever the terms of the parent d^n have different seniorities these are denoted by the letters A and B, the lower calculated term being designated by A. Whenever a calculated term has a corresponding experimental term the small letters z,y,x . . . are used as in AEL. The terms of d^3sp are denoted by $d^3v_1S_1L_1(sp^{1,3}P)SL$. The terms of d^4p are differentiated from those of d^2s^2p by using a star for the latter terms.

The entries in the columns "J", "OBS. LEVEL cm^{-1}", "CALC. LEVEL cm^{-1}" "OBS. g-FACT." and "CALC. g-FACT." are self evident. In the column "PERCENTAGE" for each calculated level either the three highest contributions or all those contributions exceeding 5 percent are given.

Whenever the experimental and calculated term designations differ, the experimental designation is entered in the column "AEL", using the notation of C. E. Moore [8]. In many instances the exchanges involve complete terms rather than isolated levels. Unless specified otherwise the entries in the column "AEL" pertain to exchanges in terms.

The column "O–C" gives the difference between the observed and calculated values of the levels.

The entries are in the order of increasing energy of the calculated terms.

The work described in this paper was supported in part by the National Bureau of Standards, Washington, D.C.

TABLE 2. *Observed and calculated levels of* V I $(3d+4s)^4 4p$

Name	J	Percentage	AEL		Obs. level (cm^{-1})	Calc. level (cm^{-1})	O–C	Obs. g-factor	Calc. g-factor
			Config.	Desig.					
$^4F(^3P)^6G$	3/2	100	$3d^34s(a\,^5F)4p$	$z\,^6G$	16,361	16,354	7	0.00	0.000
	5/2	100			16,450	16,426	24	0.78	0.857
	7/2	100			16,573	16,527	46	1.10	1.143
	9/2	100			16,729	16,655	74	1.22	1.273
	11/2	100			16,917	16,810	107	1.26	1.343
	13/2	100			17,136	16,992	144	1.43	1.385
$^4F(^3P)^6D$	1/2	$90+8\ (^5D)^6D$	$3d^34s(a\,^5F)4p$	$z\,^6D$	18,086	18,075	11	3.20	3.331
	3/2	$89+8\ (^5D)^6D$			18,126	18,117	9	1.76	1.865
	5/2	$89+8\ (^5D)^6D$			18,198	18,187	11	1.58	1.656
	7/2	$89+8\ (^5D)^6D$			18,302	18,287	15	1.56	1.586
	9/2	$89+8\ (^5D)^6D$			18,438	18,417	21	1.55	1.555
$^4F(^3P)^6F$	1/2	95	$3d^34s(a\,^5F)4p$	$z\,^6F$	18,120	18,174	−54	−0.44	−0.665
	3/2	95			18,174	18,218	−44	1.14	1.068
	5/2	95			18,259	18,291	−32	1.28	1.315
	7/2	95			18,372	18,392	−20	1.28	1.398
	9/2	95			18,513	18,519	−6	1.38	1.435
	11/2	96			18,680	18,673	7	1.42	1.454
$^4F(^3P)^4D$	1/2	90	$3d^34s(a\,^3F)4p$	$z\,^4D$	20,606	20,649	−43	−0.04	0.000
	3/2	90			20,688	20,723	−35	1.21	1.200
	5/2	90			20,828	20,850	−22	1.35	1.371
	7/2	90			21,033	21,032	1	1.45	1.429
$^4F(^3P)^4G$	5/2	93	$3d^34s(a\,^3F)4p$	$z\,^4G$	21,841	21,948	−107	0.55	0.572
	7/2	93			21,964	22,049	−85	0.96	0.984
	9/2	93			22,121	22,180	−59	1.16	1.172
	11/2	93			22,314	22,342	−28	1.24	1.273
$^4F(^3P)^4F$	3/2	94	$3d^34s(a\,^3F)4p$	$z\,^4F$	23,088	23,118	−30	0.39?	0.404
	5/2	94			23,211	23,209	2	0.98?	1.029
	7/2	95			23,353	23,328	25	1.23	1.238
	9/2	95			23,520	23,476	44	1.31	1.333
$^4F(^3P)^2D$	3/2	89	$3d^34s(a\,^3F)4p$	$z\,^2D$	23,609	23,997	−388	0.76	0.796
	5/2	89			23,935	24,285	−350	1.32?	1.200
$(^5D)^6P$	3/2	$71+29\,^4P(^3P)^6P$			24,648	24,611	37	2.34	2.398
	5/2	$71+29\,^4P(^3P)^6P$			24,728	24,683	45	1.85	1.884
	7/2	$71+29\,^4P(^3P)^6P$			24,839	24,783	56	1.67	1.714
$(^5D)^6F$	1/2	95			24,789	24,725	64	−0.58	−0.662
	3/2	95			24,830	24,770	60	1.02	1.067
	5/2	95			24,899	24,844	55	1.23	1.314
	7/2	96			24,993	24,947	46	1.37	1.397
	9/2	96			25,112	25,076	36	1.41	1.434
	11/2	96			25,254	25,331	23	1.41	1.454

TABLE 2. *Observed and calculated levels of* V I $(3d+4s)^4 4p$ – Continued

Name	J	Percentage	AEL		Obs. level (cm^{-1})	Calc. level (cm^{-1})	O–C	Obs. g-factor	Calc. g-factor
			Config.	Desig.					
$(^5D)^4P$	1/2	89			24,771	25,067	−296	2.54	2.669
	3/2	89			24,915	25,206	−291	1.71	1.733
	5/2	89			25,131	25,424	−293	1.59	1.599
$^4F(^3P)^2G$	7/2	93	$3d^34s(a\ ^3F)4p$	$z\ ^2G$	26,022	25,954	68	0.92	0.891
	9/2	90			26,345	26,165	180	1.13	1.121
$(^5D)^4D$	1/2	$65+30\ ^4F(^1P)^4D$			26,183	26,013	170	−0.06	0.000
	3/2	$65+29\ ^4F(^1P)^4D$			26,249	26,073	176	1.17	1.196
	5/2	$65+28\ ^4F(^1P)^4D$			26,353	26,167	186	1.34	1.364
	7/2	$63+27\ ^4F(^1P)^4D$			26,480	26,281	199	1.39	1.419
$(^5D)^4F$	3/2	$76+17\ ^4F(^1P)^4F$			25,931	26,179	−248	0.42	0.412
	5/2	$73+16\ ^4F(^1P)^4F$			26,004	26,245	−241	0.98	1.051
	7/2	$67+15\ ^4F(^1P)^4F$			26,122	26,328	−206	1.15	1.269
	9/2	$64+14\ ^4F(^1P)^4F+11(^5D)^6D$			26,172	26,420	−248	1.23	1.353
$(^5D)^6D$	1/2	$82+10\ ^4F(^3P)^6D$			26,397	26,327	70	3.25	3.326
	3/2	$82+10\ ^4F(^3P)^6D$			26,438	26,367	71	1.86	1.860
	5/2	$81+10\ ^4F(^3P)^6D$			26,506	26,437	69	1.59	1.643
	7/2	$78+10\ ^4F(^3P)^6D$			26,605	26,545	60	1.58	1.564
	9/2	$72+10(^5D)\ ^4F+9\ ^4F(^3P)^6D$			26,738	26,697	41	1.50	1.526
$^4F(^3P)^2F$	5/2	97	$3d^34s(a\ ^3F)4p$	$z\ ^2F$	27,188	27,100	88	1.01?	0.857
	7/2	97			27,471	27,345	126	1.01	1.143
$^4P(^3P)^6D$	1/2	91	$3d^34s(a\ ^5P)4p$	$x\ ^6D$	28,314	28,327	−13	3.23	3.330
	3/2	91			28,369	28,369	0	1.82	1.866
	5/2	91			28,462	28,440	22	1.58	1.657
	7/2	91			28,596	28,542	54	1.52	1.587
	9/2	91			28,768	28,676	92	1.47	1.555
$^4P(^3P)^6P$	3/2	$71+29(^5D)^6P$	$3d^34s(a\ ^5P)4p$	$y\ ^6P$	29,203	29,009	194	2.32	2.399
	5/2	$71+29(^5D)^6P$			29,296	29,086	210	1.76	1.885
	7/2	$71+29(^5D)^6P$			29,418	29,185	233	1.62	1.714
$^2G(^3P)^4H$	7/2	$87+10\ ^2H(^3P)^4H$				29,583			0.667
	9/2	$87+10\ ^2H(^3P)^4H$				29,677			0.970
	11/2	$87+10\ ^2H(^3P)^4H$				29,796			1.133
	13/2	$88+10\ ^2H(^3P)^4H$				29,942			1.231
$^4P(^3P)^4P$	1/2	$80+9\ A^2D(^3P)^4P$	$3d^34s(c\ ^3P)4p$	$y\ ^4P$	30,022	30,095	−73	2.67	2.664
	3/2	$82+8\ A^2D(^3P)^4P$			30,095	30,148	−53	1.74	1.733
	5/2	$83+7\ A^2D(^3P)^4P$			30,121	30,172	−51	1.67	1.605
$^2G(^3P)^4G$	5/2	$65+30\ ^4F(^1P)^4G$	$3d^34s(b\ ^3G)4p$	$y\ ^4G$	30,636	30,453	183	0.53	0.572
	7/2	$68+27\ ^4F(^1P)^4G$			30,694	30,528	166	0.93	0.984
	9/2	$70+25\ ^4F(^1P)^4G$			30,772	30,622	150	1.13	1.171
	11/2	$73+22\ ^4F(^1P)^4G$			30,864	30,732	132	1.21	1.272
$^4P(^3P)^6S$	5/2	96	$3d^34s(a\ ^5P)4p$	$z\ ^6S$	30,833	31,018	−185		1.985
$^2G(^3P)^4F$	3/2	$79+7\ A^2D(^3P)^4F$	$3d^34s(b\ ^3G)4p$	$x\ ^4F$	31,200	31,393	−193	0.38	0.401
	5/2	$80+7\ A^2D(^3P)^4F$			31,229	31,412	−183	1.01	1.029
	7/2	$80+6\ A^2D(^3P)^4F$			31,268	31,441	−173	1.21	1.238
	9/2	$81+6\ A^2D(^3P)^4F$			31,318	31,481	−163	1.32	1.333

TABLE 2. *Observed and calculated levels of* V I $(3d+4s)^4 4p$ – Continued

Name	J	Percentage	AEL		Obs. level (cm^{-1})	Calc. level (cm^{-1})	O–C	Obs. g-factor	Calc. g-factor
			Config.	Desig.					
$^2P(^3P)^4P$	1/2	$63+10A^2D(^3P)^4P$		$z\,^2S$	31,786	31,385	401	2.30	2.661
	3/2	$62+11A^2D(^3P)^4P$				31,467			1.731
	5/2	$61+13A^2D(^3P)^4P$				31,669			1.607
$^4F(^1P)^4G$	5/2	$62+23^2G(^3P)^4G$	$3d^34s(a\,^5F)4p$	$x\,^4G$	31,398	31,518	−120	0.53	0.572
	7/2	$64+20^2G(^3P)^4G$			31,541	31,616	−75	0.95	0.984
	9/2	$66+18^2G(^3P)^4G$			31,722	31,743	−21	1.12	1.171
	11/2	$69+15^2G(^3P)^4G$			31,937	31,902	35	1.20	1.272
$^2P(^3P)^4D$	1/2	$56+16^4P(^3P)^4D$		$x\,^4D$	32,349	32,093	256	0.08	0.003
	3/2	$58+16^4P(^3P)^4D$			32,456	32,191	265	1.17	1.200
	5/2	$59+14^4P(^3P)^4D$			32,660	32,340	320	1.29	1.370
	7/2	$60+12^4P(^3P)^4D$			32,891	32,523	368	1.35	1.427
$(A^3P)^2S$	1/2	$33+34^2P(^3P)^2S+10^4P(^3P)^2P$		$y\,^2S$	31,962	32,342	−380	2.21	1.734
$^4F(^1P)^4F$	3/2	$61+20(^5D)^4F$	$3d^34s(a\,^5F)4p$	$w\,^4F$	32,738	32,587	151	0.52	0.402
	5/2	$61+19(^5D)^4F$			32,847	32,679	168	1.01	1.029
	7/2	$61+19(^5D)^4F$			32,989	32,805	184	1.18	1.238
	9/2	$61+19(^5D)^4F$			33,155	32,963	192	1.30	1.333
$^2H(^3P)^4H$	7/2	$62+22(^3H)^4H$	$3d^34s(b\,^3G)4p$	$z\,^4H$	32,692	32,739	−47	0.68	0.689
	9/2	$64+23(^3H)^4H$			32,788	32,818	−30	0.98	0.980
	11/2	$68+25(^3H)^4H$			32,898	32,908	−10	1.11	1.133
	13/2	$69+25(^3H)^4H$			32,964	32,965	−1	1.21	1.231
$^4P(^3P)^2P$	1/2	$53+15(A^3P)^2P+8^2P(^3P)^2S$		$z\,^2P$	32,725	32,828	−103	0.73?	0.899
	3/2	$64+18(A^3P)^2P$			32,768	32,824	−56	1.22	1.329
$^2G(^3P)^2G$	7/2	$81+6^2H(^3P)^4H$		$y\,^2G$	33,360	33,377	−17	0.91	0.871
	9/2	$84+5^2H(^3P)^4H$			33,307	33,307	0	1.03	1.099
$^2G(^3P)^2H$	9/2	$85+8^2H(^3P)^2H$		$z\,^2H$	33,640	33,546	94	0.92	0.910
	11/2	$87+8^2H(^3P)^2H$			33,695	33,588	107	1.09	1.090
$^2G(^3P)^2F$	5/2	$79+8A^2D(^3P)^2F$		$y\,^2F$	33,538	33,758	−230	0.85	0.864
	7/2	$76+8A^2D(^3P)^2F$			33,481	33,698	−217	1.11	1.152
$^4P(^3P)^4D$	1/2	$68+14^2P(^3P)^4D$	$3d^34s(c\,^3P)4p$	$w\,^4D$	33,967	33,946	21	0.09	0.003
	3/2	$57+12^2P(^3P)^4D$			33,976	33,923	53	0.80	1.136
	5/2	$63+13^2P(^3P)^4D$			34,066	33,935	131	1.30	1.353
	7/2	$68+12^2P(^3P)^4D$			34,128	33,965	163	1.35	1.416
$^2P(^3P)^4S$	3/2	$70+6^4P(^3P)^4S$		1^0	34,019	34,065	−46		1.802
$^2P(^3P)^2D$	3/2	$26+16A^2D(^3P)^2D$ $+16A^2D(^3P)^4F$		$v\,^4F$	34,030	34,060	−30	0.86	0.965
	5/2	$38+24A^2D(^3P)^2D$ $+14A^2D(^3P)^4F$		$v\,^4F$	34,168	34,189	−21	1.32?	1.179
$^2P(^3P)^2S$	1/2	$64+25(A^3P)^2S$				34,476			1.985
$A^2D(^3P)^4F$	3/2	$62+8^2P(^3P)^2D$		$y\,^2D$	34,429	34,480	−51	0.73	0.507
	5/2	$66+7^2P(^3P)^2D+7(^3G)^4F$		$y\,^2D$	34,487	34,509	−22	1.18	1.066
	7/2	$81+9(^3G)^4F$		$v\,^4F$	34,375	34,547	−172	1.21	1.241
	9/2	$82+9(^3G)^4F$			34,530	34,668	−138	1.41	1.333
$^4F(^1P)^4D$	1/2	$24+18(A^3P)^4D+16^2P(^3P)^4D$	$3d^34s(a\,^5F)4p$	$v\,^4D$	34,477	34,710	−233	0.00	0.004
	3/2	$25+16(A^3P)^4D+16^2P(^3P)^4D$			34,537	34,785	−248	1.05	1.197
	5/2	$27+17(A^3P)^4D+15^2P(^3P)^4D$			34,620	34,911	−291	1.28	1.369
	7/2	$28+15(A^3P)^4D+15^2P(^3P)^4D$			34,747	35,082	−335	1.35	1.427

TABLE 2. *Observed and calculated levels of* V I $(3d+4s)4p$ – Continued

Name	J	Percentage	AEL		Obs. level (cm^{-1})	Calc. level (cm^{-1})	O–C	Obs. g-factor	Calc. g-factor
			Config.	Desig.					
$^2H(^3P)^4I$	9/2	98				34,950			0.730
	11/2	99				35,019			0.966
	13/2	100				35,109			1.108
	15/2	100				35,223			1.200
$A^2D(^3P)^4D$	1/2	$58+16^4F(^1P)^4D$		$u\,^4D$	35,013	35,120	−107		0.022
	3/2	$58+15^4F(^1P)^4D$			35,092	35,172	−80	1.12	1.208
	5/2	$63+16^4F(^1P)^4D$			35,225	35,283	−58	1.32	1.371
	7/2	$67+16^4F(^1P)^4D$			35,379	35,399	−20	1.33	1.428
$A^2D(^3P)^2P$	1/2	$40+34^2P(^3P)^2P$				35,749			0.662
	3/2	$41+34^2P(^3P)^2P$				35,484			1.328
$(^3G)^2G$	7/2	$13+21(A^3F)^2G+13^2G(^3P)^2G$	$3d^4(b\,^3F)4p$	$x\,^2G$	36,461	36,656	−195	0.85	1.001
	9/2	$19+31(A^3F)^2G+19^2G(^3P)^2G$			36,539	36,728	−189	1.05	1.103
$(A^3F)^2F$	5/2	$26+25^2G(^3P)^2F+22A^2D(^3P)^2F$		$x\,^2F$	36,766	36,656	110	0.89	0.857
	7/2	$24+22^2G(^3P)^2F+19A^2D(^3P)^2F$			36,926	36,822	104	1.05	1.001
$^4P(^3P)^2D$	3/2	$38+17(A^3P)^2D+14(A^3F)^2D$		$x\,^2D$	36,416	36,769	−353	0.89	0.867
	5/2	$36+14(A^3P)^2D+13(A^3F)^2D$			36,701	36,818	−117	1.13	1.237
$^2H(^3P)^4G$	5/2	$42+19(A^3F)^4G+14(^3G)^4G$	$3d^34s(b\,^3H)4p$	$w\,^4G$	36,763	36,752	11		0.619
	7/2	$27+11(A^3F)^4G+8(^3G)^4G$			36,823	36,749	74	1.06	1.003
	9/2	$46+14(A^3F)^4G+13(^3G)^4G$			36,898	36,830	68	1.17	1.160
	11/2	$54+15(A^3F)^4G+15(^3G)^4G$			36,938	36,867	71	1.26	1.272
$A^2D(^3P)^4P$	1/2	$69+18^2P(^3P)^4P$	$3d^4(a\,^3P)4p$	$x\,^4P$	36,695	36,862	−167	2.51	2.629
	3/2	$44+24^4P(^3P)^4S+11^2P(^3P)^4P$			36,815	36,689	126	1.77	1.800
	5/2	$59+15^2P(^3P)^4P$			36,612	36,773	−161	1.54	1.513
$(A^3P)^2P$	1/2	$31(A^3P)^2P+32A^2D(^3P)^2P$			36,478	36,888	−410	0.74	0.683
	3/2	$29(A^3P)^2P+31A^2D(^3P)^2P$			36,580	37,090	−510	1.17	1.313
$^2H(^3P)^2H$	9/2	$67+9(^3H)^2H$		$y\,^2H$	37,181	36,936	245	0.73	0.925
	11/2	$74+10(^3H)^2H$			37,211	36,888	323	1.08	1.090
$^4P(^3P)^4S$	3/2	$41+25A^2D(^3P)^4P$	$3d^4(a\,^3P)4p$	$y\,^4S$	36,408	36,966	−558	1.85	1.881
$(^3H)^2G$	7/2	$60+11^2H(^3P)^2G$		$v\,^2G$	37,175	37,088	87	0.99	0.915
	9/2	$52+20(^3H)^4I+11^2H(^3P)^2G$			37,362	37,223	139	1.05	1.031
$(^3H)^4I$	9/2	$76+14(^3H)^2G$			37,285	37,124	161	0.87	0.814
	11/2	98			37,316	37,192	124	0.96	0.969
	13/2	99			37,404	37,301	103	1.08	1.109
	15/2	100			37,518	37,431	87	1.15	1.200
$(A^3P)^4D$	1/2	$46+14^4F(^1P)^4D$	$3d^4(b\,^3F)^4p$	$t\,^4D$	37,757	37,298	459	0.01	0.017
	3/2	$46+14^4F(^1P)^4D$			37,835	37,386	449	1.18	1.198
	5/2	$45+13^4F(^1P)^4D$			37,960	37,532	428	1.33	1.368
	7/2	$44+15^4F(^1P)^4D$			38,116	37,734	382	1.35	1.425
$A^2D(^3P)^2F$	5/2	$34+16(A^3F)^2F+13^2G(^3P)^2F$	$3d^4(b\,^3F)4p$	$w\,^2F$	37,343	37,532	−189	0.84	0.863
	7/2	$37+20(A^3F)^2F+13^2G(^3P)^2F$			37,475	37,632	−157	1.08	1.129
$(A^3F)^2D$	3/2	$30+27^4P(^3P)^2D+22^2P(^3P)^2D$			37,458	37,502	−44	0.80	0.804
	5/2	$35+26^4P(^3P)^2D+23^2P(^3P)^2D$			37,753	37,744	9	1.18	1.197
$(^3H)^2I$	11/2	$45+44^2H(^3P)^2I$			37,530	37,730	−200	0.94	0.927
	13/2	$42+46^2H(^3P)^2I$			37,606	37,787	−181	1.06	1.077

TABLE 2. *Observed and calculated levels of* V I $(3d+4s)^4 4p$—Continued

Name	J	Percentage	AEL		Obs. level (cm^{-1})	Calc. level (cm^{-1})	O–C	Obs. g-factor	Calc. g-factor
			Config.	Desig.					
$(A^3F)^4G$	5/2	$62+30^2H(^3P)^4G$			37,499	37,801	−302	0.60	0.574
	7/2	$57+26^2H(^3P)^4G$			37,556	37,831	−275	1.02	0.957
	9/2	$57+24^2H(^3P)^4G$			37,644	37,894	−250	1.15	1.147
	11/2	$58+23^2H(^3P)^4G$			37,765	37,995	−230	1.22	1.254
$(^3H)^4H$	7/2	$46+27(^3G)^4H+13^2H(^3P)^4H$			38,246	38,064	182	0.67	0.696
	9/2	$43+24(^3G)^4H+12^2H(^3P)^4H$			38,324	38,144	180	0.93	0.988
	11/2	$45+23(^3G)^4H+12^2H(^3P)^4H$			38,405	38,229	176	1.11	1.140
	13/2	$52+27(^3G)^4H+14^2H(^3P)^4H$			38,483	38,311	172	1.22	1.229
$(^3H)^2H$	9/2	$55+17^2H(^3P)^2H$			38,124	38,213	−89	0.88	0.914
	11/2	$54+18^2H(^3P)^2H$			38,221	38,299	−78	1.10	1.095
$^2H(^3P)^2G$	7/2	$78+9^2F(^3P)^2G$		$u\ ^2G$	38,611	38,676	−65	0.88?	0.890
	9/2	$78+9^2F(^3P)^2G$			38,530	38,618	−88	0.99	1.111
$^2H(^3P)^2I$	11/2	$53+46(^3H)^2I$			39,009	38,687	322	0.92	0.924
	13/2	$50+49(^3H)^2I$			39,081	38,748	333	1.06	1.078
$(A^3P)^4S$	3/2	$40+14(A^3P)^4P+13^4P(^3P)^4S$	$3d^34s(c\ ^3P)4p$	$x\ ^4S$	39,847	39,279	568	2.00	1.539
$(A^3F)^4F$	3/2	$47+13(A^3P)^4S$			39,267	39,280	−13	0.54	0.803
	5/2	$67+9^2F(^3P)^4F$			39,300	39,329	−29	1.00	1.027
	7/2	$66+9^2F(^3P)^4F$			39,342	39,357	−15	1.21	1.234
	9/2	$66+9^2F(^3P)^4F$			39,391	39,389	2	1.30	1.330
$(A^3P)^4P$	1/2	$72+16^2P(^3P)^4P$	$3d^34s(a\ ^5P)4p$	$w\ ^4P$	39,237	39,413	−176	2.57	2.655
	3/2	$43+16(A^3P)^4S+9^2P(^3P)^4P$			39,249	39,625	−376	1.60	1.615
	5/2	$52+11^2P(^3P)^4P$			39,423	39,605	−182	1.52	1.496
$(A^3P)^2D$	3/2	$40+17(A^3F)^2D$			39,884	39,556	328	0.92	0.987
	5/2	$40+16(A^3F)^2D$			40,119	39,934	185	1.14	1.155
$A^2D(^3P)^2D$	3/2	$37+21^2P(^3P)^2D$	$3d^34s(a\ ^1P)4p$	$u\ ^2D$	40,225	39,957	268	0.70	0.967
	5/2	$43+27^2P(^3P)^2D$		$v\ ^2F$	40,154	39,849	305		1.276
$^2P(^3P)^2P$	1/2	$51+21A^2D(^3P)^2P$		$x\ ^2P$	40,329	39,893	436		0.673
	3/2	$35+14A^2D(^3P)^2P$ $+13A^2D(^3P)^2D$			40,437	40,076	361	1.52	1.167
$(^3H)^4G$	5/2	$32+21(^3G)^4G+9^2H(^3P)^4G$			39,962	39,999	−37	0.53	0.686
	7/2	$38+25(^3G)^4G+11^2H(^3P)^4G$			40,001	40,031	−30	0.99	0.995
	9/2	$42+27(^3G)^4G+12^2H(^3P)^4G$			40,039	40,064	−25	1.19	1.170
	11/2	$42+28(^3G)^4G+13^2H(^3P)^4G$			42,064	40,070	−6	1.23	1.270
$(A^3F)^4D$	1/2	$63+18(A^3P)^4D$	$3d^4(a\ ^3P)4p$	$s\ ^4D$	39,878	40,066	−188	0.01	0.011
	3/2	$59+18(A^3P)^4D$			39,935	40,111	−176	1.10	1.189
	5/2	$46+16(A^3P)^4D$			40,000	40,190	−190	1.33	1.277
	7/2	$44+18(A^3P)^4D$			40,126	40,228	−102	1.38	1.330
$(^3G)^2F$	5/2	$40+12(A^3F)^4D+12A^2D(^3P)^2F$	$3d^34s(a\ ^1P)4p$	$u\ ^2D$	40,326	40,250	76	1.12	0.912
	7/2	$44+14(A^3F)^4D+13A^2D(^3P)^2F$		$v\ ^2F$	40,587	40,286	301	1.01	1.183
$(^3G)^4H$	7/2	$59+22(^3H)^4H+7^2H(^3P)^4H$			40,315	40,270	45	0.65	0.718
	9/2	$66+24(^3H)^4H+8^2H(^3P)^4H$			40,379	40,328	51	0.92	0.974
	11/2	$67+23(^3H)^4H+8^2H(^3P)^4H$			40,452	40,411	41	1.08	1.134
	13/2	$70+23(^3H)^4H+7^2H(^3P)^4H$			40,536	40,508	28	1.22	1.230
$(A^3F)^2G$	7/2	$44+30(^3G)^2G$	$3d^34s(b\ ^1G)4p$	$t\ ^2G$	41,437	41,043	394	0.90	0.890
	9/2	$42+30(^3G)^2G$			41,539	41,137	402	1.04	1.106

TABLE 2. *Observed and calculated levels of* V I $(3d+4s)^4 4p$—Continued

Name	J	Percentage	AEL		Obs. level (cm^{-1})	Calc. level (cm^{-1})	O–C	Obs. g-factor	Calc. g-factor
			Config.	Desig.					
$(^3G)^2H$	9/2	$66+11^2G(^3P)^2H$		$w\ ^2H$	40,981	41,232	−251	0.99	0.914
	11/2	$71+10^2G(^3P)^2H$			40,920	41,199	−279	0.96?	1.092
$(^3D)^2F$	5/2	$41+19(A^3F)^2F+12(^3F)^2F^*$	$3d^34s(b\ ^1D)4p$	$u\ ^2F$	41,950	41,479	471	0.84	0.858
	7/2	$43+13(A^3F)^2F+11(^3F)^2F^*$			42,021	41,526	495	1.11	1.143
$^2G(^1P)^2H$	9/2	$43+28(^1I)^2H$	$3d^34s(a\ ^1H)4p$	$v\ ^2H$	41,501	41,653	−152	0.87	0.916
	11/2	$42+30(^1I)^2H$			41,660	41,750	−90	1.05	1.095
$(^3G)^4F$	3/2	$47+20(^3D)^4F$			41,389	41,828	−439	0.42	0.406
	5/2	$25+27(^3G)^4G+14(^3D)^4F$			41,429	41,705	−276	0.89?	0.810
	7/2	$26+26(^3G)^4G+13(^3D)^4F$			41,492	41,736	−244	1.15	1.121
	9/2	$27+23(^3G)^4G+12(^3D)^4F$			41,599	41,817	−217	1.23	1.260
$(^3D)^2P$	1/2	$36+28^2P(^3P)^2P$	$3d^34s(a\ ^1P)4p$	$v\ ^2P$	42,481	41,863	618	1.14	0.672
	3/2	$35+30^2P(^3P)^2P$			42,318	41,783	535	1.34	1.344
$(^3G)^4G$	5/2	$27+22(^3G)^4F+17(^3H)^4G$			41,655	41,870	−215	0.58	0.796
	7/2	$26+26(^3G)^4F+13(^3H)^4G$			41,758	41,957	−199	1.03	1.102
	9/2	$29+18(^3G)^4F+18(^3H)^4G$			41,861	42,031	−170	1.20	1.239
	11/2	$52+30(^3H)^4G$			41,918	41,954	−36	1.20	1.267
$^4P(^1P)^4P$	1/2	$43+39(^3D)^4P$		$v\ ^4P$	41,752	42,087	−335	2.56	2.467
	3/2	$39+38(^3D)^4P$			41,848	42,135	−287	1.62	1.652
	5/2	$38+40(^3D)^4P$			42,010	42,211	−201	1.48	1.572
$^4P(^1P)^4D$	1/2	$53+17(^3F)^4D^*$	$3d^34s(a\ ^5P)4p$	$r\ ^4D$	41,928	42,095	−167	0.04	0.164
	3/2	$49+16(^3F)^4D^*$			41,999	42,164	−165	1.20	1.267
	5/2	$51+16(^3F)^4D^*$			42,138	42,240	−102	1.33	1.394
	7/2	$58+18(^3F)^4D^*$			42,246	42,327	−81	1.36	1.427
$^4P(^3P)^2S$	1/2	$83+10(A^3P)^2S$		$w\ ^2S$	42,362	42,279	83	1.50?	2.020
$^4P(^1P)^4S$	3/2	$70+14(A^3P)^4S$	$3d^34s(a\ ^5P)4p$	$w\ ^4S$	42,969	42,879	90	1.94	1.993
$(^1I)^2K$	13/2	100				43,678			0.934
	15/2	100				43,800			1.067
$(A^1G)^2F$	5/2	$40+28(A^3F)^2F$				43,857			0.858
	7/2	$37+25(A^3F)^2F$				43,818			1.111
$(^3D)^4F$	3/2	$73+18(^3G)^4F$				43,921			0.412
	5/2	$72+18(^3G)^4F$				43,946			1.033
	7/2	$72+18(^3G)^4F$				43,985			1.238
	9/2	$73+19(^3G)^4F$				44,033			1.333
$(A^1G)^2H$	9/2	$58+10(^3H)^2H$				44,112			0.959
	11/2	$40+38(^1I)^2I$				44,090			1.009
$(^3F)^2G^*$	7/2	$25+24(^3G)^2G+15^2H(^1P)^2G$				44,173			0.923
	9/2	$21+19(^3G)^2G+16(A^1G)^2H$				44,180			1.064
$(^3F)^2D^*$	3/2	$26+18(A^3P)^2D+17A^2D(^3P)^2D$				44,103			0.799
	5/2	$24+18(A^3P)^2D+17A^2D(^3P)^2D$				44,396			1.199
$(^1I)^2I$	11/2	$39+37(^3H)^2H$				44,263			1.006
	13/2	$78+15^2H(^1P)^2I$				44,226			1.077

TABLE 2. *Observed and calculated levels of* V I $(3d+4s)^4 4p$—Continued

Name	J	Percentage	AEL		Obs. level (cm^{-1})	Calc. level (cm^{-1})	O–C	Obs. g-factor	Calc. g-factor
			Config.	Desig.					
$(^3D)^2D$	3/2	$41+32(^3D)^4D$				44,398			0.965
	5/2	$57+16^2P(^1P)^2D+8(^3D)^4D$				44,265			1.209
$(^3D)^4D$	1/2	$77+16A^2D(^3P)^4D$				44,435			0.002
	3/2	$45+28(^3D)^2D+9A^2D(^3P)^4D$				44,474			1.028
	5/2	$70+12A^2D(^3P)^4D$				44,466			1.355
	7/2	$75+13A^2D(^3P)^4D$				44,470			1.425
$(^3F)^4G^*$	5/2	$49+33^2F(^3P)^4G$				44,501			0.575
	7/2	$47+35^2F(^3P)^4G$				44,592			0.985
	9/2	$45+38^2F(^3P)^4G$				44,706			1.172
	11/2	$42+41^2F(^3P)^4G$				44,844			1.272
$(A^1G)^2G$	7/2	$42+16^2H(^1P)^2G$				44,919			0.891
	9/2	$36+17^2H(^1P)^2G$				44,961			1.112
$(A^1S)^2P$	1/2	$65+15(^3D)^2P$				45,179			0.667
	3/2	$65+14(^3D)^2P$				45,277			1.333
$^2F(^3P)^4F$	3/2	$83+9(^3G)^4F$				45,485			0.401
	5/2	$82+9(^3G)^4F$				45,487			1.027
	7/2	$82+9(^3G)^4F$				45,492			1.236
	9/2	$81+9(^3G)^4F$				45,501			1.329
$(^3F)^2F^*$	5/2	$39+28(^3D)^2F$				45,608			0.859
	7/2	$41+29(^3D)^2F$				45,776			1.143
$^2F(^3P)^2D$	3/2	$28+34(A^1D)^2D$				46,078			0.808
	5/2	$26+31(A^1D)^2D$				46,035			1.223
$(^3D)^4P$	1/2	$48+40^4P(^1P)^4P$				46,158			2.622
	3/2	$48+41^4P(^1P)^4P$				46,148			1.721
	5/2	$44+41^4P(^1P)^4P$				46,122			1.575
$^2P(^1P)^2P$	1/2	$29+15A^2D(^1P)^2P$				46,478			0.705
	3/2	$26+11^2F(^3P)^4D$ + $14A^2D(^1P)^2P$				46,753			1.317
$^2F(^3P)^4D$	1/2	$80+5(^3D)^4D$				46,775			0.008
	3/2	$70+4(^3D)^4D$				46,730			1.218
	5/2	$80+5(^3D)^4D$				46,687			1.370
	7/2	$79+6(^3D)^4D$				46,613			1.426
$A^2D(^1P)^2F$	5/2	$19+28^2F(^3P)^4G+17(A^1D)^2F$				46,955			0.722
	7/2	$16+19(A^1D)^2F+11(A^1G)^2F$				46,917			1.137
$^2F(^3P)^4G$	5/2	$31+18(^3F)^4G^*+14(A^1D)^2F$				46,893			0.709
	7/2	$54+34(^3F)^4F^*$				46,968			0.992
	9/2	$54+39(^3F)^4G^*$				47,056			1.172
	11/2	$51+42(^3F)^4G^*$				47,179			1.273
$^2P(^1P)^2S$	1/2	$55+19(^3P)^2S^*$				47,278			1.989
$(^1I)^2H$	9/2	$19+25^2G(^1P)^2H+16^2H(^1P)^2H$				47,486			0.938
	11/2	$23+31^2G(^1P)^2H+17^2H(^1P)^2H$				47,565			1.090
$(^3F)^4F^*$	3/2	$75+15^4F(^1P)^4F$				47,501			0.406
	5/2	$75+14^4F(^1P)^4F$				47,617			1.030

TABLE 2. *Observed and calculated levels of* V I $(3d+4s)^4 4p$—Continued

Name	J	Percentage	AEL		Obs. level (cm^{-1})	Calc. level (cm^{-1})	O–C	Obs. g-factor	Calc. g-factor
			Config.	Desig.					
	7/2	$71+15{}^4F(^1P){}^4F$				47,771			1.218
	9/2	$63+14{}^4F(^1P){}^4F$				47,960			1.294
$^2G(^1P)^2G$	7/2	$32+18(A^1G)^2G+10(^3G)^2G$				47,584			0.910
	9/2	$24+14(A^1G)^2G+12(^3F)^4F^*$				47,780			1.120
$^2F(^3P)^2G$	7/2	$63+13(^1F)^2G$				48,054			0.890
	9/2	$62+15(^1F)^2G$				48,148			1.111
$(A^1D)^2D$	3/2	$37+23{}^2F(^1P)^2D+20(^3F)^2D^*$				48,125			0.795
	5/2	$36+24{}^2F(^1P)^2D+18(^3F)^2D^*$				48,205			1.192
$(A^1D)^2F$	5/2	$34+19(^1F)^2F+18{}^2F(^1P)^2F$				48,606			0.858
	7/2	$30+21(^1F)^2F+21{}^2F(^1P)^2F$				48,670			1.142
$^2H(^1P)^2I$	11/2	$86+11(^1I)^2I$				49,312			0.924
	13/2	$87+11(^1I)^2I$				49,440			1.077
$^2F(^3P)^2F$	5/2	$60+15(A^1D)^2F$				49,365			0.858
	7/2	$56+18(A^1D)^2F$				49,471			1.143
$A^2D(^1P)^2P$	1/2	$20+21(^3D)^2P+15(^1D)^2P^*$				49,563			0.675
	3/2	$19+19(^3D)^2P+15(^1D)^2P^*$				49,464			1.331
$^2H(^1P)^2H$	9/2	$49+35(^1I)^2H$				49,845			0.910
	11/2	$51+33(^1I)^2H$				49,881			1.091
$^2P(^1P)^2D$	3/2	$38+15(^3D)^2D$				49,973			0.806
	5/2	$39+15(^3D)^2D$				50,019			1.194
$(A^1D)^2P$	1/2	$56+20{}^2P(^1P)^2P$				50,919			0.667
	3/2	$52+20{}^2P(^1P)^2P$				51,076			1.328
$(^1F)^2F$	5/2	$39+20A^2D(^1P)^2F$				51,266			0.863
	7/2	$38+19A^2D(^1P)^2F$				51,209			1.143
$^2G(^1P)^2F$	5/2	$19+17(^1F)^2F+10(^3D)^2F$				51,452			0.860
	7/2	$19+17(^1F)^2F+10(^3F)^2F^*$				51,611			1.145
$(^3F)^4D^*$	1/2	$56+19{}^4P(^1P)^4D$				51,751			0.001
	3/2	$55+18{}^4P(^1P)^4D$				51,796			1.192
	5/2	$54+18{}^4P(^1P)^4D$				51,883			1.364
	7/2	$54+17{}^4P(^1P)^4D$				52,026			1.425
$(^1F)^2G$	7/2	$68+18{}^2F(^1P)^2G$				52,108			0.890
	9/2	$69+18{}^2F(^1P)^2G$				52,243			1.111
$A^2D(^1P)^2D$	3/2	$19+19(^3F)^2D^*+17(^1F)^2D$				52,424			0.808
	5/2	$17+20(^1F)^2D+20(^3F)^2D^*$				52,563			1.203
$(B^3P)^2D$	3/2	$47+30{}^2F(^1P)^2D$				52,684			0.801
	5/2	$47+30{}^2F(^1P)^2D$				52,541			1.202
$(B^3P)^4P$	1/2	90				54,607			2.661
	3/2	90				54,572			1.730
	5/2	89				54,548			1.598
$(^1F)^2D$	3/2	$28+26(B^3F)^2D$				55,068			0.773
	5/2	$26+27(B^3F)^2D$				54,936			1.199

TABLE 2. *Observed and calculated levels of* V I $(3d+4s)^4 4p$ – Continued

Name	J	Percentage	AEL		Obs. level (cm^{-1})	Calc. level (cm^{-1})	O–C	Obs. g-factor	Calc. g-factor
			Config.	Desig.					
$^2H(^1P)^2G$	7/2	$18+23(^3F)^2G^*+16(^1G)^2G^*$				55,259			0.900
	9/2	$19+23(^3F)^2G^*+16(^1G)^2G^*$				55,432			1.118
$(B^3F)^4F$	3/2	89				55,447			0.443
	5/2	$82+6(^3F)^4F^*$				55,439			1.054
	7/2	$60+15(B^3P)^4D$				55,423			1.284
	9/2	$83+7(^3F)^4F^*$				55,476			1.327
$(B^3P)^4D$	1/2	$49+33(B^3F)^4D$				55,580			0.004
	3/2	$48+30(B^3F)^4D$				55,575			1.188
	5/2	$45+29(B^3F)^4D$				55,559			1.343
	7/2	$36+30(B^3F)^4D$				55,524			1.371
$^2F(^1P)^2F$	5/2	$20+26(B^3F)^2F+10(^1D)^2F^*$				55,658			0.840
	7/2	$16+21(B^3F)^4G+19(B^3F)^2F$				55,804			1.094
$(B^3P)^2S$	1/2	$52+37(^3P)^2S^*$				55,852			1.997
$(B^3F)^4G$	5/2	87				55,919			0.596
	7/2	$66+15(B^3F)^2F$				55,930			1.034
	9/2	91				56,005			1.170
	11/2	95				56,062			1.273
$(B^3F)^4D$	1/2	$36+26B^2D(^3P)^4D$				56,483			0.001
	3/2	$37+26B^2D(^3P)^4D$				56,474			1.199
	5/2	$37+25B^2D(^3P)^4D$				56,452			1.371
	7/2	$38+24B^2D(^3P)^4D$				56,406			1.428
$(B^3F)^2F$	5/2	$36+22(^1D)^2F^*+19^2F(^1P)^2F$				58,583			0.867
	7/2	$35+21(^1D)^2F^*+20^2F(^1P)^2F$				57,555			1.128
$(B^3F)^2D$	3/2	$25+20(^1F)^2D+14^2F(^1P)^2D$				57,650			0.859
	5/2	$24+22(^1F)^2D+14^2F(^1P)^2D$				57,726			1.190
$(B^3P)^4S$	3/2	$44+29(B^3P)^2P$				57,885			1.626
$^2F(^1P)^2G$	7/2	$29+32(B^3F)^2G+15(^3F)^2G^*$				57,854			0.903
	9/2	$31+40(B^3F)^2G$				58,042			1.111
$(B^3P)^2P$	1/2	$67+23(^1D)^2P^*$				58,037			0.669
	3/2	$34+42(B^3P)^4S$				57,974			1.648
$(B^3F)^2G$	7/2	$55+23^2F(^1P)^2G$				58,145			0.891
	9/2	$45+23^2F(^1P)^2G$				57,897			1.111
$(^1D)^2D^*$	3/2	$54+14B^2D(^1P)^2D$				59,061			0.810
	5/2	$46+13B^2D(^1P)^2D$				59,106			1.172
$(^1D)^2F^*$	5/2	$20+19(B^1G)^2F+8(^1D)^2D^*$				59,350			1.003
	7/2	$18+19(B^1G)^2F$ $+16B^2D(^3P)^4D$				59,266			1.255
$B^2D(^3P)^4D$	1/2	$38+36(^3P)^4D^*+20(B^3F)^4D$				59,237			0.001
	3/2	$38+34(^3P)^4D^*+19(B^3F)^4D$				59,270			1.192
	5/2	$31+25(^3P)^4D^*+18(B^3F)^4D$				59,344			1.254
	7/2	$26+18(^3P)^4D^*+13(^1D)^2F^*$				59,450			1.316

TABLE 2. *Observed and calculated levels of* V I $(3d+4s)^4 4p$—Continued

Name	J	Percentage	AEL		Obs. level (cm^{-1})	Calc. level (cm^{-1})	O–C	Obs. g-factor	Calc. g-factor
			Config.	Desig.					
$(B^1G)^2H$	9/2	$88+6(^1G)^2H^*$				59,575			0.910
	11/2	$88+6(^1G)^2H^*$				59,722			1.091
$B^2D(^3P)^4F$	3/2	93				60,177			0.401
	5/2	93				60,185			1.029
	7/2	92				60,199			1.238
	9/2	93				60,222			1.333
$B^2D(^3P)^4P$	1/2	$49+23(^3P)^4P^*$				60,550			2.472
	3/2	$38+16(^3P)^4P^*+15(B^1D)^2D$				60,617			1.311
	5/2	$41+16(^3P)^4P^*$				60,522			1.432
$^2F(^1P)^2D$	3/2	$20+24B^2D(^3P)^4P$ $+16B^2D(^3P)^2D$				60,586			1.218
	5/2	$20+23B^2D(^3P)^4P$ $+19B^2D(^3P)^2D$				60,633			1.366
$(^3P)^4S^*$	3/2	$41+20(^1D)^2P^*+11^4P(^1P)^4S$				60,619			1.687
$(^3P)^2S^*$	1/2	$24+30(B^3P)^2S+19B^2D(^3P)^4P$				60,660			2.076
$(^1D)^2P^*$	1/2	$40+13(B^3P)^2P$				61,113			0.754
	3/2	$24+35(^3P)^4S^*$				60,917			1.628
$(^3P)^4D^*$	1/2	$47+24B^2D(^3P)^4D$				61,102			0.032
	3/2	$42+21B^2D(^3P)^4D$				61,123			1.157
	5/2	$41+18B^2D(^3P)^4D$				61,165			1.334
	7/2	$55+21B^2D(^3P)^4D$				61,229			1.424
$B^2D(^3P)^2D$	3/2	$44+16(^3P)^2D^*$				61,292			0.863
	5/2	$39+15(^3P)^2D^*$				61,329			1.237
$B^2D(^3P)^2F$	5/2	$57+17(B^1G)^2F$				61,707			0.859
	7/2	$47+16(B^1G)^2F$				61,720			1.117
$(B^1G)^2G$	7/2	$67+18^2F(^1P)^2G$				61,950			0.919
	9/2	$71+20^2F(^1P)^2G$				61,977			1.111
$(^3P)^2P^*$	1/2	$73+21B^2D(^3P)^2P$				63,190			0.667
	3/2	$73+22B^2D(^3P)^2P$				63,184			1.333
$(^3P)^4P^*$	1/2	$62+30B^2D(^3P)^4P$				63,541			2.665
	3/2	$64+29B^2D(^3P)^4P$				63,560			1.733
	5/2	$66+26B^2D(^3P)^4P$				63,600			1.599
$(B^1G)^2F$	5/2	$28+27B^2D(^3P)^2F+25^2F(^1P)^2F$				65,001			0.857
	7/2	$27+27B^2D(^3P)^2F+24^2F(^1P)^2F$				65,013			1.143
$(^1G)^2G^*$	7/2	$67+13^2H(^1P)^2G$				65,450			0.889
	9/2	$66+15^2H(^1P)^2G$				65,465			1.110
$B^2D(^3P)^2P$	1/2	93				66,142			0.667
	3/2	93				66,126			1.333
$(^1G)^2H^*$	9/2	$89+8(B^1G)^2H$				66,065			0.910
	11/2	$90+8(B^1G)^2H$				66,210			1.091

TABLE 2. *Observed and calculated levels of* V I $(3d+4s)^4 4p$ – Continued

Name	J	Percentage	AEL		Obs. level (cm^{-1})	Calc. level (cm^{-1})	O–C	Obs. g-factor	Calc. g-factor
			Config.	Desig.					
$(^3P)^2D^*$	3/2	$29+32^2F(^1P)^2D+12(^1D)^2D^*$				67,350			0.800
	5/2	$29+31^2F(^1P)^2D+12(^1D)^2D^*$				67,266			1.200
$(^1G)^2F^*$	5/2	$55+23B^2D(^1P)^2F$				68,160			0.857
	7/2	$55+24B^2D(^1P)^2F$				68,130			1.143
$(B^1D)^2P$	1/2	$79+7(^3P)^2P^*$				70,861			0.667
	3/2	$79+7(^3P)^2P^*$				70,768			1.333
$(B^1D)^2F$	5/2	$87+5(^1G)^2F^*$				71,444			0.858
	7/2	$87+5(^1G)^2F^*$				71,575			1.143
$(B^1D)^2D$	3/2	$65+27B^2D(^1P)^2D$				72,521			0.800
	5/2	$63+28B^2D(^1P)^2D$				72,560			1.199
$B^2D(^1P)^2D$	3/2	$56+26(B^1D)^2D$				75,334			0.803
	5/2	$55+26(B^1D)^2D$				75,357			1.200
$B^2D(^1P)^2P$	1/2	$49+13(^1S)^2P^*$				75,908			0.667
	3/2	$48+14(B^1S)^2P$				75,925			1.330
$B^2D(^1P)^2F$	5/2	$67+22(^1G)^2F^*$				76,208			0.857
	7/2	$67+22(^1G)^2F^*$				76,100			1.143
$(B^1S)^2P$	1/2	$66+24B^2D(^1P)^2P$				84,425			0.667
	3/2	$66+23B^2D(^1P)^2P$				84,548			1.333
$(^1S)^2P^*$	1/2	$79+15(B^1S)^2P$				91,043			0.667
	3/2	$79+16(B^1S)^2P$				91,193			1.333

5. References

[1] Racah, G., and Shadmi, Y., Bull. Res. Counc. Israel **8F**, No. 1, 15 (1959).

[2] Shadmi, Y., Bull. Res. Counc. Israel **10F**, No. 3, 109 (1962).

[3] Roth, C., Nat. Bur. Stand. (U.S.), 72A (Phys. and Chem.) No. 5, 505–520 (Sept.–Oct. 1968).

[4] Roth, C., Nat. Bur. Stand. (U.S.), 73A (Phys. and Chem.) No. 2, 125–157 (Mar.–Apr. 1969).

[5] Roth, C., Nat. Bur. Stand. (U.S.), 73A (Phys. and Chem.) No. 2, 159–171 (Mar.–Apr. 1969).

[6] Roth, C., Nat. Bur. Stand. (U.S.), **73A** (Phys. and Chem.), No. 5, 497–510 (Sept.–Oct. 1969).

[7] Roth, C., Nat. Bur. Stand. (U.S.), **73A** (Phys. and Chem.), No. 6, 599–609 (Nov.–Dec. 1969).

[8] Moore, C. E., "Atomic Energy Levels," Nat. Bur. Stand. (U.S.), Circ. 467, Vol. I. (1949), referred to as AEL

[9] Racah, G., Bull. Res. Counc. Israel **3**, 290 (1954).

[10] Condon, E. U., and Shortley, G. H., The Theory of Atomic Spectra (Cambridge University Press, 1935), referred to as TAS.

[11] Racah, G., Phys. Rev. **62**, 438 (1942), referred to as RII.

[12] Racah, G., Phys. Rev. **85**, 381 (1952).

[13] Meggers, W. F., and Russell, H. N., J. Res. NBS **17**, 125 (1936) RP906.

(Paper 74A2–588)

JOURNAL OF RESEARCH of the National Bureau of Standards—A. Physics and Chemistry
Vol. 74A, No. 2, March–April 1970

A Theoretical Investigation of the Configurations $(3d+4s)^5\,4p$ in Neutral Chromium (Cr I)

C. Roth*

(October 13, 1969)

Experimental levels of the configurations $(3d+4s)^5 4p$ in Cr I were compared with corresponding calculated values. On fitting 296 experimental levels by means of 20 free parameters a rms error of 183 cm^{-1} was obtained. All the 684 theoretically predicted levels and g-factors are calculated.

It is shown that the correction parameters β and T are not significant here.

Key words: Chromium; configurations in Cr I; configurations $(3d+4s)^5 4p$ in Cr I; configuration interaction; Cr I; energy levels of Cr I; first spectrum; g-values Cr I; parameters; theory; Zeeman effect.

1. Introduction

Theoretical investigations of odd configurations for trebly and doubly ionized atoms of the iron group were performed by the author [1–4][1,2]. The configurations $(3d+4s)^n 4p$ were considered previously for the arc spectra of calcium, scandium, titanium, and vanadium [5–7].

The configurations $(d+s)^5 p$ comprise 272 terms splitting into 684 levels. In AEL [8], 94 terms splitting into 310 levels are assigned to the configurations $3d^5 4p + 3d^4 4s 4p$. In addition 2 terms splitting into 6 levels have no configuration designation and 3 further odd levels are given with no term designations.

The initial parameters were obtained after examining the final values of Ca I, Sc I, Ti I, and V I [6–7]. By using least squares optimization the best straight lines were obtained for all the parameters[3] and then the values of Cr I were extrapolated. Then, initially

$$\begin{aligned} B &= 610 \\ B' &= 800 \\ C &= 2700 \\ C' &= 2860 \\ G'_{ds} &= 1430 \\ F_2 &= 170 \\ F'_2 &= 280 \\ G'_{ps} &= 6200 \\ G_1 &= 230 \\ G'_1 &= 250 \\ G_3 = G'_3 &= 17 \\ \alpha = \alpha' &= 65 \\ H &= 125 \\ J &= 1000 \\ K &= 2500 \\ \zeta = \zeta'_d &= 200 \\ \zeta_p = \zeta'_p &= 170. \end{aligned} \tag{1}$$

For J and K the final values of V I were taken, since these parameters did not behave regularly from Ca I to V I. For H only the values of Ti I and V I were considered.

The initial value for the height of the configuration d^4sp was obtained by considering the electrostatic matrices of ^{7}F, ^{7}D, and ^{5}I, [9], all of order 1.

Now,

$$A' - 21B' - 4G'_{ds} - 2F'_2 - G'_{ps} - 10G'_1 - 20G'_3 + 6\alpha' = {}^7\mathrm{F}_{\mathrm{C.G.}} = 25{,}430$$

$$A' - 21B' - 4G'_{ds} + 7F'_2 - G'_{ps} - 10G'_1 - 35G'_3 + 6\alpha' = {}^7\mathrm{D}_{\mathrm{C.G.}} = 27{,}611$$

$$A' - 17B' + 4C' - 3G'_{ds} + F'_2 - G'_{ps} - 10G'_1 - 10G'_3 + 30\alpha' = {}^5\mathrm{I}_{\mathrm{C.G.}} = 44{,}458.$$

*An invited paper. Present address: McGill University, Montreal, Canada.

[1] Figures in brackets indicate literature references at the end of this paper.

[2] The reader is referred to these papers for an explanation of the method used, notation and significance of the various parameters. The numerical values of all levels and parameters are in cm^{-1}

[3] Unprimed parameters refer to the configuration $3d^5 4p$, primed parameters to $3d^4 4s 4p$ and doubly primed parameters to $3d^3 4s^2 4p$.

By using the values of the parameters in (1) we obtain for the average value of A'

$$A' = 57260. \tag{2}$$

The height of d^5p is then obtained by using the electrostatic matrix of ^7P and the fact that its trace should equal the sum of the eigenvalues of $z^7P_{C.G.}$ at 23,415 and $y^7P_{C.G.}$ at 27,848.
Since,

$$\begin{array}{ll} (^6S)^7P & \left[\begin{array}{ll} A-35B-10G_1-35G_3 & \sqrt{2}(K-J) \\ \sqrt{2}(K-J) & A'-21B'-7F_2'-4G_{ds}'-G_{ps}' \\ & \qquad -35G_3'+6\alpha' \end{array}\right. \\ {}^5D(^3P)^7P & \end{array}$$

from (1) and (2) we obtain

$$A = 49130. \tag{3}$$

The parameters β and T improved the results for the configurations $3d^n4p$ in the third spectra by 25 percent and in the second spectra by 21 percent [1, 2]. Hence it was natural to consider the effects of these parameters in the first spectra, as well. For Ti I and V I, β and T were not significant.

In the diagonalization of the second iteration the parameter β, β', T, and T' were inserted with values of zero, and then in the least squares with these parameters eliminated the rms error was reduced to 285 with

$$\beta = \beta' = -840 \pm 14. \tag{4}$$

However, the parameter T was not significant as, furthermore, with $T = T'$ we had

$$\begin{aligned} \beta = \beta' &= -829 \pm 18 \\ T = T' &= -0.5 \pm 0.6 \\ \text{rms error} &= 285. \end{aligned} \tag{5}$$

Partly, this result is as anticipated, since as Racah has shown [11], for d^5 it is only necessary to consider β, and furthermore, since T is not important in d^4p (V I) we would expect a similar result for d^4sp (Cr I). However, it is disturbing that β should only be relevant for Cr I and not for the first spectra of the lighter atoms.

Since in V I [7], the results were greatly improved by considering the configuration $3d^24s^24p$ and its interactions with $3d^34s4p$ and $3d^44p$, a similar investigation was attempted for Cr I.

By using the final values of the parameters for V I and equations (8) and (9) of [7] we obtain for the difference between the weighted averages of the terms of these configurations

$$D''(\text{V}) = M''(3d^24s^24p) - M'(3d^34s4p) = 17{,}410. \tag{6}$$

Then from equations (11), (14) of [7] and (6) we obtain

$$D''(\text{Cr}) = M''(3d^34s^24p) - M'(3d^44s4p) = 22{,}650. \tag{7}$$

The parameters with their standard errors obtained in the least squares optimization of the second iteration for the configurations $3d^54p + 3d^44s4p$ with β and β' eliminated, are given in table 1.

TABLE 1. *Final parameters for* Cr I—$(3d+4s)^54p$

Parameter	$3d^54p + 3d^44s4p$	$3d^54p + 3d^44s4p + 3d^34s^24p$
A	50,207 ± 231	51,030 ± 228
A'	56,128 ± 286	56,738 ± 271
A''	.....	73,448 ± 502
B	670 ± 8	677 ± 7
B'	802 ± 5	755 ± 5
B''	.....	833 (Arith. Progress.)
C	2,592 ± 15	2,445 ± 15
C'	2,731 ± 12	2,918 ± 12
C''	.....	3,391 (Arith. Progress.)
G_{ds}'	1,583 ± 18	1,590 ± 19
$G = G_{ds}'$	.....	1,590
F_2	201 ± 10	187 ± 10
F_2'	268 ± 5	275 ± 5
F_2''	.....	363 (Arith. Progress.)
G_{ps}^7	6,091 ± 49	6,155 ± 45
G_1	223 ± 7	224 ± 7
G_1'	237 ± 5	236 ± 5
G_1''	.....	248 (Arith. Progress.)
G_3	15 ± 1	16 ± 1
G_3'	15 (Equal)	16 (Equal)
$G_3'' = G_3'$	.....	16
α	60 ± 1	63 ± 1
α'	60 (Equal)	63 (Equal)
$\alpha'' = \alpha'$	.....	63
H	162 ± 6	157 ± 4
$H' = H$	.....	157
J	879 ± 38	954 ± 32
$J' = J$	.....	954
K	2,160 ± 35	2,311 ± 30
K'	.....	3,011 (Fixed Diff.)
$\zeta_d = \zeta_d'$	280 ± 26	247 ± 24
$\zeta_d'' = \zeta_d'$	.....	247
$\zeta_p = \zeta_p'$	142 ± 59	184 ± 51
$\zeta_p'' = \zeta_p'$	.....	184
rms error	359	183.1

By assuming that the parameters B, C, and G_1 are in arithmetic progression for the three configurations, i.e.,

$$\begin{aligned} B'' &= 934 \\ C'' &= 2870 \\ G_1'' &= 251 \end{aligned}$$

and using eqs (8) and (9) of [7] we obtain

$$\begin{aligned} M'(3d^44s4p) &= 54{,}977 \\ M''(3d^34s^24p) &= A'' + 2269. \end{aligned} \tag{8}$$

Then from eqs (6) and (8)

$$A'' = 75{,}358. \tag{9}$$

2. Results and Discussion

As for V I, when the configurations $(3d+4s)^5 4p$ were considered rather than $3d^5 4p + 3d^4 4s 4p$ the results improved greatly. Interestingly, the effect of β was of a very different magnitude than for the case of two configurations. In the final results the rms error was 181 with

$$\beta = \beta' = \beta'' = -184 \pm 92. \tag{10}$$

When, in addition the parameter T was left to vary the rms error *rose* to 182 with

$$T = T' = T'' = -0.56 \pm 0.61. \tag{11}$$

When both β and T were eliminated the rms error was only 183. Thus it is evident that in the case of two configurations the considerable reduction in the rms error when β was left to vary freely is due to the fact that this parameter absorbed some of the effects of the interactions with the configuration $3d^3 4s^2 4p$. Thus the previous value of -840 for β is not significant.

In the least squares calculation of the final iteration of the "uniform treatment" (see ref. [6], β and T eliminated) 85 experimental terms splitting into 296 levels were inserted to yield an rms error of only 183. The comparison of the experimental and calculated values of the levels and g-factors obtained from the final least squares calculations of the uniform treatment is given in table 2. As for V I, A'' was allowed to vary freely, and thus the calculated values, percentage compositions and g-factors for all the 684 theoretically predicted levels are given in table 2. The final values of the parameters are given in table 1.

The main reasons for fixing $\zeta_d = \zeta_d'$ and $\zeta_p = \zeta_p'$. are that the fitted values of the parameters are reasonable, and only small differences occur between ζ_d and ζ_d' as well as ζ_p and ζ_p', but *very* large standard errors are associated with them. Furthermore, as the results are from a uniform treatment, consideration was also given to the results of keeping ζ_p' and ζ_d' free in Sc I, Ti I and V I, [6], [7]. There the above effects are even more pronounced.

Since G'_{ps} is much larger than G'_{ds}, the $p-s$ interaction is stronger than the $d-s$ interaction. Consequently the terms of d^4sp are coupled as $d^4(v_1 S_1 L_1) sp\,(^{1,3}\mathrm{P})SL$ and not $d^4s(S_2 L_1)pSL$ as given in AEL, [8].

The four high experimental terms r^3H, q^3H, p^3H and p^3G, all above 62,000 cm^{-1} were not included in the least-squares calculation as it was doubtful to which theoretical terms they should be assigned (see table 2).

Below 62,000 cm^{-1} the following 28 levels were excluded:

1. The three levels of $3d^4 4s(a^4\mathrm{D})4px\,^5\mathrm{P}$
2. The three levels of $3d^5(a^4\mathrm{P})4pw\,^5\mathrm{P}$
3. The five levels of $3d^5(b^4\mathrm{D})4pv\,^5\mathrm{F}$
4. The level $3d^4 4s(c^4\mathrm{D})4pt\,^5\mathrm{F}_4$
5. The three levels of $3d^4 4s(a^4\mathrm{F})4px\,^3\mathrm{G}$
6. The three levels of $3d^5(a^2\mathrm{I})4pv\,^3\mathrm{H}$
7. The three levels of $3d^5(a^2\mathrm{F})4pu\,^3\mathrm{F}$
8. The three levels of $3d^5(a^2\mathrm{F})4pt\,^3\mathrm{D}$
9. The three levels of $3d^5(\mathrm{b}^4\mathrm{F})4pq\,^3\mathrm{F}$
10. The level 3° at 61,676.

From the initial diagonalization it is evident that one of the four experimental terms x^5P, w^5P, v^5P, and t^5P in the range 40,000 to 50,000 can not be assigned to $3d^5 4p + 3d^4 4s 4p$, as in the wider range 30,000 to 54,000 only three terms ^{5}P are theoretically predicted. We note, however, that since $3d^5(a^6\mathrm{S})4pz\,^7\mathrm{P}_{\mathrm{C.G.}}$ is at 23,400, $3d^5(a^6\mathrm{S})5px\,^7\mathrm{P}_{\mathrm{C.G.}}$ is at 42,260 and $3d^5(\mathrm{a}^6\mathrm{S})4pz\,^5\mathrm{P}_{\mathrm{C.G.}}$ is at 26,800 we would expect that the lowest term ^{5}P of $(3d+4s)^5 5p$, i.e., $3d^5(a^6\mathrm{S})5p\,^5$P should be at around the height of the experimental term $w\,^5$P. More specifically, by considering diagonal elements we have

$$(^6\mathrm{S})\,^7\mathrm{P} : A - 35B - 10G_1 - 35G_3$$

$$(^6\mathrm{S})\,^5\mathrm{P} : A - 35B + 2G_1 + 7G_3.$$

Thus, $(^6$S$)^5$P is higher than $(^6$S$)^7$P by approximately $12G_1 + 42G_3$, which from table 1 equals 3360, almost exactly the difference between $z\,^5\mathrm{P}_{\mathrm{C.G.}}$ and $z\,^7\mathrm{P}_{\mathrm{C.G.}}$. By making the approximation that the values of the parameters pertaining to configurations containing a $5p$ electron are about half of the corresponding values for configurations with a $4p$ electron[4] we calculate $3d^5(a^6\mathrm{S})5p\,^5\mathrm{P}_{\mathrm{C.G.}}$ to be at 44,000. Thus, the experimental term $w\,^5$P should be assigned as $3d^5(a^6\mathrm{S})5pw\,^5$P.

The calculated value for the term $^5\mathrm{D}(^1\mathrm{P})x\,^5\mathrm{P}_{\mathrm{C.G.}}$ is at 42,500 and thus higher by 1,500 than the experimental value for $x\,^5\mathrm{P}_{\mathrm{C.G.}}$. However, this very large difference can be attributed to the fact that the interaction with $3d^5(a^6\mathrm{S})5pw\,^5$P is very strong, since the difference between the heights of the unperturbed terms $x\,^5$P and $w\,^5$P is very small. As this interaction was not considered explicitly, the term $x\,^5$P was not included in the least-squares calculations. It is interesting to note that the levels of $x\,^5$P are based on combinations with levels of eleven even terms, whereas $w\,^5$P is based on combinations with levels of only four even terms, [10].

In the range 45,200 to 48,200 there are five experimental ^{5}F terms assigned to $(3d+4s)^5 4p$. However, in the wider range 41,500 to 50,000, only three theoretical ^{5}F terms are predicted. The experimental terms $x\,^5$F and $w\,^5$F fit the two theoretical terms $\mathrm{A}^3\mathrm{F}(^3\mathrm{P})^5\mathrm{F}$ and $^3\mathrm{G}(^3\mathrm{P})^5\mathrm{F} + (^4\mathrm{D})^5\mathrm{F}$, respectively. To the theoretical term $(^4\mathrm{G})^5\mathrm{F} + \mathrm{A}^3\mathrm{F}(^3\mathrm{P})^5\mathrm{F}$, we can assign either $v\,^5$F, $u\,^5$F or $t\,^5$F.

As for the case of $w\,^5$P we note that since $z\,^5\mathrm{F}_{\mathrm{C.G.}}$ is near 31,000, one of the experimental terms $v\,^5$F, $u\,^5$F, $t\,^5$F or $s\,^5$F should be assigned $3d^4\,^5\mathrm{D}(4s5p\,^3\mathrm{P})^5\mathrm{F}$. Since in this spectrum there are many more experimental terms than electrostatic parameters, initially the two theoretical terms $(^4\mathrm{G})^5\mathrm{F} + \mathrm{A}^3\mathrm{F}(^3\mathrm{P})^5\mathrm{F}$ at around 48,000 and $(^4\mathrm{D})^5$F at around 50,000 were left vacant (none of the experimental terms $v\,^5$F, $u\,^5$F, $t\,^5$F or $s\,^5$F was inserted).

[4] This assumption is quite reasonable especially in view of the results for Ni I, where we also considered the configurations $3d^9 4p + 3d^8 4s 4p + 3d^8 5p$ as well as the configuration $3d^8 5p$ alone. Results to be published soon.

Since in the last iteration the calculated values of the levels of $(^4D)^5F$ corresponded very closely to the experimental levels of $3d^44s(a\,^6D)5ps\,^5F$ (mean deviation of −49), we assigned the experimental term $s\,^5F$ to $(^4D)^5F$. It should be noted that the difference between $s\,^5F_{C.G.}$ and $z\,^5F_{C.G.}$ is approximately the same as the difference between $y\,^7P_{C.G.}$ and $z\,^7P_{C.G.}$. Since $z\,^5F_{C.G.}$ is higher by about 7600 than $z\,^7P_{C.G.}$, and since, furthermore, the parameters of $(3d+4s)^55p$ are considerably smaller than the corresponding parameters of $(3d+4s)^54p$, it is evident that $s\,^5F$ is too high to designate as the lowest term ^5F of $(3d+4s)^55p$.

Then, guided by the fact that due to the much smaller values of ζ_d and ζ_p for $(3d+4s)^55p$, the splitting of the term $3d^4(4s5p\,^3P)^5F$ should be quite small, it is probable that the experimental term $v\,^5F$ is really the lowest term ^5F of $(3d+4s)^55p$, i.e., $3d^4(4s5p^3P)^5F$. (It should be noted that the much larger splitting of the experimental term s^5F seems to reaffirm that it belongs to $(3d+4s)^54p$.) In addition, the height of $v\,^5F$ above $y\,^7P$ is very reasonable for the assignment as the lowest term ^5F of $(3d+4s)^55p$.

The intervals between the four experimental levels assigned to $t\,^5F$ are irregular and it is very doubtful whether these four levels belong to a single term. Thus, the experimental term $u\,^5F$ was assigned to the theoretical term $(^4G)^5F+A^3F(^3P)^5F$. There was a close correspondence between the experimental and calculated values of the levels and g-factors.

Examination of the combinations given by Kiess for t^5F, [10], indicates that the levels $t^5F_{1,2,3}$ have considerably more combinations than t^5F_4. Also, since the irregularity in the splitting of t^5F occurs for t^5F_4, the levels $t^5F_{1,2,3}$ were assigned to the previously vacant term $A^3F(^3P)^3D$. Conceivably the level t^5F_4 could be assigned to $^3H(^3P)^1G$. However, since the resulting deviation would be around −520, and since the combinations of t^5F_4 also include several quintets, the level t^5F_4 was neglected.

Below 53,800, three theoretical terms ^3G are predicted. However, below 50,000 the four experimental terms $z\,^3G$, $y\,^3G$, $x\,^3G$ and $w\,^3G$ are assigned to $(3d+4s)^54p$ in AEL. The experimental terms $z\,^3G$ and $y\,^3G$ fit very well the theoretical terms with the same assignments. The experimental term $w\,^3G$ corresponds very nicely to the theoretical term $A^3F(^3P)^3G$ (mean deviation −118, whereas $x\,^3G$ would yield deviations of around −1000 if assigned to $A^3F(^3P)^3G$).

Below 49,800 the only theoretical terms with no corresponding experimental terms are $A^3F(^3P)^3F$, $^3H(^3P)^1G$ and $A^3P(^3P)^1S$, all between 48,500 and 49,150. Thus, even if the level $x\,^3G_3$ is assigned to $A^3F(^3P)^3F_3$, and $x\,^3G_4$ to either $A^3F(^3P)^3F_4$ or $^3H(^3P)^1G$, the level $x\,^3G_5$ cannot be assigned to any predicted level of $(3d+4s)^54p$. From C. C. Kiess' paper [10], an examination of the combinations for the levels of $x\,^3G$ reveals that this term is based on 30 combinations with 12 even terms. Of these, 15 are with $x\,^3F_5$ and thus it is not reasonable to fit the levels with J equal to 3 and 4 and neglect the level having the most combinations. The assumption that $x\,^3G$ belongs to $(3d+4s)^55p$ is also difficult to justify. The lowest term ^3G of $(3d+4s)^55p$ is expected to lie much higher. Not only are the terms ^7F and ^7D of $3d^44s5p$ expected to be lower than $x\,^3G$, but also the levels $x\,^3G_4$ and $x\,^3G_5$ have combinations with singlets. There is also a possibility that $v\,^5F$ should actually be assigned to ^7D of $3d^44s5p$ and that the levels $x\,^3G$ belong to $3d^4\,^5D$ $(4s5p^3P)^5F$. Actually, however, we can only conclude that the experimental levels $x\,^3G$ can definitely not be assigned to a theorectical term ^3G of $(3d+4s)^54p$, and that it is not reasonable to assign the two levels $x\,^3G_3$ and $x\,^3G_4$ either to $A^3F(^3P)^3F_{3,4}$ or to $A^3F(^3P)^3F_3$ and $^3H(^3P)^1G$, and then reject the level $x\,^3G_5$. Thus, none of the levels of $x\,^3G$ was included in the least-squares calculations.

Only one of the experimental terms $w\,^3H$ and $v\,^3H$ can be assigned to the theoretical term $^3H(^1P)^3H$. Since the two experimental terms $w\,^3H$ and $v\,^3H$ are so close, their respective deviations furnish no aid in deciding which term to assign as $^3H(^1P)^3H$. Furthermore, in each case the number of combinations with even levels is 30. However, as the experimental designation of $w\,^3H$ is the same as the theoretical designation, $^3H(^1P)^3H$, and since the intervals between the calculated levels correspond much more closely to the intervals of $w\,^3H$, we assigned the levels of $w\,^3H$ to $^3H(^1P)^3H$.

Again, by remembering that the electrostatic parameters of $(3d+4s)^55p$ are much smaller than those of $(3d+4s)^54p$, it is conceivable that $v\,^3H$ should be designated as $3d^5(a\,^4G)5pv\,^3H$ i.e., as the lowest term ^3H of $(3d+4s)^55p$. Thus, the levels of $v\,^3H$ were not included in the least squares calculation.

The case of the two terms $v\,^3F$ and $u\,^3F$ is quite similar to that of $v\,^3H$ and $w\,^3H$. To the theoretically predicted term $(A^2D)^3F+(A^2F)^3F$ at 55,000 the term $v\,^3F$ was assigned mainly because the splitting of the theoretical term (positive intervals) is similar to the splitting of $v\,^3F$, whereas for $w\,^3F$ it is quite different (negative intervals). The deviations are then 200 cm^{-1} lower than if the levels of $u\,^3F$ were inserted. The term $u\,^3F$ is certainly high enough to belong to a term ^3F of $(3d+4s)^55p$. However, it is probable that $u\,^3F$ should be assigned to the second lowest ^3F term of $(3d+4s)^55p$, i.e., $3d^5(a\,^4G)5pu\,^3F$, since the lowest term ^3F of $(3d+4s)^55p$ is expected to lie below 50,000.

As for $v\,^3F$ and $u\,^3F$, the experimental term $u\,^3D$ was assigned to the theoretical term $(^4F)^3D+^3D(^3P)^3D$ predicted at the height, whereas the term $t\,^3D$ was neglected. Again the main consideration here was the similar splitting of the calculated term and the experimental term $u\,^3D$, whereas the splitting of $t\,^3D$ is quite different. From table 2 it is evident that the levels of $t\,^3D$ could be assigned to the theoretical levels $(^4F)^5D_{1,2,3}$ with very small deviations. However, here again it is quite probable that $t\,^3D$ should be assigned to the second lowest term ^3D of $(3d+4s)^55p$, i.e., $3d^5(a\,^4P)5pt\,^3D$; the levels $t\,^3D$ were, therefore, not included in the least-squares calculation.

The experimental term $t\,^3F$ cannot be assigned to a theoretical term ^3F of $(3d+4s)^54p$. Although the levels of $t\,^3F$ fit very nicely to $[3d^34s^2(^4F)4p^5G+3d^5(^4F)4p\,^5G]_{2,3,4}$, they conceivably are levels of a term ^3F of $(3d+4s)^55p$, and thus were not included in the least-squares calculation. Similarly the level 3° at

61676 was not inserted although it could be assigned to either $(^4F)^5F_3^*$ or to $A^3F(^1P)^3D_3$ with small deviations.

The following changes in assignment[5] were performed:

1. AEL $d^4s(a\,^4H)py^5G \longrightarrow A^3F(^3P)y\,^5G$
2. AEL $d^5(a\,^4P)pw^5D \longrightarrow A^3F(^3P)w\,^5D$
3. $(^4G)^5F \longleftrightarrow {}^3G(^3P)^5F$
4. AEL $d^4s(c\,^4D)pu^5P \longrightarrow (^4P)u\,^5P$
5. AEL $d^4s(b\,^4G)px^5G \longrightarrow {}^3H(^3P)x\,^5G$
6. AEL $d^5(b\,^4D)pv^5D \longrightarrow (^4P)v\,^5D$
7. AEL $d^4s(c\,^4D)pt^5F_{1,2,3} \longrightarrow A^3F(^3P)^3D$
8. AEL $d^4s(a\,^4F)pw^5G \longrightarrow {}^3G(^3P)w\,^5G$
9. AEL $d^4s(b\,^4G)pw^3G \longrightarrow A^3F(^3P)w\,^3G$
10. AEL $d^4s(a\,^6D)5ps^5F \longrightarrow (^4D)s\,^5F$
11. AEL $d^4s(c\,^4D)pu^5D \longrightarrow (^4D)u\,^5D$
12. AEL $d^4s(a\,^4F)pw^3F \longrightarrow {}^3G(^3P)w\,^3F$
13. $(^2D)^1H \longleftrightarrow {}^3H(^3P)\,^1H$
14. AEL $d^4s(a\,^4F)pt^5D \longrightarrow {}^3D(^3P)t\,^5D$
15. AEL $d^5(a\,^2I)py^3I \longrightarrow {}^1I(^3P)y\,^3I$
16. AEL $d^5(b\,^4F)pr^5F \longrightarrow {}^3D(^3P)r\,^5F$
17. AEL $d^4s(a\,^2G)pv^3G \longrightarrow d^3s^2(^4F)^3G^*$
18. AEL $d^4s(a\,^2H)pz^1I \longrightarrow {}^1I(^3P)^3K_6$
19. AEL $d^5(a\,^2D)pv^3D \longrightarrow {}^3D(^3P)v\,^3D$
20. AEL $d^4s(c^2F)pv^3F \longrightarrow (A^2D)v\,^3F$
21. AEL $d^4s(a\,^2H)px^3I \longrightarrow (^2I)x\,^3I$
22. AEL $d^5(b\,^2H)pu^3H \longrightarrow {}^1I(^3P)u\,^3H$
23. AEL $d^5(a\,^2D)pv^3P \longrightarrow {}^3D(^3P)v\,^3P$
24. AEL $d^5(b\,^2F)pt^3F \longrightarrow d^3s^2(^4F)t\,^3F^*$
25. AEL $d^5(b\,^2H)pu^3G \longrightarrow A^3F(^1P)u\,^3G$
26. AEL $d^4s(c\,^2G)pt^3G \longrightarrow (A^2F)t\,^3G$
27. AEL $d^4s(a\,^2P)pu^3P \longrightarrow A^1S(^3P)u\,^3P$
28. AEL $d^4s(a\,^2P)pu^3D \longrightarrow (^4F)u\,^3D$
29. AEL $d^4s(a\,^2G)pr^3F \longrightarrow A^3F(^1P)r\,^3F$
30. AEL $d^4s(a\,^2G)pt^3H \longrightarrow (^2I)t\,^3H$
31. AEL $d^5(b\,^2H)pw^3I \longrightarrow {}^3H(^1P)w\,^3I$
32. AEL $d^4s(b\,^2I)pv^3I \longrightarrow (^2H)v\,^3I$
33. AEL $d^5(b\,^2F)ps^3D \longrightarrow (A^2D)s\,^3D$
34. AEL $d^4s(c\,^2G)ps^3H \longrightarrow (A^2G)s\,^3H$
35. AEL $d^5(b\,^2G)pr^3G \longrightarrow (^2H)r\,^3G$
36. AEL $d^4s(c\,^2G)pp^3F \longrightarrow (B^2F)p\,^3F$

The reasons for the changes 7 and 10 were discussed in detail previously.

Theoretically, the lowest term ^1I is predicted at 50126 with no corresponding experimental level which can be fitted to it. The next highest term ^1I is $(^2I)\,^1I$ to which corresponds the experimental term $(^2I)\,y^1I$. Thus, the experimental term $d^4s(a\,^2H)pz^1I$ at 54,800 can not be assigned to ^1I. As $z\,^1I$ is based on combinations with six even terms, [10], it is a valid level. The only possible level to which it can be assigned for J equal to 6 is $^1I(^3P)^3K_6$, yielding a deviation of only 76. This is indicated by change 18. The other changes are similar to those performed for Ti I and V I, [6], [7], reaffirming the fact that it is very difficult to predict the assignments, especially of the higher-lying terms prior to a theoretical investigation.

The level 1_3° has 16 combinations with the 7 even terms $d\,^3F$, $a\,^1G$, $b\,^3G$, $a\,^3F$, $a\,^3G$, $a\,^5G$, and $a\,^5D$, [10]. Thus, the assignment of this level to the vacant theoretical level $A^3F(^3P)^3F_3$ seems very reasonable. The deviation is only -77.

[5] For the theoretical term designations used the reader is referred to section 3 of this paper.

The level 2_1° is based on combinations with the six even terms $a\,^1H$, $b\,^3H$, $a\,^3I$, $b\,^3G$, $a\,^3G$, and $a\,^3H$, [10]. This level is assigned to the theoretical level $^3G(^3P)^3G_4$, yielding a deviation of 218.

The terms $s\,^3G$ and $q\,^3G$, given without configuration designations in AEL, are assigned to the theoretical terms whose major contributions are $(A^2G)^3G$ and $(^4F)^3G$, respectively.

Most of the experimental g-factors correspond quite closely to the calculated g-factors. However, as for V I there are some exceptions caused by unsuitably calculated eigenvectors. In general, there is very strong mixing, and especially the eigenfunctions of the higher-lying levels have a marked degree of impurity. Thus, it is very important to state the percentage composition of each level rather than just give one particular term designation (see table 2). The four experimental g-factors for levels with J equal to zero were ignored, since from the defining equation used to obtain the calculated g-factors, a g-value for a level of J equal to zero is meaningless.

Finally, some differences between the experimental data given in AEL [8], and in C. C. Kiess' paper [10], should be mentioned. Firstly, the term $t\,^5P$ is assigned as $3d^44s(a\,^6D)5pt\,^5P$ by C. C. Kiess, [10]. However, as explained before, the term $w\,^5P$ is the lowest term ^5P of $(3d+4s)^55p$. Since the term $3d^44s(a\,^6D)4py\,^5P$ is about 3000 higher than $3d^5(a\,^6S)4pz\,^5P$, we would expect that since the term $3d^5(a\,^6S)5p\,^5P$ is at 44,200, the term $3d^44s(a\,^6D)5p\,^5P$ should not be higher than 46,000 (the interaction parameters of $(3d+4s)^55p$ are about half of those for $(3d+4s)^44p$). In addition, the term $t\,^5P$ fits very nicely to the theoretical term with the same assignment as in AEL.

The term $s\,^5P$, which Kiess designates as $3d^44s(a\,^4D)5ps\,^5P$ is not given in AEL. Although there is a theoretical term ^5P predicted at that height for $(3d+4s)^54p$, we cannot assign the term $s\,^5P$ to it. Firstly, the splitting of the theoretical term $^3D(^3P)^5P$ is opposite to that of $s\,^5P$. Secondly, the assignment which Kiess gives to this term is probably correct, as it is reasonable to expect the theoretical term $3d^4(a\,^5D)(4s5p\,^3P)^5P$ at that height.

Then, Kiess also gives the three terms $3d^44s(a\,^6D)6p\,^5D$ and $3d^44s(a\,^4D)6p\,^5P$, ^5F, which are not given in AEL. The level 3_2° at 61676 in AEL is not given by Kiess, a fact which further justifies our not including this level in the least-squares. Kiess, however, gives the level 4_3° at 57142. Since this level is based on combinations with singlets, triplets, and quintets, it may perhaps be assigned to $^3D(^3P)^3F_3$. However, the resulting deviation would be about 480, and so the level 4_3° was not considered.

The rejected term $3d^5(b\,^4F)4pq\,^3F$ is designated by Kiess as $3d^5(d^2G)4pq\,^3F$. The terms $s\,^3G$ and $r\,^3G$ Kiess designates as $3d^5(b\,^2H)4ps\,^3G$ and $3d^5(b\,^2F)4pr\,^3G$, respectively, neither of which corresponds to the theoretical designations.

The term $3d^44s(a\,^2P)4pt\,^3P$, not given in AEL, fits excellently as the theoretical term $A^1D(^3P)^3P$. Since our source for the experimental data is AEL, (especially as many more experimental g-factors are given there), we did not include this term specifically

in the least-squares calculation. In table 2 the approximate values of the deviations, if this term had been inserted into the least-squares, are given in parentheses.

Below 62,100 (the limit of the experimental data inserted) there are 86 theoretical levels with no corresponding experimental levels. The lowest of these is the level $^3H(^3P)^1G$ at 48,567.

3. Table of the Observed and Calculated Levels and g-Factors

In the column "NAME" the calculated designation of the term is given. Whenever the terms of d^n have different seniorities these are denoted by the letters A and B (for $d^5\,^2D$ by A, B, and C) the lower calculated term being designated by A. Whenever a calculated term has a corresponding experimental term the small letters z, y, x, . . . are used as in AEL. The terms of d^4sp are denoted by $d^4v_1S_1L_1(sp^1,{}^3P)SL$. The terms of d^5p are differentiated from those of d^3s^2p by using a star for the latter terms.

The entries in the columns "J", "OBS. LEVEL cm^{-1}," "CALC. LEVEL cm^{-1}," are self-evident. In the column "PERCENTAGE" for each calculated level either the three highest contributions or all those contributions exceeding seven percent are given.

Whenever the experimental and calculated term designations differ, the experimental designation is entered in the column "AEL", using the notation of C. E. Moore, [8]. In many instances the exchanges involve complete terms rather than isolated levels. Unless specified otherwise, the entries in the column "AEL" pertain to exchanges in terms.

The columns "OBS.g-FACTOR", "CALC.g-FACTOR" give the observed and calculated values of the g-factors, respectively.

The entries are in the order of increasing energy of the calculated terms.

TABLE 2. *Observed and calculated levels of* Cr I $(3d+4s)^5$4p

Name	J	Percentage	AEL		Obs. level (cm^{-1})	Calc. level (cm^{-1})	O–C	Obs. g-factor	Calc. g-factor
			Config.	Desig.					
$(^6S)^7P$	2	$69+31\,^5D(^3P)^7P$			23305	23134	171	2.334	2.332
	3	$70+30\,^5D(^3P)^7P$			23386	23239	147	1.92	1.916
	4	$71+29\,^5D(^3P)^7P$			23499	23385	114	1.752	1.750
$^5D(^3P)^7F$	0	100	$3d^44s(a\,^6D)4p$	$z\,^7F$	24971	25034	−63		
	1	100			25011	25074	−63	1.52	1.500
	2	100			25089	25152	−63	1.50	1.500
	3	100			25206	25268	−62	1.49	1.500
	4	100			25360	25422	−62	1.51	1.500
	5	100			25549	25610	−61	1.51	1.500
	6	100			25771	25833	−62	1.53	1.500
$(^6S)^5P$	1	92			26802	26759	43	2.512	2.500
	2	91			26796	26720	76	1.830	1.843
	3	92			26788	26673	115	1.670	1.670
$^5D(^3P)^7D$	1	99	$3d^44s(a\,^6D)4p$	$z\,^7D$	27300	27390	−90	3.01	2.993
	2	$66+23\,^5D(^3P)^7P+10(^6S)^7P$			27382	27438	−56	1.99	2.110
	3	$58+29\,^5D(^3P)^7P+12(^6S)^7P$			27500	27562	−62	1.76	1.817
	4	$58+30\,^5D(^3P)^7P+12(^6S)^7P$			27650	27723	−73	1.66	1.692
	5	100			27825	27960	−135	1.61	1.599
$^5D(^3P)^7P$	2	$44+34\,^5D(^3P)^7D+21(^6S)^7P$	$3d^44s(a\,^6D)4p$	$y\,^7P$	27729	27366	363	2.341	2.212
	3	$40+41\,^5D(^3P)^7D+18(^6S)^7P$			27820	27497	323	1.929	1.845
	4	$41+42\,^5D(^3P)^7D+17(^6S)^7P$			27935	27654	281	1.761	1.708
$^5D(^3P)^5P$	1	95	$3d^44s(a\,^6D)4p$	$y\,^5P$	29421	29266	155	2.513	2.504
	2	95			29585	29448	137	1.836	1.834
	3	96			29825	29718	107	1.669	1.667
$^5D(^3P)^5F$	1	96	$3d^44s(a\,^6D)4p$	$z\,^5F$	30787	30787	0	0.002	0.001
	2	96			30859	30860	−1	0.997	1.000
	3	96			30965	30968	−3	1.245	1.250
	4	95			31106	31113	−7	1.345	1.356
	5	96			31280	31293	−13	1.396	1.400

TABLE 2. *Observed and calculated levels of* Cr I $(3d+4s)^5 4p$—Continued

Name	J	Percentage	AEL		Obs. level (cm^{-1})	Calc. level (cm^{-1})	O–C	Obs. g-factor	Calc. g-factor
			Config.	Desig.					
$^5D(^3P)^5D$	0	$89+8\,^5D(^3P)^3P$	$3d^44s(a\,^6D)4p$	$z\,^5D$	33338	33353	−15		
	1	93			33424	33420	4	1.499	1.500
	2	96			33542	33528	14	1.497	1.500
	3	97			33672	33665	7	1.497	1.499
	4	97			33816	33828	−12	1.499	1.499
$^5D(^3P)^3P$	0	$88+8\,^5D(^3P)^5D$	$3d^44s(a\,^4D)4p$	$z\,^3P$	33763	33900	−137		
	1	92			33897	34059	−162	1.49	1.500
	2	95			34190	34383	−193	1.55	1.499
$^5D(^3P)^3F$	2	95	$3d^44s(a\,^4D)4p$	$z\,^3F$	35898	35825	73		0.668
	3	95			36034	35976	58		1.084
	4	95			36212	36177	35		1.250
$^5D(^3P)^3D$	1	96	$3d^44s(a\,^4D)4p$	$z\,^3D$	38597	38605	−8		0.500
	2	96			38731	38751	−20		1.166
	3	96			38911	38948	−37		1.333
$^5D(^1P)^5F$	1	$84+12(^4G)^5F$	$3d^44s(a\,^4D)4p$	$y\,^5F$	40906	40791	115	0.004	0.005
	2	$83+12(^4G)^5F$			40971	40872	99	1.28	1.003
	3	$83+12(^4G)^5F$			41086	40994	92	1.246	1.251
	4	$82+13(^4G)^5F$			41225	41154	71	1.360	1.350
	5	$82+14(^4G)^5F$			41393	41350	43		1.400
$^5D(^1P)^5D$	0	$52+14(^4P)^5D$	$3d^44s(a\,^4D)4p$	$y\,^5D$	41225	41373	−148		
	1	$54+14(^4P)^5D$			41289	41440	−151	1.503	1.501
	2	$56+13(^4P)^5D$			41409	41572	−163	1.504	1.501
	3	$58+13(^4P)^5D$			41575	41766	−191	1.503	1.500
	4	$62+14(^4P)^5D$			41782	42023	−241	1.500	1.499
$^5D(^1P)^5P$	1	$68+7(^4P)^5P$	$3d^44s(a\,^4D)4p$	$x\,^5P$	(40930)	42367		(2.455)	2.441
	2	$56+7(^4P)^5P$			(40983)	42471		(1.76)	1.782
	3	$55+8(^4P)^5P$			(41043)	42635		(1.640)	1.627
$^3H(^3P)^5H$	3	$61+20(^4G)^5H$	$3d^44s(a\,^4H)4p$	$z\,^5H$	42026	42330	−304		0.530
	4	$55+19(^4G)^5H$			42080	42378	−298		0.938
	5	$48+17(^4G)^5H$			42154	42444	−290		1.142
	6	$38+25(^4G)^5G+14(^4G)^5H$			42252	42531	−279		1.263
	7	$65+24(^4G)^5H$			42387	42724	−337		1.285
$A^3P(^3P)^5D$	0	$49+26\,^5D(^1P)^5D$	$3d^34s(b\,^4P)4p$	$x\,^5D$	42218	42152	66		
	1	$47+26\,^5D(^1P)^5D$			42293	42215	78	1.501	1.553
	2	$43+21\,^5D(^1P)^5D$			42439	42343	96	1.494	1.554
	3	$40+22\,^5D(^1P)^5D$			42648	42543	105	1.498	1.533
	4	$45+20\,^5D(^1P)^5D$			42909	42841	68	1.497	1.498
$(^4G)^5G$	2	$61+20\,^3H(^3P)^5G$			42515	42552	−37	0.35	0.336
	3	$57+19\,^3H(^3P)^5G$			42539	42587	−48		0.892
	4	$53+18\,^3H(^3P)^5G$			42565	42627	−62		1.114
	5	$47+16\,^3H(^3P)^5G$			42589	42669	−80	1.23	1.225
	6	$37+27\,^3H(^3P)^5H+13\,^3H(^3P)^5G$			42606	42708	−102	1.32	1.284
$A^3P(^3P)^5S$	2	$46+46(^4P)^5S$	$3d^34s(b\,^4P)4p$	$z\,^5S$	43125	42919	206	1.96	1.984

TABLE 2. *Observed and calculated levels of* Cr I $(3d+4s)^5 4p$ – Continued

Name	J	Percentage	AEL		Obs. level (cm^{-1})	Calc. level (cm^{-1})	O–C	Obs. g-factor	Calc. g-factor
			Config.	Desig.					
$^3H(^3P)^5I$	4	99	$3d^4 4s(a\,^4H)4p$	$z\,^5I$	44247	44009	238		0.603
	5	99			44308	44108	200		0.903
	6	99			44393	44224	169		1.073
	7	99			44514	44354	160		1.179
	8	100			44667	44496	171		1.250
$A^3F(^3P)^5G$	2	85	$3d^4 4s(a\,^4H)4p$	$y\,^5G$	44300	44505	−205	0.35	0.359
	3	80			44373	44562	−189	0.93	0.948
	4	$68+18A^3F(^3P)^5F$			44534	44636	−102		1.190
	5	$46+29A^3F(^3P)^5F$			44591	44723	−132	1.25	1.325
	6	$85+5^3G(^3P)^5G$			44746	44938	−192	1.34	1.329
$A^3P(^3P)^5P$	1	$78+8(^4D)^5P$	$3d^4 4s(b\,^4P)4p$	$v\,^5P$	44667	44683	−16	2.47	2.481
	2	$76+9(^4D)^5P$			44875	44938	−63		1.827
	3	$70+13(^4D)^5P$			45113	45172	−59	1.65	1.658
$A^3F(^3P)^5F$	1	$66+28(^4G)^5F$	$3d^4 4s(a\,^4F)4p$	$x\,^5F$	45202	44759	443		0.003
	2	$63+27(^4G)^5F$			45225	44784	441		0.975
	3	$58+26(^4G)^5F$			45256	44818	438		1.215
	4	$50+23(^4G)^5F$			45286	44856	430		1.305
	5	$34+37A^3F(^3P)^5G$			45306	44895	411	1.41	1.336
$(^4G)^3H$	4	$59+25(^4G)^5H$			45359	45722	−363		0.834
	5	$49+32(^4G)^5H$			45354	45582	−228		1.064
	6	$68+16(^4G)^5H$			45349	45586	−237		1.179
$(^4G)^5H$	3	$76+22^3H(^3P)^5H$			45566	45573	−7	0.52	0.505
	4	$51+28(^4G)^3H+15^3H(^3P)^5H$			45615	45577	38		0.870
	5	$43+38(^4G)^3H+13^3H(^3P)^5H$			45663	45770	−107		1.071
	6	$58+20(^4G)^3H$			45707	45812	−105		1.204
	7	$74+25^3H(^3P)^5H$			45741	45834	−93	1.29	1.285
$(^4P)^3P$	0	$39+31A^3P(^3P)^3P$			45723	45803	−80		
	1	$45+24A^3P(^3P)^3P$			45719	45787	−68		1.515
	2	$49+20A^3P(^3P)^3P$			45734	45821	−87		1.431
$(^4G)^3F$	2	$75+8A^3F(^3P)^3F$			45966	45933	33		0.737
	3	$80+8A^3F(^3P)^3F$			46000	45981	19		1.090
	4	$83+7A^3F(^3P)^3F$			46058	46051	7		1.249
$A^3F(^3P)^5D$	0	$40+25A^3P(^3P)^5D$	$3d^5(a\,^4P)4p$	$w\,^5D$	46081	46068	13		
	1	$42+20A^3P(^3P)^5D$			46298	46058	240		1.352
	2	$40+22A^3P(^3P)^5D$			46350	46088	262		1.410
	3	$36+27A^3P(^3P)^5D$			46368	46170	198		1.440
	4	$39+34A^3P(^3P)^5D$			46422	46325	97		1.460
$(^4P)^3D$	1	$22+19(^4D)^5F+14^3G(^3P)^5F$			46077	46364	−287		0.429
	2	$23+14(^4D)^5F+11^3G(^3P)^5F$			46109	46440	−331	1.24	1.172
	3	$37+15A^3F(^3P)^5D$			46174	46463	−289	1.33	1.352
$^3G(^3P)^5F$	1	$21+18(^4D)^5F+20(^4P)^3D$	$3d^5(a\,^4G)4p$	$w\,^5F$	46678	46638	40		0.405
	2	$20+18(^4D)^5F+23(^4P)^3D$			46677	46624	53		1.048
	3	$23+22(^4D)^5F+11(^4P)^3D$			46688	46602	86	1.25	1.227
	4	$23+24(^4D)^5F+15A^3F(^3P)^5D$			46721	46623	98		1.336
	5	$33+30(^4D)^5F+9^3D(^3P)^5F$			46705	46596	109	1.37	1.362

TABLE 2. *Observed and calculated levels of* Cr I $(3d+4s)^5 4p$—Continued

Name	J	Percentage	AEL		Obs. level (cm^{-1})	Calc. level (cm^{-1})	O–C	Obs. g-factor	Calc. g-factor
			Config.	Desig.					
$^3H(^3P)^3G$	3	$42+20A^3F(^3P)^3G$	$3d^44s(a\,^4H)4p$	$z\,^3G$	46847	46737	110		0.775
	4	$40+21A^3F(^3P)^3G$			46905	46786	119		1.077
	5	$34+20(^4G)^3G$			46986	46840	146		1.223
$A^3P(^3P)^3S$	1	$72+8(^4P)^3S$	$3d^44s(b\,^4P)4p$	$z\,^3S$	47088	46763	325		1.810
$(^4P)^5P$	1	$55+20(^4D)^5P+13^3D(^3P)^5P$	$3d^44s(c\,^4D)4p$	$u\,^5P$	47022	47171	−149	2.43	2.475
	2	$51+20(^4D)^5P+13^3D(^3P)^5P$			46968	47081	−113	1.83	1.814
	3	$47+20(^4D)^5P+13^3D(^3P)^5P$			46879	46943	−64	1.68	1.654
$(^4G)^3G$	3	$73+12^3H(^3P)^3G$			47048	47118	−70		0.748
	4	$69+16^3H(^3P)^3G$			47055	47149	−94		1.050
	5	$62+24^3H(^3P)^3G$			47055	47188	−133		1.201
$^3H(^3P)^5G$	2	$67+15(^4G)^5G$	$3d^44s(b\,^4G)4p$	$x\,^5G$	47047	47022	25	0.45	0.389
	3	$62+14(^4G)^5G$			47126	47085	41	0.96	0.949
	4	$60+15(^4G)^5G$			47190	47144	46		1.172
	5	$63+16(^4G)^5G$			47229	47187	42	1.27	1.279
	6	$70+19(^4G)^5G$			47222	47192	30	1.44	1.333
$^3H(^3P)^3I$	5	$61+28^3G(^3P)^5H$	$3d^44s(a\,^4H)4p$	$z\,^3I$	47586	47640	−54		0.929
	6	$57+34^3G(^3P)^5H$			47630	47674	−44		1.099
	7	$52+40^3G(^3P)^5H$			47693	47731	−38		1.206
$^3G(^3P)^5H$	3	$79+12^3H(^3P)^5H$	$3d^44s(b\,^4G)4p$	$x\,^5H$	47621	47553	68		0.522
	4	$82+11^3H(^3P)^5H$			47689	47628	61		0.909
	5	$56+30^3H(^3P)^3I$			47794	47771	23		1.014
	6	$53+35^3H(^3P)^3I$			47942	47940	2		1.143
	7	$49+42^3H(^3P)^3I$			48140	48142	−2		1.222
$(^4P)^5D$	0	$46+27A^3F(^3P)^5D$	$3d^5(b\,^4D)4p$	$v\,^5D$	47788	47835	−47		
	1	$49+26A^3F(^3P)^5D$			47772	47877	−105	1.37	1.468
	2	$49+26A^3F(^3P)^5D$			47786	47938	−152	1.39	1.469
	3	$49+25A^3F(^3P)^5D$			47814	48025	−211	1.53	1.474
	4	$52+23A^3F(^3P)^5D$			47866	48149	−283	1.50	1.479
$(^4G)^5F$	1	$15+15A^3P(^3P)^3P+9A^3F(^3P)^5F$	$3d^44s(b\,^4G)4p$	$u\,^5F$	47878	47998	−120	0.00	0.459
	2	$35+19A^3F(^3P)^5F$			47918	48054	−136	1.04	1.029
	3	$35+20A^3F(^3P)^5F$			47975	48151	−176	1.36	1.329
	4	$39+23A^3F(^3P)^5F$			48014	48371	−357		1.360
	5	$39+25A^3F(^3P)^5F$			47986	48351	−365	1.38	1.385
$A^3F(^3P)^3D$	1	$59+7(^4G)^5F$	$3d^44s(c\,^4D)4p$	$t\,^5F$	48210	48407	−197		0.627
	2	$61+6(^4G)^5F$			48218	48382	−164		1.164
	3	$64+5(^4G)^5F$			48252	48379	−127		1.266
$A^3P(^3P)^3P$	0	$29+24(^4P)^3P+11A^3P(^3P)^1S$	$3d^44s(b\,^4P)4p$	$x\,^3P$	48226	48133	93		
	1	$28+15(^4P)^3P+15(^4G)^5F$			48331	48413	−82		0.943
	2	$42+19(^4P)^3P$			48459	48508	−49		1.481
$^3H(^3P)^3H$	4	$76+4(^4G)^3H$	$3d^44s(a\,^4H)4p$	$y\,^3H$	48288	48177	111		0.820
	5	89			48310	48308	2		1.042
	6	83			48445	48440	5		1.165
$^3H(^3P)^1G$	4	$32+21A^3F(^3P)^1G$				48567			1.067

TABLE 2. *Observed and calculated levels of* Cr I $(3d+4s)^5 4p$ – Continued

Name	J	Percentage	AEL		Obs. level (cm^{-1})	Calc. level (cm^{-1})	O–C	Obs. g-factor	Calc. g-factor
			Config.	Desig.					
$A^3F(^3P)^3F$	2	$59+16^3G(^3P)^3F$				48650			0.659
	3	$60+15^3G(^3P)^3F$		1°	48636	48713	−77		1.068
	4	$38+18^3H(^3P)^1G$				48925			1.155
$A^3P(^3P)^1S$	0	$74+19A^3P(^3P)^3P$				49153			
$A^3P(^3P)^3D$	1	$38+20(^4P)^3D$	$3d^44s(b\,^4P)4p$	$x\,^3D$	48840	49107	−267		0.535
	2	$46+14(^4P)^3D$			49028	49220	−192		1.165
	3	$61+7(^4P)^3D$			49311	49368	−57		1.278
$^3G(^3P)^5G$	2	$65+18(^4G)^5G$	$3d^44s(a\,^4F)4p$	$w\,^5G$	49467	49358	109		0.373
	3	$53+14(^4G)^5G$			49520	49373	147	1.04	0.923
	4	$63+19(^4G)^5G$			49573	49430	143		1.140
	5	$70+17(^4G)^5G$			49618	49565	113		1.264
	6	$73+17(^4G)^5G$			49635	49590	45	1.35	1.328
$A^3F(^3P)^3G$	3	$40+12^3G(^3P)^5G+9^3H(^3P)^3G$	$3d^44s(b\,^4G)4p$	$w\,^3G$	49371	49498	−127		0.807
	4	$40+13^3H(^3P)^3G$			49454	49583	−129		1.073
	5	$51+17^3H(^3P)^3G$			49538	49637	−99		1.202
$(^4P)^5S$	2	$30+31A^3P(^3P)^5S+15(^4D)^5P$			49823	49512	311	2.00	1.915
$(^4D)^5P$	1	$46+30(^4P)^5P+12^3D(^3P)^5P$			49589	49601	−12	2.48	2.476
	2	$14+20A^3F(^3P)^1D+11(^4P)^5P$			49598	49822	−224	1.88	1.456
	3	$31+26(^4P)^5P$			49812	49878	−66	1.77	1.588
$(^4D)^3F$	2	$37+18^3G(^3P)^3F$			49653	49702	−49		0.751
	3	$43+18^3G(^3P)^3F$			49650	49679	−29		1.141
	4	$56+15^3G(^3P)^3F$			49621	49651	−30		1.252
$(^4P)^3S$	1	$73+17A^3P(^3P)^3S$			49477	49821	−344		1.954
$A^3F(^3P)^1D$	2	$31+11(^4D)^5P$				49839			1.342
$(^4D)^3D$	1	$66+11(^4P)^3D$			50106	49965	141		0.487
	2	$57+14(^4P)^3D$			50184	50081	103		1.149
	3	$51+18(^4P)^3D$			50264	50206	58		1.346
$A^3P(^3P)^1P$	1	86				50125			0.982
$^3H(^3P)^1I$	6	$88+5^3G(^3P)^3H$				50126			1.013
$(^4D)^5F$	1	$44+29^3G(^3P)^5F+10(^4G)^5F$	$3d^44s(a\,^6D)5p$	$s\,^5F$	50019	50058	−39		0.051
	2	$43+29^3G(^3P)^5F+10(^4G)^5F$			50058	50112	−54		1.022
	3	$44+29^3G(^3P)^5F+9(^4G)^5F$			50102	50186	−84	1.27	1.258
	4	$30+29(^4D)^5D+21^3G(^3P)^5F$			50211	50237	−26	1.25	1.401
	5	$46+33^3G(^3P)^5F$			50253	50296	−43	1.39	1.395
$(^4D)^5D$	0	$69+10(^4P)^5D$	$3d^44s(c\,^4D)4p$	$u\,^5D$	50661	50455	206		
	1	$71+9(^4P)^5D$			50663	50476	187	1.46	1.514
	2	$68+8(^4P)^5D$			50655	50484	171	1.51	1.510
	3	$60+7(^4P)^5D$			50628	50467	161	1.54	1.507
	4	$44+15(^4D)^5F$			50558	50336	222	1.54	1.437
$A^3F(^3P)^1F$	3	$58+12^3D(^3P)^1F$				50858			0.996

TABLE 2. *Observed and calculated levels of* Cr I $(3d+4s)^5 4p$—Continued

Name	J	Percentage	AEL		Obs. level (cm^{-1})	Calc. level (cm^{-1})	O–C	Obs. g-factor	Calc. g-factor
			Config.	Desig.					
$^3G(^3P)^3H$	4	$77+7^3H(^3P)^3H$				50801			0.806
	5	$67+10^3H(^3P)^1H$				50893			1.031
	6	$76+6^3H(^3P)^1I$				51084			1.157
$^3G(^3P)^3F$	2	$41+27(^4D)^3F$	$3d^44s(a\,^4F)4p$	$w\,^3F$	50890	50919	−29		0.683
	3	$42+26(^4D)^3F$			50950	50994	−44		1.092
	4	$46+23(^4D)^3F$			51060	51102	−42		1.251
$^3H(^3P)^1H$	5	$68+11(^2I)^1H$	$3d^5(a\,^2I)4p$	$z\,^1H$	51401	50998	403		1.006
$(^4D)^3P$	0	$71+11A^3P(^3P)^3P$			51177	50965	212		
	1	$68+8A^3P(^3P)^3P$			51247	51069	178		1.527
	2	$45+32A^3P(^3P)^1D$			51287	51073	214		1.319
$A^3P(^3P)^1D$	2	$57+27(^4D)^3P$				51311			1.185
$^3D(^3P)^5D$	0	94	$3d^44s(a\,^4F)4p$	$t\,^5D$	52000	52113	−113		
	1	94			52003	52115	−112		1.494
	2	93			52012	52122	−110		1.495
	3	92			52032	52138	−106		1.496
	4	92			52064	52167	−103		1.497
$A^3F(^3P)^1G$	4	$56+22^3H(^3P)^1G$				52262			0.980
$^3G(^3P)^3G$	3	$69+15^3H(^3P)^3G$				52459			0.773
	4	$72+14^3H(^3P)^3G$		2°	52720	52502	218		1.053
	5	$53+14^3G(^3P)^1H$				52490			1.135
$^1I(^3P)^3I$	5	$48+33(^2I)^3I$	$3d^5(a\,^2I)4p$	$y\,^3I$	52592	52583	9		0.893
	6	$58+39(^2I)^3I$			52661	52620	41		1.025
	7	$59+39(^2I)^3I$			52678	52641	37		1.143
$^3G(^3P)^1H$	5	$67+10^3H(^3P)^1H$				52811			1.008
$^3G(^3P)^1F$	3	$63+21A^3F(^3P)^1F$				52903			0.985
$A^1G(^3P)^3H$	4	$47+26(^2I)^3H$	$3d^44s(b\,^4G)4p$	$x\,^3H$	52963	53169	−206		0.837
	5	$57+27(^2I)^3H$			52885	53136	−251		1.034
	6	$68+26(^2I)^3H$			52915	53162	−247		1.166
$^3D(^3P)^5F$	1	$85+6(^4D)^5F$	$3d^5(b\,^4F)4p$	$r\,^5F$	53012	53116	−104		0.008
	2	$84+6(^4D)^5F$			53038	53138	−100		1.004
	3	$83+6(^4D)^5F$			53074	53167	−93		1.252
	4	$81+6(^4D)^5F$			53118	53200	−82		1.336
	5	$85+7(^4D)^5F$			53172	53236	−64	1.42	1.399
$A^1G(^3P)^3F$	2	$59+15(A^2F)^3F$				53690			0.674
	3	$60+14(A^2F)^3F$				53567			1.082
	4	$62+11(A^2F)^3F$				53434			1.245
$(^4F)^3G^*$	3	$28+22(^4F)^3G$	$3d^44s(a\,^2G)4p$	$v\,^3G$	53805	53736	69		0.758
	4	$26+22(^4F)^3G$			53928	53873	55		1.044
	5	$25+22(^4F)^3G$			54078	54063	15		1.188
$(A^2D)^1D$	2	$32+30(A^2F)^1D$				53969			1.036

TABLE 2. *Observed and calculated levels of* Cr I $(3d+4s)^5 4p$—Continued

Name	J	Percentage	AEL		Obs. level (cm^{-1})	Calc. level (cm^{-1})	O−C	Obs. g-factor	Calc. g-factor
			Config.	Desig.					
$(A^2D)^3P$	0	$29+26A^1S(^3P)^3P$				54161			
	1	$17+14A^1S(^3P)^3P+13(^4F)^3D^*$				54164			1.022
	2	$25+17A^1S(^3P)^3P+16^3D(^3P)^3P$				54201			1.402
$(^2I)^3K$	6	$56+42^1I(^3P)^3K$			54317	54213	104		0.860
	7	$54+46^1I(^3P)^3K$			54405	54316	89		1.018
	8	$59+41^1I(^3P)^3K$			54498	54376	122		1.125
$(^4F)^3D^*$	1	$16+13A^1S(^3P)^3P$				54299			0.979
	2	$26+24A^3P(^3P)^3D$				54595			1.211
	3	$12+12A^3P(^3P)^3D+11(A^2D)^3F$				54914			1.170
$^3D(^3P)^5P$	1	$71+23(^4D)^5P$				54504			2.495
	2	$69+23(^4D)^5P$				54390			1.812
	3	$71+24(^4D)^5P$				54207			1.664
$^3H(^1P)^3H$	4	$42+20(^2I)^3H+18A^1G(^3P)^3H$	$3d^44s(a\,^2H)4p$	$w\,^3H$	54737	54484	253		0.816
	5	$41+21(^2I)^3H+17A^1G(^3P)^3H$			54799	54558	241		1.048
	6	$42+24(^2I)^3H+17A^1G(^3P)^3H$			54887	54608	279		1.156
$(A^2D)^3F$	2	$30+20(A^2F)^3F$	$3d^44s(c\,^2F)4p$	$v\,^3F$	54993	54708	285		0.720
	3	$22+15(A^2F)^3F+10(A^2D)^3D$			55102	54840	262		1.081
	4	$30+19^3G(^3P)^1G+18(A^2F)^3F$			55207	54954	253		1.163
$^1I(^3P)^3K$	6	$55+40(^2I)^3K$	$3d^44s(a\,^2H)4p$	$z\,^1I$	54800	54724	76		0.869
	7	$46+36(^2I)^3K+17(^2I)^1K$				54808			1.015
	8	$59+41(^2I)^3K$				54899			1.125
$A^1G(^3P)^3G$	3	$41+19(A^2F)^3G$				54897			0.895
	4	$33+17^3G(^3P)^1G$				54868			1.081
	5	$60+19(A^2F)^3G$				55053			1.197
$(^2I)^1K$	7	$79+10(^2I)^3K$			54970	54973	−3		1.005
$(A^2D)^1F$	3	$26+18(A^2F)^1F+9(^4F)^3D^*$				55090			1.085
$^3G(^3P)^1G$	4	$39+25A^1G(^3P)^3G$				55095			1.044
$^3D(^3P)^3D$	1	$33+28(A^2D)^3D$	$3d^5(a\,^2D)4p$	$v\,^3D$	54957	55179	−222		0.514
	2	$30+26(A^2D)^3D$			55153	55109	44		1.147
	3	$30+19(A^2D)^3D$			55452	55067	385		1.259
$(^2I)^1I$	6	$35+28^1I(^3P)^3H$			55517	55759	−242		1.077
$(^2I)^3I$	5	$29+30^1I(^3P)^3I+28^3H(^3P)^3I$	$3d^44s(a\,^2H)4p$	$x\,^3I$	55686	55709	−23		0.860
	6	$34+30^1I(^3P)^3I+25^3H(^3P)^3I$			55741	55818	−77		1.209
	7	$39+32^1I(^3P)^3I+24^3H(^3P)^3I$			55799	55861	−62		1.142
$(^2I)^1H$	5	$43+12^3G(^3P)^1H+9^1I(^1P)^1H$	$3d^44s(a\,^2H)4p$	$y\,^1H$	55945	55824	121		0.982
$(A^2F)^3D$	1	$30+14(^4F)^3D^*+13(A^2D)^1P$				55937			0.621
	2	$31+17A^3F(^3P)^3D+13(^4F)^3D^*$				56058			1.180
	3	$31+16A^3F(^3P)^3D+11(^4F)^3D^*$				56080			1.278
$^1I(^3P)^3H$	4	$67+12(^2H)^3H$	$3d^5(b\,^2H)4p$	$u\,^3H$	55916	56038	−122		0.802
	5	$61+12(^2H)^3H$			55875	55993	−118		1.030
	6	$37+37(^2I)^1I$			55908	56049	−141		1.083

TABLE 2. *Observed and calculated levels of* Cr I $(3d+4s)^5 4p$—Continued

Name	J	Percentage	AEL		Obs. level (cm^{-1})	Calc. level (cm^{-1})	O–C	Obs. g-factor	Calc. g-factor
			Config.	Desig.					
$(^4F)^5G$	2	$46+44(^4F)^5G^*$			56155	56119	36		0.353
	3	$43+38(^4F)^5G^*$			56210	56196	14		0.962
	4	$51+40(^4F)^5G^*$			56280	56321	−41		1.151
	5	$55+38(^4F)^5G^*$			56362	56455	−93		1.266
	6	$59+34(^4F)^5G^*$			56449	56600	−151		1.333
$^3D(^3P)^3P$	0	$56+19(A^2D)^3P$	$3d^5(a\,^2D)4p$	$v\,^3P$	56802	56537	265		
	1	$40+10^3D(^3P)^1P$			56723	56364	359		1.306
	2	$42+18(A^2D)^3P$			56592	56291	301		1.449
$(A^2D)^1P$	1	$26+20^3D(^3P)^1P$				56560			1.065
$^3D(^3P)^3F$	2	$36+20(^4F)^3F$				56624			0.687
	3	$43+18(^4F)^3F$				56663			1.088
	4	$31+29(A^2F)^1G$				56584			1.150
$(A^2F)^1G$	4	$45+22^3D(^3P)^3F$				56855			1.114
$(^4F)^3F^*$	2	$14+24^3D(^3P)^3F$	$3d^5(b\,^2F)4p$	$t\,^3F$	57221	57036	185		0.672
	3	$10+10(^4F)^3F+9^3D(^3P)^3F$			57276	57200	76		0.924
	4	$13+16(^4F)^3F+15(A^2F)^3G$			57335	57324	11		1.180
$A^3F(^1P)^3G$	3	$21+16^3D(^3P)^3F+9^3H(^3P)^3G$	$3d^5(b\,^2H)4p$	$u\,^3G$	56986	57044	−58		0.921
	4	$24+15^3H(^3P)^3G+12(A^2F)^3G$			57034	57153	−119		1.125
	5	$25+23^3H(^3P)^3G+22(A^2F)^3G$			57088	57297	−209		1.218
$A^1S(^3P)^3P$	0	$40+22(A^2D)^3P+18A^3P(^3P)^3P$	$3d^4 4s(a\,^2P)4p$	$u\,^3P$	57155	57313	−158		
	1	$40+21(A^2D)^3P+16A^3P(^3P)^3P$			57133	57319	−186		1.482
	2	$43+22(A^2D)^3P+11A^3P(^3P)^3P$			57088	57293	−205		1.475
$(^4F)^5F$	1	$69+14(^4F)^5F^*$				57483			0.026
	2	$70+13(^4F)^5F^*$				57504			1.005
	3	$57+10(^4F)^5F^*$				57518			1.169
	4	$53+16(A^2F)^3G+8(^4F)^5F^*$				57609			1.293
	5	$62+9(^4F)^5F^*$				57635			1.360
$(A^2F)^3G$	3	$40+14(^4F)^5F+11(A^2F)^3F$	$3d^4 4s(c\,^2G)4p$	$t\,^3G$	57557	57591	−34		0.919
	4	$21+18(^4F)^5F+14(A^2F)^3F$			57587	57526	61		1.174
	5	$58+20A^3F(^3P)^3G$			57702	57788	−86		1.216
$A^1D(^3P)^3D$	1	$41+20^3D(^3P)^3D$				57815			0.502
	2	$30+14(A^2F)^3F+12(A^2D)^3F$				57954			0.957
	3	$39+16^3D(^3P)^3D$				58058			1.269
$(A^2F)^3F$	2	$26+24A^1D(^3P)^3D+15(A^2D)^3F$	$3d^5(a\,^2D)4p$	$s\,^3F$	58163	57900	263		0.892
	3	$25+23(A^2D)^3F+20(A^2F)^3G$			58203	57993	210		1.071
	4	$25+23(A^2F)^3G+20(A^2D)^3F$			58168	58069	99		1.170
$A^1D(^3P)^3F$	2	$56+25(A^2G)^3F$				58655			0.679
	3	$50+19(A^2G)^3F$				58658			1.089
	4	$48+16(A^2G)^3F+16(^4F)^5D$				58747			1.299
$^3D(^3P)^1F$	3	$29+24(A^2F)^1F$				58927			1.104

TABLE 2. *Observed and calculated levels of* Cr I $(3d+4s)^5 4p$—Continued

Name	J	Percentage	AEL		Obs. level (cm^{-1})	Calc. level (cm^{-1})	O–C	Obs. g-factor	Calc. g-factor
			Config.	Desig.					
$(^4F)^5D$	0	$75+8(^4F)^5D^*$				58939			
	1	$42+15(^4F)^3D$				58912			1.136
	2	$75+6(^4F)^5D^*$				58966			1.480
	3	$69+5(^4F)^5D^*$				58955			1.456
	4	$60+13A^1D(^3P)^3F$				59028			1.435
$(^2I)^3H$	4	$16+23(^2H)^3H+16^1I(^3P)^3H$	$3d^4 4s(a\,^3G)4p$	$t\,^3H$	58728	58950	−222		0.818
	5	$17+24(^2H)^3H+16^1I(^3P)^3H$			58755	58986	−231		1.038
	6	$17+26(^2H)^3H+16^1I(^3P)^3H$			58775	59016	−241		1.165
$(^4F)^3D$	1	$18+33(^4F)^5D+13^3D(^3P)^1P$	$3d^4 4s(a\,^2P)4p$	$u\,^3D$	58725	58945	−220		1.041
	2	$39+28^3D(^3P)^3D+15(A^2D)^3D$			58860	59138	−278		1.157
	3	$25+25^3D(^3P)^3D$			59122	59292	−170		1.248
$^3D(^3P)^1P$	1	$29+25(A^2D)^1P+16(^4F)^3D$				59396			0.815
$A^3F(^1P)^3F$	2	$51+11(^4F)^3F$	$3d^4 4s(a\,^2G)4p$	$r\,^3F$	59358	59316	42		0.692
	3	$46+9(^4F)^3F$			59417	59415	2		1.079
	4	$50+9(^4F)^3F$			59488	59457	31		1.240
$(A^2F)^1D$	2	$42+18^3D(^3P)^1D+14A^3F(^3P)^1D$				59493			0.989
$^3H(^1P)^3I$	5	$64+16(^2H)^3I+10(^2I)^3I$	$3d^5(b\,^2H)4p$	$w\,^3I$	59806	59650	156		0.848
	6	$74+13(^2I)^3I+9(^2H)^3I$			59884	59808	76		1.026
	7	$77+13(^2I)^3I+7(^2H)^3I$			59957	59947	10		1.143
$(^2H)^3I$	5	$50+16(A^2G)^1H+14(^2H)^1H$	$3d^4 4s(b\,^2I)4p$	$v\,^3I$	60428	59965	463		0.916
	6	$74+11(A^2G)^3H$			60528	60244	284		1.042
	7	$85+6(^2I)^3I$			60656	60433	223		1.142
$(^4F)^5G^*$	2	$50+48(^4F)^5G$				60015			0.338
	3	$52+45(^4F)^5G$				60120			0.916
	4	$54+41(^4F)^5G$				60259			1.142
	5	$44+29(^4F)^5G$				60398			1.219
	6	$54+30(^4F)^5G$				60650			1.296
$(A^2G)^1G$	4	$42+29(^2H)^1G+15(A^2F)^1G$				60335			1.006
$(A^2F)^1F$	3	$21+17(A^2D)^1F+17(A^2G)^3G$				60348			1.010
$(^2H)^1H$	5	$13+20(A^2G)^3G+18(^2H)^3I$			60006	60385	−279		1.054
$(A^2G)^3G$	3	$33+16(A^2F)^1F+7(^2H)^3G$		$s\,^3G$	60518	60383	135		0.846
	4	$40+9(^2H)^3G+6(^2H)^1G$			60504	60375	129		1.042
	5	$30+21(^2H)^3I+11(^4F)^5G^*$			60468	60328	140		1.098
$A^3P(^1P)^3S$	1	$48+19A^3P(^1P)^3P+10(A^2F)^3D$	$3d^4 4s(a\,^2P)4p$	$x\,^3S$	60084	60406	−322		1.751
$(A^2D)^3D$	1	$29+22A^1D(^3P)^3D+19(^4F)^3D$	$3d^5(b\,^2F)4p$	$s\,^3D$	60678	60408	270		0.532
	2	$25+24A^1D(^3P)^3D+20(^4F)^3D$			60630	60295	335		1.161
	3	$17+24(^4F)^3D+17A^1D(^3P)^3D$			60616	60151	465		1.236

TABLE 2. *Observed and calculated levels of* Cr I $(3d+4s)^5 4p$ – Continued

Name	J	Percentage	AEL		Obs. level (cm^{-1})	Calc. level (cm^{-1})	O–C	Obs. g-factor	Calc. g-factor
			Config.	Desig.					
$(A^2G)^3H$	4	$52+13^3H(^1P)^3H+8(^2H)^3H$	$3d^44s(c\,^2G)4p$	$s\,^3H$	60871	60669	202		0.834
	5	$41+11^3H(^1P)^3H+7(^2H)^3H$			61008	60862	146		1.072
	6	$35+27(^2H)^1I+7(^2H)^3H$			61192	61243	−51		1.112
$A^3P(^1P)^3P$	0	$47+17(A^2D)^3P$				60750			
	1	$20+26A^3P(^1P)^3S+10(A^2F)^3D$				61037			1.369
	2	$29+10(A^2F)^3D$				60996			1.288
$(^2H)^3G$	3	$24+19(B^2F)^3G+16(^4F)^3G$	$3d^5(b\,^2G)4p$	$r\,^3G$	61078	60837	241		0.760
	4	$19+15(B^2F)^3G+12(^4F)^3G$			61123	60903	220		1.030
	5	$15+15(A^2G)^3H+12(B^2F)^3G$			61161	60989	173		1.160
$(^2H)^1I$	6	$49+17(A^2G)^3H+10(^2I)^1I$			60441	60911	−470		1.074
$^3D(^3P)^1D$	2	$18+16(B^2F)^3F+12(A^2D)^1D$				61062			0.905
$(B^2F)^3F$	2	$11+11^3D(^3P)^1D+10(B^2F)^3D$				61380			1.079
	3	$40+21^1F(^3P)^3F$	$3d^44s(c\,^2G)4p$	$p\,^3F$	60820	61168	−348		1.087
	4	$39+24^1F(^3P)^3F+10A^1D(^3P)^3F$			60961	61115	−154		1.241
$A^3F(^1P)^3D$	1	$24+22(A^2F)^3D+20A^3P(^1P)^3D$				61297			0.879
	2	$21+11^3D(^3P)^1D+10(B^2F)^3D$				61457			1.104
	3	$31+27(B^2F)^3D+22A^3P(^1P)^3D$				61363			1.327
$(^2H)^1G$	4	$25+26(A^2G)^1G+26A^1G(^1P)^1G$				61499			1.006
$A^1D(^3P)^3P$	0	$77+7(A^2D)^3P$	$3d^44s(a\,^2P)4p$	$t\,^3P$	(61388)	61569	(−181)		
	1	$65+8(A^2D)^3P$			(61527)	61647	(−120)		1.444
	2	$58+8(^4F)^5F^*$			(61676)	61753	(−74)		1.411
$^3G(^1P)^3H$	4	$46+17(^2I)^3H+15(A^2G)^3H$				61823			0.833
	5	$36+18(^4F)^3G+13(^2I)^3H$				61895			1.081
	6	$52+18(A^2G)^3H+16(^2I)^3H$				62048			1.165
$(^4F)^5F^*$	1	$77+16(^4F)^5F$				61886			0.033
	2	$68+14(^4F)^5F$				61967			1.048
	3	$77+15(^4F)^5F$				62159			1.243
	4	$59+10(^4F)^5F$				62272			1.268
	5	$80+12(^4F)^5F$				62618			1.390
$(^4F)^5D^*$	0	$77+12(^4F)^5D$				62075			
	1	$76+12(^4F)^5D$				62123			1.489
	2	$76+10(^4F)^5D$				62225			1.491
	3	$77+8(^4F)^5D$				62386			1.492
	4	$75+6(^4F)^5D$				62599			1.479
$(^4F)^3G$	3	$48+15^3G(^1P)^3G+9(^4F)^3G^*$		$q\,^3G$	61930	62166	−236		0.769
	4	$32+20(^4F)^5F^*+10(B^2F)^3G$			61976	62227	−251		1.115
	5	$31+15^3G(^1P)^3H+11(B^2F)^3G$			62038	62114	−76		1.153
$(^4F)^3F$	2	$23+21(A^2G)^3F+19(^4F)^3F^*$				62702			0.675
	3	$19+18(A^2G)^3F+18(^4F)^3F^*$				62700			1.067
	4	$18+20(A^2G)^3F+18(^4F)^3F^*$				62779			1.251

TABLE 2. *Observed and calculated levels of* Cr I $(3d+4s)^5 4p$ – Continued

Name	J	Percentage	AEL	Obs. level (cm^{-1})	Calc. level (cm^{-1})	O–C	Obs. g-factor	Calc. g-factor
$(A^2G)^1F$	3	$64+10A^1D(^1P)^1F$			62780			1.007
$(A^2G)^1H$	5	$50+32(^2H)^1H$			62992			1.008
$(B^2F)^3D$	1	$44+25(^4F)^3D^*+10^3D(^1P)^3D$			63218			0.505
	2	$44+24(^4F)^3D^*+8^3D(^1P)^3D$			63337			1.166
	3	$40+22(^4F)^3D^*+9^3D(^1P)^3D$			63498			1.254
$(B^2F)^1G$	4	$58+5(^2H)^3H$			63294			0.988
$(B^2F)^1D$	2	$73+13^3D(^3P)^1D$			63373			1.002
$^3H(^1P)^3G$	3	$17+23(A^2G)^3G+14(B^2F)^3G$			63493			0.843
	4	$20+21(B^2F)^1G+14(A^2G)^3G$			63444			0.986
	5	$19+17(A^2G)^3G+17(^2H)^3H$			63508			1.132
$(^2H)^3H$	4	$30+15(A^2G)^3G+13^3H(^1P)^3H$			63768			0.897
	5	$27+16(A^2G)^3G+12^3H(^1P)^3H$			63862			1.101
	6	$43+23^3G(^1P)^3H$			63784			1.165
$(B^2F)^1F$	3	$54+30A^1G(^1P)^1F$			63964			1.001
$^1F(^3P)^3F$	2	$18+17^3G(^1P)^3F+16(^4F)^3F$			64245			0.674
	3	$18+16(^4F)^3F+15^3G(^1P)^3F$			64263			1.077
	4	$19+16(^4F)^3F+16^3G(^1P)^3F$			64254			1.240
$A^1D(^1P)^1P$	1	$24+25(^2S)^1P+15A^1S(^1P)^1P$			64549			1.067
$^1F(^3P)^3G$	3	$76+14(^2H)^3G$			64795			0.756
	4	$77+13(^2H)^3G$			64887			1.053
	5	$77+13(^2H)^3G$			64997			1.199
$^3D(^1P)^3P$	0	$51+19(^2S)^3P+19(^4P)^3P^*$			65007			
	1	$44+17(^2S)^3P+15(^4P)^3P^*$			65038			1.427
	2	$53+19(^4P)^3P^*+15(^2S)^3P$			64984			1.494
$(A^2G)^3F$	2	$22+18(B^2F)^3F+15^3D(^1P)^3F$			65192			0.669
	3	$26+20(B^2F)^3F+15^3D(^1P)^3F$			65200			1.067
	4	$27+25(B^2F)^3F+19^3D(^1P)^3F$			65227			1.245
$^3D(^1P)^3D$	1	$42+12(^4F)^3D$			65466			0.506
	2	$42+11^1F(^3P)^3D$			65454			1.165
	3	$40+17^1F(^3P)^3D$			65424			1.329
$(B^2F)^3G$	3	$44+17(^2H)^3G+10^3H(^1P)^3G$			65446			0.769
	4	$46+17(^2H)^3G+11^3H(^1P)^3G$			65538			1.054
	5	$47+15(^2H)^3G+8^1F(^3P)^3G$			65637			1.197
$^3G(^1P)^3F$	2	$18+24(B^2F)^3F+19^1F(^3P)^3F$			66000			0.718
	3	$17+22(B^2F)^3F+17^1F(^3P)^3F$			66115			1.128
	4	$20+26(B^2F)^3F+19^1F(^3P)^3F$			66174			1.250
$^1F(^3P)^3D$	1	$74+8^3D(^1P)^3D$			66219			0.502
	2	$62+9^3D(^1P)^3D$			66138			1.123
	3	$54+9^3D(^1P)^3D$			65979			1.291

TABLE 2. *Observed and calculated levels of* Cr I $(3d+4s)^5 4p$—Continued

Name	J	Percentage	AEL	Obs. level (cm^{-1})	Calc. level (cm^{-1})	O−C	Obs. g-factor	Calc. g-factor
$^1I(^1P)^1H$	5	$27+37A^1G(^1P)^1H$			66527			1.005
$^1I(^1P)^1K$	7	93			67188			1.000
$^1I(^1P)^1I$	6	$77+9(^2H)^1I$			67255			1.001
$A^3P(^1P)^3D$	1	$33+34(B^2F)^3D+12(B^2D)^3D$			67309			0.513
	2	$32+30(B^2F)^3D+11(B^2D)^3D$			67409			1.142
	3	$29+20(B^2F)^3D+10(B^2D)^3D$			67568			1.345
$B^3P(^3P)^5P$	1	91			67556			2.417
	2	$85+6B^3P(^3P)^5S$			67413			1.824
	3	$75+7(B^2F)^3D$			67436			1.593
$B^3F(^3P)^5F$	1	91			67572			0.065
	2	88			67596			0.995
	3	$79+3(^4F)^3F^*$			67619			1.232
	4	$64+10A^1G(^1P)^1G$			67674			1.260
	5	94			67623			1.399
$^3G(^1P)^3G$	3	$23+25(^4F)^3G^*+9(A^2G)^3G$			67574			0.767
	4	$21+24(^4F)^3G^*+10(A^2G)^3G$			67738			1.060
	5	$19+25(^4F)^3G^*+9(A^2G)^3G$			67944			1.162
$A^1G(^1P)^1G$	4	$18+19B^3F(^3P)^5F+13(^2G)^1G^*$			67769			1.108
$^3D(^1P)^3F$	2	$35+20(^4F)^3F^*+10^3G(^1P)^3F$			67698			0.713
	3	$26+14(^4F)^3F^*+12^3G(^1P)^3F$			67834			1.136
	4	$31+25(^4F)^3F^*+10^3G(^1P)^3F$			67969			1.232
$(^2S)^3P$	0	$59+11(^4P)^3P^*+10(B^2D)^3P$			67778			
	1	$59+10(^4P)^3P^*+10(B^2D)^3P$			67851			1.482
	2	$59+12(B^2D)^3P+10(^4P)^3P^*$			67967			1.492
$B^3P(^3P)^5D$	0	$73+18B^3F(^3P)^5D$			68152			
	1	$60+19B^3F(^3P)^5D$			68138			1.522
	2	$68+17B^3F(^3P)^5D$			68087			1.513
	3	$67+17B^3F(^3P)^5D$			68015			1.503
	4	$71+15B^3F(^3P)^5D$			67870			1.487
$A^1G(^1P)^1H$	5	$35+14^1I(^1P)^1H+13(^2G)^1H^*$			68150			1.038
$(^2S)^1P$	1	$51+29(B^2D)^1P$			68406			0.998
$B^3F(^3P)^5G$	2	98			68572			0.336
	3	98			68608			0.917
	4	98			68649			1.150
	5	98			68687			1.266
	6	99			68714			1.333
$A^1G(^1P)^1F$	3	$23+21(B^2D)^1F+14(^2G)^1F^*$			68695			1.000
$B^3P(^3P)^5S$	2	$78+13(^4P)^5S^*$			68777			1.980
$A^1D(^1P)^1F$	3	$27+28(B^2F)^1F+19A^1G(^1P)^1F$			69433			1.001

372-505 O - 70 - 3

TABLE 2. *Observed and calculated levels of* Cr I $(3d+4s)^5 4p$ – Continued

Name	J	Percentage	AEL	Obs. level (cm^{-1})	Calc. level (cm^{-1})	O–C	Obs. g-factor	Calc. g-factor
$A^1D(^1P)^1D$	2	$53+20(B^2D)^1D$			69795			1.014
$B^3F(^3P)^5D$	0	$52+40(^4P)^5D^*$			69957			
	1	$53+39(^4P)^5D^*$			69969			1.498
	2	$56+37(^4P)^5D^*$			69987			1.498
	3	$56+34(^4P)^5D^*$			69994			1.498
	4	$61+30(^4P)^5D^*$			69970			1.499
$A^1S(^1P)^1P$	1	$33+25A^1D(^1P)^1P+8(^2P)^1P^*$			70048			0.896
$B^3P(^3P)^3D$	1	$43+19B^3F(^3P)^3D$			70229			0.615
	2	$45+18B^3F(^3P)^3D$			70103			1.169
	3	$52+16B^3F(^3P)^3D$			70087			1.336
$(^4P)^3P^*$	0	$28+37(B^2D)^3P+19B^3P(^3P)^3P$			70539			
	1	$28+36(B^2D)^3P+18B^3P(^3P)^3P$			70518			1.493
	2	$29+32(B^2D)^3P+18B^3P(^3P)^3P$			70445			1.480
$B^3F(^3P)^3F$	2	$69+16(B^2D)^3F$			70623			0.670
	3	$70+16(B^2D)^3F$			70642			1.084
	4	$72+16(B^2D)^3F$			70689			1.251
$B^3P(^3P)^1D$	2	$44+27(B^2D)^1D$			71354			0.997
$(^4P)^5P^*$	1	95			71377			2.493
	2	95			71506			1.831
	3	95			71665			1.665
$(B^2D)^3F$	2	$60+20B^3F(^3P)^3F$			71953			0.673
	3	$61+21B^3F(^3P)^3F$			72025			1.081
	4	$62+20B^3F(^3P)^3F$			72139			1.247
$B^3P(^3P)^3P$	0	$48+17(^4P)^3P^*$			72448			
	1	$49+18(^4P)^3P^*$			72438			1.501
	2	$43+13(^4P)^3P^*$			72329			1.354
$(^2G)^3H^*$	4	$66+10(B^2G)^3H$			72474			0.808
	5	$52+18B^3F(^3P)^3G+10(B^2G)^3H$			72617			1.068
	6	$65+12(B^2G)^3H$			72942			1.166
$(B^2D)^1F$	3	$39+14(^2G)^1F^*+10^1F(^1P)^1F$			72577			0.961
$(B^2D)^1D$	2	$16+15A^1D(^1P)^1D+10^1F(^1P)^1D$			72610			1.146
$B^3F(^3P)^3G$	3	$72+8(B^2D)^1F$			72607			0.793
	4	84			72572			1.045
	5	$69+15(^2G)^3H^*$			72624			1.165
$(B^2D)^3D$	1	$61+12(^4P)^3D^*$			72899			0.527
	2	$60+11(^4P)^3D^*$			72970			1.179
	3	$62+8(^4P)^3D^*$			73071			1.335
$B^3P(^3P)^3S$	1	75			73216			1.930
$B^3F(^3P)^1F$	3	$79+10(B^2G)^1F$			73515			1.001
$B^3F(^3P)^1G$	4	$50+28^1F(^1P)^1G+12(^2H)^1G^*$			73686			1.000

TABLE 2. *Observed and calculated levels of* Cr I $(3d+4s)^5 4p$ – Continued

Name	J	Percentage	AEL	Obs. level (cm^{-1})	Calc. level (cm^{-1})	O–C	Obs. g-factor	Calc. g-factor
$^4P(^5D)^*$	0	$49+24B^3F(^3P)^5D$			73609			
	1	$50+23B^3F(^3P)^5D$			73644			1.507
	2	$52+21B^3F(^3P)^5D$			73701			1.487
	3	$58+20B^3F(^3P)^5D$			73799			1.494
	4	$65+20B^3F(^3P)^5D$			73918			1.500
$(B^2D)^3P$	0	$32+31B^3P(^3P)^3P$			73702			
	1	$32+29B^3P(^3P)^3P$			73675			1.513
	2	$35+30B^3P(^3P)^3P$			73603			1.494
$(^2P)^1S^*$	0	$64+21B^3P(^3P)^1S$			74127			
$(^4P)^3D^*$	1	$52+22B^3F(^3P)^3D$			74478			0.509
	2	$40+16B^3F(^3P)^3D+12(^2P)^1D^*$			74399			1.125
	3	$57+29B^3F(^3P)^3D$			74601			1.330
$B^3P(^3P)^1P$	1	$47+26(B^2D)^1P$			74565			1.013
$(^2P)^1D^*$	2	$30+22^1F(^1P)^1D+14(^4P)^3D^*$			74875			1.044
$(^2G)^3G^*$	3	$52+18(B^2G)^3G+8^3H(^1P)^3G$			75101			0.755
	4	$51+20(B^2G)^3G+9^3H(^1P)^3G$			75235			1.049
	5	$27+21(^2G)^1H^*+18(^2H)^1H^*$			75350			1.099
$(^2G)^1H^*$	5	$18+18(B^2G)^3G+15(^2H)^1H^*$			75487			1.118
$B^1G(^3P)^3G$	3	$73+18(B^2G)^3G$			75376			0.754
	4	$73+17(B^2G)^3G$			75421			1.049
	5	$60+18(^2G)^3G^*+13(B^2G)^3G$			75544			1.180
$^1F(^1P)^1F$	3	$45+25(B^2G)^1F+15(B^2D)^1F$			75509			0.998
$B^3F(^3P)^3D$	1	$45+18B^3P(^3P)^3D$			76101			0.766
	2	$51+30B^3P(^3P)^3D$			76052			1.108
	3	$50+27B^3P(^3P)^3D$			75987			1.297
$(B^2D)^1P$	1	$29+33B^3P(^3P)^1P+12(^2P)^1P^*$			76187			1.002
$B^3P(^3P)^1S$	0	$67+27(^2P)^1S^*$			76228			
$(^4P)^3S^*$	1	$38+23B^3P(^3P)^3S+18(^2P)^3S^*$			76239			1.729
$(^2G)^3F^*$	2	$28+31B^1G(^3P)^3F+16(B^2G)^3F$			76311			0.723
	3	$24+30B^1G(^3P)^3F+17(B^2G)^3F$			76286			1.115
	4	$13+14B^1G(^3P)^3F+13(B^2G)^3F$			76190			1.129
$^1F(^1P)^1G$	4	$10+13B^1G(^3P)^3F+12(^2G)^3F^*$			76307			1.109
$B^1G(^3P)^3H$	4	$72+21(B^2G)^3H$			76419			0.814
	5	$75+22(B^2G)^3H$			76490			1.035
	6	$75+23(B^2G)^3H$			76590			1.167
$(^4P)^5S^*$	2	$83+14B^3P(^3P)^5S$			76937			1.990
$(^2G)^1G^*$	4	$24+25B^3F(^3P)^1G+19^1F(^1P)^1G$			77098			0.987
$B^1G(^3P)^3F$	2	$35+31(A^2D)^3F^*$			77452			0.724
	3	$27+20^1F(^1P)^1F+12(^2G)^1F^*$			77500			1.045
	4	$22+14^1F(^1P)^1G+12(^2G)^3F^*$			77640			1.235
$(^2G)^1F^*$	3	$12+16B^1G(^3P)^3F+17(B^2G)^1F$			77598			1.055

TABLE 2. *Observed and calculated levels of* Cr I $(3d+4s)^5 4p$ – Continued

Name	J	Percentage	AEL	Obs. level (cm^{-1})	Calc. level (cm^{-1})	O–C	Obs. g-factor	Calc. g-factor
$(^2P)^3P^*$	0	$47+28(A^2D)^3P^*$			77529			
	1	$45+27(A^2D)^3P^*$			77700			1.506
	2	$30+25(^2P)^3D^*+9(A^2D)^3P^*$			78191			1.340
$(B^2G)^3H$	4	$60+13(^2H)^3H^*+9(^2G)^3H^*$			77673			0.830
	5	$65+16(^2H)^3H^*+11(^2G)^3H^*$			77745			1.033
	6	$67+15(^2H)^3H^*+12(^2G)^3H^*$			77894			1.166
$(^2P)^3D^*$	1	$72+15B^3F(^3P)^3D$			77981			0.510
	2	$41+12(^2P)^3P^*$			78101			1.149
	3	$45+20(B^2G)^3F+9(^2G)^3F^*$			78380			1.228
$(B^2G)^3F$	2	$42+19B^3F(^1P)^3F+10B^1G(^3P)^3F$			78202			0.830
	3	$39+27(^2P)^3D^*+21B^3F(^1P)^3F$			78203			1.168
	4	$56+24B^3F(^1P)^3F+12(^2G)^3F^*$			78162			1.248
$(A^2D)^1D^*$	2	$21+16(B^2G)^3F+9(^2P)^1D^*$			78383			1.011
$B^3F(^3P)^1D$	2	$61+20B^3P(^3P)^1D$			78680			1.030
$(B^2G)^1H$	5	$75+8(^2H)^3I^*$			78822			0.988
$(^2P)^3S^*$	1	$53+24(^4P)^3S^*+13B^3P(^3P)^3S$			78892			1.948
$(^2H)^3H^*$	4	$53+15(B^2G)^3H+12(^2G)^3H^*$			79032			0.847
	5	$42+15(B^2G)^3G+10(^2H)^3I^*$			79162			1.055
	6	$61+16(^2H)^3I^*+10(^2G)^3H^*$			79376			1.142
$(B^2G)^3G$	3	$42+27B^3F(^1P)^3G+15(^2G)^3G^*$			79101			0.753
	4	$40+19B^3F(^1P)^3G+15(^2G)^3G^*$			79202			1.028
	5	$30+25(^2H)^3H^*+12(^2G)^3G^*$			79371			1.116
$(A^2D)^3P^*$	0	$31+20(^2P)^3P^*+19B^3P(^1P)^3P$			79193			
	1	$32+15(^2P)^3P^*+15B^3P(^1P)^3P$			79112			1.530
	2	$34+21B^3P(^1P)^3P+16(^2P)^3P^*$			79027			1.422
$(^2H)^3I^*$	5	$72+8(B^2G)^3G+7(B^2G)^1H$			79422			0.912
	6	$81+9(^2H)^3H^*$			79640			1.048
	7	98			79625			1.143
$(B^2G)^1G$	4	$48+35(^2G)^1G^*+9(^2H)^3H^*$			79768			0.980
$(B^2G)^1F$	3	$37+14(^2G)^1F^*+11(^2H)^3G^*$			79904			0.932
$(^2H)^3G^*$	3	$28+26(B^2G)^3G+15(B^2G)^1F$			80175			0.828
	4	$40+29(B^2G)^3G+16B^3F(^1P)^3G$			80205			1.054
	5	$40+31(B^2G)^3G+16B^3F(^1P)^3G$			80256			1.199
$(A^2D)^3F^*$	2	$43+28(^2G)^3F^*$			80717			0.673
	3	$42+27(^2G)^3F^*$			80821			1.078
	4	$45+26(^2G)^3F^*$			80914			1.243
$B^3P(^1P)^3D$	1	77			82133			0.510
	2	73			81980			1.168
	3	80			81698			1.332
$(A^2D)^3D^*$	1	$75+8^3D(^1P)^3D$			81944			0.547
	2	$76+7^3D(^1P)^2D$			82108			1.168
	3	$50+16(A^2D)^1F^*$			82304			1.209

TABLE 2. *Observed and calculated levels of* Cr I $(3d+4s)^5 4p$ – Continued

Name	J	Percentage	AEL	Obs. level (cm^{-1})	Calc. level (cm^{-1})	O–C	Obs. g-factor	Calc. g-factor
$(A^2D)^1F^*$	3	$37+30(A^2D)^3D^*$			81992			1.126
$(^2H)^1H^*$	5	$42+29(^2G)^1H^*+20^1I(^1P)^1H$			82237			1.000
$(^2H)^1I^*$	6	92			82252			1.001
$(A^2D)^1P^*$	1	$68+14A^1S(^1P)^1P$			82773			0.978
$(^2H)^1G^*$	4	$54+26^1F(^1P)^1G+14B^1G(^1P)^1G$			82801			1.006
$B^3F(^1P)^3F$	2	$73+16(B^2G)^3F$			83311			0.670
	3	$71+17(B^2G)^3F$			83365			1.084
	4	$70+18(B^2G)^3F$			83409			1.245
$(^2P)^1P^*$	1	$52+27A^1D(^1P)^1P+8(^2P)^1P$			83595			0.983
$B^3F(^1P)^3D$	1	$53+12(^4P)^3D^*$			85283			0.717
	2	$49+11(^4P)^3D^*$			85200			1.253
	3	$70+16(B^2G)^3F$			85224			1.331
$B^3P(^1P)^3P$	0	$30+25(B^2D)^3P^*+23(^2P)^3P$			85523			
	1	$31+22(B^2D)^3P^*+16(^2P)^3P$			85516			1.285
	2	$33+21(B^2D)^3P^*+14(^2P)^3P$			85452			1.408
$B^3F(^1P)^3G$	3	$52+32(^2H)^3G^*$			86638			0.755
	4	$53+32(^2H)^3G^*$			86653			1.050
	5	$55+33(^2H)^3G^*$			86647			1.199
$B^1G(^1P)^1F$	3	$40+26(^2F)^1F^*+15(A^2D)^1F^*$			87247			0.998
$^1F(^1P)^1D$	2	$25+29(A^2D)^1D^*+23(^2P)^1D^*$			87510			1.013
$(^2P)^3P$	0	$48+20(C^2D)^3P+15B^3P(^1P)^3P$			87486			
	1	$48+19(C^2D)^3P+13B^3P(^1P)^3P$			87496			1.531
	2	$48+17(C^2D)^3P+13B^1D(^3P)^3P$			87654			1.479
$B^1G(^1P)^1G$	4	$45+40(^2F)^1G^*$			88071			1.001
$(^2P)^1D$	2	$41+28(^2P)^3D+16(C^2D)^1D$			88166			1.067
$B^3P(^1P)^3S$	1	$43+21(^4P)^3S^*$			88353			1.963
$(^2P)^3D$	1	$79+8(C^2D)^3D$			88338			0.503
	2	$51+24(^2P)^1D$			88483			1.111
	3	$80+10(C^2D)^3D$			88440			1.332
$(^2P)^1S$	0	$79+10B^3P(^3P)^1S$			88482			
$B^1D(^3P)^3P$	0	$69+20(B^2D)^3P$			88763			
	1	$73+21(B^2D)^3P$			88667			1.502
	2	$69+22(B^2D)^3P$			88583			1.498
$(^2F)^3F^*$	2	$52+35B^1D(^3P)^3F$			89512			0.671
	3	$53+35B^1D(^3P)^3F$			89548			1.083
	4	$54+33B^1D(^3P)^3F$			89599			1.249
$(^2P)^1P$	1	$78+6(^2P)^1P^*$			89665			1.033

TABLE 2. *Observed and calculated levels of* Cr I $(3d+4s)^5 4p$—Continued

Name	J	Percentage	AEL	Obs. level (cm^{-1})	Calc. level (cm^{-1})	O−C	Obs. g-factor	Calc g-factor
$B^1G(^1P)^1H$	5	$84+10(^2H)^1H^*$			89871			1.001
$(^2P)^3S$	1	$79+16B^3P(^1P)^3S$			90104			1.960
$B^1D(^3P)^3F$	2	$48+39(^2F)^3F^*$			91733			0.671
	3	$39+38(^2F)^3G^*+20(^2F)^3F^*$			91804			0.942
	4	$38+40(^2F)^3G^*+23(^2F)^3F^*$			92008			1.160
$(^2F)^3G^*$	3	$51+20B^1D(^3P)^3F+18(^2F)^3F^*$			91975			0.894
	4	$49+27B^1D(^3P)^3F+15(^2F)^3F^*$			91870			1.140
	5	$89+7(^2H)^3G^*$			92072			1.200
$(C^2D)^1D$	2	$51+20(^2F)^1D^*+12(^2P)^1D^*$			92513			1.015
$B^1D(^3P)^3D$	1	$65+17(^2F)^3D^*$			92563			0.501
	2	$56+16(^2F)^3D^*$			92585			1.132
	3	$66+20(^2F)^3D^*$			92597			1.325
$(C^2D)^3F$	2	$77+14B^1D(^3P)^3F$			92876			0.688
	3	$76+15B^1D(^3P)^3F$			92947			1.090
	4	$82+15B^1D(^3P)^3F$			93056			1.250
$(^2F)^1D^*$	2	$55+16(C^2D)^1D+11(^2P)^1D$			93606			0.998
$(C^2D)^1F$	3	$56+34(^2F)^1F^*$			93669			1.002
$(C^2D)^3D$	1	$61+25B^1D(^3P)^3D$			94122			0.503
	2	$60+27B^1D(^3P)^3D$			94171			1.166
	3	$54+30B^1D(^3P)^3D$			94223			1.332
$(C^2D)^1P$	1	$83+15B^1D(^1P)^1P$			94282			0.999
$(C^2D)^3P$	0	$65+17(^2P)^3P$			95463			
	1	$69+16(^2P)^3P$			95376			1.474
	2	$65+16(^2P)^3P$			95205			1.492
$(^2F)^3D^*$	1	$52+17(C^2D)^3D$			95687			0.527
	2	$50+15(C^2D)^3D+12B^3F(^1P)^3D$			95602			1.173
	3	$45+20(C^2D)^3D+11B^3F(^1P)^3D$			95481			1.332
$(^2F)^1G^*$	4	$53+33B^1G(^1P)^1G$			95731			1.000
$(^2F)^1F^*$	3	$23+24B^1G(^1P)^1F+22(C^2D)^1F$			97065			1.001
$B^1D(^1P)^1D$	2	$45+45(B^2D)^1D^*$			102494			1.000
$B^1D(^1P)^1P$	1	$76+8(^2P)^1P$			103232			1.000
$B^1D(^1P)^1F$	3	$82+8(^2F)^1F^*$			104434			1.000
$(B^2D)^3D^*$	1	91			108022			0.505
	2	90			108022			1.169
	3	92			108043			1.333
$B^1S(^3P)^3P$	0	$84+12(B^2D)^3P^*$			108492			
	1	$83+15(B^2D)^3P^*$			108554			1.496
	2	$80+18(B^2D)^3P^*$			108672			1.498

TABLE 2. *Observed and calculated levels of* Cr I $(3d+4s)^5 4p$—Continued

Name	J	Percentage	AEL	Obs. level (cm^{-1})	Calc. level (cm^{-1})	O—C	Obs. g-factor	Calc. g-factor
$(B^2D)^3F^*$	2	94			109706			0.667
	3	94			109704			1.083
	4	95			109733			1.250
$(B^2D)^1F^*$	3	91			111383			1.001
$(B^2D)^1P^*$	1	$40+31(B^2D)^3P^*+18B^1S(^1P)^1P$			112076			1.216
$(B^2D)^3P^*$	0	$83+14B^1S(^3P)^3P$			112286			
	1	$52+30(B^2D)^1P^*+12B^1S(^3P)^3P$			112181			1.283
	2	$78+18B^1S(^3P)^3P$			112084			1.499
$(B^2D)^1D^*$	2	$48+40B^1D(^1P)^1D$			112825			1.001
$B^1S(^1P)^1P$	1	$74+23(B^2D)^1P^*$			124551			1.000

TABLE 3. *Orders of the submatrices for* $(d+s)^5p$

J	Order
0	39
1	107
2	144
3	145
4	117
5	76
6	39
7	14
8	3

The approximate time for the diagonalization routine on the IBM 7040 computer was 4 1/2 hr.

The work described in this paper was supported in part by the National Bureau of Standards, Washington, D. C.

4. References

[1] Roth, C., Nat. Bur. Stand. (U.S.), **72A** (Phys. and Chem.) No. 5, 505–520 (Sept—Oct. 1968).
[2] Roth, C., Nat. Bur. Stand. (U.S.), **73A** (Phys. and Chem.) No. 2, 125–157 (Mar.–Apr. 1969).
[3] Roth, C., Nat. Bur. Stand. (U.S.), **73A** (Phys. and Chem.) No. 2, 159–171 (Mar.–Apr. 1969).
[4] Roth, C., Nat. Bur. Stand. (U.S.), **73A** (Phys. and Chem.) No. 6, 509–609 (Nov.–Dec. 1969).
[5] Rohrlich, F., Phys. Rev. **74,** 1381 (1948).
[6] Roth, C., Nat. Bur. Stand. (U.S.), **73A** (Phys. and Chem.) No. 5, 497–510 (Sept.–Oct. 1969).
[7] Roth, C., Nat. Bur. Stand. (U.S.), **74A** (Phys. and Chem.), No. 2. (Mar.–Apr. 1970).
[8] Moore, C. E., Atomic Energy Levels, Nat. Bur. Stand. (U.S.), Circ. 467, Vol. II (1952), referred to as AEL.
[9] Roth, C., J. Math. Phys. **9,** No. 4, 686 (1968).
[10] Kiess, C. C., J. Res. NBS **51,** No. 5,247, (1953) RP2457.
[11] Racah, G., J. Quant. Spectrosc. Radiat. Transfer **4,** 617 (1964).

(Paper 74A2–589)

JOURNAL OF RESEARCH of the National Bureau of Standards—A. Physics and Chemistry
Vol. 74A, No. 2, March–April 1970

A Theoretical Investigation of the Configurations $(3d+4s)^7 4p$ in Neutral Iron

C. Roth*

(November 24, 1969)

Experimental levels of the configurations $(3d+4s)^7 4p$ were compared with corresponding calculated values. On fitting 248 experimental levels by means of 20 free parameters an rms error of 213 cm^{-1} was obtained.

It was shown that the correction parameters β and T were not significant.

Key words: Arc spectrum; configurations $(3d+4s)^7 4p$; configuration interactions; energy levels; g-factors; iron.

1. Introduction

Theoretical investigations of odd configurations for trebly and doubly ionized atoms of the iron group were performed by the author [1−4].[1, 2]

The configurations $(3d+4s)^n 4p$ were considered previously for the arc spectra of calcium, scandium, titanium, vanadium, chromium, manganese, and copper [5−12].

The configurations $(d+s)^7 p$ comprise 272 terms splitting into 684 levels. In AEL [13], 72 terms splitting into 223 levels are assigned to the configurations $3d^7 4p + 3d^6 4s 4p + 3d^5 4s^2 4p$, 17 terms splitting into 32 levels are given without configuration assignments and 12 unclassified odd levels have no term designations.

As for Mn I [12], the initial values for the parameters[3] B, B', C, C' and α were obtained by linear extrapolation from the results of the other neutral spectra. Then initially for Fe I

$$\begin{aligned} B &= 800 \\ B' &= 930 \\ C &= 3160 \\ C' &= 3430 \\ \alpha = \alpha' &= 83 \end{aligned} \qquad (1)$$

The numerical values of all parameters and levels are in cm^{-1} throughout the text.

The initial values for the other parameters were taken from the final values for Mn I, [12].

The initial value for the height of the configuration $d^7 p$ was obtained from $3d^7(a\,^4\mathrm{F})4pz\,^5\mathrm{G}$ since for this term only the interaction with $3d^6 4s(a\,^4\mathrm{H})4py\,^5\mathrm{G}$, i.e., $[22/15]^{1/2}\ (K-J)$, [14] needs to be taken into account. The other terms ^{5}G of $d^6 sp$ are not only distant from $z\,^5$G, but also the coefficients of K and J in the interactions between configurations are small in these cases. Then, from ref. [14] and [15]

$$z\,^5\mathrm{G}_{\mathrm{C.G.}} = A - 15B + F_2 + 12\alpha - \frac{22}{15}\frac{(K-J)^2}{(y\,^5\mathrm{G} - z\,^5\mathrm{G})} \qquad (2)$$

where the difference $y\,^5\mathrm{G} - z\,^5\mathrm{G}$ should be the distance between the centers of gravity of the unperturbed terms $z\,^5$G and $y\,^5$G. However, taking the experimental values of the centers of gravity does not cause a large difference. Hence we obtain initially

$$A = 46280. \qquad (3)$$

The height of $d^6 sp$ is obtained either from ^{7}D or ^{7}F (they only differ by $9F_2'$ [14], [15]). Then, from ref. [14] and [15]

$$^7\mathrm{D}_{\mathrm{C.G.}} = A' - 21B' - 4G_{ds}' - 7F_2' - G_{ps}' + 6\alpha'$$

and hence

$$A' = 53600. \qquad (4)$$

The height of the configuration $d^5 s^2 p$ was obtained from the matrix of ^{7}P. Now, the configuration $d^5 s^2 p$ is considered here as 5 holes in the d-shell. The necessary changes to convert the configuration $d^5 p$ (5 electrons in the d-shell) to $d^5 s^2 p$ (5 holes in the d-shell) are described in section 4, [14]. However, the addition of $10G_1'' + 35G_3''$ to each diagonal element was not performed since this factor can be incorporated into the height A'' (of course, due compensation for

*An invited paper. Present address: Department of Mathematics, McGill University, Montreal, Canada.

[1] Figures in brackets indicate literature references at the end of this paper.

[2] The reader is referred to these papers for an explanation of the method used, notation and significance of the various parameters.

[3] Unprimed parameters refer to the configuration $3d^7 4p$, primed parameters to $3d^6 4s 4p$ and doubly primed parameters to $3d^5 4s^2 4p$.

this factor must be made when calculating $D''(d^5s^2p)$ [12]). Then, the matrix of ^7P is given by

$$\begin{array}{l} (^6S)^7P^* \\ {}^5D(^3P)^7P \end{array} \begin{bmatrix} A''-35B''-10G_1''-35G_3'' & \sqrt{2}J' \\ \sqrt{2}J' & A'-21B'-4G_{ds}' \\ & +7F_2'-G_{ps}'+6\alpha' \end{bmatrix} \quad (5)$$

Assuming that the parameters B, B', and B'' are in arithmetic progression and using the fact that the trace equals the sum of the eigenvalues ($z\,^7P_{C.G.}$ equals 24057 and $y\,^7P_{C.G.}$ equals 40262) we obtain

$$A''=80680. \quad (6)$$

2. Results and Discussion

As for Mn I, four iterations were performed. The parameters β and T were completely ineffective here. In the least-squares of the final iteration in the "uniform treatment"[4] 84 terms splitting into 240 levels and 8 unclassified odd levels were inserted to yield an rms error of 213. Since A'' was allowed to vary freely, the calculated values, percentage compositions and g-factors for all of the 684 predicted levels are given in table 3. The final parameters in the uniform treatment are given in table 2.

The three high terms $r\,^3G$, $t\,^3H$, and $q\,^3G$, all above 60,000, were not included in the least-squares as it is doubtful to which theoretical terms they should be assigned. Also, 5 of these 9 levels are listed in AEL as uncertain. Below 60,000 the following 10 levels are not included:

1. The three levels of $3d^7(a\,^4P)4pv\,^5P$
2. The four unclassified odd levels 2°, 5°, 7°, and 9°
3. The level $z\,^1D$
4. The level $s\,^3D_3$
5. The level $3d^64s(b\,^4D)4pt\,^5P_3$

The calculated levels of the term[5] $(^6S)^5P^*+(^4P)^5P$ are approximately 1900 cm^{-1} higher than the experimental levels of $3d^7(a\,^4P)4pv\,^5P$. Most, or all of this difference can be attributed to the interaction between $(^6S)^5P^*+(^4P)^5P$ and $^5D(4s5p\,^3P)u\,^5P$, since the difference between the unperturbed terms $v\,^5P$ and $u\,^5P$ is expected to be very small. This interaction was not considered explicitly here, and hence the levels of $v\,^5P$ were not inserted.

It is evident from table 3 that there are no conceivable theoretical levels to which any of the levels 2°, $z\,^1D$, 5°, and 7° could be assigned. It is apparent from the paper of Russell, Moore, and Weeks [16], that the above 4 levels are based on very few combinations and thus they may not be valid levels.

The level 9° was not included in the least-squares as it could be assigned to either $^3D(^3P)^5F_4$ or $^3G(^3P)^3F_4$ with a deviation of around −300 in each case.

The only theoretical level to which the experimental level $s\,^3D_3$ could be assigned is $^3D(^3P)^5F_3$. As then the resulting deviation would be around −600 and since the level $s\,^3D_3$ is quoted as uncertain in AEL, this assignment was not performed.

When the level $t\,^5P_3$ was assigned to the theoretical level $^3D(^3P)^5P_3$ the deviation was −630. This value contrasts with deviations of 102 and 57 for the other two levels $t\,^5P_{1,2}$. Since, in addition, the level $t\,^5P_3$ is given as uncertain in AEL, it was not included. Instead, the level 11_3° was assigned to $^3D(^3P)^5P_3$ yielding a deviation of only −20. It should be noted, however, that had the level $t\,^5P_3$ not been marked as uncertain, it would have been assigned to the level $^3D(^3P)^5F_3$, as then the deviation would be only −190.

The following changes in assignment were performed:

1. AEL $d^6s(b\,^4P)pw\,^5D \longrightarrow A^3F(^3P)^5D$
2. AEL $d^6s(b\,^4F)pv\,^5D_4 \longrightarrow A^3F(^3P)^5F_4$
3. AEL $d^6s(b\,^4F)pv\,^5D_{0,1,2,3} \longrightarrow A^3P(^3P)^5D_{0,1,2,3}$
4. AEL $d^6s(b\,^4F)pw\,^5F_4 \longrightarrow A^3P(^3P)^5D_4$
5. $d^5s^2(a^6S)^5P^* \longleftrightarrow (^4P)^5P$
6. $(^4P)^3D_{2,3} \longleftrightarrow (^4P)^5D_{2,3}$
7. AEL $d^7(a\,^2G)px\,^3F_{2,3} \longrightarrow A^3F(^3P)^3F_{2,3}$
8. AEL $d^7(a\,^2G)px\,^3F_4 \longrightarrow (^4P)^5D_4$
9. AEL $d^7(a\,^4P)pu\,^5D_4 \longrightarrow A^3F(^3P)^3F_4$
10. AEL $d^6s(b\,^4F)px\,^3G_{3,4,5} \longrightarrow {}^3G(^3P)^5H_{3,4,5}$
11. AEL $d^7(a\,^2H)py\,^1G \longrightarrow {}^3H(^3P)^1G$
12. AEL $d^6s(b\,^4F)pw\,^3F \longrightarrow (^2G)^3F$
13. AEL $d^7(a\,^2D)pw\,^3P \longrightarrow (^2P)^3P$
14. AEL $d^6s(a\,^4G)pv\,^3F \longrightarrow (A^2D)^3F$
15. AEL $d^7(a\,^2H)pu\,^3G \longrightarrow {}^3G(^3P)^3G$
16. AEL $d^7(a\,^2P)py\,^1D \longrightarrow A^3F(^3P)^1D$
17. AEL $d^7(a\,^2P)pv\,^3P_1 \longrightarrow (^2P)^3S$
18. $(A^2D)^3D_1 \longleftrightarrow (^2P)^1P$
19. AEL $d^7(a\,^2P)px\,^3S \longrightarrow (A^2D)^3P_1$
20. AEL $d^7(a\,^2P)pv\,^3P_2 \longrightarrow (A^2D)^3P_2$
21. AEL $s\,^3D_2 \longrightarrow {}^3D(^3P)^5F_2$
22. AEL $d^7(a\,^2H)py\,^1H \longrightarrow {}^3G(^3P)^1H$
23. AEL $x\,^1F \longrightarrow {}^3G(^3P)^3F_3$
24. AEL $d^6s(b\,^2H)pu\,^3H \longrightarrow {}^1I(^3P)^3H$
25. AEL $d^6s(a\,^4G)pt\,^3G \longrightarrow (^2H)^3G$
26. AEL $d^7(a\,^2D)pu\,^3F \longrightarrow A^1G(^3P)\,^3F$
27. AEL $d^6s(b\,^2H)px\,^3I \longrightarrow {}^1I(^3P)^3I$

In each of the changes 1, 5, 7, 12, 14, 15, 16, 17, 19, 25, and 26 there is strong mixing between the experimentally assigned term and others. On the other hand, in 3, 11, 13, 20, 22, 24, and 27 the compositions of the theoretical levels contain only minimal contributions of the experimental designations.

After the changes 2 and 4, not only is there closer agreement between the experimental and theoretical values of the levels and g-factors of $w\,^5D_4$ and $w\,^5F_4$, but also the theoretical and experimental splittings of the two terms $w\,^5D$ and $w\,^5F$ correspond more closely.

Similarly changes 6, 8, and 9 improve the agreement between the experimental and theoretical levels of $w\,^3D$, $x\,^3F$ and $u\,^5D$ and cause the splittings of these three terms to correspond more closely to the experimental splittings.

[4] The parameters A, A', A'', G_{ds}' and G_{ps}' are allowed to change freely. The parameters B, C, F_2, and G_1 are in arithmetic progression. The parameters G_3, α, ζ_d, and ζ_p are kept equal, and for the parameters of the interactions between configurations H' was kept equal to H, J' to J, G to G_{ds}' and $K'=K+828$ (fixed difference).

[5] See section 3 of this paper for the theoretical term designations.

In the vicinity of 48,000 there is only one theoretical term ^{3}G predicted. The levels of $w\,^3$G fit much better than $x\,^3$G to the theoretical term $A^3F(^3P)^3G$. The levels of $x\,^3$G are then assigned to the theoretical levels $^3G(^3P)^5H_{3,4,5}$ yielding a mean deviation of only 18 cm^{-1}. The g-factors of $w\,^3$G also correspond closely to the calculated g-factors of $^3G(^3P)^5H_{3,4,5}$.

The calculated values of the levels $(^2P)^1P$ and $(A^2D)^3D_1$ are 52012 and 53274 respectively. As the experimental values for these two levels are 53230 and 52181 respectively, it is necessary to exchange the assignments of these levels as indicated by 18. After the change the deviations are 169 and -44.

The levels of $s\,^3$D cannot be assigned to a theoretical term ^{3}D (see table 3). The only vacant theoretical level to which $s\,^3D_2$ can be assigned is $^3D(^3P)^5F_2$, as indicated by change 21. The deviation here is -264.

Similarly the experimental level $x\,^1$F could not be assigned to a theoretical term ^{1}F. However, when $x\,^1$F is assigned to the vacant level $^3G(^3P)^3F$ the deviation is only -129. The experimental g-factor of 1.079 corresponds to the calculated value of 1.060.

Table 1 below indicates how the 8 unclassified odd levels were assigned. It should be noted that the level $3d^7(a\,^2P)4px\,^3S$ at 52858 is given as 8° in the original paper of Russell, Moore and Weeks, [16].

TABLE 1. *Miscellaneous odd levels of* Fe I

Level	Assignment	Deviation	Obs. g-factor	Calc. g-factor
1°_2	$A^3P(^3P)^1D$	-254	1.137	1.140
3°_3	$A^3F(^3P)^1F+(^2G)^1F$	-116	.....	1.020
4°_4	$^3G(^3Px\,^3H_4$	-77	0.953	0.924
6°_5	$^3H(^3P)^1H$	82	1.061	1.101
10°_3	$^3D(^3P)^3D_3$	-135	1.476	1.505
11°_3	$^3D(^3P)^3P_3$	-20	.....	1.633
12°_5	$^3D(^3P)^5F_5$	234	1.356	1.398
13°_4	$^3D(^3P)^5D_4$	145	.....	1.489

Below 58,000 (the limit of the experimental data inserted) there are 31 theoretical levels with no corresponding experimental values. The lowest of these are the levels of $^3H(^3P)^5I$ at around 42900.

The highest deviations occur for the levels of $s\,^3$G (mean deviation 650). An examination of the paper of Russell, Moore and Weeks [16], indicates, however, that the levels of $s\,^3$G are based upon combinations with 41 even levels and thus they are definitely valid levels. The high deviations cannot be explained as being due to perturbations with higher lying levels of ^{3}G belonging to $(3d+4s)^7 5p$ since the deviations are positive. It may be argued, however, that conceivably the levels $s\,^3$G are high enough in order to belong to either $3d^7(a\,^4F)5p\,^5F$, $3d^7(a\,^4F)5p\,^5G$ or $3d^7(a\,^4F)5p\,^3G$ (although the difference between $3d^6 4s(a\,^6D)5px\,^7P$ and $3d^6 4s(a\,^6D)4pz\,^7P$ is almost 26,000, we would expect the difference between $3d^7(a\,^4F)5p\,^3G$ and $3d^7(a\,^4F)4pz\,^3G$ to be considerably smaller since $z\,^3G$ is higher than $z\,^7P$ by 12,000 and the parameters of $(3d+4s)^7 5p$ are expected to be considerably smaller than the corresponding parameters of $(3d+4s)^7 4p$). However, unlike the terms $w\,^5$P in Cr I, [11] and $w\,^4$P in Mn I, [12] which are superfluous to $(3d+4s)^n 4p$ at their respective heights, here the theoretical term $A^1G(^3P)^3G$ is in the neighborhood of $s\,^3$G. In addition, the terms $w\,^5$P and $w\,^4$P coincide in height with the lowest predicted terms ^{5}P and ^{4}P for $(3d+4s)^5 5p$ and $(3d+4s)^6 5p$, respectively, whereas here it is impossible to calculate even the approximate value of the lowest term ^{3}G of $(3d+4s)^7 5p$ since the height of $3d^7 5p$ is not known. Furthermore, although the mean deviation of the levels $s\,^3$G is more than three times the rms error obtained, there are other levels which also suffer high deviations. As an example, the low level $x\,^5D_4$ at 39065 has a deviation of 561. Thus, the variation which we consider as final is the one including the levels $s\,^3$G. In another variation, based on the same diagonalization, and not including the levels $s\,^3$G, an rms error of 192 was obtained. All the parameters were nearly identical in the two cases.

For 13 of the 17 terms given in AEL without configuration assignments, the theoretical assignments are given in table 3 (the terms $z\,^1$D, $r\,^3$G, $t\,^3$H and $q\,^3$G are not inserted).

Two misprints in AEL should be noted. The configuration assignments for the odd levels 10° and 12° should be $3d^6 4s(b\,^4D)4p$: and not $3d^6 4s(b\,^4D)4d$: as given for each case in AEL.

3. Table of the Observed and Calculated Levels and g-Factors

In the column "NAME" the calculated designation of the term is given. Whenever the terms of the parent d^n have different seniorities these are denoted by the letters A and B (for $d^5\,^2$D by A, B, and C), the lower calculated term being designated by A. The terms of $d^6 sp$ are denoted by $d^6 v_1 S_1 L_1 (sp\,^{1,3}P)SL$. The terms of $d^7 p$ are differentiated from those of $d^5 s^2 p$ by using a star for the latter terms.

The entries in the columns "J", "OBS. LEVEL cm^{-1}", "CALC. LEVEL cm^{-1}", "OBS. g-FACTOR" and "CALC. g-FACTOR", are self-evident. In the column "PERCENTAGE", for each calculated level either the three highest contributions or all those contributions exceeding six percent are given.

Whenever the experimental and calculated term designations differ, the experimental designation is entered in the column "AEL" using the notation of C. E. Moore, [13]. In many instances the exchanges involve complete terms rather than isolated levels. Unless specified otherwise, the entries in the column "AEL" pertain to exchanges in terms.

The column "O–C" gives the difference between the observed and calculated values of the levels.

The entries are in increasing energy of the calculated terms.

TABLE 2. *Parameters for* Fe I $(3d+4s)^7 4p$

Parameter	Initial value	Final value
A	46,280	$45{,}626 \pm 572$
A'	53,600	$54{,}552 \pm 512$
A''	80,680	$83{,}934 \pm 629$
B	800	738 ± 9
B'	930	943 ± 7
B''	1,060	1,148 (Arith. Progress.)
C	3,160	$3{,}310 \pm 29$
C'	3,430	$3{,}509 \pm 14$
C''	3,700	3,708 (Arith. Progress.)
$G'_{ds}=G$	1,530	$1{,}536 \pm 24$
F_2	190	173 ± 10
F'_2	310	305 ± 5
F''_2	430	437 (Arith. Progress.)
G_1	230	202 ± 8
G'_1	245	245 ± 7
G''_1	260	288 (Arith. Progress.)
$G_3=G'_3=G''_3$	18	20 ± 2
G'_{ps}	6,650	$7{,}116 \pm 58$
$\alpha=\alpha'=\alpha''$	83	74 ± 2
$H=H'$	70	85 ± 6
$J=J'$	1,300	$1{,}183 \pm 41$
K	2,600	$2{,}459 \pm 45$
K'	3,428	3,287 (Fixed Diff.)
$\zeta_d=\zeta'_d=\zeta''_d$	320	410 ± 23
$\zeta_p=\zeta'_p=\zeta''_p$	210	200 ± 68
rms error		213.4

TABLE 3. *Observed and calculated levels of* Fe I $(3d+4s)^7 4p$

Name	J	Percentage	AEL		Obs. Level (cm^{-1})	Calc. Level (cm^{-1})	O–C	Obs. g-Factor	Calc. g-Factor
			Config.	Desig.					
$^5D(^3P)^7D$	1	100	$3d^6 4s(a\,^6D)4p$	$z\,^7D$	20,020	20,158	−138	2.999	2.998
	2	99			19,913	20,045	−132	2.008	1.999
	3	99			19,757	19,880	−123	1.746	1.749
	4	99			19,562	19,671	−109	1.642	1.649
	5	100			19,351	19,437	−86	1.597	1.599
$^5D(^3P)^7F$	0	100	$3d^6 4s(a\,^6D)4p$	$z\,^7F$	23,270	22,905	365		
	1	100			23,245	22.875	370	1.549	1.501
	2	100			23,193	22,813	380	1.504	1.501
	3	99			23,111	22,717	394	1.513	1.500
	4	99			22,997	22,585	412	1.493	1.500
	5	99			22,846	22,413	433	1.498	1.500
	6	100			22,650	22,194	456	1.498	1.500
$^5D(^3P)^7P$	2	99	$3d^6 4s(a\,^6D)4p$	$z\,^7P$	24,507	24,331	176	2.333	2.332
	3	98			24,181	23,998	183	1.908	1.916
	4	98			23,711	23,527	184	1.747	1.749

TABLE 3. *Observed and calculated levels of* Fe I $(3d+4s)^7 4p$—Continued

Name	J	Percentage	AEL		Obs. Level (cm^{-1})	Calc. Level (cm^{-1})	O–C	Obs. g-Factor	Calc. g-Factor
			Config.	Desig.					
$^5D(^3P)^5D$	0	93	$3d^64s(a\,^6D)4p$	$z\,^5D$	26,551	26,534	17		
	1	92			26,479	26,461	18	1.495	1.497
	2	91			26,340	26,316	24	1.503	1.498
	3	91			26,140	26,108	32	1.500	1.498
	4	91			25,900	25,853	47	1.502	1.499
$^5D(^3P)^5F$	1	95	$3d^64s(a\,^6D)4p$	$z\,^5F$	27,666	27,706	−40	−0.012	0.005
	2	95			27,560	27,595	−35	1.004	1.003
	3	94			27,395	27,424	−29	1.250	1.252
	4	94			27,167	27,189	−22	1.355	1.351
	5	94			26,875	26,889	−14	1.399	1.400
$^5D(^3P)^5P$	1	97	$3d^64s(a\,^6D)4p$	$z\,^5P$	29,733	29,929	−196	2.487	2.498
	2	97			29,469	29,668	−199	1.835	1.832
	3	97			29,056	29,266	−210	1.657	1.666
$^5D(^3P)^3D$	1	91	$3d^64s(a\,^4D)4p$	$z\,^3D$	31,937	31,655	282	0.513	0.503
	2	90			31,686	31,397	289	1.168	1.164
	3	89			31,323	31,017	306	1.321	1.330
$^5D(^3P)^3F$	2	93	$3d^64s(a\,^4D)4p$	$z\,^3F$	32,134	32,298	−164	0.682	0.672
	3	93			31,805	31,963	−158	1.086	1.087
	4	94			31,307	31,474	−167	1.250	1.250
$(^4F)^5D$	0	$58+40\,^5D(^1P)^5D$			34,122	34,231	−109		
	1	$58+39\,^5D(^1P)^5D$			34,017	34,108	−91	1.492	1.492
	2	$57+38\,^5D(^1P)^5D$			33,802	33,861	−59	1.495	1.494
	3	$59+38\,^5D(^1P)^5D$			33,507	33,499	8	1.492	1.495
	4	$60+37\,^5D(^1P)^5D$			33,096	33,020	76	1.496	1.498
$(^4F)^5F$	1	$83+13\,^5D(^1P)^5F$			34,692	34,786	−94	−0.016	0.009
	2	$81+13\,^5D(^1P)^5F$			34,547	34,611	−64	0.998	0.997
	3	$80+13\,^5D(^1P)^5F$			34,329	34,349	−20	1.244	1.245
	4	$79+13\,^5D(^1P)^5F$			34,040	34,005	35	1.344	1.344
	5	$82+13\,^5D(^1P)^5F$			33,695	33,601	94	1.417	1.396
$^5D(^3P)^3P$	0	97	$3d^64s(a\,^4D)4p$	$z\,^3P$	34,556	34,744	−188		
	1	96			34,363	34,542	−179	1.496	1.498
	2	96			33,947	34,112	−165	1.493	1.498
$(^4F)^5G$	2	92			35,856	35,715	141	0.335	0.342
	3	$84+7(^4F)^3G$			35,612	35,495	117	0.887	0.912
	4	$71+20(^4F)^3G$			35,257	35,179	78	1.103	1.134
	5	$50+43(^4F)^3G$			34,782	34,751	31	1.218	1.239
	6	94			34,844	34,578	266	1.332	1.333
$(^4F)^3G$	3	$86+7(^4F)^5G$			36,079	36,400	−321	0.791	0.769
	4	$72+20(^4F)^5G$			35,768	35,946	−178	1.100	1.078
	5	$53+41(^4F)^5G$			35,379	35,389	−10	1.248	1.231
$^5D(^1P)^5P$	1	$58+34(^6S)^5P^*$	$3d^64s(a\,^4D)4p$	$y\,^5P$	37,410	37,338	72	2.502	2.498
	2	$59+33(^6S)^5P^*$			37,158	37,122	36	1.836	1.832
	3	$60+32(^6S)^5P^*$			36,767	36,786	−19	1.661	1.659

TABLE 3. *Observed and calculated levels of* Fe I $(3d+4s)^7 4p$ – Continued

Name	J	Percentage	AEL		Obs. Level (cm^{-1})	Calc. Level (cm^{-1})	O–C	Obs. g-Factor	Calc. g-Factor
			Config.	Desig.					
$(^4F)^3F$	2	87			37,521	37,645	−124	0.688	0.679
	3	82			37,163	37,228	−65	1.086	1.096
	4	85			36,686	36,692	−6	1.246	1.245
$(^4F)^3D$	1	$87+7^5D(^3P)^3D$			38,996	39,021	−25	0.493	0.501
	2	$85+7^5D(^3P)^3D$			38,678	38,669	9	1.151	1.157
	3	$82+8^5D(^3P)^3D$			38,175	38,110	65	1.324	1.322
$^5D(^1P)^5D$	0	$47+22(^4F)^5D+13A^3P(^3P)^3D$	$3d^64s(a\,^4D)4p$	$x\,^5D$	40,491	40,038	453		
	1	$47+21(^4F)^5D+13A^3P(^3P)^3D$			40,405	39,939	466	1.498	1.499
	2	$47+22(^4F)^5D+13A^3P(^3P)^3D$			40,231	39,743	488	1.501	1.502
	3	$48+20(^4F)^5D+12A^3P(^3P)^3D$			39,970	39,452	518	1.504	1.500
	4	$50+24(^4F)^5D+13A^3P(^3P)^3D$			39,626	39,065	561	1.489	1.500
$(^6S)^7P^*$	2	98			40,052	40,188	−136	2.340	2.330
	3	98			40,207	40,283	−76	1.908	1.915
	4	99			40,422	40,417	5	1.751	1.749
$A^3P(^3P)^5S$	2	$56+36(^4P)^5S$	$3d^64s(b\,^4P)4p$	$z\,^5S$	40,895	41,089	−194	1.985	1.987
$^5D(^1P)^5F$	1	$85+7(^4F)^5F$	$3d^64s(a\,^4D)4p$	$x\,^5F$	41,131	41,443	−312	−0.006	0.003
	2	$85+7(^4F)^5F$			41,018	41,325	−307	0.998	1.001
	3	$85+7(^4F)^5F$			40,842	41,142	−300	1.254	1.250
	4	$85+7(^4F)^5F$			40,594	40,889	−295	1.328	1.350
	5	$86+6(^4F)^5F$			40,257	40,555	−298	1.390	1.400
$^3H(^3P)^5I$	4	$73+15^3H(^3P)^5H$				42,992			0.702
	5	$65+18^3H(^3P)^5H$				42,905			0.988
	6	$66+18^3H(^3P)^5H$				42,851			1.133
	7	$81+16^3H(^3P)^5H$				42,843			1.199
	8	100				42,899			1.250
$A^3P(^3P)^5P$	1	$85+6(^4P)^5P$	$3d^64s(b\,^4P)4p$	$x\,^5P$	43,079	43,225	−146	2.464	2.466
	2	$78+12(^4P)^5S$			42,860	43,036	−176	1.822	1.838
	3	88			42,533	42,722	−189	1.650	1.658
$^3H(^3P)^5G$	2	$46+45A^3F(^3P)^5G$	$3d^64s(a\,^4H)4p$	$y\,^5G$	43,210	43,371	−161	0.331	0.336
	3	$31+32A^3F(^3P)^5G+24^3H(^3P)^5H$			43,138	43,277	−139	0.905	0.800
	4	$36+32A^3F(^3P)^5G+17^3H(^3P)^5I$			43,023	43,217	−194	1.024	1.042
	5	$42+31A^3F(^3P)^5G+18^3H(^3P)^5I$			42,912	43,129	−217	1.203	1.201
	6	$49+30A^3F(^3P)^5G+13^3H(^3P)^5I$			42,784	43,014	−230	1.342	1.297
$^3H(^3P)^5H$	3	$63+17^3H(^3P)^5G+11A^3F(^3P)^5G$	$3d^64s(a\,^4H)4p$	$z\,^5H$	43,326	43,475	−149	0.509	0.628
	4	$67+11^3H(^3P)^5G+9^3H(^3P)^5I$			43,109	43,490	−381	0.871	0.917
	5	$69+16^3H(^3P)^5I+6^3H(^3P)^5G$			42,992	43,477	−485	1.054	1.083
	6	$71+20^3H(^3P)^5I$			43,321:	43,437	−116		1.189
	7	$75+19^3H(^3P)^5I$				43,362			1.265
$(^4P)^5S$	2	$45+38A^3P(^3P)^5S$			44,512	44,355	157	1.888	1.911
$A^3F(^3P)^5D$	0	$60+24(^4P)^5D+11A^3P(^3P)^5D$	$3d^64s(b\,^4P)4p$	$w\,^5D$	44,459	44,457	2		
	1	$58+24(^4P)^5D+12A^3P(^3P)^5D$			44,411	44,410	1	1.315	1.480
	2	$54+23(^4P)^5D+12A^3P(^3P)^5D$			44,184	44,301	−117	1.533	1.487
	3	$50+21(^4P)^5D+14A^3P(^3P)^5D$			43,923	44,167	−244	1.481	1.486
	4	$37+22A^3P(^3P)^5D+15(^4P)^5D$			43,500	43,963	−463	1.492	1.497

TABLE 3. *Observed and calculated levels of* Fe I $(3d+4s)^7 4p$ – Continued

Name	J	Percentage	AEL		Obs. Level (cm^{-1})	Calc. Level (cm^{-1})	O–C	Obs. g-Factor	Calc. g-Factor
			Config.	Desig.					
$A^3F(^3P)^5F$	1	$82+6^3D(^3P)^5F$	$3d^64s(b\,^4F)4p$	$w\,^5F$	44,378:	44,637	−259	0.283	0.035
	2	$70+5^3D(^3P)^5F$			44,285	44,580	−295	1.117	1.083
	3	$46+20A^3P(^3P)^5D$			44,166	44,445	−279	1.351	1.334
	4	$71+8A^3F(^3P)^5D$	$3d^64s(b\,^4F)4p$	$v\,^5D$	44,415	44,555	−140	1.401	1.364
	5	$85+4^3D(^3P)^5F$	$3d^64s(b\,^4F)4p$	$w\,^5F$	44,244	44,437	−193	1.382	1.393
$A^3P(^3P)^5D$	0	$78+8^5D(^1P)^5D$	$3d^64s(b\,^4F)4p$	$v\,^5D$	44,827	45,360	−533		
	1	$52+8(^4P)^3D$			44,761	45,235	−474	1.389	1.233
	2	$33+20A^3P(^3P)^3D+10(^4P)^3D$			44,664	44,975	−311	1.378	1.345
	3	$26+28A^3F(^3P)^5F+11A^3F(^3P)^5D$			44,551	44,711	−160	1.386	1.377
	4	$46+27A^3F(^3P)^5F+12A^3F(^3P)^5D$	$3d^64s(b\,^4F)4p$	$w\,^5F$	44,023	44,189	−166	1.444	1.475
$A^3P(^3P)^3D$	1	$30+34(^4P)^3D+15A^3P(^3P)^5D$	$3d^64s(b\,^4P)4p$	$x\,^3D$	45,552	45,610	−58	0.556	0.784
	2	$29+35A^3P(^3P)^5D+26(^4P)^3D$			45,282	45,399	−117	1.200	1.310
	3	$33+32(^4P)^3D+15A^3P(^3P)^5D$			45,221	45,305	−84	1.352	1.377
$^3H(^3P)^3G$	3	$52+21(^2G)^3G$	$3d^64s(a\,^4H)4p$	$y\,^3G$	45,563	45,649	−86	0.765	0.758
	4	$51+22(^2G)^3G$			45,428	45,516	−88	1.053	1.054
	5	$52+24(^2G)^3G$			45,295	45,405	−110	1.207	1.202
$A^3F(^3P)^5G$	2	$52+45^3H(^3P)^5G$	$3d^64s(b\,^4F)4p$	$x\,^5G$	45,965	45,855	110	0.323	0.342
	3	$51+41^3H(^3P)^5G$			45,914	45,811	103	0.928	0.914
	4	$52+38^3H(^3P)^5G$			45,833	45,730	103	1.158	1.146
	5	$55+36^3H(^3P)^5G$			45,726	45,619	107	1.269	1.261
	6	$61+34^3H(^3P)^5G$			45,608:	45,493	115	1.336	1.327
$^3H(^3P)^3I$	5	95	$3d^64s(a\,^4H)4p$	$z\,^3I$	46,136	46,191	−55	0.833	0.839
	6	93			46,027	46,088	−61	1.040	1.030
	7	93			45,978:	46,018	−40	1.149	1.148
$(^4P)^5P$	1	$41+28(^6S)^5P^*+10A^3P(^3P)^5P$	$3d^54s^2(a\,^6S)4p$	$w\,^5P$	46,410	46,156	254	2.436	2.413
	2	$46+32(^6S)^5P^*+8^5D(^1P)^5P$			46,314	46,151	163	1.822	1.813
	3	$49+35(^6S)^5P^*+8^5D(^1P)^5P$			46,137	45,998	139	1.658	1.660
$(^4P)^3P$	0	$36+35A^3P(^3P)^3P+10(^2P)^1S$			46,673	46,709	−36		
	1	$30+28(^4P)^3S+15A^3P(^3P)^3P$			46,902	46,819	83	1.600	1.812
	2	$52+25A^3P(^3P)^3P$			46,727	46,602	125	1.444	1.482
$A^3P(^3P)^3S$	1	$41+20A^3P(^3P)^3P+13(^4P)^3P$	$3d^64s(b\,^4P)4p$	$z\,^3S$	46,601	46,791	−190	1.888	1.815
$(^4P)^3D$	1	$22+27(^4P)^3S+20A^3F(^3P)^3D$			47,272	47,252	20	0.767	1.120
	2	$45+18A^3F(^3P)^3D$	$3d^7(a\,^4P)4p$	$u\,^5D$	46,889	46,913	−24	1.260	1.183
	3	$50+17A^3F(^3P)^3D$			46,745	46,702	43	1.397	1.334
$A^3F(^3P)^3F$	2	$44+26^3G(^3P)^3F+22(^2G)^3F$	$3d^7(a\,^2G)4p$	$x\,^3F$	47,197	47,278	−81	0.743	0.583
	3	$45+32(^2G)^3F+10^3G(^3P)^5G$			47,093	47,169	−76	1.159	1.066
	4	$38+32(^2G)^3F+14^3G(^3P)^5G$	$3d^7(a\,^4P)4p$	$u\,^5D$	46,721	46,873	−152	1.341	1.224
$^3H(^3P)^3H$	4	$23+18(^2G)^3H+10(^2G)^1G$	$3d^64s(a\,^4H)4p$	$z\,^3H$	47,107	47,261	−154	0.880	0.996
	5	$33+34(^2G)^3H+10^3G(^3P)^5G$			47,008	47,146	−138	1.060	1.072
	6	$29+33^3G(^3P)^5H+27(^2G)^3H$			46,982	47,086	−104	1.200	1.226

TABLE 3. *Observed and calculated levels of* Fe I $(3d+4s)^7 4p$ – Continued

Name	J	Percentage	AEL		Obs. Level (cm^{-1})	Calc. Level (cm^{-1})	O–C	Obs. g-Factor	Calc. g-Factor
			Config.	Desig.					
$(^4P)^5D$	0	$51+26A^3F(^3P)^5D+10^3D(^1P)^5D$			47,172:	47,428	−256		
	1	$50+25A^3F(^3P)^5D+10^3D(^1P)^5D$			47,177	47,409	−232	1.410	1.484
	2	$39+20A^3F(^3P)^5D+9A^3P(^3P)^1D$	$3d^7(a\,^4P)4p$	$w\,^3D$	47,136	47,331	−135	1.216	1.393
	3	$50+22A^3F(^3P)^5D+8^5D(^1P)^5D$			47,017	47,163	−146	1.346	1.481
	4	$46+21A^3F(^3P)^5D+10^5D(^1P)^5D$	$3d^7(a\,^2G)4p$	$x\,^3F$	46,889	47,036	−147	1.344	1.399
$(^4P)^3S$	1	$26+19(^4P)^3D+14A^3P(^3P)^3S$			47,556	47,226	330	1.884	1.303
$(^2G)^1G$	4	$23+22^3H(^3P)^1G+14^3G(^3P)^5G$			47,453	47,534	−81	1.025	0.994
$A^3P(^3P)^1D$	2	$44+10A^3F(^3P)^1D+10(^4P)^5D$		1°	47,420	47,674	−254	1.137	1.140
$^3G(^3P)^5G$	2	$65+16(^2G)^3F+11A^3F(^3P)^3F$	$3d^64s(a\,^4G)4p$	$w\,^5G$	47,831	47,822	9	0.472	0.448
	3	$71+8(^2G)^3F+6^3G(^3P)^5H$			47,693	47,646	47	0.931	0.910
	4	$68+7(^2G)^3F$			47,590	47,575	15	1.145	1.097
	5	$76+8(^2G)^3H$			47,420	47,438	−18	1.305	1.233
	6	$59+22(^2G)^3H+10^3H(^3P)^3H$			47,363	47,361	2	1.306	1.270
$^3G(^3P)^5H$	3	$41+30A^3F(^3P)^3G+10^3G(^3P)^5G$	$3d^64s(b\,^4F)4p$	$x\,^3G$	47,834	47,826	8	0.668	0.656
	4	$38+32A^3F(^3P)^3G+12^3G(^3P)^5G$			47,812	47,831	−19	1.061	0.983
	5	$32+20A^3F(^3P)^3G+11^3G(^3P)^5F$			47,835	47,861	−26	1.203	1.165
	6	$87+9^3H(^3P)^5H$				47,830			1.213
	7	$88+8^3H(^3P)^5H$				47,706			1.280
$^3H(^3P)^1I$	6	$87+6(^2H)^1I$				48,073			1.009
$^3G(^3P)^5F$	1	$64+6^3D(^3P)^5F$	$3d^64s(a\,^4G)4p$	$v\,^5F$	48,351	48,549	−198	0.230	0.253
	2	$72+7^3D(^3P)^5F$			48,239	48,457	−218	1.267	1.024
	3	$59+10^3G(^3P)^5H$			48,123	48,318	−195	1.236	1.121
	4	$62+12^3G(^3P)^5H$			47,930	48,099	−169	1.264	1.273
	5	$41+38^3G(^3P)^5H$			47,606	47,745	−139	1.317	1.246
$A^3F(^3P)^3G$	3	$30+31^3G(^3P)^5H+15^3G(^3P)^5F$		$w\,^3G$	48,476	48,414	62	0.584	0.770
	4	$36+33^3G(^3P)^5H+12^3G(^3P)^5F$			48,362	48,286	76	0.934	1.035
	5	$34+29^3G(^3P)^5F+13^3G(^3P)^5H$			48,231	48,116	115	1.27:	1.246
$(^2G)^1H$	5	$65+8^3H(^3P)^1H$			48,383	48,448	−65	1.028	1.061
$A^3P(^3P)^3P$	0	$30+42(^4P)^3P+22A^3P(^3P)^1S$	$3d^64s(b\,^4P)4p$	$x\,^3P$	48,460	48,412	48		
	1	$36+25(^4P)^3P+11^3G(^3P)^5F$			48,516	48,511	5	1.547	1.290
	2	$40+18(^4P)^3P+8(^2P)^3P$			48,305	48,400	−95	1.263	1.446
$A^3P(^3P)^1S$	0	$23+22(^2P)^1S+22A^3P(^3P)^3P$				48,669			
$(^2G)^3F$	2	$44+27A^3F(^3P)^3F+16^3G(^3P)^3F$	$3d^64s(b\,^4F)4p$	$w\,^3F$	49,433	49,333	100	0.677	0.667
	3	$29+28A^3F(^3P)^3F+13^3G(^3P)^3F$			49,243	49,079	164	1.165	1.107
	4	$22+18A^3F(^3P)^3F+15^3G(^3P)^3F$			49,109	48,862	247	1.181	1.178
$^3H(^3P)^1G$	4	$37+11(^2G)^1G+9(^2G)^3F$	$3d^7(a\,^2H)4p$	$y\,^1G$	48,703	49,170	−161	1.063	1.061
$(^6S)^5P^*$	1	$20+21(^4P)^5P+18^5D(^1P)^5P$	$3d^7(a\,^4P)4p$	$v\,^5P$	(48,290)	50,273		(2.213)	2.242
	2	$18+28(^2P)^3P+13(^4P)^5P$			(48,163)	49,953		(1.740)	1.683
	3	$27+25(^4P)^5P+23^5D(^1P)^5P$			(47,967)	49,928		(1.646)	1.648

TABLE 3. *Observed and calculated levels of* Fe I $(3d+4s)^7 4p$ – Continued

Name	J	Percentage	AEL		Obs. Level (cm^{-1})	Calc. Level (cm^{-1})	O–C	Obs. g-Factor	Calc. g-Factor
			Config.	Desig.					
$A^3F(^3P)^3D$	1	$34+20A^3P(^3P)^3D+15(^2P)^3D$	$3d^64s(b\,^4F)4p$	$v\,^3D$	49,298	49,274	24	0.562	0.589
	2	$39+23A^3P(^3P)^3D+14(^2P)^3D$			49,243	49,237	6	0.954	1.170
	3	$33+17A^3P(^3P)^3D+12(^2P)^3D$			49,135	49,193	−58	1.211	1.273
$A^3F(^3P)^1F$	3	$39+40(^2G)^1F$		3°	49,227	49,343	−116		1.020
$(^2G)^3H$	4	$46+30^3H(^3P)^3H$			49,727	49,480	247	0.929	0.833
	5	$41+23^3H(^3P)^3H$			49,604	49,375	229	1.075	1.063
	6	$41+37^3H(^3P)^3H$			49,434	49,267	167	1.17:	1.161
$(^2G)^3G$	3	$44+22A^3F(^3P)^3G+15^3H(^3P)^3G$			49,851	49,860	−9	0.763	0.765
	4	$35+15A^3F(^3P)^3G+15^3H(^3P)^3G$			49,628	49,717	−89	0.914	1.019
	5	$32+18A^3F(^3P)^3G+13^3H(^3P)^3G$			49,461	49,546	−85	1.163	1.164
$(^2P)^3P$	0	$64+7(^4P)^3P$	$3d^7(a\,^2D)4p$	$w\,^3P$	49,951	49,873	78		
	1	$48+12A^3P(^3P)^3P+6(^6S)^5P$			50,043	49,959	84	1.389	1.594
	2	$35+13(^4P)^5P+9(^6S)^5P$			50,187	50,270	−83	1.469	1.595
$(^2G)^1F$	3	$21+21(A^2D)^1F+16^3G(^3P)^1F$			50,587	50,612	−25	1.018	1.010
$A^3F(^3P)^1G$	4	$59+9(^2H)^1G$		$x\,^1G$	50,614	50,618	−4	0.978	0.981
$A^3P(^3P)^1P$	1	$72+10(A^2D)^1P$				50,827			1.063
$^3G(^3P)^3H$	4	$40+14(^2H)^3G+13^3G(^3P)^3G$		4°	51,409	51,486	−77	0.953	0.924
	5	$56+11^3H(^3P)^1H$	$3d^64s(a\,^4G)4p$	$x\,^3H$	51,069	51,146	−77	1.038	1.056
	5	$77+17^3H(^3P)^3H$			51,023	51,077	−54	1.161	1.165
$(A^2D)^3F$	2	$25+19^3G(^3P)^3F+11A^3P(^3P)^1D$	$3d^64s(a\,^4G)4p$	$v\,^3F$	51,201	51,131	70	0.803	0.788
	3	$30+23^3G(^3P)^3F+12A^3F(^3P)^3F$			51,365	51,281	84	1.096	1.087
	4	$31+24^3G(^3P)^3F+17A^3F(^3P)^3F$			51,305	51,257	48	1.122	1.227
$^3G(^3P)^3G$	3	$41+36(^2H)^3G$	$3d^7(a\,^2H)4p$	$u\,^3G$	51,826	51,805	21	0.801	0.775
	4	$24+23(^2H)^3G+18^3G(^3P)^3H$			51,668	51,589	79	1.067	0.971
	5	$19+19^3H(^3P)^1H+11(^2H)^3G$			51,374	51,266	108	1.140	1.077
$^3H(^3P)^1H$	5	$30+24(^2H)^3G+18^3G(^3P)^3G$		6°	51,630	51,548	82	1.061	1.101
$(^2P)^1D$	2	$32+19A^3P(^3P)^1D+17A^3F(^3P)^1D$		$x\,^1D$	51,762	51,738	24	0.883	0.937
$A^3F(^3P)^1D$	2	$36+29(A^2D)^1D+16(^2P)^1D$	$3d^7(a\,^2P)4p$	$y\,^1D$	51,708	51,814	−106	1.025	1.018
$(^2P)^1P$	1	$41+15(A^2D)^3D+11(A^2D)^3P$	$3d^7(a\,^2D)4p$	$t\,^3D$	52,181	52,012	169	0.801	0.961
$(^2P)^3D$	1	$47+25A^3F(^1P)^3D+9(^2P)^1P$			52,512	52,328	184	0.700	0.623
	2	$46+39A^3F(^1P)^3D+8(A^2D)^3D$			52,297	52,185	112	1.156	1.160
	3	$63+15A^3F(^1P)^3D$			51,969	51,934	35	1.306	1.304
$(^2H)^3H$	4	$59+17^3H(^1P)^3H+15^1I(^3P)^3H$			52,769	52,724	45	0.810	0.814
	5	$60+18^3H(^1P)^3H+14^1I(^3P)^3H$			52,613	52,557	56	1.033	1.036
	6	$62+21^3H(^1P)^3H+15^1I(^3P)^3H$			52,431	52,366	65	1.177	1.166
$(^2H)^3I$	5	$85+9^1I(^3P)^3I$			52,899	52,971	−72	0.830	0.839
	6	$61+27(^2H)^1I+5^1I(^3P)^3I$			52,514	52,595	−81	1.019	1.016
	7	$88+8^1I(^3P)^3I$			52,655:	52,691	−36	1.147	1.143

372-505 O - 70 - 4

TABLE 3. *Observed and calculated levels of* Fe I $(3d+4s)^7 4p$ – Continued

Name	J	Percentage	AEL		Obs. Level (cm^{-1})	Calc. Level (cm^{-1})	O–C	Obs. g-Factor	Calc. g-Factor
			Config.	Desig.					
$(A^2D)^3D$	1	$33+10(^2P)^3S+10(^2P)^3D$	$3d^7(a\,^2P)4p$	$z\,^1P$	53,230	53,274	−44	1.266	0.937
	2	$59+14(^2P)^3D$			52,683	52,981	−298	1.145	1.152
	3	$72+15A^3F(^1P)^3D$			52,213	52,403	−190	1.317	1.332
$(A^2D)^3P$	0	$53+23A^3P(^1P)^3P+10(^2P)^3P$				53,418			
	1	$21+13A^3P(^1P)^3P+12(^2P)^3S$	$3d^7(a\,^2P)4p$	$x\,^3S$	52,858	52,907	−49	1.246	1.374
	2	$55+25A^3P(^1P)^3P$	$3d^7(a\,^2P)4p$	$v\,^3P$:	52,916	52,723	193	1.495	1.488
$(^2H)^1I$	6	$61+25(^2H)^3I$			53,094	53,307	−213	1.010	1.012
$^3G(^3P)^1H$	5	$77+17^3H(^3P)^1H$	$3d^7(a\,^2H)4p$	$y\,^1H$	53,722	53,416	306	1.03:	1.006
$^3D(^3P)^5F$	1	$77+10^3G(^3P)^5F$				53,517			0.129
	2	$84+11^3G(^3P)^5F$		$s\,^3D$	53,275	53,539	−264		1.003
	3	$83+10^3G(^3P)^5F$				53,581			1.244
	4	$81+9^3G(^3P)^5F$				53,659			1.343
	5	$87+9^3G(^3P)^5F$		12°	54,014	53,780	234	1.356	1.398
$(A^2D)^1F$	3	$39+17(^2G)^1F+14A^3F(^3P)^1F$		$y\,^1F$	53,661	53,672	−11	1.21:	0.992
$^3D(^3P)^5D$	0	$88+7A^3F(^3P)^5D$				53,418			
	1	$86+7A^3F(^3P)^5D$				53,964			1.521
	2	$87+7A^3F(^3P)^5D$				53,983			1.487
	3	$74+12^3D(^3P)^5P+6A^3F(^3P)^5D$		10°	53,892	54,027	−135	1.476	1.505
	4	$88+7A^3F(^3P)^5D$		13°	54,301	54,156	145		1.489
$(^2P)^3S$	1	$17+18(A^2D)^3P+11(^2P)^1P$	$3d^7(a\,^2P)4p$	$v\,^3P$	53,808	53,755	53	1.418	1.535
$^3G(^3P)^3F$	2	$38+33(A^2D)^3F+12A^1G(^3P)^3F$				54,171			0.722
	3	$30+27(A^2D)^3F+12A^1G(^3P)^3F$		$x\,^1F$	53,763	53,892	−129	1.079	1.060
	4	$36+29(A^2D)^3F+12A^1G(^3P)^3F$				53,601			1.244
$^3D(^3P)^5P$	1	$69+10(^4P)^5P$	$3d^64s(b\,^4D)4p$	$t\,^3P$	54,271	54,169	102		2.393
	2	$78+10(^4P)^5P$			54,112	54,055	57	1.70:	1.806
	3	$69+12^3D(^3P)^5D+9(^4P)^5P$		11°	54,005	54,025	−20		1.633
$^1I(^3P)^3K$	6	99				54,164			0.859
	7	99				54,253			1.019
	8	100				54,361			1.125
$(^2H)^3G$	3	$33+25^3G(^3P)^3G+8^3H(^1P)^3G$	$3d^64s(a\,^4G)4p$	$t\,^3G$	54,600	54,614	−14	0.922	0.826
	4	$36+31^3G(^3P)^3G+12^3H(^1P)^3G$			54,237	54,272	−35	1.183	1.068
	5	$37+37^3G(^3P)^3G+13^3H(^1P)^3G$			53,983	54,000	−17	1.234	1.194
$^3G(^3P)^1G$	4	$42+25(^2H)^1G+19(^2G)^1G$		$w\,^1G$	54,811	54,736	75	1.001	0.998
$A^1G(^3P)^3H$	4	$85+5^1I(^3P)^3H$		$v\,^3H$	55,446	54,996	450	0.804	0.806
	5	$82+5^1I(^3P)^3H$			55,430	55,071	359	1.057	1.039
	6	$82+8^1I(^3P)^3H$			55,490	55,111	379	1.169	1.164
$(^3P)^1S$	0	$52+43A^3P(^3P)^1S$				55,042			
$(A^2D)^1P$	1	$39+22^3D(^3P)^1P+13(^2P)^1P$				55,161			1.045

TABLE 3. *Observed and calculated levels of* Fe I $(3d+4s)^7 4p$ – Continued

Name	J	Percentage	AEL		Obs. Level (cm^{-1})	Calc. Level (cm^{-1})	O–C	Obs. g-Factor	Calc. g-Factor
			Config.	Desig.					
$A^1G(^3P)^3G$	3	$73+6^3G(^1P)^3G$		s^3G	56,098	55,481	617	0.857	0.770
	4	$76+6^3G(^1P)^3G$			55,906	55,246	660		1.045
	5	$66+15(^2H)^1H+6^3G(^1P)^3G$			55,907	55,235	672	1.145	1.154
$(^2H)^1H$	5	$59+13A^1G(^3P)^3G+9^3H(^3P)^1H$		x^1H	55,526	55,574	−48	1.018	1.036
$(A^2D)^1D$	2	$56+15(^2P)^1D+14A^3F(^3P)^1D$			55,754	55,668	86	0.990	0.969
$^3G(^3P)^1F$	3	$61+13A^3F(^3P)^1F+12(A^2D)^1F$		w^1F	55,791	55,911	−120	0.908	0.985
$^1I(^3P)^3H$	4	$35+21A^1G(^3P)^3F+8^3H(^1P)^3H$	$3d^64s(b\,^2H)4p$	u^3H	56,423	56,326	97	0.859	0.981
	5	$62+12^3H(^1P)^3H$			56,383	56,325	58	1.029	1.036
	6	$63+13^3H(^1P)^3H+13A^1G(^3P)^3H$			56,334	56,208	126	1.166	1.166
$A^1G(^3P)^3F$	2	$30+23^3D(^3P)^3P+14(A^2D)^3F$	$3d^7(a\,^2D)4p$	u^3F	56,859	56,721	138	0.687	0.974
	3	$55+19(A^2D)^3F$			56,783	56,587	196	1.077	1.084
	4	$34+26^1I(^3P)^3H+9(A^2D)^3F$			56,593	56,441	152	1.148	1.063
$^3D(^3P)^3P$	0	$55+35A^1S(^3P)^3P$				56,866			
	1	$60+34A^1S(^3P)^3P$				56,863			1.490
	2	$43+15A^1G(^3P)^3F+12A^1S(^3P)^3P$				56,755			1.221
$(^2H)^1G$	4	$41+27^3G(^3P)^1G+14^3H(^3P)^1G$		v^1G	56,951	56,986	−35	1.053	1.013
$^1I(^3P)^3I$	5	$85+7(^2H)^3I$	$3d^64s(b\,^2H)4p$	x^3I	57,104	57,138	−34	0.832	0.836
	6	$86+6(^2H)^3I$			57,070	57,114	−44	1.028	1.025
	7	$86+5(^2H)^3I$			57,028:	57,082	−54	1.145	1.143
$^3D(^3P)^3D$	1	89				57,199			0.512
	2	$83+5A^1S(^3P)^3P$				57,234			1.192
	3	$85+6A^3F(^1P)^3D$				57,302			1.323
$^3D(^3P)^3F$	2	$59+9(^2F)^3F$		t^3F	57,709	57,407	302	0.698	0.669
	3	$61+8^3G(^1P)^3F$			57,641	57,398	243		1.092
	4	$65+8^3G(^1P)^3F$			57,550	57,386	164	1.235	1.248
$A^1S(^3P)^3P$	0	$32+18A^1D(^3P)^3P+16^3D(^3P)^3P$				58,100			
	1	$34+19A^1D(^3P)^3P+13^3D(^3P)^3P$				57,851			1.498
	2	$45+21A^3P(^1P)^3P+17A^1D(^3P)^3P$				57,522			1.474
$^3H(^1P)^3G$	3	$50+25(^2F)^3G$				58,980			0.781
	4	$55+24(^2F)^3G$				58,923			1.054
	5	$58+22(^2F)^3G$				58,838			1.199
$^3H(^1P)^3I$	5	90				59,291			0.839
	6	91				59,170			1.026
	7	90				58,993			1.142
$^3D(^3P)^1F$	3	$80+5^3G(^3P)^1F$				59,765			1.006
$^3D(^3P)^1D$	2	$58+25A^3P(^1P)^3D$				59,803			1.056
$A^3P(^1P)^3D$	1	$51+15^3D(^3P)^1P$				59,955			0.683
	2	$47+29^3D(^3P)^1D$				59,601			1.124
	3	$76+5(^2F)^3D$				59,019			1.310

TABLE 3. *Observed and calculated levels of* Fe I $(3d+4s)^7 4p$ – Continued

Name	J	Percentage	AEL		Obs. Level (cm^{-1})	Calc. Level (cm^{-1})	O–C	Obs. g-Factor	Calc. g-Factor
			Config.	Desig.					
$^3D(^3P)^1P$	1	$40+25A^3P(^1P)^3S+10(A^2D)^1P$				60,060			1.323
$A^3P(^1P)^3S$	1	$39+15^3D(^3P)^1P+13(^2P)^3S$				60,194			1.476
$A^3F(^1P)^3F$	2	$28+17A^1D(^3P)^3F+11^3G(^1P)^3F$				60,199			0.685
	3	$27+12A^1D(^3P)^3F+11^3G(^1P)^3F$				60,226			1.084
	4	$23+15^3D(^3P)^3F+12(^2F)^3F$				60,257			1.236
$A^3F(^1P)^3G$	3	83				60,876			0.765
	4	$69+5(^2F)^3F$				60,768			1.063
	5	80				60,588			1.188
$A^1D(^3P)^3F$	2	$53+25(^2F)^3F$				60,851			0.679
	3	$57+19(^2F)^3F$				60,868			1.077
	4	$62+15(^2F)^3F$				60,855			1.229
$A^3F(^1P)^3D$	1	$60+19(^2F)^3D$				61,289			0.504
	2	$53+22(^2F)^3D$				61,236			1.147
	3	$50+21(^2F)^3D$				61,125			1.299
$^3H(^1P)^3H$	4	$42+18(^2H)^3H+10^3G(^3P)^3G$				61,338			0.887
	5	$44+19(^2H)^3H+15^3G(^3P)^3G$				61,176			1.077
	6	$61+25(^2H)^3H$				61,073			1.166
$A^1D(^3P)^3P$	0	$64+20A^1S(^3P)^3P$				61,698			
	1	$63+19A^1S(^3P)^3P$				61,813			1.495
	2	$65+16A^1S(^3P)^3P$				62,002			1.491
$A^3P(^1P)^3P$	0	$46+18(A^2D)^3P+13A^1D(^3P)^3P$				62,162			
	1	$40+14(A^2D)^3P+11A^1D(^3P)^3P$				61,985			1.442
	2	$40+16(A^2D)^3P+6A^1D(^3P)^3P$				61,344			1.468
$^3G(^1P)^3G$	3	$19+22A^1D(^3P)^3D+9(^2F)^3G$				62,095			1.053
	4	$28+16A^3F(^1P)^3F+11(^2F)^3G$				62,453			1.123
	5	$44+16(^2F)^3G$				62,046			1.160
$A^1D(^3P)^3D$	1	$69+8A^3P(^1P)^3D$				62,449			0.579
	2	$67+8A^3P(^1P)^3D$				62,373			1.147
	3	$44+18^3G(^1P)^3G$				62,262			1.123
$^3G(^1P)^3F$	2	$24+26A^3F(^1P)^3F+11A^1D(^3P)^3F$				62,622			0.726
	3	$20+19A^3F(^1P)^3F+13^3G(^1P)^3G$				62,644			1.005
	4	$21+17A^3F(^1P)^3F+11^3H(^1P)^3H$				61,929			1.106
$(^2F)^1D$	2	$75+6^3D(^3P)^1D$				63,079			0.983
$(^2F)^1G$	4	89				63,731			1.000
$^3G(^1P)^3H$	4	86				63,850			0.806
	5	86				63,660			1.036
	6	89				63,314			1.165
$(^2F)^3D$	1	$49+17A^3F(^1P)^3D+11^3D(^1P)^3D$				64,369			0.502
	2	$50+20A^3F(^1P)^3D+11^3D(^1P)^3D$				64,378			1.159
	3	$48+12A^3F(^1P)^3D+11^3D(^1P)^3D$				64,398			1.301

TABLE 3. *Observed and calculated levels of* Fe I $(3d+4s)^7 4p$ – Continued

Name	J	Percentage	AEL		Obs. Level (cm^{-1})	Calc. Level (cm^{-1})	O–C	Obs. g-Factor	Calc. g-Factor
			Config.	Desig.					
$(^2F)\,^1F$	3	$76+10A^1G(^1P)\,^1F$				64,728			1.024
$(^2F)\,^3F$	2	$28+38^3G(^1P)\,^3F+7A^1D(^3P)\,^3F$				65,483			0.674
	3	$27+30^3G(^1P)\,^3F+7A^1D(^3P)\,^3F$				65,472			1.042
	4	$32+28^3G(^1P)\,^3F+8A^1D(^3P)\,^3F$				65,478			1.227
$(^2F)\,^3G$	3	$38+24^3G(^1P)\,^3G$				65,681			0.799
	4	$42+24^3G(^1P)\,^3G$				65,688			1.072
	5	$53+26^3G(^1P)\,^3G$				65,694			1.199
$^1F(^3P)\,^3G$	3	$83+9^3G(^1P)\,^3G$				66,475			0.752
	4	$86+6^3G(^1P)\,^3G$				66,591			1.051
	5	91				66,748			1.200
$^1F(^3P)\,^3D$	1	$82+7^3D(^1P)\,^3D$				67,401			0.509
	2	$82+7A^1D(^3P)\,^3D$				67,302			1.172
	3	$83+7A^1D(^3P)\,^3D$				67,168			1.336
$^3D(^1P)\,^3F$	2	$72+13(^4G)\,^3F^*$				67,856			0.668
	3	$72+13(^4G)\,^3F^*$				67,896			1.084
	4	$73+13(^4G)\,^3F^*$				67,993			1.250
$^1I(^1P)\,^1K$	7	98				68,142			1.000
$A^1G(^1P)\,^1H$	5	91				68,554			1.001
$^3D(^1P)\,^3D$	1	$58+7(^2F)\,^3D$				68,773			0.624
	2	$57+6(^4D)\,^3D$				68,764			1.220
	3	$68+8(^4D)\,^3D$				68,841			1.334
$^3D(^1P)\,^3P$	0	$77+5(^4P)\,^3P$				68,914			
	1	$76+4(^4P)\,^3P$				68,909			1.405
	2	$74+10^3D(^1P)\,^3D$				68,988			1.455
$B^3P(^3P)\,^5D$	0	$48+41B^3F(^3P)\,^5D$				69,095			
	1	$49+43B^3F(^3P)\,^5D$				69,171			1.463
	2	$48+45B^3F(^3P)\,^5D$				69,290			1.480
	3	$44+48B^3F(^3P)\,^5D$				69,416			1.480
	4	$35+48B^3F(^3P)\,^5D$				69,497			1.454
$A^1G(^1P)\,^1G$	4	$79+5(^2G)\,^1G$				69,309			1.017
$^1F(^3P)\,^3F$	2	$74+11(^2F)\,^3F$				69,784			0.671
	3	$72+11(^2F)\,^3F$				69,770			1.097
	4	$62+10(^2F)\,^3F$				69,784			1.280
$^1I(^1P)\,^1I$	6	$89+6(^2I)\,^1I$				69,857			1.000
$^1I(^1P)\,^1H$	5	$78+9(^2H)\,^1H$				70,146			1.001
$A^1G(^1P)\,^1F$	3	$72+10(A^2D)\,^1F$				70,198			1.003

TABLE 3. *Observed and calculated levels of* Fe I $(3d+4s)^7 4p$ – Continued

Name	J	Percentage	AEL		Obs. Level (cm^{-1})	Calc. Level (cm^{-1})	O–C	Obs. g-Factor	Calc. g-Factor
			Config.	Desig.					
$(^4G)^5G^*$	2	$73+25B^3F(^3P)^5G$				71,050			0.336
	3	$73+25B^3F(^3P)^5G$				71,085			0.916
	4	$73+24B^3F(^3P)^5G$				71,124			1.148
	5	$73+24B^3F(^3P)^5G$				71,160			1.265
	6	$73+25B^3F(^3P)^5G$				71,189			1.332
$(^4G)^5H^*$	3	99				71,835			0.504
	4	98				71,894			0.904
	5	98				71,958			1.103
	6	98				72,023			1.216
	7	100				72,083			1.286
$A^1S(^1P)^1P$	1	$83+7(A^2D)^1P$				72,282			1.000
$B^3F(^3P)^5G$	2	$73+24(^4G)^5G^*$				72,302			0.336
	3	$73+24(^4G)^5G^*$				72,353			0.916
	4	$73+24(^4G)^5G^*$				72,408			1.149
	5	$73+24(^4G)^5G^*$				72,458			1.265
	6	$72+25(^4G)^5G^*$				72,487			1.332
$B^3P(^3P)^5S$	2	$79+11(^4P)^5S$				72,554			1.982
$B^3P(^3P)^5P$	1	$80+6(^4P)^5P^*$				73,237			2.431
	2	$66+10(^4P)^5P^*$				73,716			1.772
	3	$42+27(^4G)^5F^*$				74,067			1.514
$(^4P)^5D^*$	0	$65+13B^3F(^3P)^5D+12B^3P(^3P)^5D$				73,513			
	1	$63+11B^3F(^3P)^5D+11B^3P(^3P)^5D$				73,545			1.466
	2	$51+11B^3F(^3P)^5D+10B^3P(^3P)^5D$				73,598			1.503
	3	$49+21(^4G)^5F^*+10B^3P(^3P)^5D$				73,724			1.438
	4	$51+22(^4G)^5F^*+10B^3P(^3P)^5D$				74,102			1.461
$(^4G)^5F^*$	1	$87+5B^3F(^3P)^5F$				74,079			0.045
	2	$79+7B^3F(^3P)^5F$				74,068			1.061
	3	$41+36B^3P(^3P)^5P$				74,008			1.453
	4	$68+17(^4P)^5D^*$				73,881			1.385
	5	$90+5B^3F(^3P)^5F$				73,877			1.400
$B^3P(^3P)^3S$	1	89				74,162			2.036
$B^3F(^3P)^3D$	1	$51+26B^3P(^3P)^3D$				74,513			0.509
	2	$56+24B^3P(^3P)^3D+13(B^2D)^1D$				74,590			1.173
	3	$57+21B^3P(^3P)^3D+12(B^2D)^3D$				74,744			1.337
$(^4P)^5S^*$	2	$82+13B^3P(^3P)^5S$				74,750			1.985
$A^1D(^1P)^1D$	2	$77+9(B^2D)^1D$				74,796			1.001
$A^1D(^1P)^1F$	3	82				74,828			1.002
$(^4G)^3H^*$	4	91				74,847			0.803
	5	91				74,831			1.038
	6	92				74,779			1.167
$A^1D(^1P)^1P$	1	84				74,870			1.007

TABLE 3. *Observed and calculated levels of* Fe I $(3d+4s)^2 4p$ — Continued

Name	J	Percentage	AEL		Obs. Level (cm^{-1})	Calc. Level (cm^{-1})	O–C	Obs. g-Factor	Calc. g-Factor
			Config.	Desig.					
$B^3F(^3P)^5D$	0	$40+33A^3P(^3P)^5D+18(^4P)^5D^*$				74,790			
	1	$38+33A^3P(^3P)^5D+17(^4P)^5D^*$				74,856			1.475
	2	$36+34A^3P(^3P)^5D+15(^4P)^5D^*$				74,989			1.504
	3	$31+34A^3P(^3P)^5D+9(^4P)^5D^*$				75,191			1.526
	4	$34+43A^3P(^3P)^5D+16(^4P)^5D^*$				75,393			1.498
$B^3F(^3P)^5F$	1	90				74,849			0.030
	2	91				74,891			1.004
	3	90				74,939			1.252
	4	90				74,974			1.348
	5	91				74,969			1.394
$B^3P(^3P)^1S$	0	$85+6B^3P(^3P)^3P$				75,549			
$(^4P)^5P^*$	1	$72+14(^4D)^5P^*$				75,951			2.433
	2	$67+15(^4D)^5P^*$				75,767			1.802
	3	$57+18(^4D)^5P^*+8(^4P)^5D^*$				75,524			1.634
$B^3F(^3P)^3G$	3	91				76,097			0.752
	4	90				76,059			1.051
	5	93				76,075			1.201
$B^3P(^3P)^3P$	0	$29+28(^4P)^3P^*+27(B^2D)^3P$				76,401			
	1	$30+30(^4P)^3P^*+26(B^2D)^3P$				76,357			1.550
	2	$30+23(^4P)^3P^*+18(B^2D)^3P$				76,332			1.463
$(^4G)^3F^*$	2	$40+18(B^2D)^3F+7(^4P)^3P^*$				76,453			0.834
	3	$53+13(B^2D)^3F$				76,504			1.084
	4	$56+13(B^2D)^3F$				76,567			1.249
$B^3F(^3P)^1D$	2	$45+27(B^2D)^1D+18B^3P(^3P)^1D$				76,696			0.988
$(^4P)^3P^*$	0	$41+32B^3P(^3P)^3P$				77,475			
	1	$35+34B^3P(^3P)^3P$				77,368			1.444
	2	$34+15B^3P(^3P)^3P+15(B^2D)^3P$				77,360			1.374
$(B^2D)^3F$	2	$38+31B^3F(^3P)^3F+15(^4G)^3F^*$				77,676			0.682
	3	$39+32B^3F(^3P)^3F+12(^4G)^3F^*$				77,779			1.091
	4	$21+37B^3F(^3P)^1G+17B^3F(^3P)^3F$				77,810			1.126
$B^3P(^3P)^3D$	1	$58+18B^3F(^3P)^3D$				77,682			0.567
	2	$47+16B^3F(^3P)^3D$				77,895			1.186
	3	$43+35(^4P)^3D^*$				78,067			1.322
$B^3F(^3P)^1G$	4	$38+20(B^2D)^3F+9^1F(^1P)^1G$				77,936			1.125
$(^4P)^3D^*$	1	$59+19(^4D)^5F^*$				78,229			0.399
	2	$61+8(^4D)^5F^*$				78,130			1.133
	3	$36+31B^3P(^3P)^3D$				78,169			1.324
$(^4G)^3G^*$	3	$75+9B^3F(^3P)^3G$				78,425			0.756
	4	$76+8B^3F(^3P)^3G$				78,446			1.052
	5	$77+8B^3F(^3P)^3G$				78,451			1.204
$^1F(^1P)^1D$	2	$31+40(^4D)^5F+10(B^2D)^1D$				78,776			1.008

TABLE 3. *Observed and calculated levels of* Fe I $(3d+4s)^7 4p$ – Continued

Name	J	Percentage	AEL		Obs. Level (cm^{-1})	Calc. Level (cm^{-1})	O–C	Obs. g-Factor	Calc. g-Factor
			Config.	Desig.					
$(^4D)^5F^*$	1	$70+17(^4P)^3D^*$				78,855			0.126
	2	$40+23\,^1F(^1P)^1D+13(^4P)^3D^*$				78,881			1.032
	3	$86+4(^4G)^5F^*$				78,885			1.255
	4	$89+4(^4G)^5F^*$				78,941			1.350
	5	90				79,004			1.395
$(B^2D)^1P$	1	$44+44B^3P(^3P)^1P$				79,295			0.986
$(B^2D)^1F$	3	$65+19B^3F(^3P)^1F$				79,310			1.003
$(B^2D)^3P$	0	$52+40B^3P(^3P)^3P$				79,504			
	1	$47+38B^3P(^3P)^3P$				79,498			1.519
	2	$48+33B^3P(^3P)^3P$				79,611			1.478
$B^3F(^3P)^3F$	2	$59+25(B^2D)^3F$				79,602			0.670
	3	$56+26(B^2D)^3F$				79,612			1.083
	4	$51+26(B^2D)^3F$				79,647			1.249
$(^4P)^3S^*$	1	$71+20B^3P(^3P)^3S$				79,715			1.968
$(B^2D)^3D$	1	$48+32B^3F(^3P)^3D$				80,166			0.508
	2	$47+30B^3F(^3P)^3D$				80,251			1.169
	3	$34+34(^4D)^5D^*+19B^3F(^3P)^3D$				80,382			1.402
$(^4D)^5D^*$	0	$80+15(^4P)^5D^*$				80,785			
	1	$76+14(^4P)^5D^*$				80,715			1.543
	2	$75+13(^4P)^5D^*$				80,606			1.511
	3	$44+20(B^2D)^3D+19B^3F(^1P)^3D$				80,451			1.431
	4	$82+12(^4P)^5D^*$				80,282			1.497
$^1F(^1P)^1G$	4	$72+19B^3F(^3P)^1G$				80,630			0.997
$B^3P(^3P)^1D$	2	$55+32B^3F(^3P)^1D$				80,675			1.018
$B^3F(^3P)^1F$	3	$44+43\,^1F(^1P)^1F$				81,005			0.999
$(^4D)^5P^*$	1	$77+12(^4P)^5P^*$				81,125			2.441
	2	$74+15(^4P)^5P^*$				81,311			1.814
	3	$72+19(^4P)^5P^*$				81,523			1.657
$B^1G(^3P)^3H$	4	95				81,288			0.805
	5	97				81,365			1.034
	6	97				81,474			1.167
$B^3P(^3P)^1P$	1	$49+44(B^2D)^1P$				81,779			0.999
$(^4D)^3F^*$	2	$74+10B^3F(^1P)^3F$				82,431			0.693
	3	$64+7(^4D)^3D^*$				82,424			1.108
	4	$73+6B^1G(^3P)^3F$				82,455			1.241
$B^1G(^3P)^3G$	3	$74+10B^1G(^3P)^3F$				82,700			0.826
	4	$81+6(^4D)^3F^*$				82,747			1.082
	5	96				82,830			1.200

TABLE 3. *Observed and calculated levels of* Fe I $(3d+4s)^7 4p$ – Continued

Name	J	Percentage	AEL		Obs. Level (cm^{-1})	Calc. Level (cm^{-1})	O–C	Obs. g-Factor	Calc. g-Factor
			Config.	Desig.					
$(^4D)^3D^*$	1	$68+10^3D(^1P)^3D$				82,813			0.516
	2	$52+16B^1G(^3P)^3F$				82,818			1.069
	3	$49+10B^1G(^3P)^3F+8^3D(^1P)^3D$				82,863			1.250
$^1F(^1P)^1F$	3	$27+15B^3F(^3P)^1F+12(^4D)^3F^*$				82,922			1.040
$B^1G(^3P)^3F$	2	$58+11(^4D)^3D^*$				82,990			0.762
	3	$40+17B^1G(^3P)^3G$				83,106			1.036
	4	$64+11B^1G(^3P)^3G$				83,087			1.229
$(B^2D)^1D$	2	$42+22^1F(^1P)^1D$				83,636			1.004
$(^4D)^3P^*$	0	$63+21B^3P(^1P)^3P+9(^4P)^3P^*$				83,442			
	1	$60+20B^3P(^1P)^3P+11(^4P)^3P^*$				83,647			1.492
	2	$57+19B^3P(^1P)^3P+13(^4P)^3P^*$				83,908			1.481
$(^2I)^3K^*$	6	97				85,859			0.862
	7	99				86,012			1.018
	8	100				86,159			1.125
$(^2I)^3I^*$	5	93				86,815			0.838
	6	93				86,942			1.020
	7	$88+8(^2I)^1K^*$				86,861			1.132
$(^2I)^1K^*$	7	$90+8(^2I)^3I^*$				87,284			1.011
$B^3P(^1P)^3D$	1	$78+8(^4F)^3D^*$				86,930			0.507
	2	$76+9(^4F)^3D^*$				87,281			1.162
	3	$59+10(^4F)^3D^*$				87,797			1.327
$B^3F(^1P)^3G$	3	85				87,684			0.752
	4	82				87,747			1.050
	5	$73+10(^2I)^1H^*$				87,676			1.170
$B^3F(^1P)^3D$	1	$71+14(^4F)^3D^*$				87,911			0.504
	2	$68+13(^4F)^3D^*$				87,969			1.088
	3	$60+20(^4F)^3D^*$				87,995			1.330
$(A^2D)^1D^*$	2	$35+18(A^2F)^3F+17(A^2D)^3F^*$				88,159			0.919
$(^2I)^1H^*$	5	$69+11B^3F(^1P)^3G+10B^1G(^1P)^1H$				88,248			1.026
$(A^2D)^3F^*$	2	$41+22(A^2D)^1D^*+16(A^2F)^1D^*$				88,636			0.804
	3	$62+30(A^2F)^3F^*$				88,632			1.079
	4	$69+24(A^2F)^3F^*$				88,904			1.229
$B^3F(^1P)^3F$	2	$68+14(^4F)^3F^*$				88,903			0.708
	3	$72+17(^4F)^3F^*$				88,859			1.083
	4	$73+17(^4F)^3F^*$				88,844			1.234
$(^2I)^3H^*$	4	87				89,341			0.819
	5	91				89,325			1.034
	6	92				89,251			1.166
$(A^2D)^1F^*$	3	$50+32(A^2F)^3G^*+14(A^2F)^1F^*$				90,257			0.930

TABLE 3. *Observed and calculated levels of* Fe I $(3d+4s)^7 4p$ — Continued

Name	J	Percentage	AEL		Obs. Level (cm^{-1})	Calc. Level (cm^{-1})	O−C	Obs. g-Factor	Calc. g-Factor
			Config.	Desig.					
$B^3P(^1P)^3S$	1	$79+14(^4P)^3S^*$				90,466			1.954
$(A^2D)^3P^*$	0	$51+33B^3P(^1P)^3P$				90,926			
	1	$72+22B^3P(^1P)^3P$				90,918			1.480
	2	$74+18B^3P(^1P)^3P$				90,819			1.467
$(A^2F)^1G^*$	4	$61+27(A^2F)^3G^*+7(^2H)^1G^*$				90,922			1.013
$(^2I)^1I^*$	6	$90+5^1I(^1P)^1I$				91,139			1.002
$(A^2D)^3D^*$	1	85				91,706			0.513
	2	$80+7(A^2D)^3F^*$				91,640			1.106
	3	$69+18(A^2F)^3G^*$				91,316			1.202
$(A^2F)^3G^*$	3	$57+25(A^2D)^1F^*+16(A^2D)^3D^*$				91,813			0.932
	4	$62+21(A^2F)^3F^*+15(A^2F)^1G^*$				91,428			1.090
	5	93				91,376			1.199
$B^3P(^1P)^3P$	0	$41+42(A^2D)^3P^*$				92,053			
	1	$40+19(A^2D)^3P^*+11(^4D)^3P^*$				92,194			1.449
	2	$57+13(A^2D)^3P^*+13(^4D)^3P^*$				92,291			1.464
$(A^2F)^3F^*$	2	$43+33(^4F)^5G^*+14(A^2D)^3F^*$				92,699			0.610
	3	$41+31(^4F)^5G^*+15(A^2D)^3F^*$				92,785			1.060
	4	$47+22(A^2D)^3F^*+13(^4F)^5G^*$				92,712			1.205
$(^4F)^5G^*$	2	$63+20(A^2F)^3F^*+12(A^2D)^3F^*$				93,291			0.464
	3	$55+23(A^2F)^3F^*+10(A^2D)^3F^*$				93,245			1.007
	4	$82+8(A^2F)^3F^*$				93,054			1.158
	5	95				92,971			1.263
	6	95				93,008			1.328
$(A^2F)^3D^*$	1	$56+27(A^2D)^1P^*$				93,249			0.712
	2	$70+12(A^2D)^3P^*$				93,668			1.212
	3	$72+9(^4F)^5G^*$				93,165			1.291
$B^1G(^1P)^1H$	5	$68+27(^2H)^1H^*$				93,663			1.006
$B^1G(^1P)^1G$	4	$53+27(^2H)^1G^*$				93,814			1.044
$(^4F)^5F^*$	1	90				94,225			0.049
	2	$88+5(^4F)^5D^*$				94,169			1.026
	3	$87+7(^4F)^5D^*$				94,109			1.264
	4	$75+9B^1G(^1P)^1G$				94,041			1.300
	5	89				94,088			1.383
$(^2H)^3H^*$	4	$56+35(A^2G)^3H^*$				94,313			0.821
	5	$54+36(A^2G)^3H^*$				94,457			1.040
	6	$54+37(A^2G)^3H^*$				94,658			1.161
$(A^2D)^1P^*$	1	$62+26(A^2F)^3D^*$				94,900			0.916
$(^2H)^3G^*$	3	$32+49(^4F)^3G^*+11(B^2F)^3G^*$				94,917			0.762
	4	$34+48(^4F)^3G^*+10(B^2F)^3G^*$				94,966			1.051
	5	$37+46(^4F)^3G^*+10(B^2F)^3G^*$				95,018			1.198

TABLE 3. *Observed and calculated levels of* Fe I $(3d+4s)^7 4p$ – Continued

Name	J	Percentage	AEL		Obs. Level (cm^{-1})	Calc. Level (cm^{-1})	O–C	Obs. g-Factor	Calc. g-Factor
			Config.	Desig.					
$(^4F)^5D^*$	0	94				95,038			
	1	85				95,064			1.422
	2	$88+5(^4F)^5F^*$				95,045			1.470
	3	$87+6(^4F)^5F^*$				95,019			1.475
	4	$88+5(^4F)^5F^*$				94,967			1.487
$B^1G(^1P)^1F$	3	$56+22(A^2F)^1F^*$				95,292			1.000
$(^2H)^3I^*$	5	92				95,329			0.843
	6	92				95,463			1.030
	7	96				95,616			1.142
$(^4F)^3G^*$	3	$26+42(A^2G)^3G^*+18(^2H)^3G^*$				96,477			0.762
	4	$29+39(A^2G)^3G^*+18(^2H)^3G^*$				96,399			1.050
	5	$33+36(A^2G)^3G^*+16(^2H)^3G^*$				96,293			1.199
$(A^2F)^1D^*$	2	$58+30(A^2D)^1D^*$				96,581			0.998
$(A^2G)^1G^*$	4	$52+20(A^2F)^1G^*+15(^2H)^1G^*$				96,730			1.009
$(A^2F)^1F^*$	3	$50+30^3G(^1P)^1F+10(A^2D)^1F^*$				96,731			0.996
$(^2H)^1I^*$	6	93				96,857			1.004
$(A^2G)^3F^*$	2	$59+27(4F)^3F^*$				98,018			0.677
	3	$57+27(^4F)^3F^*$				98,021			1.088
	4	$56+26(^4F)^3F^*$				98,198			1.237
$B^1D(^3P)^3D$	1	95				98,571			0.500
	2	95				98,595			1.163
	3	95				98,635			1.331
$(A^2G)^3H^*$	4	$59+37(^2H)^3H^*$				99,217			0.807
	5	$59+35(^2H)^3H^*$				99,245			1.039
	6	$61+35(^2H)^3H^*$				99,382			1.165
$(^4F)^3D^*$	1	$57+21(B^2F)^3D^*$				100,156			0.503
	2	$54+22(B^2F)^3D^*$				100,063			1.158
	3	$50+21(B^2F)^3D^*$				99,965			1.317
$(A^2G)^1H^*$	5	$60+24(A^2G)^3G^*+11(B^2F)^3G^*$				100,323			1.072
$(A^2G)^3G^*$	3	$45+17(B^2F)^3G^*+15(^4F)^3G^*$				100,790			0.791
	4	$46+22(B^2F)^3G^*+13(^4F)^3G^*$				100,747			1.065
	5	$33+30(A^2G)^1H^*+14(B^2F)^3G^*$				100,437			1.113
$(^4F)^3F^*$	2	$29+24(B^2F)^3F^*+20B^1D(^3P)^3F$				100,948			0.671
	3	$41+21(B^2G)^3F^*+14(B^2F)^3F^*$				100,829			1.082
	4	$38+22(B^2F)^3F^*+22(B^2G)^3F^*$				100,602			1.238
$B^1D(^3P)^3F$	2	$69+15(^4F)^3F^*$				100,778			0.668
	3	$76+14(B^2F)^3F^*$				100,841			1.056
	4	$84+11(B^2F)^3F^*$				100,955			1.241
$(A^2G)^1F^*$	3	$76+8(B^2F)^1F^*$				101,827			1.003

TABLE 3. *Observed and calculated levels of* Fe I $(3d+4s)^7 4p$ – Continued

Name	J	Percentage	AEL		Obs. Level (cm^{-1})	Calc. Level (cm^{-1})	O–C	Obs. g-Factor	Calc. g-Factor
			Config.	Desig.					
$(B^2F)^1G^*$	4	$64+19(A^2G)^1G^*+6(^2H)^1G^*$				101,671			1.006
$(^2H)^1H^*$	5	$53+22B^1G(^1P)^1H+9(^2I)^1H^*$				102,138			1.010
$B^1D(^3P)^3P$	0	95				102,242			
	1	95				102,211			1.500
	2	95				102,147			1.499
$(B^2F)^3F^*$	2	$70+13(A^2G)^3F^*$				102,750			0.675
	3	$73+12(A^2G)^3F^*$				102,809			1.083
	4	$69+10(A^2G)^3F^*+9(^4F)^3F^*$				102,915			1.247
$(B^2F)^1D^*$	2	$83+8(B^2D)^1D^*$				103,163			0.997
$(B^2F)^3G^*$	3	$70+25(^2H)^3G^*$				103,655			0.753
	4	$70+25(^2H)^3G^*$				103,764			1.051
	5	$69+25(^2H)^3G^*$				103,882			1.199
$(B^2F)^3D^*$	1	$77+9(^4F)^3D^*$				104,973			0.507
	2	$74+11(^4F)^3D^*$				105,129			1.168
	3	$72+13(^4F)^3D^*$				105,341			1.332
$(^2H)^1G^*$	4	$32+31(B^2F)^1G^*+23(A^2G)^1G^*$				106,455			1.001
$(^2S)^3P^*$	0	$83+13(B^2D)^3P^*$				107,066			
	1	$83+13(B^2D)^3P^*$				107,164			1.495
	2	$83+12(B^2D)^3P^*$				107,371			1.497
$(B^2F)^1F^*$	3	$83+8(A^2G)^1F^*$				107,873			1.001
$(^2S)^1P^*$	1	$79+10(B^2D)^1P^*+9B^1D(^1P)^1P$				108,476			0.999
$B^1D(^1P)^1D$	2	$76+21(B^2D)^1D^*$				110,880			1.000
$B^1D(^1P)^1F$	3	$78+16(B^2G)^1F^*$				113,463			1.000
$B^1D(^1P)^1P$	1	$75+19(B^2D)^1P^*$				115,224			0.991
$(B^2D)^3D^*$	1	96				115,523			0.511
	2	95				115,589			1.165
	3	$91+6(B^2D)^3F^*$				115,698			1.320
$(B^2D)^3F^*$	2	92				115,524			0.669
	3	90				115,612			1.095
	4	94				115,746			1.250
$(B^2D)^1F^*$	3	89				116,688			1.000
$(B^2D)^3P^*$	0	$81+12(^2S)^3P^*$				117,777			
	1	$81+12(^2S)^3P^*$				117,800			1.496
	2	$82+12(^2S)^3P^*$				117,850			1.499
$(B^2D)^1P^*$	1	$70+16(^2S)^1P^*+10B^1D(^1P)^1P$				118,501			1.002
$(B^2D)^1D^*$	2	$75+19B^1D(^1P)^1D$				120,088			1.000

TABLE 3. *Observed and calculated levels of* Fe I $(3d+4s)^7 4p$ – Continued

Name	J	Percentage	AEL		Obs. Level (cm^{-1})	Calc. Level (cm^{-1})	O–C	Obs. g-Factor	Calc. g-Factor
			Config.	Desig.					
$B^1S(^3P)^3P$	0	92				122,270			
	1	92				122,356			1.500
	2	92				122,532			1.500
$(B^2G)^3H^*$	4	98				123,645			0.801
	5	98				123,693			1.034
	6	98				123,777			1.167
$(B^2G)^3G^*$	3	$88+11(B^2G)^3F^*$				124,705			0.788
	4	96				124,837			1.055
	5	98				124,926			1.199
$(B^2G)^3F^*$	2	93				125,023			0.667
	3	$84+11(B^2G)^3G^*$				124,929			1.046
	4	91				124,729			1.244
$(B^2G)^1H^*$	5	98				125,484			1.001
$(B^2G)^1G^*$	4	96				126,557			1.001
$(B^2G)^1F^*$	3	$80+10B^1D(^1P)^1F$				129,093			1.000
$B^1S(^1P)^1P$	1	$85+10(C^2D)^1P^*$				134,135			1.000
$(^2P)^3P^*$	0	$75+24(C^2D)^3P^*$				138,527			
	1	$75+23(C^2D)^3P^*$				138,631			1.500
	2	$75+23(C^2D)^3P^*$				138,877			1.499
$(^2P)^1S^*$	0	99				141,049			
$(^2P)^1D^*$	2	$42+43(^2P)^3D^*+10(C^2D)^1D^*$				141,744			1.078
$(^2P)^3D^*$	1	$93+5(C^2D)^3D^*$				142,012			0.501
	2	$49+38(^2P)^1D^*+10(C^2D)^1D^*$				142,162			1.089
	3	$91+7(C^2D)^3D^*$				142,092			1.333
$(^2P)^3S^*$	1	99				143,800			1.998
$(^2P)^1P^*$	1	$75+12(C^2D)^1P^*+10B^1S(^1P)^1P$				145,679			0.999
$(C^2D)^3F^*$	2	95				149,953			0.673
	3	95				149,997			1.086
	4	96				150,099			1.250
$(C^2D)^3D^*$	1	$93+6(^2P)^3D^*$				150,910			0.503
	2	$91+6(^2P)^3D^*$				151,048			1.162
	3	$91+7(^2P)^3D^*$				151,252			1.330
$(C^2D)^1D^*$	2	$77+18(^2P)^1D^*$				152,034			1.009
$(C^2D)^1F^*$	3	96				152,174			1.001
$(C^2D)^3P^*$	0	$75+24(^2P)^3P^*$				153,610			
	1	$75+24(^2P)^3P^*$				153,440			1.498
	2	$74+23(^2P)^3P^*$				153,150			1.491
$(C^2D)^1P^*$	1	$78+16(^2P)^1P^*$				157,198			1.001

TABLE 4. *Orders of the submatrices of* $(d+s)^7p$

J	Order
0	39
1	107
2	144
3	145
4	117
5	76
6	39
7	14
8	3

The approximate time for the diagonalization routine on the IBM 7040 computer was $4\frac{1}{2}$ hr.

The work described in this paper was supported in part by the National Bureau of Standards, Washington, D.C.

4. References

[1] Roth, C., Nat. Bur. Stand. (U.S.), **72A** (Phys. and Chem.), No. 5, 505–520 (Sept.–Oct. 1968).
[2] Roth, C., Nat. Bur. Stand. (U.S.), **73A** (Phys. and Chem.), No. 2, 125–157 (Mar.–Apr. 1969).
[3] Roth, C., Nat. Bur. Stand. (U.S.), **73A** (Phys. and Chem.), No. 2, 159–171 (Mar.–Apr. 1969).
[4] Roth, C., Nat. Bur. Stand. (U.S.), **73A** (Phys. and Chem.), No. 6, 509–609 (Nov.–Dec. 1969).
[5] Rohrlich, F., Phys. Rev., **74** 1381 (1948).
[6] Roth, C., Nat. Bur. Stand. (U.S.), **73A** (Phys. and Chem.), No. 5, 497–510 (Sept.–Oct. 1969).
[7] Smith, G., and Siddall, J., J. Opt. Soc. Am. **59,** 419 (1969).
[8] Martin, W. C., and Sugar, J., J. Opt. Soc. Am. **59,** 1266 (1969).
[9] Wilson, M., J. Phys. B, Ser. 2, Vol. **2,** 524 (1969).
[10] Roth, C., Nat. Bur. Stand. (U.S.), **74A** (Phys. and Chem.) No. 2 (Mar.–Apr. 1970).
[11] Roth, C., Nat. Bur. Stand. (U.S.), **74A** (Phys. and Chem.) No. 2 (Mar.–Apr. 1970).
[12] Roth, C., Nat. Bur. Stand. (U.S.) (Phys. and Chem.) to be submitted.
[13] Moore, C. E., Atomic Energy Levels, Nat. Bur. Stand. (U.S.), Circ. 467, Vol. **II,** (1952).
[14] Roth, C., J. Math. Phys., **10,** No. 6, 1038 (1969).
[15] Roth, C., J. Math. Phys., **9,** No. 4, 686 (1968).
[16] Russell, H. N., Moore, C. E., and Weeks, D. W., Trans. Am. Phil Soc., **34,** Part 2, 111 (1944).

(Paper 74A2–590)

JOURNAL OF RESEARCH of the National Bureau of Standards—A. Physics and Chemistry
Vol. 74A, No. 2, March–April 1970

The Intensity as a Function of Temperature of the Low-Angle X-Ray Diffraction Maxima of the *n*-Paraffins: Hexatriacontane, Tetratetracontane, and Tetranonacontane

Peter K. Sullivan* and James J. Weeks

Institute for Materials Research, National Bureau of Standards, Washington, D.C. 20234

(October 15, 1969)

The diffraction of x-rays by the crystalline *n*-paraffins, $C_{36}H_{74}$, $C_{44}H_{90}$, and $C_{94}H_{190}$, was examined at small angles—below seven degrees 2θ—as a function of temperature. The Bragg maxima (00*l*) that occur at these angles result from a lamellar repeat distance which depends on the molecular length. In general the intensity of these maxima was found to increase with increasing temperature in an approximately reversible manner. All the samples experienced solid-solid phase transitions in the temperature range of observation. Several possible mechanisms consistent with the temperature dependence of the intensity are considered.

Key words: Defects; *n*-paraffins; phase transition; temperature dependence; x-ray diffraction.

1. Introduction

Some polymers which exhibit high crystallinity [1, 2][1] display low-angle x-ray diffraction maxima which correspond to a lamellar repeat distance. In the case of linear polyethylene and a number of other polymers, it has been observed [3–5] that the intensities of the low-angle maxima increase with increasing temperature and that this phenomenon occurs reversibly.

Normally, one expects that the intensity of x-ray diffraction maxima from crystalline solids should decrease with increasing temperature. This is evidenced by the Debye-Waller factor [6] in structure calculations and in the experimental observation of the change in intensity of the diffraction maxima with temperature for a variety of solids [7].

The question which arises is whether the intensity behavior of the low-angle maxima with temperature is unique to these crystalline polymers or occurs in other compounds, such as the long-chain *n*-paraffins. Both the paraffins and polyethylene have the same —CH_2— repeat unit; however, a pure paraffin is essentially a single molecular species, while the polymer has a broad distribution in molecular weights. Both systems crystallize as lamellae, with very similar crystallographic subcells [8–12]. However, the basal surfaces of the paraffin lamellae are composed of methyl groups, while in the polymer lamellae these end surfaces are composed of more or less regular chain-folds [1].

In this article we present our observations of the intensities of the low-angle x-ray diffraction maxima as a function of temperature for three crystalline *n*-paraffins: *n*-$C_{36}H_{74}$, *n*-$C_{44}H_{90}$, and *n*-$C_{94}H_{190}$. We also discuss some possible causes of the observed intensity changes with temperature.

2. Experimental Detail

2.1. Apparatus

Diffraction intensities at angles up to 7° in 2θ were obtained using nickel-filtered copper radiation. The detector system consisted of a scintillation counter, pulse-height analyzer, and printer. A Kratky low-angle camera[2] with a 120 μ entrance slit was used for beam collimation. The detector slit width was commonly 270 μ and the sample to detector distance was 238.7 mm. Scanning was accomplished automatically with a Kratky step-scanner. Generally a counting time of 1 min was used at each angle. No slit-smearing corrections were made. The samples were contained either in a 1.5 mm diam glass capillary (0.01 mm wall thickness) or in a stainless steel holder ($25 \times 2.5 \times 3$ mm^3) with beryllium foil sides. The capillary tube or holder was held in a small oven which had beryllium windows and $\frac{1}{2}$ in thick balsa wood insulation. Temperature control was achieved with a thermistor system which could maintain a constant sample temperature above

*NBS–NRC Postdoctoral Associate 1965–1967.

[1] Figures in brackets indicate the literature references at the end of this paper.

[2] Certain commercial materials and equipment are identified in this paper in order to specify adequately the experimental procedure. In no case does such identification imply recommendation or endorsement by the National Bureau of Standards, nor does it imply that the material or equipment is necessarily the best available for the purpose.

room temperature to within 0.1 K for a period of several days. Below room temperature the sample container was cooled with a stream of gas from liquid nitrogen; dry nitrogen gas (warmed) was blown across the beryllium windows to prevent ice formation. Temperature control was not as good as under these conditions, but constancy to ± 0.1 K could be maintained during the diffraction scan, which typically lasted about 90 min.

When the sample was inhomogeneous with respect to thickness or crystallite orientation small adjustments in the height of the oven above the optical bench were necessary to keep the same portion of the sample in the x-ray beam as the temperature was changed. It was found that an observation of the intensity of the (00*l*) Bragg maximum as the sample was moved gave a profile of the inhomogeneities, so that a local maximum or minimum of intensity could be used as a reference point at any temperature.

2.2. Samples

a. Tetrananocontane, n-$C_{94}H_{190}$ (mp 387.4 K [13])

This compound was synthesized by Reinhard [13] and a sample was kindly supplied to us by Dr. John Crissman,[3] who had crystallized it from the melt in a Bridgman apparatus [14] (4 K gradient; drop rate of 0.4 mm/hr). The resulting polycrystalline sample was found to be highly oriented by examination with an x-ray camera having pinhole collimation. The diffraction spots of the long spacing showed no arcing. A Differential Scanning Calorimeter (DSC) scan of this sample—to be called "C_{94} (orig)"—is shown in figure 1(a).

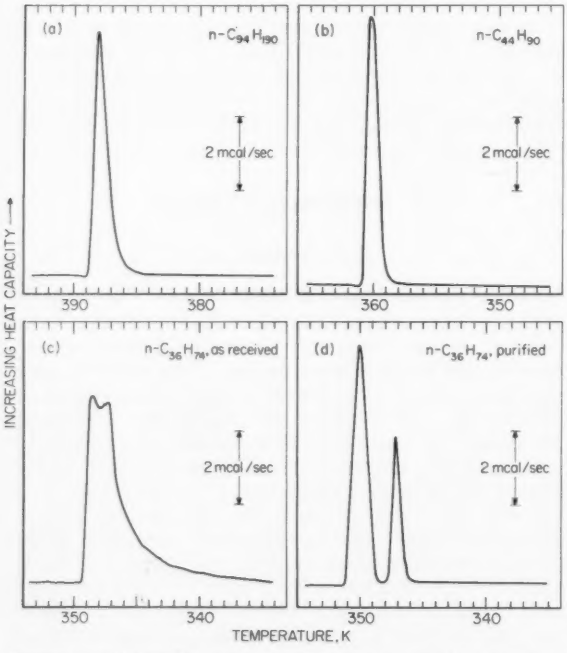

FIGURE 1. *Differential scanning calorimeter traces of the melting of (a)* n-$C_{94}H_{190}$, *as received, (b)* n-$C_{44}H_{90}$, *(c)* n-$C_{36}H_{74}$, *as received, and (d)* n-$C_{36}H_{74}$ *after purification as described in the text.*

The lower temperature peak in n-$C_{36}H_{74}$ is a solid-solid transition to the hexagonal phase. Heating rate was 2.5 deg/min in each case.

[3] Metallurgy Division, National Bureau of Standards, Washington, D.C. 20234.

In order to estimate the effect of slit-smearing on the low-angle *d*-spacings obtained with the Kratky camera, part of the n-$C_{94}H_{190}$ sample was melted into a 1.5 mm thin-walled capillary tube and crystallized with approximately random orientation of the lamellae. Measurements on this sample will be designated, "C_{94} (m. c.)".

Orthorhombic n-$C_{94}H_{190}$ may be obtained by crystallization from dilute solution [12]. Samples were prepared from butyl acetate and from xylene. In the former case, a 0.06 wt percent solution was very slowly cooled from 377 K. Precipitation occurred above 350 K. Using a phase-contrast optical microscope the crystals were observed to be growth spirals on twinned laths, typically about ten layers thick. The acute angle between adjacent (110) faces was found to be 66.3 deg, in agreement with what one calculates for the orthorhombic unit cell [12]. The sample was separated by filtration, dried at room temperature under high vacuum and cut into strips, which were compacted at a pressure of approximately 400 psi. This produced a semioriented sample or mat, as was evidenced by examination in the pinhole camera. The mat was then placed in the steel holder for subsequent x-ray examination and will be referred to as "C_{94} (s. c.)".

The second solution-grown sample of n-$C_{94}H_{190}$ was prepared by cooling a 0.2 wt percent xylene solution from 383 K to room temperature. Crystallization occurred near 340 K. The sample was filtered and dried, and the mat cut into strips, which were examined without being compacted. This sample was annealed overnight at 382 K, after which time the lamellar *d*-spacing at 382 K indicated that the substance was no longer in a pure orthorhombic phase. This sample will be designated "C_{94} (annealed)".

b. Tetratetracontane, n-$C_{44}H_{90}$ (mp 359.6 K [15])

This compound was synthesized by Clark [16] and a sample was made available to us by Dr. Crissman. A DSC scan of the original sample is shown in figure 1(b). A 0.34 wt percent toluene solution of the n-$C_{44}H_{90}$ was prepared and the sample crystallized by cooling from 329 to 289 K; precipitation began at 312 K. The toluene was removed by filtration and the crystal mat dried under vacuum at room temperature for 3.5 days. For x-ray examination, the mat was cut into strips and stacked in the steel holder parallel to the x-ray beam.

c. Hexatriacontane, n-$C_{36}H_{74}$ (mp 348.7 K [9])

The n-$C_{36}H_{74}$ was obtained commercially with a stated purity of 97 percent. Measurements were made on the original material as well as on a sample which was purified both by recrystallization from dilute benzene solution and subsequent zone refinement for 35 days (15 zones at 7 mm/hr). Both samples were crystallized from the melt before x-ray examination.

DSC traces of the original and purified samples are shown in figures 1(c) and 1(d) respectively. By comparison one sees that most of the impurities which broadened the transitions in the original material have been removed by the purification scheme.

For the case of n-$C_{36}H_{74}$ the preparation conditions were varied in an attempt to determine if there were any contribution of primary extinction to the intensity changes with temperature. Samples of n-$C_{36}H_{74}$ were crystallized under conditions which should lead to small and imperfect crystals. One sample was dissolved in toluene (0.15 wt %) and quenched by pouring the warm solution into a container which was at the temperature of a dry-ice acetone bath. A second sample was dissolved in ethanol and the solution atomized into a large beaker of rapidly stirred ice water. Each of these samples was dried at room temperature and subsequently ground at the temperature of dry ice.

2.3. Data Treatment

The low-angle x-ray diffraction maxima considered throughout this article correspond to the lamellar repeat distance, which in the case of the n-paraffins is determined by the length of a molecule.

The d-spacings were obtained from Bragg's law, $m\lambda = 2d \sin \theta$, where 2θ was measured from the peak positions of the primary beam and diffraction maximum. Because of smearing by the collimator and detector slits, most of the observed peaks were shifted toward smaller angles by amounts which depended on such variables as sample orientation and background intensity. Since the effect of smearing is angle dependent, being smaller at the larger angles, a more accurate determination of the d-spacings was obtained from the higher orders. Repeated scans on a given sample at constant temperature always gave agreement within 0.5 Å as long as no phase transformations occurred.

Unless noted otherwise the diffraction intensities reported are the integrated intensities obtained after subtracting a smooth scattering background from the observed intensities. The areas were determined by means of a planimeter. In cases where the lamellae were randomly oriented or where considerable void scattering was present, the location of the background was somewhat uncertain. However, a log-log plot of the scattered intensity against 2θ usually showed that a single, nearly linear background could be drawn under the first three orders of the d-spacing. For a given sample, the slopes of such lines were also noted to be independent of the temperature at which the scan had been made. Backgrounds from the log-log plots were transferred to linear plots and the areas then determined. Repeated x-ray scans of any sample at a given temperature always gave areas which agreed within 10 percent of each other.

3. Results

In general, the intensity effects we have observed on these n-paraffins were consistent with what has been observed in the case of polyethylene [3], that is to say, the intensity of the low-angle ($00l$) maxima increased substantially with increasing sample temperature. No broadening of the maxima was observed with the increase in intensities and the effects were found to be approximately reversible. The ($00l$) d-spacings of our n-paraffins showed changes with temperature which were in part reversible. As will be seen shortly, these changes reflect the fact that solid-solid phase transformations are taking place in the paraffins at the higher temperatures of observation.

3.1. Tetrananacontane

The observed diffraction intensity from C_{94} (orig) at a temperature of 385.2 K—two degrees below its melting point—is shown in figure 2. Four orders of the low-angle d-spacing are shown; although, with our equipment six were observable at this temperature. The first two orders were defined by points taken every 0.00042 rad, the third and fourth orders with half as many points. There is little uncertainty in the background for this sample. Integrated intensities and d-spacings (assumed to be orders of the (001) spacing) are listed in table 1, as are the half-height widths of the maxima.

The x-ray diffraction from C_{94} (orig) was determined at five different temperatures and the observed intensities (with background subtracted) of the (001) spacing are shown in figure 3. The d-spacing as a function of temperature is shown in figure 4. It is seen that both the intensity and the d-spacing vary with temperature. In table 2 are listed the values of the (001) spacing

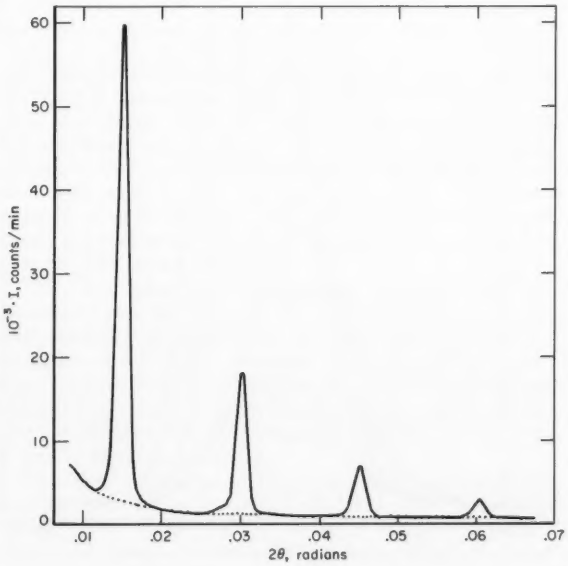

FIGURE 2. *The observed x-ray diffraction intensity as a function of the scattering angle from* n-$C_{94}H_{190}$, *as received, at a temperature of 385.2 K.*

The dotted line is the background intensity.

TABLE 1. *Observed integrated intensities and d-spacings for* n-$C_{94}H_{190}$ *(orig) at 385.2 K*

Order m	(001) spacing	Intensity	Half-height width[a]
	Å	*cts · rad · min*$^{-1}$	*rad*
1	102.6	101.7	0.0015
2	102.4	29.7	.0016
3	102.6	11.3	.0016
4	102.3	4.3	.0017

[a] Instrumental half-height width, including the effect of sample thickness, is 0.0014 rad at the 1st order and 0.0016 rad at the 4th order.

and the integrated intensities of the first (I_1) and second (I_2) orders, given in the order in which they were obtained.

While the data shown in figures 2 and 3 appear to indicate that this sample of *n*-$C_{94}H_{190}$ is in a single crystalline phase, an examination of the sample in the pinhole-collimated camera established that this was not the case. The apparent single first order maximum could be resolved into two maxima, corresponding to spacings of 100.2 and 105.8 Å, which could arise from the two monoclinic forms reported by Wyckoff et al., 102 and 107 Å [17]. The first form may be obtained from the orthorhomic unit cell by translating each —CH_2— unit, in the adjacent molecule along the *a*-axis, by four —CH_2— units parallel to the *c*-axis [18, 19]. We designate this monoclinic form as M_{201}, where the subscript is the Miller subcell index of the plane formed by the terminal methyl groups. Similarly, the second form may be obtained from the orthorhombic unit cell by translating each —CH_2— unit, in the adjacent molecule along the *b*-axis, by two —CH_2— units parallel to the *c*-axis. We designate this form as M_{011}. It appears then that for this sample of *n*-$C_{94}H_{190}$, we could not resolve the individual monoclinic phases under the conditions of our slit camera. The calculated values of the (001) spacings of several possible monoclinic phases are given in table 3 for each of the three *n*-paraffins under investigation. They are based on literature values for the orthorhombic phase of each material.

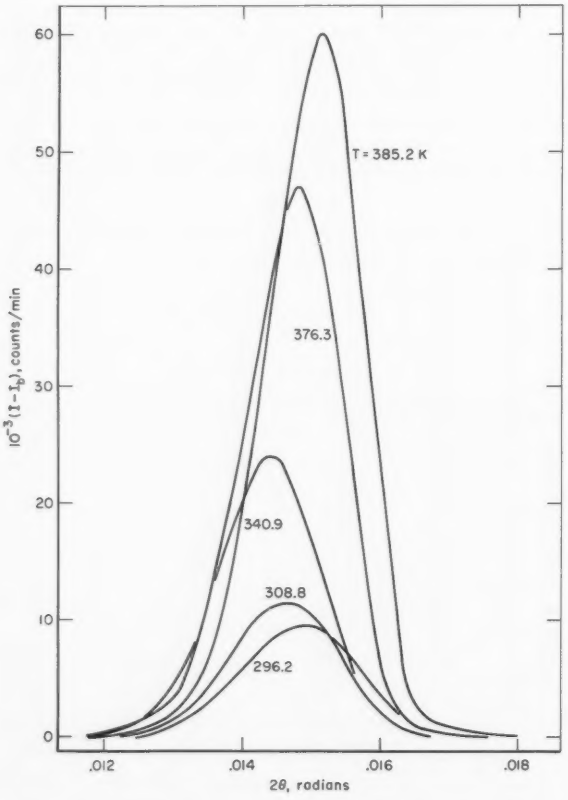

FIGURE 3. *The observed diffraction intensity, after subtraction of the background intensity, from* n-$C_{94}H_{190}$ *(orig) at the temperatures shown as a function of scattering angle.*

The maximum in 2θ corresponds to the (001) spacing.

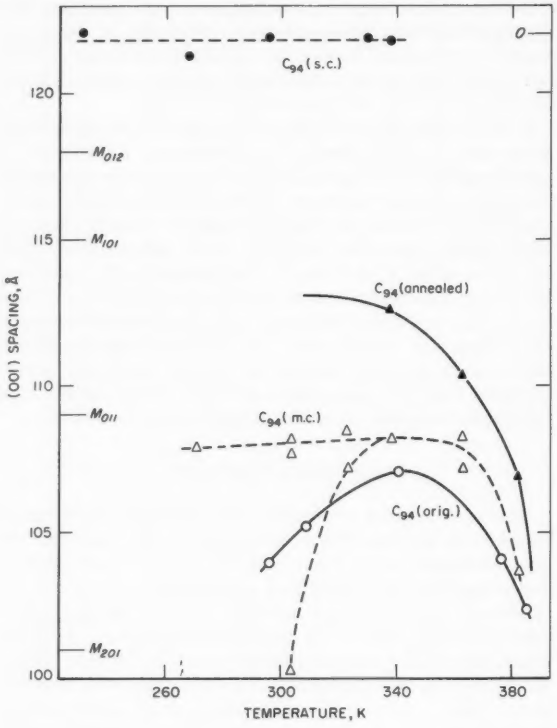

FIGURE 4. *The (001) spacings (obtained from the second order) of four different samples of* n-$C_{94}H_{190}$ *given as a function of temperature.*

Several *d*-values of possible monoclinic phases, M_{hkl}, are marked on the left margin; the value of the orthorhombic phase, 0, is indicated on the right.

TABLE 2. *Integrated intensities and values of (001) spacings for* n-$C_{94}H_{190}$, *listed in the order in which they were observed*

C_{94} (orig)					C_{94} (m.c.)				
T	(001) spacing		I_1	I_2	T	(001) spacing		I_1	I_2
	$m=1$	$m=2$				$m=1$	$m=2$		
K	Å	Å	$\frac{cts \cdot rad}{min}$	$\frac{cts \cdot rad}{min}$	K	Å	Å	$\frac{cts \cdot rad}{min}$	$\frac{cts \cdot rad}{min}$
296.2	104.0	104.0	21	7.5	303.5	101.7	100.3	4.3	1.5
376.3	104.2	104.1	86	28.3	323.3	109.1	107.2	7.3	1.9
308.8	105.4	105.2	23	8.7	338.4	109.8	108.2	10.0	3.2
340.9	107.2	107.1	45	16.5	363.0	109.1	108.3	14.6	4.0
376.3	104.6		80		382.7	104.6	103.7	20.7	5.0
385.2	102.6	102.4	102	29.7	362.9	108.5	107.2	14.8	3.7
					322.8	108.8	108.5	7.3	1.9
					303.4	108.7	108.2	4.7	1.5
C_{94} (s.c.)					303.4	108.1	107.7	5.1	1.5
					271.0	109.0	107.9	4.0	1.1
					241.7	108.6		3.3	
296.0	123.1	121.9	19.8	6.7					
268.2	122.9	121.3	19.0	6.4	C_{94} (annealed)				
231.3	123.1	122.1	18.2	6.0					
296.1	122.7		20.4						
329.7	122.3	121.9	26.5	9.2					
338.0	122.3	121.7	28.9	9.7	381.8	109.6	106.9	1990	494
					362.6	113.0	110.4	1600	485
					337.3	115.8	112.6	1240	404
					308.0	116.0		1060	
					382.9	109.0		2050	
					386.1	107.7		2030	
					386.6	106.0			

TABLE 3. *Calculated* n-*paraffin (001)-spacings in Å (at room temperature)*

Phase	Compound		
	n-$C_{36}H_{74}$	n-$C_{44}H_{90}$	n-$C_{94}H_{190}$
Orthorhombic [a]	47.6 [10]	58.3 [15]	122 [17]
Monoclinic, M_{012}	46.1	56.5	118
M_{101}	45.0	55.2	115
M_{011}	[b] 42.3	[c] 51.9	109
M_{201}	[b] 39.3	48.1	101

[a] The orthorhombic spacings are taken from the literature; the monoclinic values are based on the orthorhombic unit cell with

$a=7.42$ Å, $b=4.95$ Å, and $c_z=2.54$ Å.

[b] Ohlberg [21] has observed spacings of 47.60, 42.22, and 39.08 Å in hexatricontane.
[c] Ranby et al. [15], have observed a spacing of 52.2 Å in their sample of tetratetracontane.

Also in table 2 are reported the results obtained on C_{94} (m.c.). The intensities, listed in the order in which they were obtained, are reversible with temperature. The *d*-spacing of 100.3 Å (second order) shows that the sample was initially in the M_{201} monoclinic phase after rapid cooling from the melt. On heating to 323 K the sample was found to give a second order spacing of 107.2 Å which may indicate a phase transformation to a M_{011} phase. The second order spacings from this sample are plotted in figure 4. Comparison of spacings obtained with pinhole collimation, using film exposure, and with our camera on the same melt crystallized sample of n-$C_{94}H_{190}$ at room temperature show that these second order spacings are not in error from slit smearing by more than 0.6 Å.

The data taken on C_{94} (s.c.) and C_{94} (annealed) are likewise given in table 2. Second order values of the (001) spacing as a function of temperature are shown in figure 4 for these samples. For the orthorhombic C_{94} (s.c.) an irreversible decrease in the background intensity occurred on heating to 324 K; although the sample showed no evidence of a phase change until it was heated above 338 K.

The (00*l*) spacings of C_{94} (annealed) indicated that a conversion from the initial orthorhombic phase had taken place upon heating to 381.8 K. (No separate *d*-spacing characteristic of the orthorhombic phase was found.) Although the sample appeared to contain a mixture of phases, the intensity and value of the *d*-spacing were reversible after cooling, as may be seen by comparison of lines 1 and 5 of the data for this sample in table 2.

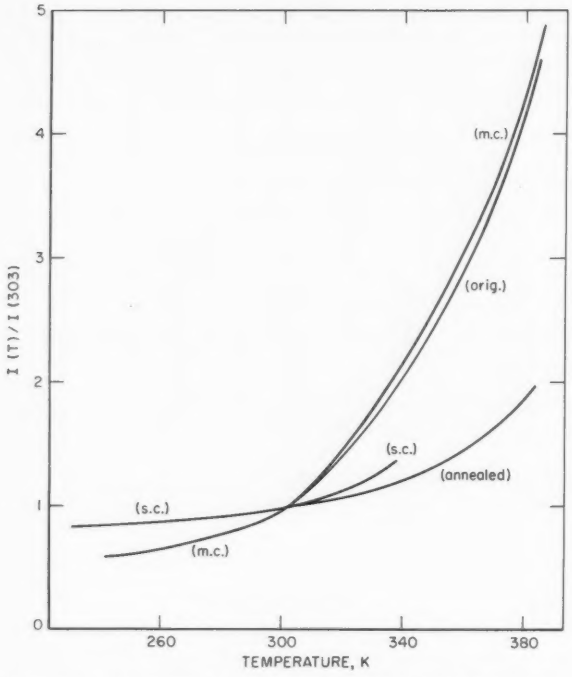

FIGURE 5. *A summary plot of the integrated x-ray diffraction intensity of the (001) maximum at temperature* T *relative to that at 303 K.*

Results on four different samples of n-$C_{94}H_{190}$ are shown.

A summarizing plot of the first order diffraction intensities as a function of temperature from the four n-$C_{94}H_{190}$ samples is given in figure 5, where the intensities are relative to the values at 303 K. The ratios were obtained from smoothed plots of the measured integrated intensities, assumed to be continuous in the temperature range of observation.

3.2. Tetratetracontane

The results of the diffraction scans on n-$C_{44}H_{90}$ are listed in table 4 and three of the as-observed scans are plotted in figure 6. The (001) spacing of the solution crystallized sample, 51.8 Å, is almost identical with that calculated for the M_{011} monoclinic phase (see table 3). When the sample was heated above 333.3 K, the (001) spacing increased abruptly to about 54.5 Å, showing the presence of a solid-solid phase transformation. The change in the d-spacing was also accompanied by a large increase in its integrated intensity. Table 3 suggests that the new phase might be an M_{101} monoclinic. After heating to a maximum temperature of 356.5 K and then cooling to room temperature, the primary d-spacing was 58.0 Å, showing that most of the sample had converted to the orthorhombic phase (d=58.3 Å [15]). However, part of the sample transformed again into its original state on cooling as may be seen from the dashed curve in figure 6.

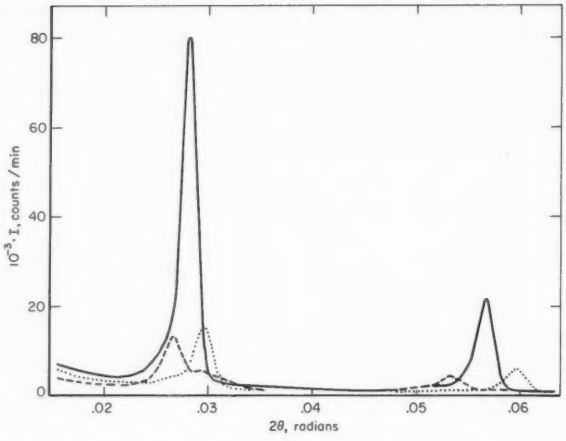

FIGURE 6. *The observed x-ray diffraction intensity from* n-$C_{44}H_{90}$ *at three temperatures as a function of scattering angle.*

The dotted line is with the sample initially at a room temperature of 297.2 K; the solid line with the sample at 356.5 K; and the dashed line again at room temperature, 296.2 K.

TABLE 4. *Integrated intensities and values of (001) spacings for* n-$C_{44}H_{90}$, *listed in the order observed*

T	(001) spacing		I_1	I_2
	$m=1$	$m=2$		
K	*Å*	*Å*	*cts·rad/min*	*cts·rad/min*
297.2	52.2	51.8	39	15.8
313.1	52.1	51.8	40	17.0
333.3	52.2	51.8	43	21.3
352.2	54.8	54.3	128	38.7
356.5	54.9	54.5	173	49.7
347.7	55.0	54.7	145	51.7
333.3	56.1	55.9	96	39.2
296.2	58.2	58.0	46	16.6

3.3. Hexatriacontane

Our n-$C_{36}H_{74}$ samples showed a rather complex diffraction pattern, especially at higher temperatures. Figure 7 is a plot of the diffraction scans from a melt-crystallized specimen of the purified sample taken at 296 and 344 K. The numerous subsidiary peaks to the left of the primary maximum make integration of the intensity of the latter uncertain.[4] For this reason, we report only the peak intensity above the background in table 5. Very similar results were obtained on both the purified sample and on the original melt-crystallized material. Table 5 also gives the peak intensities and (001) spacings of the quenched n-$C_{36}H_{74}$ samples from toluene and sprayed alcohol solution. The changes in d-spacing and peak intensity were found to be reversi-

[4]Prof. E. W. Fischer (University of Mainz) has suggested that the subsidiary peaks result from a small number of large crystals which give nonuniform smearing.

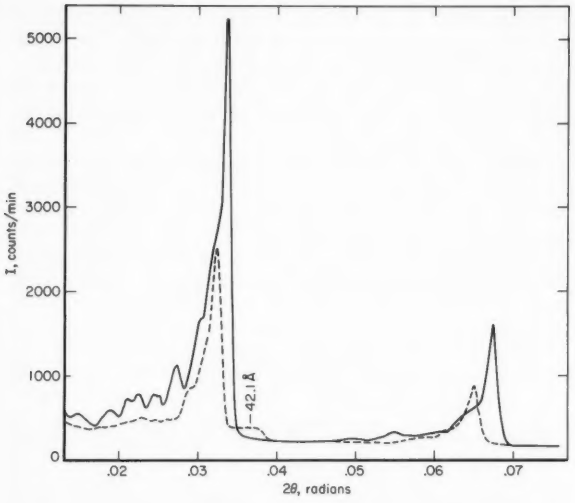

FIGURE 7. *The observed x-ray diffraction intensity from purified* n-$C_{36}H_{74}$ *at 344.2 K (solid line) and at room temperature, 296.4 K, (dashed line) as a function of the scattering angle.*

ble with temperature. Also, the magnitude of the intensity change was found to be similar to the other *n*-$C_{36}H_{74}$ samples.

The change in the orthorhombic *d*-spacing with temperature, given in table 5, is similar to that reported by Barbezat-Debreuil [20]. It would appear to be a result of a partial phase transition to either the M_{011} or M_{101} monoclinic phase (or both), such as has been described by Keller [19].

The melt-crystallized *n*-$C_{36}H_{74}$ at room temperature is in a state very similar to that which *n*-$C_{44}H_{90}$ was in after the latter was heated and then cooled to room temperature. In both cases the principle maximum is from the orthorhombic phase but a small part of the sample is in the M_{011} monoclinic phase, which in the case of *n*-$C_{36}H_{74}$ Ohlberg [21] has shown to be the more stable phase. The simultaneous occurrence of two different phases in a given sample—which has been observed in all three of our *n*-paraffins—indicates some difficulty in the initiation and/or propagation of the more stable phase. Keller [19] has observed the presence of all the different monoclinic phases listed in table 3 as well as several triclinic phases in single crystals of *n*-$C_{36}H_{74}$ which were originally orthorhombic.

Our observations indicate that neither the intensity change with temperature nor the magnitude of the (00*l*) spacing is particularly sensitive to the purity of the *n*-$C_{36}H_{74}$. In contrast to the commonly held point of view [9, 21, 22] that pure *n*-$C_{36}H_{74}$ should crystallize in the monoclinic form, we found that both our purified and impure as-received samples (when crystallized from the melt) were predominantly in the orthorhombic phase. Moreover the impure as-received *n*-$C_{36}H_{74}$ was entirely in the M_{011} monoclinic phase before being melted. For these reasons we do not consider the phase or thermodynamic state of this material to be solely

TABLE 5. *Peak intensities and values of (001) spacings for* n-$C_{36}H_{74}$ *listed in the order observed*

Original (m.c.)				
T	(*001*) spacing		I_1	I_2
	m = 1	*m* = 2		
K	*Å*	*Å*	*cts min*$^{-1}$	*cts min*$^{-1}$
297.2	48.1		2170	
342.2	47.0	46.7	5740	1610
329.9	47.9	47.3	5360	1680
297.2	48.1	47.8	2500	900
Purified (m.c.)				
297.2	48.0		1540	
344.2	45.9	45.8	4580	1370
322.5	47.0	47.0	3160	1050
296.4	47.6	47.4	2220	680
From Toluene				
297.2	48.0	47.5	579	148
335.7	47.2	47.1	834	196
345.3	45.9	45.6	1421	226
From sprayed ethanol				
297.2	48.1	47.7	237	76
345.4	46.3	46.2	570	138

controlled by the chemical purity of the sample and suggest that the crystallization conditions and history of the sample are important factors in determining the phase observed at room temperature.

4. Discussion

It is clear from the data shown in figures 4, 6, and 7 that most of our *n*-paraffin systems are mixtures of the various crystalline phases. However, the generally observed increase in the intensity of the long-spacing with increasing temperature also occurred in the pure orthorhombic phase of *n*-$C_{94}H_{190}$ prepared from dilute solution. This leads us to consider several possible mechanisms through which the intensity could increase in a single crystalline phase. The mixed phases will be discussed subsequently.

4.1. Integrated Intensities and Thermal Vibrations

For a crystalline system composed of units having a scattering factor $F(\theta_B, T)$ the integrated intensity $I(\theta_B, T)$ for a diffraction maximum from a powder is given by [6]

$$I(\theta_B, T) = \text{const.}\,|F(\theta_B, T)|^2 p \frac{1+\cos^2 2\theta_B}{\sin^2\theta_B \cos\,\theta_B}, \qquad (1)$$

where 2θ is the scattering angle, T the Kelvin temperature and p the multiplicity of the Bragg reflection at θ_B. For the low-angle maxima in our samples p is constant. Suppose there are a total of L CH_2 units in a platelet. Then the scattering factor, $F(\theta, T)$ for this platelet is approximately:

$$F(\theta, T) = \sum_{j=0}^{L-1} f_{CH_2} e^{i\mathbf{k}\cdot\mathbf{r}_j(T)}, \tag{2}$$

where [5] f_{CH_2} is the scattering factor for a CH_2 unit and we consider $f_{CH_3} \cong f_{CH_2}$.

a. Debye-Waller Factor

In the case where the oscillations of the CH_2 groups in a paraffin chain are independent and each oscillator possesses the same mean energy, then one has:

$$|F(\theta, T)|^2 = e^{-2(MT)} |F_0(\theta, T)|^2. \tag{3}$$

The Debye-Waller factor is $e^{-2M(T)}$ and $F_0(\theta, T)$ is the scattering factor for the platelet without vibrations. The quantity $M(T)$ in the Debye-Waller factor [6] is given by:

$$M(T) = 8\pi^2 \overline{u^2(T)} \left(\frac{\sin\theta}{\lambda}\right)^2. \tag{4}$$

The mean-square displacement of a CH_2 unit along $\mathbf{s}$ is $\overline{u^2(T)}$. The term $\overline{u^2(T)}$ increases approximately linearly with temperature [6, 23] so that one would expect the intensity of the maxima to decrease with increasing temperature.

One can estimate an upper bound on $\overline{u^2(T)}$ and thereby $M(T)$ as follows: Since the bonding is stronger along the paraffin chain than it is perpendicular to it, $\overline{u_\parallel^2} < \overline{u_\perp^2}$ (where $\overline{u_\parallel^2}$ is along and $\overline{u_\perp^2}$ is perpendicular to the chain). Bunn [8] has found that $8\pi^2\overline{u_\perp^2}$ is about 5 Å^2 at room temperature for the wide angle diffraction from crystalline polyethylene. The factor $\left(\frac{\sin\theta}{\lambda}\right)^2$ for the low-angle maxima is about 10^{-4} Å^{-2} for n-$C_{36}H_{74}$ and about 10^{-5} Å^{-2} for n-$C_{94}H_{190}$ at the first order. Then $M(295\text{ K})$ is about 5×10^{-4} Å^{-2} and $M(385\text{ K})$ about 7×10^{-4} Å^{-2} at most, so that $e^{-2M(T)}$ is 1.000 within 0.1 percent over our temperature range of interest.

b. Thermal Diffuse Scattering

While independent vibrations of the —CH_2— units are considered in the Debye-Waller factor, correlated vibrations such as occur in long wavelength phonons in these solids are accounted for in the thermal diffuse scattering. For discussion on this topic, the reader is referred to Warren [24] and to James [6].

Shinomura et al. [5], have attributed the origin of the low-angle maxima in several polymers to such correlated vibrations or elastic waves, with a wavelength of twice the lamellar repeat distance. The multiple peaks in the intensities were attributed to harmonics of these waves.

While the intensity of the thermal diffuse scattering increases with increasing temperature (approximately linearly for kT much larger than the energy of the phonons), these maxima are usually broader and weaker than the Bragg maxima [6]. The first order thermal diffuse scattering has maxima at angles such that

$$\frac{2\sin\theta}{\lambda} = \frac{m}{d_{001}} \pm \frac{1}{\Lambda}, \tag{5}$$

where m is the order of the (001) maxima and Λ is the wavelength of the phonon. For a broad distribution of phonon wavelengths one expects—based on eq (5)—that the intensity due to these vibrations is scattered over a wider angular range than the Bragg maximum. We expect that much of this diffuse scattering is subtracted in our background corrections.

We note that for many solids the contribution of thermal vibrations to the integrated intensity over the Bragg maxima is adequately accounted for by the Debye-Waller factor, i.e., by independent oscillations of the scattering units. This implies that the contribution of longer wavelength phonons is not a dominant component of the integrated intensity over a maximum. The vibrations that affect the thermal diffuse scattering for a given Bragg diffraction maximum have a component of their displacements along $\mathbf{s}$ for that maximum. For the low-angle maxima, some of the relevant vibrations have been studied by Schaufele and Shimanouchi [25] in their examination of the Raman spectra of n-$C_{36}H_{74}$, n-$C_{44}H_{90}$, and n-$C_{94}H_{190}$. Based on the vibrational frequencies they reported, we note that a very substantial fraction of the molecules in these systems are already excited at room temperature so that we expect no abnormally large contribution from these vibrations to the integrated intensity. It is of course difficult to estimate quantitatively the contribution of all the allowed vibrations to the intensities.

4.2. Single Crystal Versus the Mosaic Crystal

As discussed in considerable detail by James [6] and by Warren [24], the integrated intensities for diffraction maxima of nearly perfect crystals can be substantially smaller than is the case for the ideally imperfect or mosaic crystalline system. The essential idea is that rescattering processes in the more perfect crystalline system lead to wave cancellation, so that the intensities are no longer simply proportional to the volume of the irradiated sample. In the mosaic system this rescattering is interrupted by imperfections so that the process of wave cancellation is reduced. The question arises as to whether the systems we have studied were sufficiently imperfect or mosaic to begin

[5] $k = \frac{2\pi}{\lambda}$; $\mathbf{s} = \hat{\mathbf{s}}_i - \hat{\mathbf{s}}_o$, $|\mathbf{s}| = 2\sin\theta$ where $\hat{\mathbf{s}}_i$ is the unit vector of the scattered wave, $\hat{\mathbf{s}}_o$ the unit vector for the incident wave; $\mathbf{r}_j^l$ is the vector distance from an origin to the jth CH_2 unit in the platelet.

with or whether temperature induced defects changed the degree of perfection.

It was observed that in the solution-grown sample of n-$C_{94}H_{190}$, most of the growth spirals were no thicker than 20 layers. Yet this sample still displayed an intensity change with temperature, which fact argues against any extinction effects in that sample. A calculation of the relative intensity of the first and second orders of the (001) spacing for an unoriented sample under our camera conditions gives an I_2/I_1 of 0.35, which is the same as that observed for our melt-crystallized n-$C_{94}H_{190}$. Since primary extinction reduces the intensity of the first order maximum to a greater extent than the second order, we conclude that this sample did not show extinction effects. Similarly, the data shown in table 5 for n-$C_{36}H_{74}$ quenched in toluene and sprayed from ethanol also shows an intensity increase with temperature. However, such drastic treatments should surely produce very imperfect crystals having no extinction. Based on these observations, we believe that the intensity changes we have observed are not dominated by extinction effects.

4.3. The (00l) Structure Factor

Suppose there are N paraffin molecules in a platelet, which we have chosen as the unit of structure. Since the factor [6] $e^{i\mathbf{ks}\cdot\mathbf{r}(T)}$ in eq (2) only involves the projection of $\mathbf{r}_j$ onto $\mathbf{s}$, for the (00l) maxima, one may sum eq (2) over molecules, so that one has (in the plane wave approximation),[7]

$$F(\theta, T) = N \sum_{j=0}^{n} f_{CH_2} e^{i\mathbf{ks}\cdot\mathbf{r}_j(T)}, \tag{6}$$

where $n+1 = L/N$ is the number of units in one molecule.

One may define a molecular scattering factor $F'(\theta, T)$ by the relationship $F(\theta, T) = NF'(\theta, T)$. From eq (6), for the orthorhombic crystalline phase, one has for $F'(\theta, T)$:

$$F'(\theta, T) = f_{CH_2} e^{ik(\sin\theta)nx_0} \frac{\sin[k(\sin\theta)(n+1)x_0]}{\sin[k(\sin\theta)x_0]} \tag{7}$$

where x_0 is the projection of a CH_2 repeat distance onto $\mathbf{s}$ (1.27 Å). The magnitude of this (00l) scattering factor agrees with the scattering factor of Müller for orthorhombic n-$C_{29}H_{60}$ [11] and of Teare for orthorhombic n-$C_{36}H_{74}$ [10]. From eq (6), $F'(\theta, T)$ becomes for the monoclinic forms of the n-paraffins in the angular range of our interest,

$$F'(\theta, T) \cong (2f_{CH_2}) e^{ik(\sin\theta)nx_M} \frac{\sin[k(\sin\theta)(n+1)x_M]}{\sin[k(\sin\theta)2x_M]} \tag{8}$$

where $2x_M$ is the projection of a C_2H_4 repeat distance onto $\mathbf{s}$. The magnitude of $F'(\theta)$ given in eq (8) agrees with the scattering factors observed by Shearer and Vand [9] for monoclinic n-$C_{36}H_{74}$.

If we define an interlamellar distance $A(T)$ as $d(T) = (n+1)x + A(T)$ and limit eqs (7) and (8) to the Bragg maxima ($m\lambda = 2d \sin\theta_B$), we have:

$$|F'(\theta_B, T)| \cong f_{CH_2} \frac{\sin[\pi m A_0/d_0]}{\sin[\pi m x_0/d_0]} \cong f_{CH_2} \frac{A_0}{x_0} \tag{7a}$$

for the orthorhombic phase, and,

$$|F'(\theta_B, T)| \cong (2f_{CH_2}) \frac{\sin[\pi m A_M/d_M]}{\sin[\pi m 2x_M/d_M]} \cong f_{CH_2} \frac{A_M}{x_M} \tag{8a}$$

for the monoclinic phase (when $d \gg x$).

One notices that for either crystalline phase, the wave from a single molecule is mostly cancelled and depends primarily on the interlamellar distance A. From eq (1), one has

$$\frac{I(\theta_B, T_2)}{I(\theta_B, T_1)} = \left[\frac{F'(\theta_B, T_2)}{F'(\theta_B, T_1)}\right]^2 \cong \left[\frac{A(T_2)}{A(T_1)}\right]^2. \tag{9}$$

Here we assume the change in A with temperature is much larger than the change in x, since the carbon atoms are covalently bonded along the chain.

a. Interlamellar Expansion

The question arises as to whether a simple interlamellar expansion with temperature could explain the intensity effects we have observed. The magnitude of this effect on $I(\theta_B, T)$ may be estimated as follows: If one assumes that the interlamellar distance expands approximately as the a-dimension of the subcell (of the a, b and c subcell dimensions, the a expands most), then over a 100 K temperature range (e. g., 240 to 340 K), the expansion is about 0.20 Å [26]. Since the excess distance between terminal methyl groups—the interlamellar distance—is 1.98 Å for the orthorhombic n-paraffins and 2.93 Å for the M_{011} monoclinic phases [27], then from eq (9), one estimates that the intensity increase due solely to interlamellar thermal expansion is no more than 21 percent over this temperature range. The observed intensity increase over the range $231 \leq T \leq 338$ K, shown in table 2, for the orthorhombic phase of n-$C_{94}H_{190}$ is 59 percent. Thus, it appears that the intensity change with temperature does not result solely from a simple interlamellar expansion.

Let us now consider additional mechanisms by which the structure factor and thereby $A(T)$ can change with temperature. One point of view for polyethylene is considered briefly below. As far as the n-paraffins are concerned, two processes are suggested. The first, considered in section (4.3b) below, is that of chain defects or kinks, which lead to vacancy formation on the surface of the platelet and thereby essentially an

[6] We replace the distance vector $\mathbf{r}_j'(T)$ with $\mathbf{r}_j(T)$ for the nonvibrating repeat unit, since the Debye-Waller factor is negligible at low angles.

[7] In the Fresnel or spherical wave treatment [6], $F(\theta, T) = \frac{\text{const.}}{\sin\theta} N \sum_{j=0}^{n} f_{CH_2} e^{i\mathbf{ks}\cdot\mathbf{r}_j(T)}$.

increase in A. The second, discussed in section (4.3c), is that of a tilting of the molecule via a phase transformation, which also can lead to an increase in A from poorer packing of the methyl groups or possibly from void formation at the lamellar surface.

The essential idea put forward by Fischer et al. [3], and by Schultz et al. [28], to explain the temperature dependence of the intensity of the low-angle maxima in polyethylene (see fig. 8), is that the lamellar surface is disordered or amorphous and that the size of this disordered region increases reversibly with increasing temperature because of a gain in entropy. According to their discussion, if the electron density difference between the amorphous and crystalline regions changes little with temperature, then the low-angle diffraction intensity will increase as the size of the interlamellar region increases. However, we do not consider an amorphous lamellar surface, such as described by Fischer et al. and Schultz et al., appropriate for the n-paraffins since these systems are known to be polymorphic. For example, Templin [29] reported three crystalline phases for n-$C_{36}H_{74}$ (observed dilatometrically) above 333 K. Rånby et al. [15] found two phases in n-$C_{44}H_{90}$. Similarly, Khoury [18] has observed three forms of n-$C_{94}H_{190}$ (one orthorhombic and two monoclinic). The differences among the various monoclinic phases and the orthorhombic phase for the long-chain n-paraffins is only in the end-group packing—these systems all have essentially the same orthorhombic subcell (see also table 2). Now, if the surfaces of these n-paraffin lamellae were disordered, crystalline phases which are different only in end-group packing would not exist, which is contrary to experimental observation. Thus we are led to consider models other than an amorphous lamellar surface to explain the intensity changes.

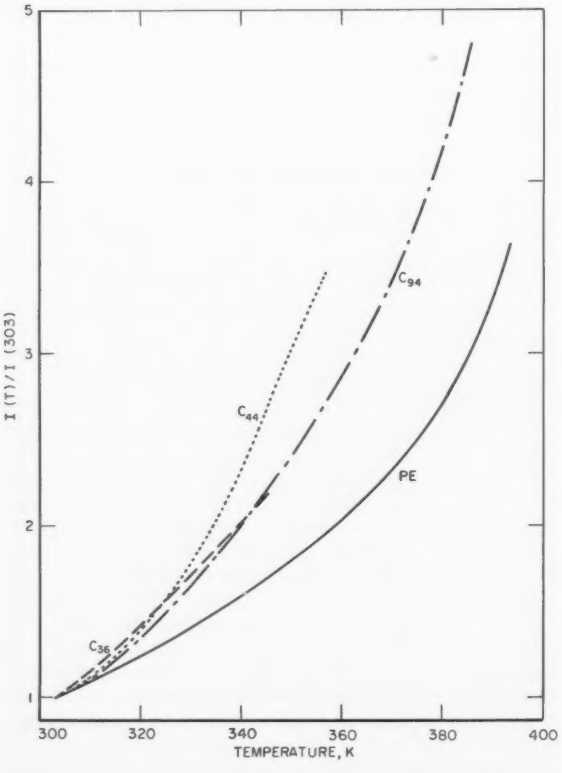

FIGURE 8. *A comparison of the relative x-ray diffraction intensity from the (001) maximum for three of our samples with data from the literature on linear polyethylene.*

Dashed line, n-$C_{36}H_{74}$ (purified); dotted line, n-$C_{44}H_{90}$ cooled from 356.5 K to room temperature; alternate dash and dot, n-$C_{94}H_{190}$ (orig); and solid line, data of Fischer et al., on polyethylene [3].

b. Chain Defects

Due to the almost total cancellation of the wave scattered from a long-chain n-paraffin molecule for the $(00l)$ maxima and the sensitivity of the intensity to the interlamellar distance, there is a mechanism by which certain types of chain defects can increase the intensity of these maxima.

The class of defects we are concerned with have been described by Reneker [30] and more recently by Pechold and Blasenbrey [31]. Keith and Passaglia [32] have considered similar chain defects in the form of dislocations and glide in paraffin crystals (see also Predecki and Statton [33]). These defects can essentially be considered—in the case of the $(00l)$ low-angle maxima—as the formation of a point vacancy at the surface of the platelet and the superposition of a unit along the chain (fig. 9). Insofar as the lamellae do not collapse into the surface voids, the point vacancies lead to an increase in the effective interlamellar distance.

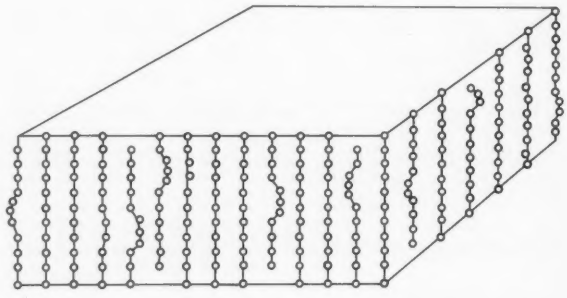

FIGURE 9. *Schematic diagram of a paraffin lamella with defects leading to surface vacancies.*

In order to estimate the fraction $\beta(T)$ of defect chains in a platelet, we write the structure factor $F(\theta, T)$ so as to include these chains. We assume the kink formation creates a surface vacancy the size of one $-CH_2-$ unit and that there is only one kink per defect chain. For the moment allowing each kink to be in the qth position, then from eq (6) one has:

$$F(\theta, T) \cong N_1(T) \sum_{j_1=0}^{n} f_{CH_2}\, e^{i\mathbf{k}_s \cdot \mathbf{r}_{j_1}}$$

$$+N_2(T)\left[\sum_{j_2=1}^{n} f_{CH_2}\, e^{i\mathbf{k}\cdot\mathbf{r}_{j_2}}+f_{CH_2}\, e^{i\mathbf{k}\cdot\mathbf{r}_q}\right]$$

$$+N_3(T)\left[\sum_{j_3=0}^{n-1} f_{CH_2}\, e^{i\mathbf{k}\cdot\mathbf{r}_{j_3}}+f_{CH_2}\, e^{i\mathbf{k}\cdot\mathbf{r}_q}\right], \qquad (10)$$

where there are N_1 nondefect chains, and (N_2+N_3) defect-containing chains. We allow for the vacancy at either the top or bottom of the platelet.

If we assume each platelet in a stack has the same number of molecules and the defect chains are in thermal equilibrium with the nondefect chains, then each platelet has the same number of defect chains. Since the distance vectors $\mathbf{r}_j$ from the origin to the $-CH_2-$ units of each chain (with or without a kink defect) are projected onto $\mathbf{s}$ and since we are only concerned with $(00l)$ maxima, then there is no effect on $F(\theta, T)$ of the location of a defect chain in a platelet. For this reason the scattering factor of every platelet in a stack is identical and only depends on the concentration of the defect chains.

Summing eq (10), one has:

$$F(\theta, T, q) \cong N_1(T) f_{CH_2} e^{ik(\sin\theta)nx}\, \frac{\sin[k(\sin\theta)(n+1)x]}{\sin[k(\sin\theta)x]}$$

$$+2N_2(T) f_{CH_2}\left[e^{ik(\sin\theta)nx}\, \frac{\sin\,[k(\sin\theta)nx]}{\sin\,[k(\sin\theta)x]}\right.$$

$$\left.+\, e^{ik(2\sin\theta)qx}\right] \qquad (11)$$

for the case $N_2=N_3$.[8] We note that $|F(\theta, T, q)|^2$ depends on q and is greatest when the superimposed group is at the center of a chain and least when near a methyl end-group.

If instead of allowing every superimposed CH_2 unit to be at position q in the defect chain, we allow the kink to be located anywhere along a chain with equal probability, then the second expression in eq (11) becomes a sum over the positions q. One can then write eq (11) as:

$$F(\theta, T) \cong N_1 f_{CH_2} e^{ik(\sin\theta)nx}\, \frac{\sin\,[k(\sin\theta)(n+1)x]}{\sin\,[k(\sin\theta)x]}$$

$$+2N_2 f_{CH_2} e^{ik(\sin\theta)nx}\, \frac{\sin\,[k(\sin\theta)nx]}{\sin\,[k(\sin\theta)x]}\left[1+\frac{1}{n}\right] \qquad (12)$$

Defining $\beta(T)$ as $2N_2=\beta(T)N$ where $(N_1+2N_2)=N$, then for orthorhombic n-$C_{94}H_{190}$ one has at the first order Bragg maximum:

$$F(\theta_B, T) \cong \frac{N f_{CH_2}}{x}\,[e^{i(A+x)/d}][(1-\beta)A+\beta(A+x)] \qquad (13)$$

so that the intensity becomes (c.f. eq (1))

$$I(\theta_B, T) \cong \text{const.}\ \frac{N^2 f_{CH_2}^2}{x^2}\,(A+\beta x)^2 p\,\frac{1+\cos^2 2\theta_B}{\sin^2\theta_B\cos\theta_B} \qquad (14)$$

If the defect-containing chains are in a Boltzmann equilibrium with the nondefect chains, then for a change in integrated intensity of 38 percent—which is the excess over the contribution due to thermal expansion estimated earlier—one arrives at an energy of 4100 cal/mol defects. Reneker has estimated this energy as 4600 cal/mol defects [30] from steric considerations. We conclude that for the solution-crystallized orthorhombic n-$C_{94}H_{190}$ the intensity change with temperature is consistent with thermal expansion of the interlamellar region and a thermal generation of vacancies, e.g., via kink formation.

We note that the maximum increase in $I(\theta_B, T)$ of eq (14) is a factor of 2.6, assuming the size of a vacancy is 1.27 Å. Also the intensity change is enhanced if most of the kinks occur at the same position in the molecules rather than at random along the chain. This would involve an interaction or cooperative effect with these defects, as for example would occur in a glide plane. However, the larger intensity changes found for C_{94} (orig.) and C_{94} (m.c.) suggest that possibly additional mechanisms are operating. One such possibility is considered below.

c. Mixtures of Phases

In view of the fact that all of the systems we have studied are polymorphic and that in the temperature range of our observations the systems must be experiencing solid-solid transitions, which can be quite slow as has been observed by Ohlberg [21], it seems likely that some of our observed intensity change is associated with these transitions.

The end-group packing and thereby the interlamellar distance is different for the various crystalline phases [27], which fact leads one to expect that the intensity of the $(00l)$ maxima should change when a system undergoes a transition. Moreover, if the transition were not complete or abrupt, so that platelets of one phase were in contact with those of a different phase, the intensity change could be enhanced due to further complications in end-group packing. For example, the (00l) planes in M_{011} and M_{201} monoclinic phases have different subcell areas, which would lead to a mismatch of the terminal CH_3-groups when these platelets are adjacent in a stack. This is so even with good packing of the lamellae. In addition to these effects, there is the possibility of void formation at the surface of the lamellae when changes of 2 to 20 Å occur in the long-spacings due to a solid-solid transition. It seems the system might experience collapse difficulties which could give rise to a substantially larger interlamellar distance than occurs in the situation with good end-group packing. An assessment of the magnitude of these effects would indeed be difficult. However, since the intensity of the low-angle maxima is so sensitive to this interlamellar dis-

[8] We have taken $\cos\,[k(\sin\theta)x] \cong 1$ in our range of 2θ.

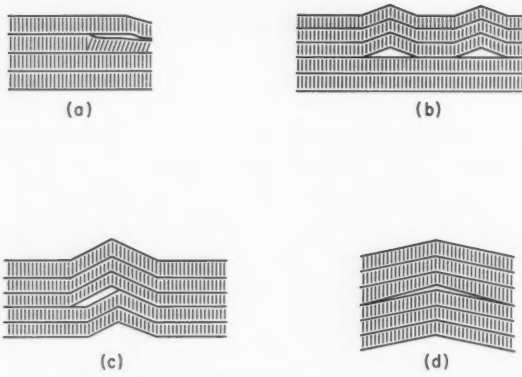

FIGURE 10. *Schematic diagrams of transitions in stacks of n-paraffin lamellae with incomplete collapse leading to surface vacancies.*

tance, it is plausible that these processes are contributing to the intensity changes observed with temperature in those samples where phase transitions are occurring.

We indicate schematically in figure 10 surface vacancies which might arise from solid-solid phase transitions. In figures 10a, b, and c are shown vacancies which could occur during the transition from the orthorhombic to the monoclinic phase. In figure 10d is shown the situation after the transition when the subsequent collapse is incomplete or for imperfect packing of end groups. This does raise the question of the reversibility of the intensity change with temperature, since one might expect the vacancies arising from the transitions to occur irreversibly. For example, Keller [19] and Baltá Calleja [34] have observed irreversible morphological changes on the surfaces of *n*-paraffin lamellae after heating. But, the fact that the low-angle diffraction intensities change so substantially in the regions where these systems undergo solid-solid transitions suggests that they are interrelated.

5. Conclusions and Summary

We have seen that the intensity of the low-angle x-ray diffraction maxima increases reversibly with increasing temperature for the *n*-paraffins which we examined. The magnitude of this intensity change was found to depend on the structure arising from the sample preparation (e.g., melt-crystallized versus solution-crystallized) in the case of n-$C_{94}H_{190}$, but was rather insensitive to physical state or purity in n-$C_{36}H_{74}$. All the samples experienced solid-solid phase transitions at temperatures below their melting points. From the observed (00l) spacings, the transitions did not appear sharp, as might be expected for a first-order transition. However, part of the gradual change in d_{00l} may have resulted from the slow elimination of microvoids which were generated during the transition. Since the structure factor of these long-chain molecules is very sensitive to the interlamellar distance, we were led to consider temperature-dependent mechanisms which change this distance. These include: (a) thermal expansion of the interlamellar distance; (b) defects which involve a contraction of the chains and give rise to surface vacancies, such as Reneker defects or glide planes; and (c) phase transitions leading to poorer packing of methyl groups in adjacent lamellae or void formation. The observations for orthorhombic n-$C_{94}H_{190}$ are consistent with processes (a) and (b). We suggest that the intensity changes for the remaining samples can be accounted for by all three processes.

The authors express their gratitude for numerous helpful discussions with their coworkers and in particular to John Hoffman for support and encouragement.

6. References

[1] Geil, P. H., Polymer Single Crystals (John Wiley and Sons, N.Y., 1963).
[2] Statton, W. O., J. Polymer Sci. **28,** 423 (1958).
[3] Nukushina, Y., Itoh, Y., and Fischer, E. W., Polymer Letters **3,** 383 (1965).
[4] O'Leary, K., and Geil, P., J. Macro. Sci. **1B,** 147 (1967).
[5] Shinomura, M., Chiba, A., and Furuichi, J., Reports Prog. Polymer Physics Japan **9,** 187 (1966).
[6] James, R. W., Optical Principles of the Diffraction of X-Rays, (Cornell Univ. Press, Ithaca, N.Y., 1965).
[7] Waller, I., and James, R. W., Proc. Roy Soc. Lond. **A117,** 214 (1927). Batterman, B. W., Phys. Rev. **126,** 1461 (1962). Flinn, P. A., and McManus, G. M., Phys. Rev. **132,** 2458 (1963). Sparks, C. J., Jr., and Borie, B. S., Adv. in X-Ray Analysis **6,** 177 (1963).
[8] Bunn, C. W., Trans. Faraday Soc. **35,** 482 (1939).
[9] Shearer, H. M. M., and Vand, V., Acta Cryst. **9,** 379 (1956).
[10] Teare, P. W., Acta Cryst. **12,** 294 (1959).
[11] Müller, A., Proc. Roy. Soc. **120,** 437 (1928).
[12] Khoury, F., J. Appl. Phys. **34,** 73 (1963).
[13] Reinhard, R. R., Ph. D. Thesis, The Penn. State Univ. (1961).
[14] Bridgman, P., Proc. Am. Acad. Arts Sci. **60,** 305 (1925). Horton, A. T., and Glasgow, A. R., Nat Bur. Stand. (U.S.) **69C** (Eng. and Instr.) No. 3, 195–198 (July–Aug. 1965).
[15] Rånby, B. G., Morehead, F. F., and Walter, N. M., J. Poly. Sci. **44,** 349 (1960).
[16] Clark, S. G., M. S. Thesis, The Penn. State Univ. (1956).
[17] Wyckoff, H. W., Khoury, F., and Hyndman, D., Bull. Am. Phys. Soc. **7,** 206 (1962).
[18] Khoury, F., Am. Chem. Soc. Polymer Preprints **3,** 104 (1962).
[19] Keller, A., Phil. Mag. **6,** 329 (1961).
[20] Barbezat-Debreuil, S., Comptes Rendus **246,** 2907 (1958).
[21] Ohlberg, S. M., J. Phys. Chem. **63,** 248 (1959).
[22] Piper, S. H., and Malkin, T., Nature **126,** 278 (1930).
[23] Becka, L. N., and Cruickshank, D. W. J., Proc. Roy. Soc. **A273,** 455 (1963).
[24] Warren, B. E., X-Ray Diffraction (Addison-Wesley Pub. Co., Reading, Mass., 1969).
[25] Schaufele, R. F., and Shimanouchi, T., J. Chem. Phys. **47,** 3605 (1967).
[26] Cole, E. A., and Holmes, D. R., J. Polymer Sci. **46,** 245 (1960). Swan, P. R., J. Polymer Sci. **56,** 403 (1962).
[27] Broadhurst, M. G., Nat. Bur. Stand. (U.S.), **66A** (Phys. and Chem.) No. 3, 241–249 (May–June 1969).
[28] Schultz, J. M., Robinson, W. H., and Pound, G. M., J. Polymer Sci. **A5,** 511 (1967).
[29] Templin, P. R., Ind. Eng. Chem. **48,** 154 (1956).
[30] Reneker, D. H., J. Poly. Sci. **59,** 539 (1962).
[31] Pechhold, W., and Blasenbrey, S., Kolloid Zeitschrift **216** 235 (1967).
[32] Keith, H. D., and Passaglia, E., Nat. Bur. Stand. (U.S.), 68A (Phys. and Chem.) No. 5, 513–518 (Sept.–Oct. 1964).
[33] Predecki, P., and Statton, W. O., J. Appl. Phys. **37,** 4053 (1966).
[34] Baltá Calleja, F. J., Rev. Real Acad. Cienc. Exact. Fis. Nat. Marid **59,** 71 (1965).

(Paper 74A2–591)

JOURNAL OF RESEARCH of the National Bureau of Standards—A. Physics and Chemistry
Vol. 74A, No. 2, March–April 1970

Photoelastic Constants of Ruby*

R. M. Waxler and E. N. Farabaugh

Institute for Materials Research, National Bureau of Standards, Washington, D.C. 20234

(October 21, 1969)

The eight piezo-optic and eight elasto-optic constants of synthetic, single crystal ruby have been determined using the cadmium red radiation of 643.8 nanometers (nm). All the constants are found to be negative in value, or to have very small positive values. The data indicate that changes in the polarizability of the oxygen ion and changes in the local field are primarily responsible for the observed changes in refractive index. Hydrostatic pressure has been used for the first time as part of a complete photoelastic investigation, and a new, screw-clamp device for easily attaining high, uniaxial stress is described.

Key words: Birefringence; crystals, lasers; photoelasticity; ruby.

1. Introduction

Thermo-optic and piezo-optic data on ruby are of interest in laser technology because of the large temperature and stress gradients created in a laser solid. The induced changes in refractive index play a large part in the distortion of the wavefront of the light generated [1].[1] Houston et. al., have reported on the change in refractive index of ruby from −180 to 70 °C [2]. Mandarino [3] has reported on the birefringence introduced into a ruby crystal by loading along the c axis, and there are some data in the literature on the photoelastic constants of sapphire [4, 5, 6, 7]. In view of the widespread use of ruby as a laser material, it was felt that a complete investigation of its photoelastic properties was appropriate.

2. Theoretical Considerations

Ruby belongs to the $\bar{3}$m point group of the trigonal system, and a sterographic projection showing the symmetry elements of this point group is presented in figure 1. In the figure, the open triangle represents the $\bar{3}$ axis, the diad symbols represent 2-fold axes, and the heavy lines indicate mirror planes. The right-handed coordinate system $x_1x_2x_3$ used to specify the photoelastic constants [8, 9] together with the corresponding hexagonal Miller-Bravais indices are also shown. Measurements made on ruby at 643.8 nm show that the refractive index of the ordinary ray, $n_\omega = 1.76569$, and the refractive index of the extraordinary ray, $n_\epsilon = 1.75759$ [10]. The refractive index ellipsoid is, therefore, an ellipsoid of revolution where the axis of infinite rotation coincides with the unique, x_3 axis of the crystal. According to Neumann's principle, the point group symmetry of the index ellipsoid, ∞/mm, must include the $\bar{3}$m symmetry of the ruby [8].

Curie's principle states that the symmetry elements common to the point group of the unstressed crystal and to the point group of the stress give the point group of the stressed crystal [8, 11, 12]. Applied hydrostatic pressure has spherical symmetry, ∞ ∞ m, and a uniaxial stress has the symmetry ∞/mm. Therefore, the symmetry elements of the index ellipsoid of ruby will not be altered if hydrostatic pressure is applied, or if a uniaxial stress is applied along the unique, x_3 axis shown in figure 1. If a uniaxial stress is applied along x_1 shown in figure 1, the 2-fold axis of rotation along the line of stress is the only symmetry element which will be retained. The refractive index ellipsoid will become triaxial; one principal radius will be pinned along the 2-fold axis, and the other two principal radii will be free to rotate in the x_2x_3 plane. If a uniaxial stress is imposed along x_2, again the 2-fold rotation axis along x_1 is the only symmetry element that is retained, and one principal direction of the ellipsoid is fixed in this direction. The other two principal radii are free to rotate in the mirror plane, as before, but now they will rotate in the opposite sense. In general, when a uniaxial stress is applied along any line lying in the x_2x_3 plane, one principal radius of the index ellipsoid will coincide with x_1, and the other two radii will lie in the x_2x_3 plane.

Ruby has eight piezo-optic constants, q_{11}, q_{12}, q_{13}, q_{14}, q_{31}, q_{33}, q_{41}, q_{44}, and eight elasto-optic constants, p_{11}, p_{12}, p_{13}, p_{14}, p_{31}, p_{33}, p_{41}, p_{44}. According to Pockels theory, when a stress, P_j is applied, the induced changes in the relative dielectric impermeability, $\mathbf{B}$ ($\mathbf{B} \equiv \mathbf{n}^{-2}$) is $\Delta B_i = q_{ij}P_j$ $i, j = 1$ to 6. Similar

*Research partially supported by the Advanced Research Projects Agency of the Department of Defense.

[1] Figures in brackets indicate the literature references at the end of this paper.

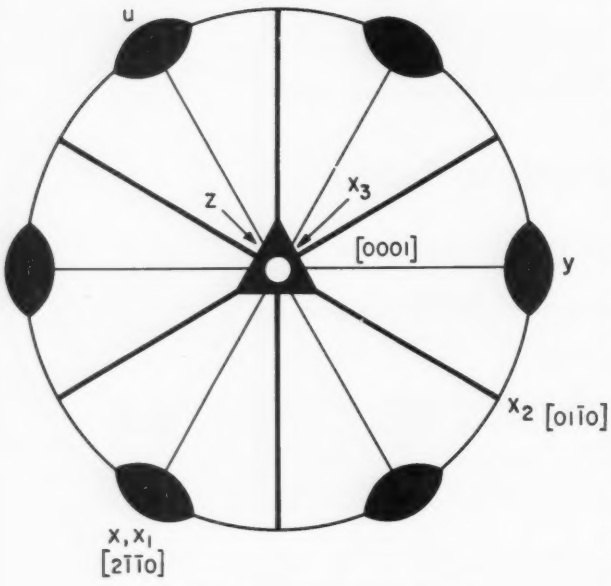

FIGURE 1. *Stereogram of point group 3m.*

$x_1x_2x_3$ represent the principal vibration directions of the refractive index ellipsoid. xyuz is the Miller-Bravais coordinate system.

relations hold between ΔB_i, p_{ij} and the strain components. The two sets of constants are related by

$$p_{ij} = \sum_{k=1}^{6} q_{ik} c_{kj} \tag{1}$$

and

$$q_{ij} = \sum_{k=1}^{6} p_{ik} s_{kj}, \tag{2}$$

where the c's and s's are respectively the elastic constants and elastic compliances [8].

3. Experimental Procedure

The general experimental approach is to stress the specimen either by uniaxial loading or applied hydrostatic pressure and then to measure the absolute changes in optical path length or the changes in optical path difference. By choosing different crystallographic directions for loading and different directions for light beam propagation, sufficient simultaneous equations can be obtained to evaluate all of q_{ij} and p_{ij}.

3.1. Preparation of Specimens

The single crystal ruby was obtained commercially in the form of a boule about 20 cm long and 3 cm in diameter. This was a Czochralski grown crystal where the optic axis made an angle of 60° with the axis of the boule. Spectrophotometric analysis indicated that the Cr_2O_3 content was 0.050 percent by weight.

Plates about 0.6 cm thick were cut with a diamond saw from an inclusion free region of the boule so that their surfaces contained the x_2x_3 plane. These plates were then ground on a surface grinder and polished on a lead lap using 4 to 8 μm diamond paste. The specimens, in the form of rectangular prisms, were cut from the plates, and the newly cut surfaces of the prisms, excluding the ends were then ground and polished.

Dimensions of the 6 prisms used for the measurements are given in table 1. The specimens all had a thickness parallel to x_1 and lengths parallel respectively to x_2, x_3, M and M' (see table 1). Using the morphological unit cell of ruby, the orientation of all specimens was accomplished by means of the Laue back-reflection x-ray technique. It should be pointed out that it is possible to distinguish between opposite ends of the 2-fold axes, and this distinction is important because the sign of the piezo-optic constants, q_{14} and q_{41} depends on which end of an axis is considered as being positive. In the present study, the convention used by Wachtman in his investigation of the elastic constants of corundum was followed [9].

In photoelastic studies, it is important that the distribution of stress be uniform in the specimen. This condition is automatically satisfied when hydrostatic pressure is applied. In applying uniaxial compression, care must be taken that the length which is also the direction of stress in the specimen be at least three times the breadth or the thickness, and that the measurements be confined to the middle portion of the specimen [13, 14]. It can be seen in table 1 that two of the prisms do not quite meet these specifications. However, when loading in compression, steel caps were placed on the ends of the specimens so that, in each case, the prism length was adequate (see sec. 3.3).

3.2. Optical Measurements

The prisms were ground and polished so that localized Fizeau-type optical interference fringes could be observed between opposite faces. Measurement of the shift in these fringes with applied stress was used to determine the absolute change in optical path length. This technique was used both for uniaxial loading [13] and applied hydrostatic pressure [15, 6]. The fringes were viewed in reflection using collimated cadmium red light of 643.8 nm at normal incidence. Use was made of a Pulfrich-type viewer which has been greatly

TABLE 1. *Dimensions of rectangular prisms*

Prism No.	Length		Breadth		Thickness	
	mm	Parallel to	mm	Parallel to	mm	Parallel to
1	27.010	x_3	9.880	x_2	8.747	x_1
2	17.850	x_3	6.510	x_2	6.388	x_1
3	31.387	x_2	5.905	x_3	5.482	x_1
4	27.851	x_2	5.894	x_3	5.580	x_1
5	24.461	x_2	5.908	x_3	5.710	x_1
6	31.463	M[a]	5.885	M'	5.648	x_1
7	17.172	M'[b]	5.330	M	5.665	x_1

[a] M indicates the direction equally inclined to x_2 and x_3 and lying in the x_2x_3 plane.
[b] M' indicates the direction equally inclined to $-x_2$ and x_3 and lying in the x_2x_3 plane.

improved by Saunders [16], and, in each experiment, a sheet of polaroid was employed to isolate changes along each of the two principal vibration directions in the crystal.

The change in optical path difference induced by uniaxial loading was also measured. In this case, the specimen was placed in a 45 degree position between crossed nicol prisms, and the relative retardation was measured with a Soleil-Babinet compensator [13].

Since in each experiment, the change in optical path length or induced optical path difference was measured, it was necessary to know the change in thickness of the specimen in order to calculate the changes in refractive index. For this purpose, the elastic constants of corundum determined by Wachtman were employed [9]. The elastic constants of corundum are the same as those of ruby within the experimental error [17].

3.3. Stressing Apparatus and Techniques

For the present problem, three different stressing apparatus were employed: (a) a hydrostatic pressure vessel, (b) a dead weight compression apparatus, and (c) a rectangular frame screw clamp.

a. Hydrostatic Pressure Vessel

For attaining hydrostatic pressures up to 1000 bars a pressure vessel equipped with glass windows was used [15]. The specimen was immersed in a highly transparent mineral oil, and hydrostatic pressure was generated by compressing the oil. In order to increase the visibility of the fringes, the specimen was fully coated with aluminum on the rear reflecting surface, and given a partial coating on the front surface. The shift of the Fizeau-type fringes past a fixed reference mark was observed visually using Saunders' viewer [16]. This technique was used to find the change in refractive index with hydrostatic pressure of the ordinary and extraordinary ray of ruby.

b. Dead Weight Compression Apparatus

A loading frame was used where a yoke with suspended weights brings a piston to bear on the specimen [14]. To insure uniformity of loading, steel caps were fabricated to fit over each end of the specimen. A small depression was machined in both the center of the cap and the center of the piston to accommodate a steel ball at the point of contact. Six calibrated 50-lb weights were used so that the total load was 300 lbs. The dead weight compression apparatus was always used in conjunction with the Soleil-Babinet compensator to determine changes in the relative retardation with a sensitivity of 1×10^{-7}. The pressures attained were of the order of 200 bars yielding data to three significant figures.

c. Rectangular Frame Screw Clamp

A special clamp was made for the purpose of easily attaining compressive stresses up to 10,000 bars. This is shown in figure 2. The screw clamp was used

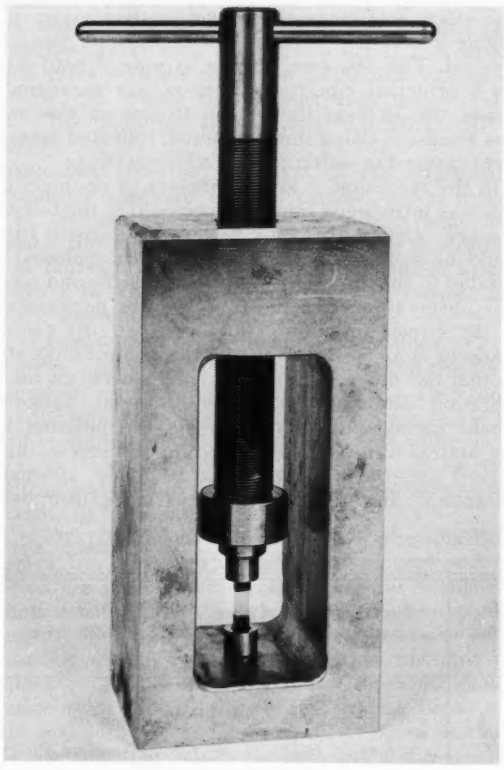

FIGURE 2. *Rectangular frame screw clamp with specimen in place.*

in conjunction with Saunders' viewing apparatus [16] to observe the shift in Fizeau-type interference fringes with load. With this technique, it is possible to note a shift of 0.1 fringe which is equivalent to a change of about 1×10^{-5} in refractive index. It was desirable to attain stresses high enough to induce a reasonably large and measurable shift of Fizeau fringes. Calculations indicated that reliable data on changes of refractive index in the fourth and fifth decimal place could be obtained by stressing to about 1,500 bars.

It can be seen in figure 2 that the thrust in the clamp is obtained from a screw which threads in to one end of the block. The screw is 1 inch in diameter, has 20 threads per inch and is built with a thrust bearing at the front so that the specimen is torque free. To insure uniformity of load on the specimen, the technique of using steel caps with steel balls to transmit the stress was employed here as in the dead weight loading apparatus.

In conducting the experiments, the specimen was first placed in the dead weight loading apparatus and the relationship between load and induced double refraction was determined. For ruby, there is evidence to indicate that this relationship is linear to pressures much greater than 200 bars [6]. Having established this linear relationship, the specimen served as its own stress gage when placed in the screw clamp.

The stress was measured by noting the change in the double refraction of the specimen as it was compressed. The absolute change in optical path length for a principal vibration direction was measured by noting the shift in the Fizeau fringes as this stress was released. Using this technique, repeated measurements agreed to within ± 0.1 of a Fizeau fringe.

In the foregoing, a known amount of double-refraction was introduced into the specimen in the following manner. Ordinarily, one pattern of Fizeau fringes could be seen when the E-vector of the polaroid was parallel to the direction of stress, and a second pattern was observable when the E-vector was perpendicular to the stress direction. These two patterns could be made to coincide by adjusting the compressive stress so that the difference in path length between the two vibration directions was some integral number of whole wavelengths. By removing the polaroid from the optical train and slowly turning the screw, the observed pattern of fringes could be made, alternately, to appear and disappear. The fringes disappeared when the optical path length between the two principal vibration directions was an odd number of half wavelengths. By adjusting to a position of complete fringe extinction, two different settings of the screw could be selected so that, in the interval between, a known number of whole wavelengths of optical path difference had been introduced into the specimen.

4. Results and Discussion

The method of calculating the photoelastic constants from the observed change in optical path length has been amply treated by Narasimhamurty [18] and Vedam [19, 13], and will not be given here. The paper by Narasimhamurty on the photoelastic constants of α-quartz is particularly pertinent to the present work because α-quartz and ruby both belong to the seventh Laue-symmetry group and the number of photoelastic constants is the same for both groups. The experimental results are presented in table 2, where the observed path retardation, δ_0, has been reported in

TABLE 2. *Optical path retardation in ruby*

Prism No.	Direction of stress	Direction of observation	Nature of observation	Expression for path retardation, δ_0	Measured value of path retardation, δ_0, cm²/dyn × 10^{13}
1	x_3	x_1	Relative	$1/2(n_3^3q_{33}-n_2^3q_{13})-s_{13}(n_3-n_2)$	−1.475
2	x_3	x_1	Absolute (P)	$n_3^3q_{33}-2n_3s_{13}$	−.98
2	x_3	x_1	Absolute (N)	$n_2^3q_{13}-2n_2s_{13}$	1.97
3	x_2	x_1	Relative	$1/2(n_2^3q_{11}-n_3^3q_{31})-s_{12}(n_2-n_3)$	−1.469
4	x_2	x_1	Absolute (P)	$n_2^3q_{11}-2n_2s_{12}$	−.25
4	x_2	x_1	Absolute (N)	$n^3q_{31}-2n_3s_{12}$	2.85
3	x_2	x_3	Relative	$1/2n_2^3(q_{11}-q_{12})$	−1.582
5	x_2	x_3	Absolute (P)	$n_2^3q_{11}-2n_2s_{13}$	−1.55
5	x_2	x_3	Absolute (N)	$n_1^3q_{12}-2n_1s_{13}$	1.62
6	M	M'	Relative	$1/8n_{23}^3(q_{11}+q_{13}-q_{14}+q_{31}+q_{33}+2q_{44}-2q_{41})$ $-1/4n_1^3(q_{12}+q_{13}+q_{14})$ $-1/4(n_{23}-n_1)(s_{11}+2s_{13}+s_{33}-s_{44})$	−1.654
6	M	M'	Absolute (P)	$1/4n_{23}^3(q_{11}+q_{13}-q_{14}+q_{31}+q_{33}+2q_{44}-2q_{41})$ $-1/2n_{23}(s_{11}+2s_{13}+s_{33}-s_{44})$	−.08
6	M	M'	Absolute (N)	$1/2n_1^3(q_{12}+q_{13}+q_{14})$ $-1/2n_1(s_{11}+2s_{13}+s_{33}-s_{44})$	3.22
7	M'	M	Relative	$1/8n_{23}^3(q_{11}+q_{13}+q_{14}+q_{31}+q_{33}+2q_{44}+2q_{41})$ $-1/4n_1^3(q_{12}+q_{13}-q_{14})$ $-1/4(n_{23}-n_1)(s_{11}+2s_{13}+s_{33}-s_{44})$	−1.974
7	M'	M	Absolute (P)	$1/4n_{23}^3(q_{11}+q_{13}+q_{14}+q_{31}+q_{33}+2q_{44}+2q_{41})$ $-1/2n_{23}(s_{11}+2s_{13}+s_{33}-s_{44})$	−.39
7	M'	M	Absolute (N)	$1/2n_1^3(q_{12}+q_{13}-q_{14})$ $-1/2n_1(s_{11}+2s_{13}+s_{33}-s_{44})$	3.55
2	Hydrostatic pressure	x_1	Absolute	$n_3^3(2q_{31}+q_{33})-2n_3(s_{11}+s_{12}+s_{13})$ (for vibrations parallel to the optic axis)	−6.63
2	Hydrostatic pressure	x_1	Absolute	$n_2^3(q_{11}+q_{12}+q_{13})-2n_2(s_{11}+s_{12}+s_{13})$ (for vibrations perpendicular to the optic axis)	−6.62

centimeters per centimeter thickness of the specimen per unit stress of 1 dyn/cm^2. The measured values of δ_0 reported in the last column represent the combined effect of change in refractive index and dimensional change. It should be noted that the relative values of δ_0 hold for a light beam traversing the specimen only once, and the absolute values pertain for a double passage of the specimen [18, 19]. The (P) and the (N) indicate measurements made with the principal vibration directions, parallel and perpendicular, respectively, to the direction of applied stress. For the different directions of loading and light propagation, theoretical expressions for δ_0 are presented in the next to last column.

Although the principal vibration directions are free to rotate in the x_2x_3 plane when stress is applied along x_2, preliminary calculations indicated that this rotation was extremely small, on the order of 0.02 circular degrees. This slight rotation was neglected, and data obtained from prisms No. 3 and 4 (see table 2) were treated as if there were no rotation at all.

Values of the s_{ij} were taken from Wachtman's paper [9] and inserted into the equations of table 2. Of the resulting 17 simultaneous equations, a computerized least-squares fit was made and the resulting q_{ij} are reported in table 3. The standard deviation of each q_{ij} was 0.02×10^{-13} cm^2/dyn or less. The p_{ij} were then computed from eq (1) and the results are given in table 3.

Mandarino [3] has reported that $(q_{33}-q_{13})=+0.697\times10^{-13}$ cm^2/dyn for ruby with 0.11 percent Cr_2O_3. Our results indicate a negative value, $(q_{33}-q_{13})=-0.54\times10^{-13}$ cm^2/dyn.

Where comparison is possible the photoelastic properties of ruby are found to be close to those of sapphire. Subjecting ruby prism No. 2 to hydrostatic pressure, it was found that the change in refractive index was -1.1×10^{-4}/Kilobar for both the ordinary and extraordinary ray. This agrees within the experimental error with the results of Davis and Vedam on sapphire [6], where they report that $\Delta n_\omega=(-1.0\pm0.2)\times10^{-4}$/Kilobar and $\Delta n_\epsilon=(-1.1\pm0.2)\times10^{-4}$/kilobar.[2]

TABLE 3. *Piezo-optic and elasto-optic constants of ruby*

	Present work	Dixon
q_{11}	−0.52	—
q_{12}	.08	—
q_{13}	.13	—
q_{14}	−.07	—
q_{31}	.01	—
q_{33}	−.41	—
q_{41}	−.01	—
q_{44}	−.71	—
p_{11}	−0.23	~0.20
p_{12}	−.03	~ .08
p_{13}	.02	~0
p_{14}	.00	—
p_{31}	−.04	~0
p_{33}	−.20	.252
p_{41}	.01	—
p_{44}	−.10	.085

All q_{ij} values in units of 10^{-13} cm^2/dyn.
All p_{ij} values are dimensionless.

Dixon has reported on some of the strain-optic constants of sapphire using a method which makes use of the acoustic scattering of a light beam [4]. Although the method does not permit the determination of the sign of the constants, the absolute values are listed in Table III for purposes of comparison with the present work, and it can be seen that there is fairly good agreement in the numerical values.

Caddes and Wilkinson have reported on the large photoelastic anisotropy of sapphire [5]. They have found the ratio of the elasto-optic constants $p_{33}/p_{13}\geq45$, which is consistent with our results. Our value of p_{13} compares favorably with the value, $p_{13}\approx0$ inferred by Davis and Vedam by analogy with the strain-optic constants of MgO [6, 20].

Pockels' phenomenological theory of photoelasticity assumes that the elastic deformations and not the stresses are primarily responsible for the changes in refractive index [21, 13]. It is interesting to note that for ruby (table 3) p_{11}, p_{12}, p_{31}, and p_{33} all show negative values. Of all the crystals studied thus far, only the covalent crystals Topaz, MgO and diamond exhibit negative values for $p_{hk}(h,\ k=1,\ 2,\ 3)$. In Topaz it is found that p_{11}, p_{22}, and p_{33} are all negative in value. MgO has negative values for both p_{11} and p_{12}, while diamond has a negative value for p_{11} only. All these crystals are noted for having strong interatomic bonding [13].

Mueller [22, 13] has developed a physical theory to explain the changes in the refractive index ellipsoid that take place when a solid is stressed. In this theory, calculations are made of the changes in the density, coulomb field, the lorentz-lorenz field, and the intrinsic polarizability of the scattering centers. The contribution of density is always positive and in most crystals exceeds the combined effect of the other three changes so that the p_{hk} are generally positive. The theory has been worked out for glasses and cubic crystals, but not for crystals of lower symmetry such as ruby (crystal class $\bar{3}$m) where the computations become extremely complicated. Although the individual contributions can not be calculated for ruby, it may be noted that the combination of the latter three changes outweighs the contribution due to change in density and, with the exception of p_{13}, the p_{hk} of ruby have negative values. Even with p_{13}, the positive numerical value is very small.

The photoelastic constants of calcite have been determined by Pockels [22, 13], and it is interesting to compare these data with the results on ruby because both crystals belong to class $\bar{3}$m. In both crystals the oxygen atoms are arranged in triangular groups per-

[2] These data also agree very well with the earlier measurements of Waxler and Weir on sapphire [15], when it is recognized that these investigators used Bridgman's compressibility data.

pendicular to the optic axis. However calcite has a true layer lattice, whereas Al_2O_3 possesses an isosthenic lattice in which the oxygen atoms are almost in hexagonal close packing. The elastic compliances of calcite are much greater than those of ruby [13]. This pronounced difference in the elastic compliances manifests itself in the photoelastic constants where it is found that the p_{hk} of calcite are all positive, and the p_{hk} of ruby are predominantly negative.

The authors are indebted to Harry B. Williams of the National Bureau of Standards for his great help in the preparation of specimens.

5. References

[1] Quelle, F. W., Appl. Opt. **5,** 633 (1966).
[2] Houston, T. W., Johnson, L. F., Kisliuk, P., and Walsh, D. J., J. Opt. Soc. Am. **53,** No. 11, 1286 (1963).
[3] Mandarino, J. A., Report from the Mineralogical Laboratory, Univ. of Michigan, Ann Arbor, Mich., cataloged by ASTIA as AD No. 146029.
[4] Dixon, R. W., J. Appl. Phys. **38,** 5149 (1967).
[5] Caddes, D. E., and Wilkinson, C. D. W., IEEE, J. Quantum Electron. QE 2, 330 (1966).
[6] Davis, T. A., and Vedam, K., J. Appl. Phys. **38,** 4555 (1967).
[7] Jeppesen, M. A., J. Opt. Soc. Am. **48,** No. 9, 629 (1958).
[8] Nye, J. F., Physical Properties of Crystals (Oxford Univ. Press, London, England, 1957).
[9] Wachtman, J. B., Jr., Tefft, W. E., Lam, D. G., Jr., and Stinchfield, R. P., Nat. Bur. Stand. (U.S.), **64A** (Phys. and Chem.), No. 3, 213–228 (May–June 1960).
[10] Malitson, I. H., and Dodge, M. J., NBS (data to be published).
[11] Peiser, H. S., Wachtman, J. B., Jr., and Dickson, R. W., Nat. Bur. Stand. (U.S.), **67A** (Phys. and Chem.) No. 5, 395–401 (Sept.–Oct. 1963).
[12] Curie, P., J. de Phys. 3 (3), 393 (1894).
[13] Krishnan, R. S., Progress in Crystal Physics, Volume **I** (Interscience Publishers, New York, London, 1958).
[14] Waxler, R. M., and Napolitano, A., J. Res. NBS **59,** No. 2, 121 (1957) RP2779.
[15] Waxler, R. M., and Weir, C. E., Nat. Bur. Stand. (U.S.), **69A** (Phys. and Chem.) No. 4, 325–333 (July–Aug. 1965).
[16] Saunders, J. B., J. Res. NBS 35, 157 (1945) RP1668.
[17] Wachtman, J. B., Jr., personal communication.
[18] Narasimhamurty, T. S., J. Opt. Soc. Am. **59,** No. 6, 682 (1968).
[19] Vedam, K., Proc. Ind. Acad. Sci. [A] **34,** 161 (1951).
[20] Vedam, K., and Schmidt, E. D. D., Phys. Rev. **146,** 548 (1966).
[21] Pockels, F., Wied. Ann. **37,** 151 (1889); Lehrbuch der Kristalloptic (B.6. Teubner, Leipzig and Berlin, 1906).
[22] Mueller, H., Phys. Rev. 47, 947 (1935).
[23] Pockels, F., Ann. Phys. (Leipzig) **11,** 726 (1903).

(Paper 74A2–592)

JOURNAL OF RESEARCH of the National Bureau of Standards—A. Physics and Chemistry
Vol. 74A2, No. 2, March–April 1970

Estimation of Critical Constants T_c, ρ_c from the $\rho(T)$ and $T(\rho)$ Relations at Coexistence*

Robert D. Goodwin**

Institute for Basic Standards, National Bureau of Standards, Boulder, Colorado 80302

(September 22, 1969)

The critical temperature T_c and the critical density ρ_c are estimated from new equations (1) for the double-valued $\rho(T)$ relation, and (2) for the single-valued $T(\rho)$ relation. For method (1) this report gives concise descriptions of the rectilinear diameter and of the densities of liquid oxygen. Calculated vapor densities agree well with experimental oxygen data over the wide range from triple- to critical-point. Method (2) is applied to hydrogen, oxygen, fluorine, and neon, giving the $T(\rho)$ relation and estimates for T_c and ρ_c all in one step from the complete set of liquid and vapor data.

Key words: Coexistence; coexistence temperatures; critical constants; critical density; critical temperatures; fluorine; neon; oxygen; orthobaric densities; parahydrogen; saturated liquid and vapor densities.

List of Symbols

Subscripts

c refers to the critical point.
t refers to the liquid triple point.
g refers to vapor at coexistence.
l refers to liquid at coexistence.

Symbols

a, b, c, d, e, f, g, constant coefficients.
A_i, constant coefficients.
β, an exponent near 0.35.
$\mathscr{d}$, density at coexistence.
$\mathscr{d}_t$, 38.203 mol/l for parahydrogen [8].
$\mathscr{d}_t$, 40.83 mol/l for oxygen [4].
$\mathscr{d}_t$, 45.2 mol/l for fluorine (estimated).
$\mathscr{d}_t$, 61.785 mol/l for neon [23].
l, the liter.
P, pressure.
$\rho \equiv \mathscr{d}/\mathscr{d}_t$, density reduced at the liquid triple point.
$\sigma \equiv \mathscr{d}/\mathscr{d}_c$, density reduced at the critical point.
T, K, temperature at coexistence (NBS 1955).
$\tau \equiv T/T_c$, temperature reduced at the critical point.
$z \equiv (1-\tau)$, reduced temperature with origin at T_c.

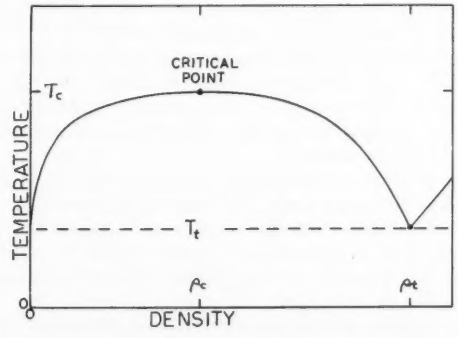

FIGURE 1. *Temperature-density phase diagram for coexisting vapor and liquid at densities to the liquid triple point, ρ_t.*

1. Introduction

This report completes protracted efforts to forge some tools needed for the computation of thermodynamic properties of fluids from experimental PVT data. These tools are concise descriptions of the data, descriptions which are essentially correct in the critical region where PVT data are least reliable. For the one-phase domain we may use the nonanalytic equation of state [1].[1] For the two-phase domain we may use the nonanalytic vapor pressure equation [2] together with the $\rho(T)$ or $T(\rho)$ relations described below and outlined by figure 1.

*This work was conducted at NBS under sponsorship of the U.S. Air Force (MIPR No. 4355–9–7).

**Cryogenics Division, NBS Laboratories, Boulder, Colo. 80302.

[1] Figures in brackets indicate the literature references at the end of this paper.

372-505 O - 70 - 6

2. The Orthobaric Densities

Guggenheim [3] has formulated approximate, general relations for the double-valued function $\rho(T)$. (Symbols are listed above.)

$$(\rho_l/\rho_c - 1) = (3/4)\cdot z + (7/4)\cdot z^{1/3}, \quad (1a)$$

$$(\rho_g/\rho_c - 1) = (3/4)\cdot z - (7/4)\cdot z^{1/3}. \quad (1b)$$

With precise data for oxygen [4] we find that (1a, 1b) are valid only in the approximate range $0.85 < T/T_c \leq 1$. Hou and Martin [5] extended the range for liquid densities by use of an expansion in powers of $z^{1/3}$.

Equations (1a, 1b) are consistent with the hypothesis of a rectilinear diameter,

$$(\rho_l + \rho_g)/2 = \rho_c + a\cdot z. \quad (1c)$$

They also are consistent with the currently accepted relation for the critical region

$$(\rho_l - \rho_g)/2 = b\cdot z^{\beta} \quad (1d)$$

where exponent $\beta = 0.350 \pm 0.015$ [6]. Again we find with oxygen data that neither (1c) nor (1d) is sufficient at $T/T_c < 0.9$. Oxygen vapor densities range through a factor greater than 60,000 [4]. To secure a precision of at least 0.03 percent in calculated vapor densities for thermal computations near the triple point, we would require a precision of about one part in 400 million in each of two functions to be differenced as in (1b).

In the following we give results of investigations on the $\rho(T)$ relations, using oxygen data from [4]. The method is awkward. Raw data for $\rho_g(T)$ and for $\rho_l(T)$ must be interpolated to the same temperatures before they can be combined.

The critical temperature is obtained by trial to minimize deviations in the logarithmic form of (1d). The coefficients log (b) and β are found by least squares. For oxygen data this expression is sufficient only in the restricted range $0.94 < T/T_c \leq 1$. Summary results are in table 1.

The critical density is obtained as the value of the rectilinear diameter (1c) at $T = T_c$. The data unfortunately are not linear, but rather are slightly sigmoid, as described within the high precision of these data by the new expression,

$$(\rho_l + \rho_g)/2 = a + b\cdot z + c\cdot \exp(-d/z) \quad (2)$$

in which $\rho_c = a$. Equation (2) is consistent with the hypothesis of a rectilinear diameter because it becomes exactly linear as $T \to T_c$. Summary results are in table 1.

The densities of liquid oxygen have been examined for deviations from forms like (1a). We thus deduce the new expression ($\beta = 0.35$),

$$(\rho_l/\rho_c - 1) = a\cdot z + b\cdot z^{\beta} + c\cdot \exp(-d\cdot \tau^2/z). \quad (3)$$

Equation (3) is consistent with (1c) and (1d) because the last term vanishes strongly as $T \to T_c$. The values for a and b are close to those generalized by Guggenheim, and the last term is merely a small adjustment, as seen by the value of c in table 1.

The densities of oxygen vapor are described quite well by the following expression,

$$\rho_g/\rho_c = \exp[a\cdot(1 - 1/\tau) + b\cdot z^{\beta} + c\cdot z + \ldots + g\cdot z^5]. \quad (4)$$

It is consistent at low densities with the ideal gas law and the basic vapor pressure equation. This exponential form excludes negative values for ρ_g, as often are obtained with difference expressions like (1b). Exponents other than $\beta = 0.35$ have not been explored. Summary results are in table 1.

TABLE 1. *Summary results for oxygen with equations of section 2*

Equation (1d). 10 points at $145 \leq T \leq 154$ K, $T_c = 154.54$ K, $b = 24.618$ mol/l, $\beta = 0.3476$, rms = 0.35%.
Following equations for 53 points at $56 \leq T \leq 150$ K
Equation (2). $a = 13.6135$ mol/l, $b = 9.7843$ mol/l, $c = 1.9306$ mol/l, $d = 0.9195$, rms = 0.020%.
Equation (3). $a = 0.7441$, $b = 1.8212$, $c = -0.0556$, $d = 5/7$, rms = 0.037%.
Equation (4). $a = 3.2305$, $b = -1.9368$, $c = -1.6989$, $d = 4.7351$, $e = -24.2531$, $f = 45.7606$, $g = -46.7552$, rms = 0.030%.

3. The Saturation Temperatures

The $T(\rho)$ relation for coexisting (saturated) liquid and vapor is single-valued (fig. 1) and therefore requires no interpolation of data for analytical work. As it is the heart of the nonanalytic equation of state [1], we have sought a description which would be simpler and more accurate than reported [7]. With symbols defined in the list, the result of new investigations with parahydrogen data of [8] is the following,

$$(1/\tau) - 1 = |\sigma - 1|^3 \cdot F(\rho) \quad (5)$$

where

$$F(\rho) \equiv A_1\cdot \log_e(1/\rho) + A_2 + A_3\cdot\rho + \ldots + A_9\cdot\rho^7.$$

Equation (5) is consistent with the ideal gas law and the basic vapor pressure equation at low densities. In the critical region it is consistent with the well-known [3] behavior, $\tau = 1 - A\cdot|\sigma - 1|^3$. At high densities we obtain $\tau \to 0$ (because $A_9 > 0$), consistent with the trend of figure 1. The argument ρ is selected because it has a maximum value of unity: we therefore may keep the same number of decimal digits in all coefficients A_i. For least squares, (5) has been used exactly as written. When the number of terms is increased from eight to nine, the rms relative deviation drops by

a factor of 1/6 for the hydrogen data [8]. Nine terms also is optimum for the oxygen data [4].

In the following we estimate the critical constants via (5) for hydrogen, oxygen, fluorine, and neon. Simultaneously we obtain a complete description of the $T(\rho)$ relation for vapor and liquid in a single formula, as compared with at least four formulas required by the familiar but awkward methods of section 2 above. Some data near ρ_c will be omitted arbitrarily from the calculations (see tables 3 and 5) because they may be of questionable accuracy, having been obtained from PVT data and a vapor pressure equation [4, 8].

We vary the assumed values for T_c and for ρ_c in (5), observing the root mean square (rms) of relative deviations $(T/T_{\text{calc}}-1)$. First results for hydrogen are shown by figure 2. Similar results at a higher precision are in table 2. For each density ρ_c the first column gives T_c and the second column gives the relative rms deviation in parts per ten thousand. The minimum in the deviation is quite well defined. Table 3 compares individual reduced data with calculated values. Table 6 gives the coefficients for (5). Table 7 compares critical constants estimated via (5) with estimates of other authors.

TABLE 2. *Parahydrogen survey for* T_c, ρ_c *in eq (5)*

T_c, K	rms · 10^4	T_c, K	rms · 10^4
DCRT, mol/l = 15.550		DCRT, mol/l = 15.610	
32.944	1.35	32.944	1.18
32.947	1.21	32.947	0.99
32.950	1.12	32.950	.86
32.953	1.10	32.953	.79
32.956	1.14	32.956	.82
32.959	1.24	32.959	.93
32.962	1.39	32.962	1.10
DCRT, mol/l = 15.570		DCRT, mol/l = 15.630	
32.944	1.21	32.944	1.29
32.947	1.05	32.947	1.12
32.950	0.93	32.950	1.00
32.953	.89	32.953	0.94
32.956	.93	32.956	.95
32.959	1.04	32.959	1.04
32.962	1.21	32.962	1.19
DCRT, mol/l = 15.590		DCRT, mol/l = 15.650	
32.944	1.15	32.944	1.48
32.947	0.97	32.947	1.32
32.950	.83	32.950	1.21
32.953	.78	32.953	1.16
32.956	.81	32.956	1.17
32.959	.93	32.959	1.24
32.962	1.11	32.962	1.36

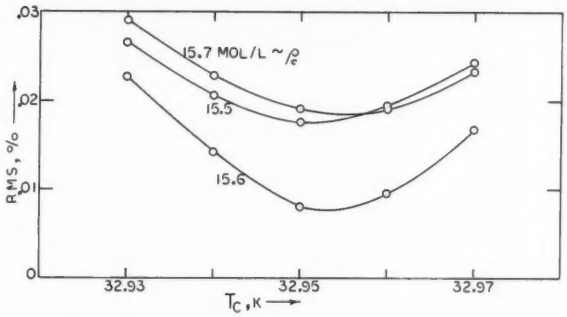

FIGURE 2. *Relative rms deviation of hydrogen temperatures from eq (5) as a function of assumed* T_c, ρ_c *values.*

The oxygen survey in table 4 is analogous to that for hydrogen. Whereas the minimum in the overall deviation is weak (as compared with that for H_2), the data extend over a much greater range of vapor densities. Table 5 compares individual data with calculated values of T/T_c. Table 7 compares critical constants.

Fluorine PVT measurements are in progress [16], and accurate vapor pressures have been reported [17]. We have obtained orthobaric densities via the vapor pressure relation and an equation of state (similar to that in [14]), kindly provided by Prydz and Straty [16].

TABLE 3. *Comparison of* $T(\rho)$ *data for parahydrogen with calculated values from (5). Part I, vapor densities*

d_c = 15.59 mol/l,		T_c = 32.953 K	
d/d_c	T/T_c	Calc	Pcnt
0.0641	0.6642	0.6642	0.00
.0962	.7180	.7180	−.00
.1283	.7592	.7592	−.00
.1604	.7926	.7926	.00
.1924	.8206	.8206	.00
.2245	.8445	.8445	.00
.2566	.8651	.8652	−.00
.2886	.8832	.8832	−.00
.3207	.8990	.8991	−.00
.3528	.9130	.9130	−.00
.3849	.9254	.9254	.00
.4169	.9364	.9363	.00
.4490	.9461	.9460	.01
.4811	.9547	.9546	.01
.5131	.9622	.9622	.00
.5452	.9689	.9689	.00
.5773	.9747	.9747	−.01
.6094	.9798	.9798	−.01
.6414	.9841	.9842	−.01
.6735	.9879	.9880	−.01
.7056	.9910	.9911	−.01
.7377	.9936	.9936	−.00
.7697	.9957	.9957	.00
.8018	.9974	.9972	.02

TABLE 3, PART II. *Parahydrogen liquid densities*

d/d_c	T/T_c	Calc	Pcnt
1.1867	0.9980	0.9978	0.02
1.2187	.9966	.9965	.01
1.2508	.9948	.9947	.00
1.2829	.9925	.9926	−.00
1.3149	.9899	.9900	−.01
1.3470	.9868	.9868	−.01
1.3791	.9831	.9832	−.01
1.4112	.9790	.9790	−.00
1.4432	.9743	.9743	−.00
1.4753	.9691	.9690	.00
1.5074	.9633	.9632	.01
1.5394	.9569	.9568	.01
1.5715	.9499	.9498	.01
1.6036	.9422	.9422	.01
1.6357	.9340	.9339	.01
1.6677	.9251	.9250	.00
1.6998	.9155	.9155	−.00
1.7319	.9052	.9052	−.00
1.7640	.8942	.8943	−.01
1.7960	.8825	.8825	−.01
1.8281	.8700	.8700	−.01
1.8602	.8567	.8567	−.01
1.8922	.8425	.8426	−.01
1.9243	.8276	.8276	−.00
1.9564	.8117	.8117	.00
1.9885	.7949	.7948	.01
2.0205	.7771	.7770	.01
2.0526	.7583	.7582	.01
2.0847	.7384	.7384	.01
2.1167	.7175	.7174	.00
2.1488	.6953	.6953	−.01
2.1809	.6719	.6720	−.01
2.2130	.6472	.6473	−.01
2.2450	.6212	.6212	−.01
2.2771	.5937	.5936	.02
2.4505	.4189	.4189	−.00

Summary results for (5) on saturated liquid and vapor from 86 through 142 K are given in table 6. Estimates for T_c and ρ_c are made only to ± 0.05 in each value because the data are preliminary. Table 7 compares critical constants.

Neon has been investigated with (5) to extend the range of types of substance. No determination of the critical density appears to have been made since the pioneer work of Mathias et al. [21]. To their orthobaric densities we have added the recent data of Gibbons [22]. Temperatures in [21] are adjusted to the ice point 273.15 K as in [23]. The combined data yield 16 vapor densities from 25.16 through 44.31 K, and 15 liquid densities from 25.16 through 44.08 K. Deviations from (5) are plotted in figure 3. Summary results are in table 6. The estimate for T_c is made only to ± 0.01 K; that for ρ_c only to ± 0.05 mol/l. Table 7 compares critical constants.

TABLE 4. *Oxygen survey for* T_c, ρ_c *in eq (5)*

T_c, K	RMS · 10^4	T_c, K	RMS · 10^4
DCRT, mol/l = 13.480		DCRT, mol/l = 13.540	
154.460	5.46	154.460	5.43
154.480	5.44	154.480	5.42
154.500	5.44	154.500	5.41
154.520	5.43	154.520	5.41
154.540	5.44	154.540	5.42
154.560	5.45	154.560	5.43
154.580	5.47	154.580	5.45
DCRT, mol/l = 13.500		DCRT, mol/l = 13.560	
154.460	5.44	154.460	5.44
154.480	5.43	154.480	5.43
154.500	5.42	154.500	5.42
154.520	5.42	154.520	5.42
154.540	5.42	154.540	5.43
154.560	5.43	154.560	5.45
154.580	5.45	154.580	5.47
DCRT, mol/l = 13.520		DCRT, mol/l = 13.580	
154.460	5.43	154.460	5.46
154.480	5.42	154.480	5.45
154.500	5.41	154.500	5.44
154.520	5.41	154.520	5.44
154.540	5.42	154.540	5.45
154.560	5.43	154.560	5.47
154.580	5.45	154.580	5.49

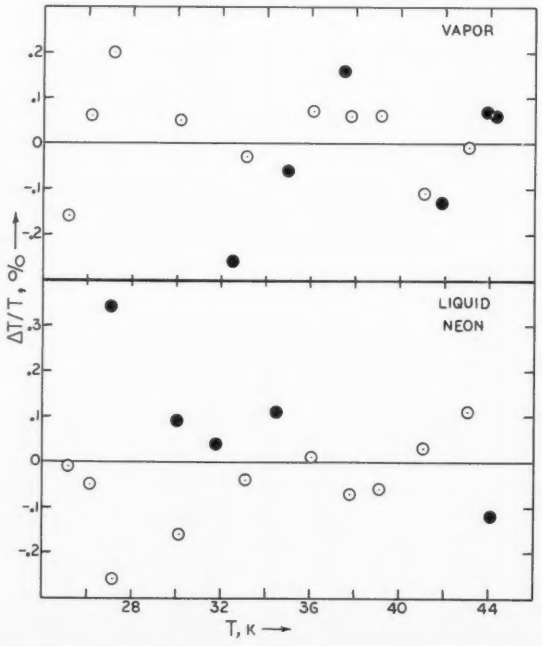

FIGURE 3. *Relative deviations of neon saturation temperatures from eq (5).*

TABLE 5. *Comparison of $T(\rho)$ data for oxygen with calculated values from (5). Part I, vapor densities*

$\rho_c = 13.52$ mol/l, $T_c = 154.52$ K

ρ/ρ_c	T/T_c	Calc	Pcnt
0.000039	0.3624	0.3618	0.18
.000066	.3754	.3749	.11
.000108	.3883	.3881	.04
.000171	.4012	.4013	−.01
.000261	.4142	.4144	−.06
.000387	.4271	.4275	−.09
.000561	.4401	.4406	−.12
.000795	.4530	.4536	−.13
.001101	.4660	.4666	−.13
.001496	.4789	.4795	−.12
.001997	.4918	.4924	−.11
.002621	.5048	.5052	−.08
.003390	.5177	.5180	−.06
.004323	.5307	.5308	−.03
.005443	.5436	.5436	−.00
.006774	.5566	.5564	.02
.008340	.5695	.5692	.05
.010166	.5824	.5820	.07
.012280	.5954	.5949	.09
.014709	.6083	.6077	.10
.017483	.6213	.6206	.11
.020632	.6342	.6335	.11
.024188	.6472	.6465	.11
.028186	.6601	.6595	.10
.032664	.6731	.6725	.09
.037658	.6860	.6855	.07
.043211	.6989	.6986	.05
.049369	.7119	.7116	.03
.056178	.7248	.7247	.01
.063697	.7378	.7378	−.01
.071985	.7507	.7509	−.03
.081109	.7637	.7640	−.04
.091132	.7766	.7770	−.06
.102160	.7895	.7901	−.07
.114275	.8025	.8031	−.07
.127589	.8154	.8160	−.07
.142234	.8284	.8289	−.07
.158365	.8413	.8418	−.06
.176176	.8543	.8546	−.04
.195880	.8672	.8674	−.02
.217781	.8801	.8802	−.00
.242234	.8931	.8929	.02
.269734	.9060	.9057	.04
.300976	.9190	.9185	.06
.336923	.9319	.9313	.06
.388905	.9474	.9470	.04
.418343	.9546	.9546	.01
.477367	.9673	.9674	−.01
.509467	.9732	.9732	.01
.627071	.9882	.9884	−.02
.718195	.9950	.9950	−.01

TABLE 5, PART II. *Oxygen liquid densities*

ρ/ρ_c	T/T_c	Calc	Pcnt
1.4126	0.9877	0.9875	0.03
1.4763	.9815	.9813	.02
1.5358	.9742	.9742	−.00
1.6050	.9644	.9643	.01
1.6654	.9542	.9541	.02
1.7188	.9440	.9438	.02
1.7837	.9299	.9298	.01
1.8180	.9218	.9217	.01
1.8578	.9119	.9118	.02
1.8881	.9037	.9037	−.00
1.9104	.8976	.8975	.01
1.9506	.8859	.8859	.00
1.9957	.8718	.8720	−.02
2.0192	.8643	.8644	−.01
2.0502	.8541	.8540	.01
2.0680	.8476	.8479	−.03
2.0914	.8396	.8396	−.01
2.1217	.8284	.8285	−.02
2.1558	.8154	.8156	−.02
2.1890	.8025	.8025	−.00
2.2205	.7895	.7896	−.01
2.2516	.7766	.7766	.01
2.2814	.7637	.7636	.01
2.3099	.7507	.7509	−.02
2.3385	.7378	.7378	−.00
2.3661	.7248	.7248	−.00
2.3936	.7119	.7116	.03
2.4195	.6989	.6990	−.01
2.4459	.6860	.6858	.03
2.4712	.6731	.6730	.01
2.4963	.6601	.6601	.01
2.5209	.6472	.6471	.00
2.5453	.6342	.6342	.00
2.5691	.6213	.6214	−.01
2.5934	.6083	.6081	.04
2.6163	.5954	.5954	−.00
2.6397	.5824	.5823	.02
2.6625	.5695	.5694	.01
2.6848	.5566	.5567	−.02
2.7073	.5436	.5437	−.01
2.7293	.5307	.5308	−.03
2.7516	.5177	.5177	.01
2.7733	.5048	.5048	−.00
2.7943	.4918	.4922	−.07
2.8166	.4789	.4787	.04
2.8371	.4660	.4662	−.05
2.8591	.4530	.4527	.06
2.8791	.4401	.4403	−.06
2.9006	.4271	.4270	.03
2.9212	.4142	.4141	.01
2.9421	.4012	.4010	.07
2.9621	.3883	.3883	−.01
2.9825	.3754	.3755	−.03
3.0030	.3624	.3624	−.01

TABLE 6. *Constants and coefficients for equation (5)*

	Hydrogen	Oxygen	Fluorine	Neon
T_c, K	32.953	154.52	143.9	44.40
ρ_c, mol/l	15.59	13.52	15.1	23.3
A_1	0.300 6242	0.185 6314	0.180 5343	0.208 9927
A_2	−0.567 0332	−0.323 1999	−0.327 0052	−0.364 1367
A_3	3.838 7436	1.997 6801	2.253 8388	2.785 5198
A_4	−19.378 2878	−5.607 8688	−10.371 1663	−10.531 0711
A_5	89.909 2005	14.689 1100	37.918 2595	27.607 2367
A_6	−237.846 2970	−33.547 8549	−85.040 7456	−49.451 6169
A_7	331.544 2639	48.360 0365	108.079 9417	56.381 3846
A_8	−231.236 7070	−36.011 9980	−71.747 6081	−35.749 6220
A_9	64.190 7466	10.667 7429	19.470 3943	9.500 5538
NP	62	105	58	31
RMS, %	0.0078	0.054	0.0086	0.126

TABLE 7. *Comparisons of critical constants*

T_c, K	ρ_c, mol/l	Reference
Parahydrogen		
32.984	15.27 ± 0.30	[9]
32.976	15.59 ± 0.05	[8]
32.934 [a]	15.59 ± 0.02 [b]	See footnotes.
32.953	15.59	Eq (5), this report.
Oxygen		
.....	13.44	[11]
154.77	12.	[12]
154.565	12.75	[13]
.....	13.333	[14]
.....	13.62	[4]
154.575 ± 0.01	13.628 ± 0.016	[15]
154.54	13.614	Table 1, this report.
154.52	13.52	Eq (5), this report.
Fluorine		
144.	.....	[18]
.....	12.4	[19]
.....	15.0	[20]
143.9	15.1	Eq (5), this report.
Neon		
44.39	23.96	[21]
44.43	.....	[24]
44.40 ± 0.02	.....	[25]
44.40	23.3	Eq (5), this report.

[a] L. A. Weber (unpublished) via data of [10].
[b] Via rectilinear diameter (R.D.G.).

4. Discussion

A long-standing problem for the computation of thermodynamic properties has been the lack of a satisfactory description of the orthobaric densities, or conversely of the saturation temperatures. The extraordinary accuracy of representation seen for H_2 and O_2 in tables 3 and 5, and for F_2 in the rms deviation of table 6, shows that eq (5) provides a solution for this problem. For oxygen in particular we see that (5) is valid over an enormous range of vapor densities. Uncertainties up to one percent in the lowest vapor density data are assigned by Weber [4].

Critical constants estimated via (5) depend upon the form of (5); upon the (often unknown) accuracy of data near T_c; and upon elimination of points near T_c. With densities derived from PVT data and a vapor pressure equation as in this report, it would be difficult to assign uncertainties to the estimated critical constants.

This report demonstrates the attractive property of eq (5) that values of T_c and ρ_c adequate for many applications are obtained in one step from the complete set of liquid and vapor densities, without the need for data close to the critical density.

5. References

[1] Goodwin, R. D., Formulation of a nonanalytic equation of state for parahydrogen, Nat. Bur. Stand. (U.S.), **73A** (Phys. and Chem.), No. 6, 585–591 (Nov.–Dec. 1969).

[2] Goodwin, R. D., Nonanalytic vapor pressure equation with data for nitrogen and oxygen, Nat. Bur. Stand. (U.S.), **73A** (Phys. and Chem.), No. 5, 487–491 (Sept.–Oct. 1969).

[3] Guggenheim, A. E., Thermodynamics, 2nd. ed., p. 141 (North-Holland Publishing Co., Amsterdam, 1950).

[4] Weber, L. A., Thermodynamic and related properties of oxygen from the triple point to 300 K at pressures to 330 atmospheres, private communication 9710, June 20, 1968.

[5] Hou, Y. C., and Martin, J. J., Physical and thermodynamic properties of trifluoromethane, J. Am. Inst. Chem. Engrs. **5** (1), 125 (1959).

[6] Fisher, M. E., Correlation functions and the critical region of simple fluids, J. Math. Phys. **5**(7), 944 (1964).
[7] Goodwin, R. D., Density-temperature formulae for coexisting liquid and vapor and for freezing liquid parahydrogen, Nat. Bur. Stand. (U.S.), **70A** (Phys. and Chem.), No. 6, 541–544 (Nov.–Dec. 1966).
[8] Roder, H. M., Weber, L. A., and Goodwin, R. D., Thermodynamic and related properties of parahydrogen from the triple point to 100 K at pressures to 340 atmospheres, Nat. Bur. Stand. (U.S.), Monogr. 94, 115 pages (Aug. 1965).
[9] Hoge, H. J., and Lassiter, J. W., Critical temperatures, pressures, and volumes of hydrogen, deuterium, and hydrogen deuteride, J. Res. NBS **47**, No. 2, 75–79 (Aug. 1951) RP2229.
[10] Diller, D. E., Refractive index of gaseous and liquid hydrogen, J. Chem. Phys. **49**(7), 3096 (1968).
[11] Mathias, E., and Kamerlingh Onnes, H., Communs. Phys. Lab. Univ. Leiden, No. 117 (1911).
[12] Hoge, H. J., Vapor pressure and fixed points of oxygen and heat capacity in the critical region, J. Res. NBS **44**, 321–345 (Mar. 1950) RP2081.
[13] Voronel, A. V., Chaskin, Yu. R., Popov, V. A., and Simkin, V. G., Soviet Phys. JETP **18**, 586 (1964).
[14] Prydz, R., Timmerhaus, K. D., and Stewart, R. B., The Thermodynamic Properties of Deuterium, Advances in Cryogenic Engineering, Vol. **13**, 384–396 (Plenum Press, 1967).
[15] Weber, L. A., The PVT surface of oxygen in the critical region; densities of saturated liquid and vapor, Cryogenic Engineering Conference, Los Angeles, June, 1969.
[16] Straty, G. C., and Prydz, R., fluorine PVT measurements and thermodynamic properties, in progress at this laboratory.
[17] Straty, G. C., and Prydz, R., The vapor pressure of liquid fluorine, presented at the Cryogenic Engineering Conference, Los Angeles, June, 1969.
[18] Cady, G. H., and Hildebrand, J. H., The vapor pressure and critical temperature of fluorine, J. Am. Chem. Soc. **52**, 3839 (1930).
[19] Fricke, E. F., The thermodynamics of oxygen, hydrazine, and fluorine, Report F–5028–101, Republic Aviation Corp., 1957.
[20] Baker & Adamson Product Information Tech. Bull. TA–85411, Fluorine Elemental, Gen. Chem. Div., Allied Chem. & Dye Corp., 40 Rector St., N.Y. 6, N.Y., October, 1961.
[21] Mathias, E., Crommelin, C. A., and Kamerlingh Onnes, H., The rectilinear diameter of neon, Ann. Physique **18**, 231 (1923).
[22] Gibbons, R. M., The equation of state of neon between 27 and 70 K, Cryogenics **9**(4), 251 (Aug., 1969).
[23] McCarty, R. D., and Stewart, R. B., Thermodynamic properties of neon from 25 to 300 K between 0.1 and 200 atmospheres, p. 84 in Advances in Thermophysical Properties, Serge Gratch, Editor, (A.S.M.E., New York 10017, 1965).
[24] Crommelin, C. A., and Gibson, R. O., Commun. Phys. Lab. Univ. Leiden, 185b (1927).
[25] Grilly, E. R., The vapor pressure of solid and liquid neon, Cryogenics **2**(4), 226 (1962).

(Paper 74A2–593)

JOURNAL OF RESEARCH of the National Bureau of Standards—A. Physics and Chemistry Vol. 74A, No. 2, March–April 1970

Synthesis and Growth of Fresnoite ($Ba_2TiSi_2O_8$) from a TiO_2 Flux and Its Relation to the System $BaTiO_3$-SiO_2

C. R. Robbins

Institute for Materials Research, National Bureau of Standards, Washington, D.C. 20234

(December 4, 1969)

Crystals of $Ba_2TiSi_2O_8$ (synthetic fresnoite) up to 5 mm in longest dimension have been grown by slow cooling of a TiO_2-rich liquid of initial composition $1BaO:1TiO_2:1SiO_2$. The synthetic crystals are essentially identical to their mineral equivalent in morphology, cleavage, optical properties and unit cell dimensions. X-ray powder diffraction data previously reported for the compound $BaTiSiO_5$ ("barium sphene") is that of $Ba_2TiSi_2O_8$. Apparently the compound $BaTiSiO_5$ has never been synthesized and the system $BaTiO_3$-SiO_2 is not binary.

Key words: $Ba_2TiSi_2O_8$; $BaTiSiO_5$; crystal growth; fresnoite; phosphor; piezoelectric; system $BaTiO_3$-SiO_2; TiO_2 solvent.

1. Introduction

Crystals of Fresnoite ($Ba_2TiSi_2O_8$) were found by Alfors, Stinson, Matthews, and Pabst [*1*][1] in a study of the minerals of eastern Fresno County, California. The mineral occurs as subhedral to euhedral tetragonal crystals, elongated slightly in the [001] direction, with forms {001}, {110} and one distinct cleavage, (001). Composition was established [*1*] to be $Ba_2TiSi_2O_8$ with traces of impurities by arc emission spectrographic analyses. The crystals ranged in size from 0.1 to 3 mm with an average longest dimension of 0.3 mm, and exhibited pleochroism in transmitted polarized light (from light yellow to colorless), anomalous blue interference colors and pale yellow fluorescence under ultraviolet light (2652 Å). The optical and x-ray data [*1*] are summarized in table 1. Alfors et al., also prepared synthetic $Ba_2TiSi_2O_8$ in formula proportions ($5\frac{1}{2}$ hr at 1350 °C) and obtained a sintered compact whose x-ray diffraction pattern was identical with that of the mineral.

The crystal structure of $Ba_2TiSi_2O_8$ was determined by Masse, Grenier, and Durif [*2*], using synthetic crystals, and independently by Moore [*3*], using a natural crystal from the type locality. Masse et al. reported growth of crystals from a stoichiometric oxide mixture melted at about 1350 °C and cooled at 40 °C per hour. They obtained a cell of $a=8.52$, $c=5.21$ Å for their synthetic crystals and Moore reported $a=8.52\pm0.01$, $c=5.210\pm0.005$ Å for the mineral crystal. Both structures were assigned to space group P4bm; R values of 11 percent for (hko), 13 percent for (okl) were obtained in reference [*2*], while an overall R value of 11.1 percent (all reflections) was obtained in reference [*3*]. Similarities of the structure of $Ba_2TiSi_2O_8$ to that of hardystonite ($Ca_2ZnSi_2O_7$) [*2*] and that of melilite $(Ca, Na)_2(Mg, Al)Si_2O_7$ [*3*] were noted. In the structure of $Ba_2TiSi_2O_8$, Si_2O_7 groups are linked to square pyramidal TiO_5 groups to form sheets that are

Table 1. *X-ray and optical crystallographic data for fresnoite* ($Ba_2TiSi_2O_8$)[a]

X-RAY DATA	
System:	Tetragonal
Space Group:	P4/mbn, P4bm or $P\bar{4}b2$
Unit Cell:	$a=8.52\pm0.01$ Å, $c=5.210\pm0.005$ Å
	$c/a=0.6115$
Density:	4.43 ± 0.02 (measured)
	4.45 (calculated)
Cell content:	$Z=2$
OPTICAL DATA	
Optic sign:	Uniaxial (−)
Refractive indices:	$w=1.775\pm0.003$
	$\epsilon=1.765\pm0.003$
Pleochroism:	O = colorless
	E = yellow

[a] Data of [*1*] for mineral type specimen from eastern Fresno County, California.

[1] Italicized figures in brackets indicate the literature references at the end of this paper.

parallel to (001) and are held together by Ba ions. An interesting feature of the structure is the presence of Ti in five-fold coordination in the square pyramid, with four Ti-O distances of 2.00 ± 0.04 Å and a fifth Ti-O distance of 1.66 ± 0.08 Å for the pyramidal oxygen atom [3].

$Ba_2TiSi_2O_8$ was prepared as a crystalline powder by Blasse [4] by heating mixtures of $BaCO_3$, TiO_2 and SiO_2 in oxygen at 1000 to 1100 °C. He obtained a unit cell of $a=8.52$, $c=5.21$ Å (in agreement with [1, 2, 3]) and reported a blue-green fluorescence under excitation with 254 mm radiation and with cathode rays. The spectral energy distribution of emission, the diffuse reflection spectra, the excitation spectra, the decay time of fluorescence ($3 \cdot 10^{-3}$s.) and the temperature dependence of the phosphor were studied. The exceptionally efficient fluorescent properties of $Ba_2TiSi_2O_8$ at room temperature were attributed to the presence in the structure of the pyramidal TiO_5 group.

The initial objectives of the present study were: (1) to grow small single crystals of $Ba_2TiSi_2O_8$ for other physical property measurements, and (2) to prepare crystals of the compound $BaTiSiO_5$ (reported by Rase and Roy [5] in their study of the system $BaTiO_3$-SiO_2) for x-ray analysis and comparison with crystals of synthetic sphene ($CaTiSiO_5$) previously described by Robbins [6], and Brower and Robbins [7].

2. Phase Relations

The phase diagram for the ternary system BaO-TiO_2-SiO_2 in the region of the composition $Ba_2TiSi_2O_8$ has not been reported. The work of Masse et al. [2] indicated congruent melting for $Ba_2TiSi_2O_8$ near 1350 °C.

In the course of the work on their phase diagram for the binary system $BaTiO_3$-SiO_2 (fig. 1) Rase and Roy [5] obtained tabular, biaxially positive crystals showing bluish interference colors and having an average index of refraction of 1.775. They assigned to them the formula $BaTiSiO_5$ and the congruent melting point 1400 °C. They noted [5] that the refractive index of the glass of mole ratio $1BaO:1TiO_2:1SiO_2$ was greater than that of the average index of the crystals (1.86 as compared with 1.77). This suggested a negative coefficient of thermal expansion for the crystals but the coefficient was found to be of the order of 50×10^{-7} per °C. Polymorphism was not observed. Rase and Roy [5] reported unindexed x-ray powder data for $BaTiSiO_5$ and suggested a structural similarity to sphene ($CaTiSiO_5$). Their x-ray data were subsequently indexed by ASTM personnel ($BaTiSiO_5$, card 11–150) on the basis of a tetragonal cell ($a=8.525$, $c=5.22$ Å), the cell later obtained by [1, 2, 3] for fresnoite, $Ba_2TiSi_2O_8$.

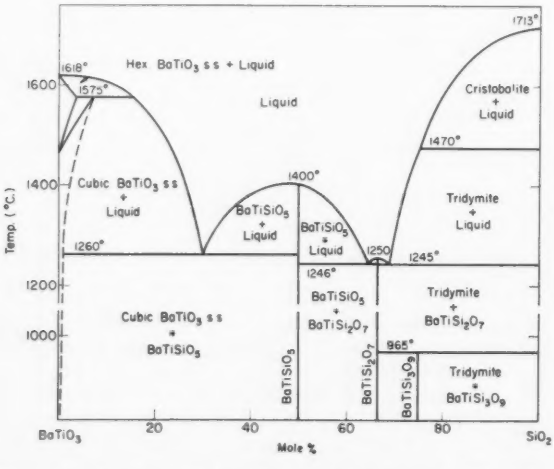

FIGURE 1. *Phase equilibrium diagram for the system* $BaTiO_3$-SiO_2, *Rase and Roy* [5].

The x-ray powder diffraction data for $BaTiSiO_5$ ([5], ASTM indexing) and for $Ba_2TiSi_2O_8$ [1] are listed in table 2 and shown schematically in figure 2. It may be concluded from comparison of the two patterns that the data are essentially identical, and the two independent studies were of the same compound. The composition $Ba_2TiSi_2O_8$ has been established by chemical analyses [1] and by single crystal x-ray structure determination [2, 3], and is therefore the composition of the phase obtained by Rase and Roy [5] in their study of the system $BaTiO_3$-SiO_2 and described by them as $BaTiSiO_5$, the barium analog of sphene. Apparently $BaTiSiO_5$ has not yet been synthesized and the system $BaTiO_3$-SiO_2 is not binary. The liquidus surface of the phase diagram for the system (fig. 1, [5]) must be that of a cut in the ternary system BaO-TiO_2-SiO_2. The congruent melting point of 1400 °C given for $BaTiSiO_5$ then represents a point on this liquidus surface at which the compound $Ba_2TiSi_2O_8$ would start to crystallize from a TiO_2-rich liquid of mole ratio $1BaO:1TiO_2:1SiO_2$. The large observed difference between index of refraction of glass and average index of crystals (1.86 versus 1.77) [5] apparently resulted from comparison of a glass of composition $1BaO:1TiO_2:1SiO_2$ with crystals of composition $2BaO \cdot 1TiO_2 \cdot 2SiO_2$.

3. Experimental Procedure

On the basis of the preceding conclusions two ternary compositions, $2BaO:1TiO_2:2SiO_2$ (fresnoite) and $1BaO:1TiO_2:1SiO_2$ ("barium sphene"), were prepared in 20 g amounts from high purity $BaCO_3$, TiO_2 and SiO_2, and thoroughly mixed mechanically. The mixtures in 40 ml platinum crucibles were heated in a platinum wound muffle furnace in air to near 1425 °C, held for 1 hr and cooled at 3 deg per hour to 1000 °C and then at 10 °C per hour to room temperature. Products obtained were examined by light microscopy, x-ray powder diffractometry and single crystal x-ray precession methods.

4. Results and Discussion

Crystals of $Ba_2TiSi_2O_8$ (fresnoite) up to 5 mm in longest dimension were obtained from the experiment

TABLE 2. *X-ray powder diffraction data for* $BaTiSiO_5$ *and* $Ba_2TiSi_2O_8$

$BaTiSiO_5$[a]			$Ba_2TiSi_2O_8$[b]		
d(Å)	*I*	*hkl*	*d*(Å)	*I*	*hkl*
			6.0	10	110
5.20	15	001	5.20	20	001
4.26	10	200	4.26	10	200
3.93	15	111	3.94	15	111
3.81	25	210	3.81+	20	210
3.29	60	201	3.305	50	201
			3.01+	10	220
2.694	30	310	2.695	20	310
2.606	45	002, 221	2.610	20	002, 221
2.394	15	311, 112	2.392	10	311, 112
2.222	15	202	2.222	10	202
2.151	35	212, 321	2.150	30	212, 321
2.069	25	410	2.065	25	410
2.010	10	330	2.010	10	330
1.971	15	222	1.975	10	401, 222
1.922	25	302, 411			
1.906	10	420			
1.882	30	331, 312	1.870	20	331, 312
1.621	15	412, 431	1.619	15	412
1.611	10	203			
1.593	15	511	1.591	15	332
1.582	20	520, 213	1.580	15	520, 213

[a] Data of Rase and Roy [5] indexed by ASTM on the basis of a tetragonal cell with $a=8.525$ Å and $c=5.22$ Å. Cu/Ni radiation, CuK$\alpha=1.5418$ Å.

[b] Data of Alfors, Stinson, Matthews and Pabst [1]. Their tetragonal unit cell has dimensions: $a=8.52$ Å, $c=5.210$ Å. Intensities were estimated from comparison with a photographic scale. Cu/Ni radiation, CuK$\alpha=1.5418$ Å.

with the $1BaO:1TiO_2:1SiO_2$ ("barium sphene") mixture described in section 3. The general appearance of the resulting product is shown in figure 3. The crystals are tetragonal first order prisms elongated in the [001] direction with forms {001} and {110}, the morphology previously observed for the mineral [1]. The crystals are transparent, colorless, uniaxial negative and show anomalous blue interference colors in transmitted polarized light. Pleochroism reported for the mineral (O = colorless, E = yellow) [1] was not observed for the synthetic material. Since chemical analyses of the type mineral [1] show a range of Fe content (Fe reported as FeO) of 0.77 to 1.0 weight percent, both the pleochroism and color of the mineral ("lemon or canary yellow" [1]) may result from the

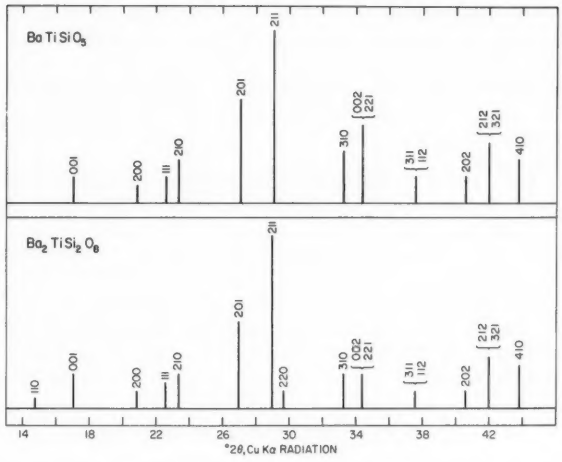

FIGURE 2. *Schematic partial x-ray powder diffraction patterns for* $BaTiSiO_5$ *and* $Ba_2TiSi_2O_8$.

The data for $BaTiSiO_5$ is from Rase and Roy [5] (ASTM indexing) and the data for $Ba_2TiSi_2O_8$ is from Alfors, Stinson, Matthews, and Pabst [1].

presence of Fe ions as a major impurity. The (001) cleavage reported for the mineral [1] was observed for the synthetic crystals. The piezoelectric response reported by [2] for synthetic $Ba_2TiSi_2O_8$ was also observed in this study. Unit cell dimensions obtained by x-ray powder diffractometry agree within limits of error, with the values $a=8.52$, $c=5.21$ Å reported by

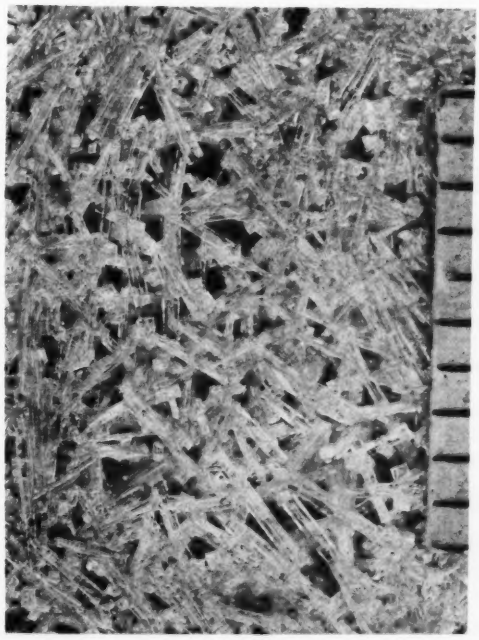

FIGURE 3. *Single crystals of* $Ba_2TiSi_2O_8$ *grown by slow cooling of a melt of initial mole ratio* $1BaO:1TiO_2:1SiO_2$.

The smallest division of the scale is 1 mm.

[1, 2, 3]. Optical and x-ray examination of a bulk sample of crystals and matrix from this experiment showed the presence of additional phases. The compound $BaTi_4O_9$ (Rase and Roy [8]) was identified by x-ray powder diffractometry as the next most abundant phase and was present in appreciable amounts.

The $2BaO:1TiO_2:2SiO_2$ experiment of section 3 gave sintered microcrystalline $Ba_2TiSi_2O_8$. The general appearance of the material suggested incipient melting. Unit cell dimensions agreed with those of crystals obtained by growth from the TiO_2 solvent ($1BaO:1TiO_2:1SiO_2$ mixture) indicating only slight solubility of TiO_2 in $Ba_2TiSi_2O_8$. Differential thermal analysis of the material to 1000 °C gave no indication of a phase transformation.

5. Summary and Conclusions

Crystals of synthetic fresnoite ($Ba_2TiSi_2O_8$) up to 5 mm in longest dimension have been grown by slow cooling of a TiO_2-rich melt of initial composition $1BaO:1TiO_2:1SiO_2$ in a small-scale experiment. The solubility of $Ba_2TiSi_2O_8$ in this liquid at 1400 °C is of the order of 86 percent by weight. The synthetic crystals are essentially identical to their mineral equivalent in morphology, cleavage, indices of refraction, anomalous interference colors and unit cell dimensions. The color and pleochroism of the type mineral may result from the presence of Fe ions as a major impurity. Solubility of TiO_2 in $Ba_2TiSi_2O_8$ is small. The system $BaTiO_3$-SiO_2 is not binary and the compound $BaTiSiO_5$ ("barium sphene") apparently has never been synthesized.

6. References

[1] Alfors, J. T., Stinson, M. C., Matthews, R. A., and Pabst, A., Seven new barium minerals from Eastern Fresno County, California, Amer. Mineral. **50,** 314–340 (1965).

[2] Masse, R., Grenier, J. C., and Durif, A., Structure Cristalline de la Fresnoite, Bull. Soc. fr. Minéral Cristallogr. **XC,** 20–23 (1967).

[3] Moore, P. B., and Louisnathan, J., Fresnoite: Unusual titanium coordination, Science **156,** 1361–1362 (1967).

[4] Blasse, G., Fluorescence of compounds with fresnoite ($Ba_2TiSi_2O_8$) Structure, J. Inorg. Nucl. Chem. **30,** 2283–2284 (1968).

[5] Rase, D. E., and Roy, R., Phase Equilibrium in the System $BaTiO_3$-SiO_2, J. Amer. Ceram. Soc. **38,** 389–395 (1955).

[6] Robbins, C. R., Synthetic $CaTiSiO_5$ and its germanium analogue ($CaTiGeO_5$), Mat. Res. Bull. **3,** 693–698 (1968).

[7] Brower, W. S., and Robbins, C. R., Growth of $CaTiSiO_5$ by the Czochralski method, J. of Cryst. Growth **5,** 233–234 (1969).

[8] Rase, D. E., and Roy, R., Phase equilibria in the system BaO-TiO_2, J. Amer. Ceram. Soc. **38,** 102–113 (1955).

(Paper 74A2–594)

JOURNAL OF RESEARCH of the National Bureau of Standards—A. Physics and Chemistry
Vol. 74A, No. 2, March–April 1970

Photoionization Study of $Fe(CO)_5$ and $Ni(CO)_4$

G. Distefano*

Institute for Materials Research, National Bureau of Standards, Washington, D.C. 20234

(December 5, 1969)

Photoionization yield curves from onset to 600Å, and ionization threshold values have been obtained for the ions $Fe(CO)_5^+$, $Fe(CO)_4^+$, $Fe(CO)_3^+$, $Fe(CO)_2^+$, $Fe(CO)^+$, Fe^+ and CO^+ from iron pentacarbonyl, and for $Ni(CO)_4^+$, $Ni(CO)_3^+$, $Ni(CO)_2^+$, $Ni(CO)^+$, Ni^+, and CO^+ from nickel tetracarbonyl. From these curves, information on the ionization-fragmentation processes of $Fe(CO)_5$ and $Ni(CO)_4$ under photon impact, have been obtained. Differences in the threshold energies as determined by photon and by electron impact methods increase with the fragmentation. The appearance potentials and the heats of formation of the metal-ions, agree within 0.1 eV, with those calculated from thermochemical data. The average bond dissociation energy of the neutral molecule agrees within 0.02 eV, with the thermochemical values. The kinetic shift for the formation of Fe^+ and Ni^+ ions is very small. The Ni^+ ion is most likely formed directly from the molecule ion rather than by a cascade fragmentation process.

Key words: Dissociation energies; $Fe(CO)_5$; heats of formation; ionization; mass spectrometry; $Ni(CO)_4$; vacuum ultraviolet spectroscopy.

1. Introduction

In recent years, the mass spectrometric study by electron impact of transition-metal carbonyls has received increasing attention [1, 2].[1] Although the data obtained in the same laboratory are well correlated [3, 4], they often differ from those obtained in other laboratories on the same molecules. Several reports are available on mass spectra and appearance potentials of the iron pentacarbonyl and nickel tetracarbonyl by electron impact [5 to 9] and one by photon impact without mass analysis [10] which determined the ionization potentials only. The agreement among the fragmentation patterns is satisfactory, considering that the spectra were obtained with different instruments, and under different experimental conditions such as electron energy and ion source temperature. However, the appearance potentials differ by as much as 1 eV or more especially for ions of low mass. Thus, the purpose of this work is to obtain more accurate values for the ionization thresholds for molecular and fragment ions, more reliable data for ion heats of formation, and bond dissociation energies in both the molecules and in the ions, and information on the ionization fragmentation processes under photon impact.

2. Experimental Procedure

Photoionization efficiency curves were obtained by means of the combined vacuum ultraviolet monochromator and mass spectrometer described in detail by Dibeler et al. [11, 12]. Data were obtained with an optical resolution of about 1Å, with an uncertainty in the absolute wavelength of 1Å or less over all wavelengths. The uncertainty in the reported relative ionization efficiency (ions per photon transmitted through the ion source) is of the order of 3 to 5 percent. It is ascribed principally to the uncertainty in measuring the number of electrons photoejected from a tungsten photon detector. At wavelength longer than 1200Å, we do not have a correction for the change of the quantum yield of the tungsten detector with the wavelength. All the data of figures 1 and 3 must be multiplied by a slowly decreasing factor going to longer wavelength. For this reason, the uncorrected part of the photoionization efficiency curves are plotted in different figures. The onset regions of the $Fe(CO)_5^+$, $Ni(CO)_4^+$ and $Ni(CO)_3^+$ ions have been repeated with a sodium salicylate detector with only minor differences noted. The samples were obtained from a commercial supplier. Mass spectrometric analysis showed no detectable impurities other than carbon monoxide. The following conversion factors were used throughout this paper.

$$1 \text{ eV molecule}^{-1} = 8065.73 \text{ cm}^{-1}$$
$$= 23.0609 \text{ kcal mol}^{-1}$$
$$1 \text{ kcal mol}^{-1} = 4.1840 \text{ kJ mol}^{-1}$$

3. Results and Discussion

Table 1 lists the relative abundances of the positive ions observed in the mass spectra of $Fe(CO)_5$ and

*NATO Fellow, Guest Worker at the National Bureau of Standards, 1968–69. Permanent address: Institute of Physical Chemistry, University of Perugia, Perugia, Italy.

[1] Figures in brackets indicate the literature references at the end of this paper.

TABLE 1. *Relative intensity of the ions in* $Fe(CO)_5$ *and* $Ni(CO)_4$ *mass spectra*

	Ref. [5][a]	Ref. [6]	Ref. [7]	Ref. [8][b]	Ref. [9]	This work
Energy in eV.	~25	30	50	50	70	21.22
Source temperature	Room temperature	250 °C	205 °C	150 °C	Room temperature	Room temperature
$Fe(CO)_5$						
$Fe(CO)_5^+$	30	25	18	43		10.3
$Fe(CO)_4^+$	24	35	22	50		11.6
$Fe(CO)_3^+$	12	18	11	22		2.2
$Fe(CO)_2^+$	95	30	24	36		18.8
$FeCO^+$	100	100	82	100		100.0
Fe^+	30	60	100	93		38.3
CO^+		10		"large"		1.8
$Ni(CO)_4$						
$Ni(CO)_4^+$	37		26	51	31.0	10.8
$Ni(CO)_3^+$	63		53	100	43.8	19.1
$Ni(CO)_2^+$	67		44	49	42.2	31.4
$Ni(CO)^+$	100		100	54	100.0	100.0
Ni^+	27		66	46	58.3	35.1
CO^+				"large"		21.3

[a] Derived from figure 2 of Ref. [5].
[b] Derived from figure 2 of Ref. [8].

$Ni(CO)_4$ at 21.22 eV (584Å). No metastable ions, double charged ions, or ions resulting from the rupture of the C—O bond were observed. The appearance potential of the CO^+ ion from these carbonyls is 14.01 ± 0.02 eV (885 ± 1Å). The threshold value and the shape of the curve (from the onset to 800Å) are exactly the same for those of CO^+/CO. Thus, the CO^+ ion is not formed by photon impact on the metal-carbonyls, but from molecular CO already present in the samples or formed by decomposition in the inlet system.

Comparing the relative abundances of table 1 with those previously reported [5, 9], we observe a smaller relative abundance for the ions of heavier mass. The apparent origin of the CO^+ and the relatively low intensity of the higher mass ions suggests that interpretation of results may be ambiguous due to decomposition [13, 14]. However, the threshold values of $Fe(CO)_4^+$, $Ni(CO)_3^+$, Fe^+ and Ni^+ ions show that these ions come from the molecular ion, and not from intermediate radicals. Therefore decomposition is not considered to have an important effect on the results. The differences between the present relative ion intensities and those previously reported can be ascribed to differences in source and inlet systems temperature [7], to the ionization beam, to its energy, to different apparatus and detectors.

$Fe(CO)_5^+$. Typical photoionization yield curves for the $Fe(CO)_5^+$ ion are shown in figures 1 and 2. The curve exhibits a weak onset at 1554 ± 1Å (7.98 ± 0.01 eV). Due to the size of the molecule, to its large number of electrons, and to the fact that the electron removed in the first ionization is a nonbonding or weakly bonding one (see later), the geometry of the ion is expected to remain the same as that of the molecule in its ground state. For these reasons the molecule ion is likely formed by $0' - 0''$ (or $1' - 1''$, etc.) transitions and no hot bands are expected on the low energy side of the threshold.

The threshold energy is lower than all electron impact data [5, 9], but it is very close to a previous photoionization value (7.95 eV) [10]. Taking the present threshold value as the heat of reaction, $\Delta H_0 = 184.0$ kcal mol^{-1} for $Fe(CO)_5 + h\nu \rightarrow Fe(CO)_5^+ + e$, and adding the heat of formation of the molecule [15],

$$\Delta Hf^\circ[Fe(CO)_5] = -175.4 \text{ kcal mol}^{-1},$$

the heat of formation of the ion, $\Delta Hf^\circ[Fe(CO)_5^+] = 8.6$ kcal mol^{-1} is obtained. This and the following thermodynamic values and threshold energies are summarized in table 2. This table also includes the lowest and highest threshold values obtained by electron impact. It is important to note that the appearance potentials for the M^+ and MCO^+ ions as measured by electron impact may differ by as much as 2 eV.

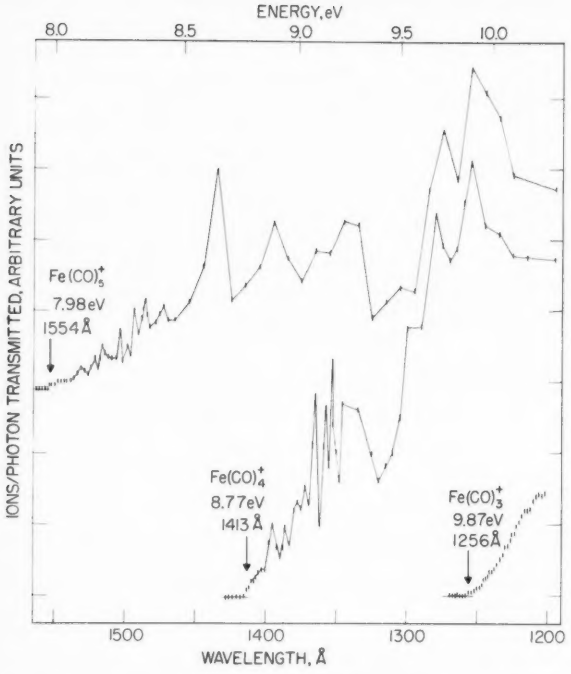

FIGURE 1. *Photoionization-yield curves from onset to 1200Å for $Fe(CO)_5^+$, $Fe(CO)_4^+$, and $Fe(CO)_3^+$ ions of iron pentacarbonyl.*

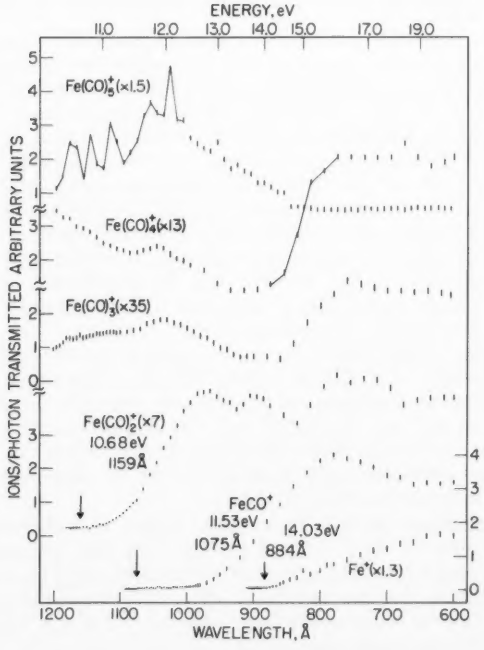

FIGURE 2. *Photoionization-yield curves from 1200 to 600Å for molecule and fragment ions of iron pentacarbonyl.*

The curve shows many autoionizing Rydberg levels from the onset to 855Å (14.50 eV) at which energy they appear to converge. The shape of the curve between 1000 and 855Å suggests that there is a slow decrease in excitation of more highly excited states of $Fe(CO)_5^+$. Where these peaks disappear, the molecule ion decomposes to form the excited $Fe(CO)_4^+$ fragment ion. At this energy the $Fe(CO)_4^+$ curve (see below) shows a new, abrupt and intense onset, which can be ascribed to a second ionization threshold. From 850 to 600Å, the molecule ion curve is very constant.

$Fe(CO)_4^+$. The $Fe(CO)_4^+$ ion shows (see figs. 1 and 2) a weak onset at 1413 ± 1Å (8.77 eV). The previous values [5, 9] range between 8.4 and 9.2 eV. Pignataro and Lossing [13] assigned the lower value to the direct ionization of the $Fe(CO)_4$ radical produced by thermal decomposition, whereas, the electron impact value of 9.1 eV was ascribed to the process

$$Fe(CO)_5 + e \rightarrow Fe(CO)_4^+ + CO + 2e.$$

The present value can be taken as the heat of reaction, $\Delta H_0 = 202.2$ kcal mol^{-1} for

$$Fe(CO)_5 + h\nu \rightarrow Fe(CO)_4^+ + CO + e.$$

Using the heats of formation for $Fe(CO)_5$ and CO (-26.416 kcal mol^{-1}) [16], the value

$$\Delta Hf^\circ[Fe(CO)_4^+] = 53.2 \pm 2 \text{ kcal mol}^{-1}$$

is obtained. From the onset to 1200Å the curve shows considerable structure due to autoionization. This is clearly correlated with the structure in the molecule ion curve, suggesting that the same processes are producing excited $Fe(CO)_5^+$ and $Fe(CO)_4^+$ ions. A similar process is observed in the $Ni(CO)_4$. From about 1200Å the $Fe(CO)_4^+$ ion curve is no longer parallel to the molecular ion curve and its intensity slowly diminishes until it exhibits a new onset at 855Å as discussed above.

$Fe(CO)_3^+$. The $Fe(CO)_3^+$ ion curve starts (see figs. 1 and 2) with a very weak steplike onset at 1256 ± 1Å (or 9.87 eV). This is a few tenths of an eV lower than the energy at which the $Fe(CO)_4^+$ ion curve begins to go down away from the molecule ion curve. From 1040 to 600Å the $Fe(CO)_3^+$ and $Fe(CO)_4^+$ ion curves are very similar. Likely the $Fe(CO)_3^+$ ion is coming from $Fe(CO)_4^+$ ion by a cascade process. The heat of formation,

$$\Delta Hf^\circ[Fe(CO)_3^+] = 105 \pm 2 \text{ kcal mol}^{-1},$$

is obtained from the threshold value.

The initial part of the curve exhibits a number of steplike features at an average interval of 426 cm^{-1}. This value may be compared with the Fe-CO stretching frequency ν_{13} in the neutral molecule of 431 cm^{-1} [17]. This initial part of the curve does not have the same shape as the curve for the distribution of the thermal energy of the neutral molecule.

$Fe(CO)_2^+$. The $Fe(CO)_2^+$ ion curve starts at 1159 ± 1Å (10.68 eV) (see fig. 2). The onset region shows a tail on the low energy side with superimposed unresolved

TABLE 2. *Threshold values and heats of formation of the positive ions from* $Fe(CO)_5$ *and* $Ni(CO)_4$.

	Photoionization threshold (eV)[a]	Electron impact threshold (eV)[b]	$\Delta Hf°$[c]	
			eV	*kcal mol*$^{-1}$
$Fe(CO)_5$				
$Fe(CO)_5^+$	7.98 ± 0.01	8.14 − 8.53	0.37 ± 0.02	8.6 ± 0.5
$Fe(CO)_4^+$	8.77 ± 0.1	8.34 − 10.0	2.31 ± 0.1	53.2 ± 2
$Fe(CO)_3^+$	9.87 ± 0.1	9.89 − 10.3	4.55 ± 0.1	105 ± 2
$Fe(CO)_2^+$	10.68 ± 0.1	10.92 − 11.8	6.51 ± 0.1	150.1 ± 2
$FeCO^+$	11.53 ± 0.1	12.9 − 14.0	8.51 ± 0.1	196.2 ± 2
Fe^+	14.03 ± 0.1	14.7 − 16.1	12.35 ± 0.1	284.7 ± 2
			[d] 12.28	[d] 283.16
$Ni(CO)_4$				
$Ni(CO)_4^+$	8.32 ± 0.01	8.35 − 8.75	2.07 ± 0.02	47.8 ± 0.5
$Ni(CO)_3^+$	8.77 ± 0.02	8.89 − 9.36	3.58 ± 0.02	82.6 ± 0.5
$Ni(CO)_2^+$	10.10 ± 0.1	10.21 − 10.7	6.14 ± 0.1	141.7 ± 2
$NiCO^+$	11.65 ± 0.1	12.17 − 13.5	8.84 ± 0.1	203.8 ± 2
Ni^+	13.75 ± 0.1	14.45 − 16.0	12.09 ± 0.1	278.7 ± 2
			[d] 12.15	[d] 280.24

[a] See text for discussion of estimated uncertainty in threshold values. Only Fe^+ and Ni^+ ions threshold have been corrected for the thermal energy the neutral molecules possess.
[b] Total range of reported electron impact values, (Refs. [5] through [9]).
[c] The assumed processes are $M(CO)_x + h\nu \rightarrow [M(CO)_{x-n}]^+ + nCO$.
[d] Calculated value from heat of formation and ionization potential of the metal atom [19, 20].

autoionization peaks, followed by steplike features at an average interval of 461 cm^{-1}. This value is to be compared with the Fe-CO stretching frequency ν_8 in the neutral molecule of 474 cm^{-1} [17]. These steplike features are a peculiarity of $Fe(CO)_3^+$ and $Fe(CO)_2^+$ ion curves. All other curves, both for iron and nickel carbonyls, show either autoionization peaks or a smooth continuum. Perhaps autoionization does not occur because the competing process of predissociation is much more probable. A similar effect has been reported for NH_3^+ molecule ion [18]. The remainder of the curve has maxima at about 960, 900, and 750Å. From 960 to 600Å the curve is very similar to that of the $Fe(CO)_4^+$ ion, again suggesting the production of the $Fe(CO)_n^+$ ions from the $Fe(CO)_{n+1}^+$ ions. From the threshold value, the $\Delta Hf°[Fe(CO)_2^+]$ is 150.1 ± 2 kcal mol^{-1}.

$FeCO^+$. The $FeCO^+$ ion curve starts with a weak, very long tail (see fig. 2) at 1075 ± 1Å (11.53 eV). From the threshold value, $\Delta Hf°(FeCO^+)$ is 196.2 ± 2 kcal mol^{-1}. The ion yield curve rises quickly starting at about 980Å and peaks at 780Å.

Fe^+. The Fe^+ ion curve also starts with a weak very long tail (see fig. 2). The onset is at 884 ± 2Å (14.03 eV), which might become 14.23 eV if the thermal energy of the molecule at 298 K (0.2 eV as calculated from ir frequencies [17]) is taken into account. From this value $\Delta Hf°(Fe^+)$=284.7 kcal mol^{-1} is obtained. By using heat of formation ($\Delta Hf°(Fe)$=99.5 kcal mol^{-1} [19],

$$\Delta Hf_0°Fe(CO)_5 = -175.8 \text{ kcal mol}^{-1} \text{ [15]},$$

$\Delta Hf_0°CO$=−27.199 kcal mol^{-1} [16]) and I(Fe)=7.87 eV [20] to calculate the theoretical threshold of the process $Fe(CO)_5 + h\nu \rightarrow Fe^+ + 5\ CO + e$, 13.92 eV is obtained if the quantities involved are considered at 0 K, and 14.16 eV at room temperature. Thus, the results agree with thermochemical values to within about 0.1 to 0.3 eV.

A calculation based on the Quasi Equilibrium Theory shows that the mean rate of decomposition for molecules of excitation energy equal to the activation energy (that is to the difference between dissociative and molecular ionization threshold) for the formation of the first fragment ion, is quite large: ~ 10^7 s^{-1} for $Fe(CO)_5$ and ~ 10^{11} s^{-1} for $Ni(CO)_4$ [21]. Very little if any kinetic shift [22] is therefore to be expected for the formation of $Fe(CO)_4^+$ and $Ni(CO)_3^+$ ions. Considering that the fragmenting ion becomes smaller and smaller with the fragmentation, the kinetic shift for the formation of the naked metal ions is expected to be no more than few hundredths of an electron volt. Actually the kinetic energy of the fragments corresponds to a temperature between 0 and 298 K. So the difference between calculated and experimental values is partially ascribed to translational energy (≤ 0.2 eV) and partially to internal excitation of the fragments. From these considerations an uncertainty of about 0.1 eV is estimated for all the fragmentation processes.

Average Bond Energies. From the threshold energies of Fe^+ from $Fe(CO)_5$, and the ionization energies of atomic iron and of $Fe(CO)_5$, it is possible to obtain the average bond dissociation energies for the neutral molecule $\bar{D}[Fe-(CO)_5]$ = 1.25 ± 0.03 eV, and for the molecular ion $\bar{D}$

$$[Fe-(CO)_5^+] = 1.23 \pm 0.03 \text{ eV}.$$

The first value must be compared with 1.20 eV from thermochemical data [21] and with 1.24 eV as calculated from the heats of formation of $Fe(CO)_5$, Fe and CO. These data suggest that the first ionization results by removing the electron from a virtually non-bonding or weakly bonding molecular orbital with a prevailing metal character. This agrees with the nature of the last occupied molecular orbital as calculated for the metal hexacarbonyls [24].

$Ni(CO)_4^+$. A typical photoionization field curve for the $Ni(CO)_4^+$ ion is shown in figures 3 and 4. The onset occurs at 1490 ± 1Å (8.32 ± 0.01eV). This value is to be compared with the previous photoionization value of 8.28 eV [10]. As discussed for the $Fe(CO)_5^+$ ion, the $Ni(CO)_4^+$ ion also is likely formed by $0'-0''$ (or $1'-1''$, etc.) transitions. From the threshold value and the heat of formation of $Ni(CO)_4$ (-144.10 kcal mol^{-1}) [15] the ionic heat of formation,

$$\Delta Hf^\circ[Ni(CO)_4^+] = 47.8 \pm 0.5 \text{ kcal mol}^{-1}$$

is obtained. Below 1450Å, the curve shows many autoionization peaks every $0.02-0.03$ eV, which compose broad maxima between 1450 and 1350Å and between 1310 and 1060Å. From the latter wavelength to 600Å, the curve is constant or slowly decreases in intensity.

$Ni(CO)_3^+$. The onset of the $Ni(CO)_3^+$ ion (see figs. 3 and 4) shows weak autoionization levels peaking at 1413, 1410, 1407, 1403, 1397, 1394, 1390, and 1388Å. These energies and the shape of the curve are the same as those of the molecular ion in the corresponding region. This again suggests that the $Ni(CO)_3^+$ ion is coming from the molecular ion and not from a $Ni(CO)_3$ radical formed by decomposition. The formation process of this ion at this energy seems to be:

$$\text{(a)}\ Ni(CO)_4 + h\nu \rightarrow Ni(CO)_4^*$$

$$\text{(b)}\ Ni(CO)_4^* \rightarrow Ni(CO)_4^{+}{}^* + e$$

$$\text{(c)}\ Ni(CO)_4^{+}{}^* \rightarrow Ni(CO)_3^+ + CO$$

Process (a) and (b) refer to the autoionization of the molecule. Process (c) is ascribed to predissociating levels of the molecule ion leading to the $Ni(CO)_3^+$ ion. If this is true, the threshold of the $Ni(CO)_3^+$ ion is not affected by the thermal energy present in the neutral molecule. The thermal energy if present would have obscured the details of the curve structure. From the threshold value of 1414 ± 1Å (8.77 eV), and the heats of formation of $Ni(CO)_4$ and CO,

$$\Delta Hf^\circ[Ni(CO)_3^+] = 82.6 \text{ kcal mol}^{-1}$$

is calculated.

$Ni(CO)_2^+$. The steplike, very weak onset for $Ni(CO)_2^+$ ion occurs at 1228 ± 1Å(10.10 eV) (see fig. 4) resulting in a heat of formation, $\Delta Hf^\circ[Ni(CO)_2^+] = 141.7 \pm 2$ kcal mol^{-1}. The curve shows a number of autoionization levels in the initial part, and a broad maximum between 985 and 895Å. From the latter energy to 600Å, the $Ni(CO)_3^+$ and $Ni(CO)_2^+$ curves are very similar.

$NiCO^+$. From the threshold value of 1064 ± 1 Å (11.65 eV) the heat of formation $\Delta Hf^\circ[NiCO^+] = 203.8$ kcal mol^{-1} is calculated. The curve, shown in figure 4, exhibits the expected tail on the low energy side.

Ni^+. The Ni^+ ion curve starts with some weak autoionization peaks (see fig. 4). The shape of the curve at

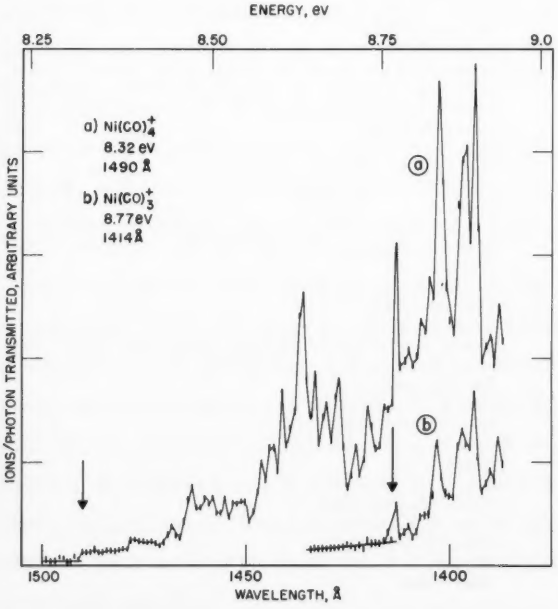

FIGURE 3. *Photionization-yield curves from onset to 1380Å for $Ni(CO)_4^+$ and $Ni(CO)_3^+$ ions from nickel tetracarbonyl.*

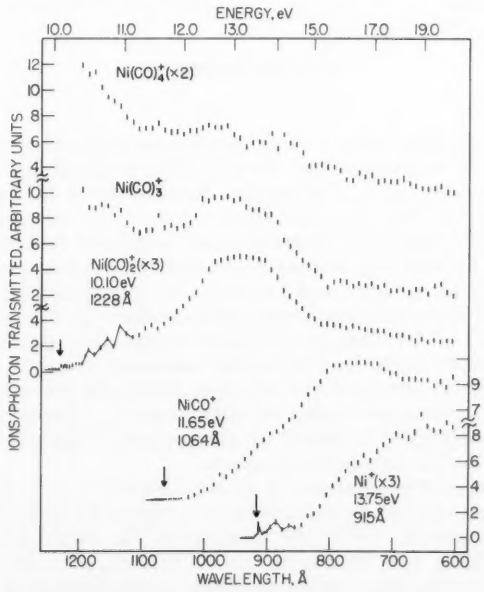

FIGURE 4. *Photoionization-yield curves from 1200 to 600Å for molecule and fragment ions of nickel tetracarbonyl.*

the onset, and the absence of a low energy tail suggest that the Ni^+ ion is not formed by a cascade process, but directly from the molecule ion. The onset is at 915±1 Å (13.55 eV). Considering the thermal energy the neutral molecule possesses at 298 K (0.2 eV as calculated from ir frequencies [25] the threshold value might become 13.75 eV. From this value $\Delta Hf°(Ni^+)=278.7$ kcal mol^{-1} is obtained.

From heats of formation ($\Delta Hf°(Ni)=102.7$ kcal mol^{-1} (19), $\Delta Hf°_0$ $Ni(CO)_4=-144.877$ kcal mol^{-1} [15] and from I(Ni)=7.63 eV [20], the theoretical threshold for the Ni^+ ion is 13.82 eV at 298 K and 13.63 eV at 0 K. As for Fe^+ ion the kinetic shift involved in the production of this ion is very small. The increase of the translational and rotational degrees of freedom due to the fragmentation, could account for the difference between calculated (at 0 K) and experimental threshold value. Again the data show that the fragments possess kinetic energy corresponding to a temperature between 0 and 298 K. From the agreement between experimental and calculated threshold value, an error of about 0.1 eV is estimated for the fragmentation processes.

Average Bond Energy. The average bond dissociation energy for the neutral molecule and for the molecule ion (obtained as for the iron-carbonyl) are $\bar{D}[Ni\text{-}(CO)_4]=1.53\pm0.03$ eV and $\bar{D}[Ni\text{-}(CO)_4^+]=1.36\pm0.03$ eV respectively. The first value should be compared with 1.53 eV obtained from the thermochemical bond energy [26] and from the heats of formation of $Ni(CO)_4$, Ni and CO. The first ionization results from removing the electron from a partially bonding molecular orbital with prevailing metal character, in agreement with a calculated molecular orbital energy level diagram [27].

4. Conclusion

In electron impact experiments, ions formed by successive decompositions show a weak long tail on the low energy side. Due to the distribution of thermal energy of the electrons ejected from a hot filament, the threshold value determination is difficult for these ions by electron impact technique. For this reason, the bond energies and the heats of formation for the metal ions calculated from data obtained by electron impact [5–9] disagree with those obtained by thermochemical methods. The better resolution obtained by photon impact and the different threshold law allow one to obtain more accurate data. In fact bond energies and $\Delta Hf°(M^+)$ obtained by photon impact agree well with the thermochemical values.

The curves obtained by photon impact show several peaks assigned to autoionization processes previously not reported. Often the features of the $M(CO)_n^+$ ion curve are very similar to that of $M(CO)_{n+1}^+$ ion curve. Likely this fact can be ascribed to the formation of the lower mass ion from that with one more CO ligand, even if metastable ions are not observed to confirm the fragmentation paths. The relative abundances of the ions differ from the values obtained by electron impact as discussed.

The author gratefully acknowledges helpful discussions with Dr. V. H. Dibeler and Dr. H. M. Rosenstock and the use of the facilities of the Mass Spectrometry Section.

5. References

[1] Bruce, M. I., Advan. Organomet. Chem., **6,** 273 (1968).
[2] Chambers, D. B., Glockling, F., and Light, J. R. C., Quart. Rev., **22,** 317 (1968).
[3] Distefano, G., Innorta, G., Pignataro, S., and Foffani, A., J. Organomet. Chem., **14,** 165 (1968).
[4] Innorta, G., Distefano, G., and Pignataro, S., Intern. J. of Mass Spectrometry and Ion Phys., **1,** 435 (1968).
[5] Winters, R. E., and Kiser, R. W., Inorg. Chem., **3,** 699 (1964).
[6] Foffani, A., Pignataro, S., Cantone, B., and Grasso, F., Z. Physik. Chem. (Frankfurt), **45,** 79 (1965).
[7] Bidinosti, D. R., and McIntyre, N. S., Can. J. Chem., **45,** 641 (1967).
[8] Junk, G. A., and Svec., H. J., Z. Naturforsch. **23b,** 1 (1968).
[9] Schildcrout, S. M., Pressley, G. A., Jr., and Stafford, F. E., J. Am. Chem. Soc., **89,** 1617 (1967).
[10] Vilesov, F. I., and Kurbatov, B. L., Doklady Akad. Nauk. SSSR, **140,** 1364 (1961).
[11] Dibeler, V. H., and Reese, R. M., J. Res. Nat. Bur. Stand. (U.S.) NBS, **68A,** 409 (Phys. and Chem.), No. 4 (July–Aug. 1964).
[12] Dibeler, V. H., and Walker, J. A., J. Opt. Soc. Am., **57,** 1007 (1967).
[13] Pignataro, S., and Lossing, F. P., J. Organomet. Chem., **11,** 571 (1968).
[14] Day, J. P., Pearson, R. G., and Basolo, F., J. Am. Chem. Soc., **90,** 6933 (1968).
[15] Wagman, D. D., and Evans, W. H., private communication.
[16] Wagman, D. D., Evans, W. H., Parker, V. B., Halow, I., Bailey, S. M., and Schumm, R. H., Selected Values of Chemical Thermodynamic Properties, Nat. Bur. Stand. (U.S.), Tech. Note 270–3 (1968).
[17] Edgell, W. F., Wilson, W. E., and Summit, R., Spectrochimica Acta, **19,** 863 (1963).
[18] Chupka, W. A., and Russell, M. E., J. Chem. Phys., **48,** 1527 (1968).
[19] J.A.N.A.F. Thermochemical Tables, The Dow Chemical Co., Midland, Michigan, PB 168 370(1965), 370–1(1966), 370–2 (1967).
[20] Moore, C. E., Atomic Energy Levels, Nat. Bur. Stand. (U.S.), Circ. 467 (1968).
[21] Rosenstock, H. M., and Krauss, M., Adv. Mass Spectrometry, Vol. 2, and references (Pergaman Press, New York, 1962).
[22] Steiner, B., Giese, C. F., and Inghram, M. G., J. Chem. Phys., **34,** 189 (1961).
[23] Cotton, F. A., Fischer, A. K., and Wilkinson, G., J. Am. Chem. Soc., **81,** 800 (1956).
[24] Beach, N. A., and Gray, H. B., J. Am. Chem. Soc., **90,** 5713 (1968).
[25] Jones, L. H., McDowell, R. S., and Goldblatt, M., J. Chem. Phys., **48,** 2663 (1963).
[26] Fischer, A. K., Cotton, F. A., and Wilkinson, G., J. Am. Chem. Soc., **79,** 2044 (1957).
[27] Schreiner, A. F., and Brown, T. L., J. Am. Chem. Soc., **90,** 3366 (1968).

(Paper 74A2–595)

Symposium on Electronic Density of States

Electronic Density of States was the subject of the 3d Materials Research Symposium, sponsored by, and held at the National Bureau of Standards, Gaithersburg, Md. on November 3–6, 1969. Attention was focussed on the correlation of various experimental and theoretical techniques such as optical methods; photoelectron, soft x-ray, and ion neutralization spectroscopy; specific heat; Knight shift; and magnetic susceptibility. Band theory and many-body effects, as they relate to the electronic density of states, were included.

Approximately 100 papers were presented at these sessions, including 16 invited presentations. Six of these invited papers are being published in this issue of the Journal; the remaining ten will appear in succeeding issues. All of the papers presented at the Symposium will be published by the National Bureau of Standards as Special Publication 323 which will appear later this year.

JOURNAL OF RESEARCH of the National Bureau of Standards—A. Physics and Chemistry
Vol. 74A, No. 2, March-April 1970

The Band Structure Problem*

J. M. Ziman

H. H. Wills Physics Laboratory, Bristol, BS 8, 1TL, England

(October 10, 1969)

The numerical solution of the Schrödinger equation for an electron in a dense assembly of atoms (*i.e.* a solid or liquid metal or semiconductor) has made great progress in the past ten years. This is not merely a consequence of greater computing power; we now have a much better grasp of the mathematical theory of such solutions.

By 1960 a number of practical methods had been devised for the computation of the electronic structure of ordered crystals, but these lacked intuitive interpretation. The first advance was to rewrite the OPW method in terms of pseudopotentials, thus making sense of the free-electron theory of metals. This development has proved particularly valuable in semiquantitative and empirical investigations of Fermi surfaces, transport properties, lattice dynamics, cohesion, *etc.*, but we have had to wait until recently for a rigorous analysis of the criteria for convergence of the various types of model potential or pseudopotential that have been postulated.

The next step was to show that the KKR (Green function) method could also be expressed as a pseudopotential, and then to demonstrate that this was also a form of APW expansion. The relative computational power of these two methods can thus be analyzed, and questions answered concerning the fulfillment of the empty lattice test, the apparent lack of uniqueness of the expansions, the advantages of "folding" matrix elements from distant points of the reciprocal lattice, and the introduction of contributions from the interstitial potential.

At this stage, the connections between the band structure problem and the t-matrix theory of scattering were uncovered, and d-bands were seen to arise as resonances of the muffin-tin wells. The KKR matrix could now be rewritten as a mixture of pseudopotential and tight-binding elements, in harmony with the empirical model Hamiltonian representations of hybridised s-p and d-bands. This method not only permits more rapid computations, but shows clearly how the width and position of such bands should depend on the atomic potential.

Some problems still remain. For example, present techniques do not seem adequate for first-principles calculations on molecular crystals, where the anisotropy of the interstitial potential (*i.e.* easy channels along bonds, but high hills between layers or chains) is probably the dominant feature.

As for disordered systems—we know little for certain and nothing quantitatively. The linear chain model has been fully studied but is quite irrelevant to the three-dimensional case. The present theoretical confusion is exemplified by the equiconcentration substitutional alloy in the tight-binding limit; some formulae give only one band, others allow two. Again, the very possibility of producing band gaps by diffraction of free electrons in a topologically disordered system (*e.g.* amorphous Ge) has not been demonstrated mathematically with any rigor.

Key words: APW; band structure; density of states; disordered systems; KKR; pseudopotential; t-matrix; molecular crystals.

1. Algebra vs. Arithmetic

Any scientific problem or puzzle can seem interesting and significant if one gets sufficiently involved in it: the difficulty sometimes is to persuade other people of this importance. How should we defend our interest in the Electronic Density of States to an unprejudiced tribunal?

Not, surely, in terms of immediate use, but of long term understanding. Electrons being the glue of all "materials", their states within condensed matter are of fundamental importance. No quantitative estimate of any property of a metal, semiconductor, insulator, glass, liquid, mineral, *etc.*, can begin without information about these states. In fact, we want all the wave

*An invited paper presented at the 3d Materials Research Symposium, *Electronic Density of States*, November 3–6, 1969, Gaithersburg, Md.

functions of all the electrons outside of the closed shells—a tall order, which cannot be fulfilled by direct experiment. The next best thing is the energy spectrum, or "density of states," although as we shall learn in the course of this symposium, that cannot always be deduced unambiguously from observed phenomena.

Progress in this field therefore depends on sound theoretical analysis of the hypothetical possibilities, as well as careful experimental investigation of the facts. The calculation of electronic band structure is thus the central mathematical problem of solid state physics. Every "exciting" topic or mysterious phenomenon—superconductivity, the Kondo effect, ferromagnetism, Fermi surfaces, the Gunn effect, Josephson tunnelling, *etc.*,—eventually depends for its computable parameters on this mundane task.

It is sometimes argued, by the deeply unimaginative follower of scientifc fashion, that this problem has been solved long ago, and can safely be left to the brute strength of more and more powerful computers. This is quite wrong; these elephants must be goaded and guided by experienced *mahouts*, whose skill is to see in advance the type of answer that is to be obtained, and then to deploy the minimum of force to lever away the obstacles. A ream of computer print-out is useless unless it agrees so perfectly with experiment that we need never look back and see why and how it went wrong. Our task is to devise techniques for the theoretical mastery of ever more complex systems, which requires at every stage that we know exactly what we are doing, analytically as well as numerically.

This is well illustrated by the recent history of our subject. Let me express this in personal terms. A little more than ten years ago, in gathering material for a monograph [1] of which one chapter covered this topic, I found that many techniques of band structure computation had been proposed and tried out, but that there were very few cases where the results had been confirmed experimentally, or where they gave any insight into the actual electronic structure of the materials. It was simply not obvious, for example, that almost all the calculated band structures for metals could have been derived from the free electron system by perturbation effects at the zone boundaries, because nobody had programmed his computer to print out the data in that form. We knew from the success of the free electron *model* that this could not be very far from the truth, but we had not the imagination to rewrite the algebra so as to see how this must arise within whatever method of calculation we might happen to use.

In the past decade, of course, computational techniques have improved enormously in accuracy and power, so that a whole body of expertise is now available for application in any particular case [2]. Given the exact one-electron potential of a crystalline solid, we can compute the band structure to almost any desired degree of accuracy. But the trouble is that we do not always have this potential, complete with all the electron-electron terms, spin-orbit interaction, core polarization, exchange and correlation effects and so on, so that our first-principles computations just miss the answers we are seeking. Without an appeal to the basic algebraic principles and governing features of the model, we then flounder around, trying to adjust the parameters by trial and error. Somebody else, using a different "method" may get a different answer: is this due to deep discrepancies in the fundamental assumptions, or to errors of approximation, or just numerical mistakes?

2. Pseudism

Now recall how our minds have been liberated by the pseudopotential concept. There is no need to explain this to the present audience. Let us suppose that we had tried to express the Bloch function of wave vector $\mathbf{k}$ by a sum of simple plane waves

$$\psi_{\mathbf{k}} = \Sigma_{\mathbf{g}} \alpha_{\mathbf{g}} e^{i(\mathbf{k}+\mathbf{g})\cdot\mathbf{r}}, \tag{1}$$

where $\mathbf{g}$ runs through the reciprocal lattice: we should have to solve the infinite set of linear equations

$$\{|\mathbf{k}+\mathbf{g}|^2 - \mathscr{E}\}\alpha_{\mathbf{g}} + \Sigma_{\mathbf{g}'} \mathscr{V}(\mathbf{g}-\mathbf{g}')\alpha_{\mathbf{g}'} = 0 \tag{2}$$

where $\mathscr{V}(\mathbf{g}-\mathbf{g}')$ is a Fourier component of the periodic potential in the lattice and $\mathscr{E}$ is the energy of the state we are after. By rewriting the equations in terms of orthogonalized plane waves we can show that the whole problem is equivalent to solving a very similar set of equations

$$\{|\mathbf{k}+\mathbf{g}|^2 - \mathscr{E}\}\beta_{\mathbf{g}} + \Sigma_{\mathbf{g}'} \Gamma_{\mathbf{g}\mathbf{g}'}\beta_{\mathbf{g}'} = 0, \tag{3}$$

in which the pseudopotential components $\Gamma_{gg'}$ are much smaller than the original set $\mathscr{V}(\mathbf{g}-\mathbf{g}')$. Thus, the whole problem is equivalent to the perturbation of free electron waves by a weak pseudopotential and can be solved by elementary computation. For a perfect Bravais lattice the value of $\mathscr{V}(\mathbf{g}-\mathbf{g}')$ or of $\Gamma_{gg'}$ is a function only of the potential associated with a single atom or ion—in the language of x-ray diffraction, it is just the "atomic form factor" in the formula for diffraction by an assembly of such objects at the appropriate Bragg angle. The band structures of most ordinary metals, and many semiconductors, can be read at a glance. Not only does this provide us with an admirable

parametrization of Fermi surfaces, optical spectra, *etc.*, in perfect crystals, but can be extended to include almost all the properties of thermally excited, impure or disordered materials—electron-phonon interactions, electrical conductivity of solid and liquid metals, lattice dynamics, phase stability of alloys, *etc.* In moments of enthusiasm [3,4,5] we may perhaps be forgiven for pretending that all the problems of the theory of metals are cured by a strong dose of "pseudism". It is a wonderful model for zeroth order calculations, and the ideal do-it-yourself kit for the enthusiastic amateur. It had the effect of turning band structure theory from a rule of thumb *technology* into an elegant *science*.

Nevertheless, the pseudopotential method is not the ultimate solution to the band structure problem. In the first place, the program of replacing the true atomic potential by a localized pseudopotential, independent of energy and momentum, cannot be fulfilled exactly. If, like Herman and his colleagues [6] one is trying to make very accurate first principles calculations, nothing is gained by rewriting the OPW equations in this form. Indeed, there is a danger that the apparent simplicity and rapid convergence of the pseudopotential equations may seduce us into further approximations which hide important effects; once having lost touch with the exact equations, we slide easily into a sloppy mess where qualitative and quantitative, first principles and parametrized, features are inextricably confused.

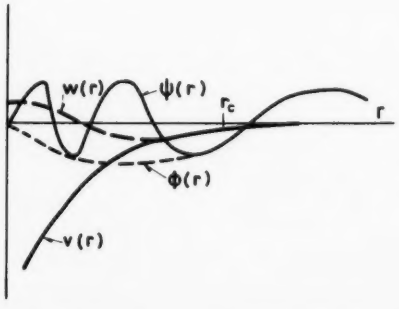

FIGURE 1. *The true wave function* $\psi(\mathbf{r})$ *in the true potential* $\theta(\mathbf{r})$ *is replaced by the pseudo wave function* $\phi(\mathbf{r})$ *in the pseudopotential* $w(\mathbf{r})$.

This type of confusion is compounded by the non-uniqueness of pseudopotentials. The original algebraic proof of this arbitrariness came as something of a surprise, but it is really quite obvious. We are asked, in effect to construct a weak potential that will reproduce the effect of a strong potential on an electron wave of given energy impinging on the atom. The boundary condition on the pseudo wave function—that it should match the true wave function on the outside—is very weak, and amounts to little more than fixing the value of a few integrals over the pseudopotential. We know, for example, that the s-wave scattering phase shift of the true potential will be reproduced at low energies if we choose the spatial average of the pseudopotential correctly—and so on. Almost any function containing a few adjustable parameters can be made to fit these conditions. Of course the problem of finding a fixed local pseudopotential that will imitate the effects of the true potential over a wide range of energy is much more difficult, and has not been solved, but that is not what we are asked to do.

This arbitrariness was exploited to the full by Heine and Abarenkov [7] who chose the most elementary pseudopotential functions so as to simplify the rest of the algebra. It was natural to reproduce the core potential of a metallic ion with a square well of depth $A_l(\mathscr{E})$, which could be continued outwards as a simple Coulomb potential; or as a screened Coulomb potential, according as one is thinking of an isolated free atom or of a "pseudo atom" in a condensed phase (fig. 2). In fact, the value of $A_l(\mathscr{E})$ for a given angular momentum can then be estimated from the optical term values, in the tradition of the quantum defect method of Kuhn and Van Vleck.

Such a "model potential" is obviously good physics, and can be more or less justified mathematically. It copes very elegantly with one of the most difficult aspects of the whole theory—the self-consistency problem for the valence electrons—about which, for reasons of brevity, I shall say very little here. According to Shaw [8], the screening corrections can be calculated accurately, although it pays to eliminate the discontinuity at the surface of the square well by treat-

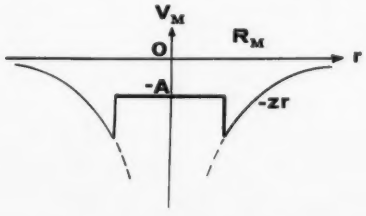

FIGURE 2*a*. *Heine-Abarenkov pseudopotential; before screening.*

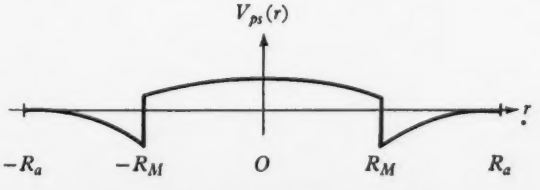

FIGURE 2*b*. *After screening (from* [5]).

ing the radius of this internal flat region as another adjustable parameter, depending also on energy and momentum (fig. 3).

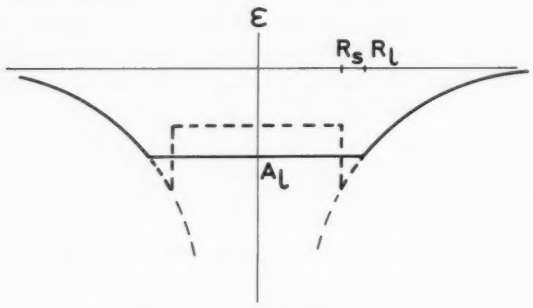

FIGURE 3. *Shaw pseudopotential.*

Notice, however, the dangers of overelaboration. An arbitrarily defined model potential in real space is valuable only in proportion to its algebraic or geometrical simplicity, and will not bear much "improvement" in the name of numerical precision or in order to get better agreement with experiment. In the event the electronic structure depends on the "form factor"—the Fourier transform of the pseudopotential—which might then just as well be derived directly from the true potential by some more powerful method, or which we could also represent by some simple empirical function [9].

From a formal point of view, the arbitrariness of the pseudopotential is certainly quite worrying. How can the electronic band structure depend uniquely on the periodic lattice potential if this arbitrary function can be interposed in the calculation? Well now, suppose we had tried to solve the equations (2) for the Bloch functions expanded in simple plane waves. Since these are an infinite set we should have had to proceed by successive approximations, just as if we are trying to sum a series term by term. But these equations really have many solutions of much lower energy than the one we are looking for, corresponding to all the narrow tight-bound bands and an expansion in powers of $\mathscr{V}(\mathbf{g}-\mathbf{g}')$ simply does not converge for energies in the valence band. We are trying to sum the Born series for scattering by one of the atomic potentials, ignoring the fact that it has numerous deep bound states. The pseudopotential trick removes all the effects of these bound states, and gives us a convergent series. It is rather like wanting to evaluate $1/(1+\chi)$ when χ is about 10: a power series in χ will not converge, but we can easily construct a new series in some new variable $y = (\chi - a)$, say, which can be made to converge in the region of interest. The actual terms in the series will depend on the value of a, which may be any arbitrary number larger than about 5—but the final answer will be independent of this choice. Thus the final value of the energy as a function of wave vector comes out the same, whatever form of pseudopotential we introduce into the equations.

This suggests a possible criterion for a "best" pseudopotential: choose the form of $\Gamma_{gg'}$ that causes the series expansion for the Bloch functions to converge most rapidly. There is a rather elaborate mathematical theory of the Born series, due to Weinberg, which can be applied to this problem [10] and which does discriminate in principle between various formulae. These investigations are not, perhaps, of very great practical value to the horny-handed programmer of computers, but they are healthy in establishing the basic mathematical foundations of the whole technique.

3. The Problem of Bound Bands

The most serious limitation of the pseudopotential concept is that it applies only to the so-called "simple" metals—those without d-states in the valence band. There is, of course, a long tradition of representing such states by the tight binding method, as a linear combination of atomic orbitals. The coefficients a_L in such combinations then have to satisfy a set of linear equations of the form

$$(\mathscr{E}_L - \mathscr{E})\, a_L + \Sigma_{L'} V_{LL'}(\mathbf{k})\, a_{L'} = 0, \qquad (4)$$

where the index L stands for different angular momentum and magnetic quantum numbers; for example, the five values of the component of angular momentum in a band of d-states. The original bound state at $\mathscr{E}_L$ is broadened into a band by the various overlap integrals $\mathscr{V}_{LL'}(\mathbf{k})$, which can in principle be evaluated, although in practice this is so complicated and inaccurate that one treats them as adjustable parameters.

It used to be thought that *all* the states in metals could be described in this way, by bringing in enough different atomic orbitals. The picture of states overlapping and broadening to make nice valence and conduction bands illustrates one of the nursery rhymes of our subject (fig. 4). Unfortunately, this is quite misleading. What happens is that as the atomic *potentials* overlap, and the barriers fall between atomic cells, most of these atomic bound-state orbitals disappear. The ordinary s and p valence levels of the atoms vanish into a nearly free-electron band which can only be described if one includes propagating wave functions from above the spectrum of bound states of the separate ions or atoms.

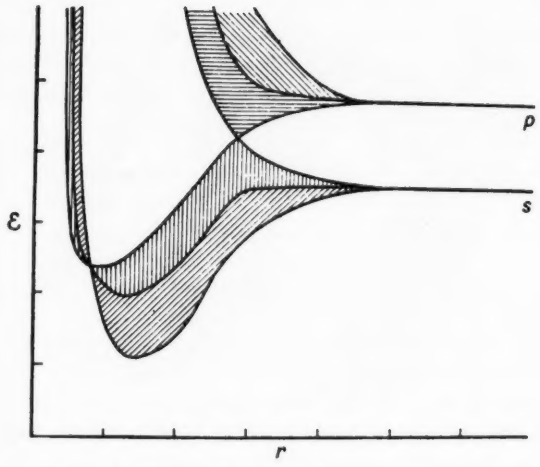

FIGURE 4. *Conventional picture of energy bands from overlap of atomic orbitals.*

We thus arrive at an impasse: we can describe ordinary s−p bands in pseudopotential language, and d-bands in tight binding language, but there seems no common tongue, even when these bands overlap and hybridize as in the transition metals.

This difficulty never seems to have worried the active calculators of band structures: they used two techniques that gave good numerical results in all cases—the augmented plane wave method and the Green function method. One of the main developments in band structure theory in the past 5 years has been to show the mathematical connections between these useful techniques and the concepts of pseudopotential and tight-binding.

The idea of an augmented plane wave is quite simple. At some given energy $\mathscr{E}$, one solves the Schrödinger equation inside a spherical potential well, of radius R_s, say. The solution is a linear combination of products or radial functions and spherical harmonics of different values of angular momentum. Now determine these coefficients so that this solution matches on to a plane wave of wave vector $\mathbf{k}$ outside the sphere. This function is still not an exact solution of the Schrödinger equation, and has a discontinuity of slope at R_s; but we can build up our Bloch function by combining a set of these with wave vectors $\mathbf{k}$, $\mathbf{k}+\mathbf{g}$, *etc.* just as in (1) and then using the variational principle for the energy. The coefficients satisfy a set of equations exactly like the pseudopotential equations (3) so that we can find

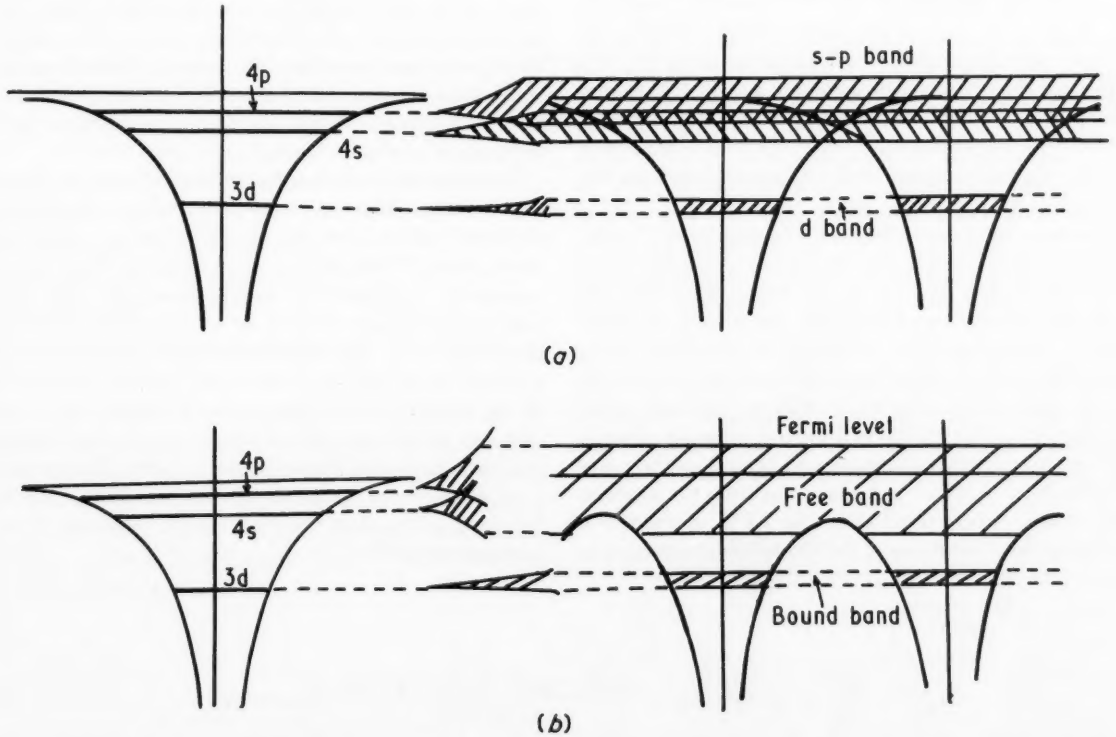

FIGURE 5. *(a) Conventional LCAO description of formation of metallic conduction band; (b) Description in terms of muffin-tin potentials.*

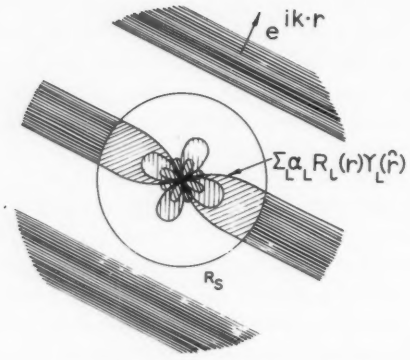

FIGURE 6. *An augmented plane wave.*

the energy $\mathscr{E}$ as a function of $\mathbf{k}$ by finding the roots of the determinant in the usual way.

The actual formula for $\Gamma_{gg'}^{APW}$ is rather elaborate, so I will not write it down; it depends upon $\mathbf{k}$, and also upon $\mathscr{E}$ through the first derivatives of the radial solutions of the Schrödinger equation at R_s. At first sight one might have thought that this could be interpreted as an elaborate energy- and momentum-dependent form factor, derivable from a pseudopotential; but this is not the case. The difficulty is that Γ^{APW} does not vanish in the elementary case of an empty lattice—whereas we should certainly expect a pseudopotential to be zero when we remove the true potential to which it is supposed to be equivalent. The connection with the tight binding formalism appears even more obscure, even though one can compute perfectly good d-bands by this method.

In desperation, we turn to the KKR method of Korringa and of Kohn and Rostoker. This is called the Green function method because it was originally derived in that somewhat abstract language, but it really depends upon a self-consistency argument; as the Bloch wave proceeds through the crystal lattice, and encounters the various atomic spheres, it suffers scattering or diffraction—but this diffraction must be exactly what is needed to reproduce the wave and keep it on the move without loss. Again, I will spare you from the algebra, and merely report that, as in the APW method, one uses the radial solutions of the Schrödinger equation in

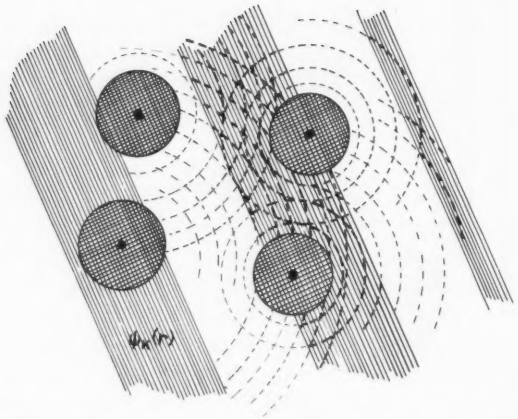

FIGURE 7. *Scattered waves recombining as plane waves in KKR method.*

each atomic sphere and plane waves outside. The result is yet another set of linear equations—this time for the coefficients of the mixture of solutions of various angular momentum in the sphere:

$$\kappa\{\cot \eta_l(\kappa) - i\} b_L + \Sigma_{L'} B_{LL'}(\mathbf{k}, \kappa) b_{L'} = 0. \tag{5}$$

In this formula, the energy $\mathscr{E}$ is κ^2, and $\eta_l(\kappa)$ is the phase shift that would have been produced by the atomic sphere in scattering a plane wave of this energy. The "structure constants" $B_{LL'}(\mathbf{K},\kappa)$ depend on the energy and momentum of the state being studied, but otherwise can be laboriously computed from the geometrical structure of the lattice.

This does not look very much like either of our previous formulae. Indeed, from the pseudopotential point of view it looks quite wrong, for when we apply the empty lattice test we make η_l tend to zero, which causes $cot\ \eta_l$ to blow up. In fact these equations need to be turned upside down if we are to understand them physically [11]. The algebra is again a bit heavy, and depends essentially on some of the analytic properties of the structure constants, each of which is in fact a sum over reciprocal lattice vectors of products of spherical harmonics and Bessel functions *etc.* The result is a set of algebraic equations of the form of (3), with the following expression for the "matrix elements of the pseudopotential":

$$\Gamma_{gg'}^{KKR} = -\frac{4\pi N}{\kappa} \Sigma_l\, (2l+1) \tan \eta_l' \frac{j_l(|\mathbf{k}-\mathbf{g}|R_s) j_l(|\mathbf{k}-\mathbf{g}'|R_s)}{|j_l(\kappa R_s)|^2} P_l(\cos \theta_{gg'}) \tag{6}$$

where

$$\cot \eta_l' = \cot \eta_l - \frac{n_l(\kappa R_s)}{j_l(\kappa R_s)}. \tag{7}$$

In this formula, j_l and η_l are spherical Bessel functions, and $P_l(cos\theta_{gg'})$ is the ordinary Legendre polynomial for the angle between vectors $\mathbf{k}-\mathbf{g}$ and $\mathbf{k}-\mathbf{g}'$.

This formula is highly instructive, for a number of reasons.

(i) Consider an empty lattice, for which $\eta_l = 0$. Then η'_l will also vanish, and with it $tan\ \eta'_l$. Thus $\Gamma_{gg'}$ is a genuine pseudopotential, which goes to zero with the true potential.

(ii) When η_l is small, the difference between, say $tan\ \eta'_l$ and $sin\ \eta_l\ exp\ (i\eta_l)$ is negligible. Ignoring the ratios of spherical Bessel functions, $\Gamma_{gg'}$ looks just like a scattering amplitude for the effect of our given potential on a single plane wave. This is good physics: the crystal is made up of an assembly of objects, each of which scatters the Bloch wave into itself.

(iii) A strong potential, with many deep bound states may, nevertheless, have quite small phase shifts, so may behave like a weak pseudopotential. Thus, the principle of subtracting away the divergences due to the bound states amounts to simply representing each phase shift as the smallest possible angle, modulo (π). This is a well-known property of phase shifts.

(iv) As shown by Lloyd [12], this form of matrix element can be derived from a simple model potential. We merely put a delta function singularity of potential over the surface of the sphere of radius R_s, of strength to match the phase shift η_l outside, for each value of l.

(v) The connection with the APW formula was discovered by Morgan [13]. Suppose we write $\Gamma^{APW}(0)$ for the values of the APW matrix elements in an empty lattice. Then

$$\Gamma^{APW} = \Gamma^{KKR} + \Gamma^{APW}(0). \tag{8}$$

The APW matrix elements have these extra parts to them, which do not really contribute to the band structure, and which do not vanish for any value of l, even for empty space. One can even derive Γ^{APW} from a model potential [12], but this is much more complicated in form than the one for Γ^{KKR} and does not vanish in empty space.

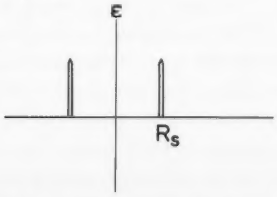

FIGURE 8. *Pseudopotential for* Γ^{KKR}.

These properties of this new form of pseudopotential suggest that it should be much easier than the APW method to use in practice for simple metals, where we need only introduce small phase shifts for a few values of angular momenta. We may also use the computational device of "folding" the determinant for large values of $\mathbf{g}-\mathbf{g}'$, as if we were treating the diffraction from distant zone boundaries as a small perturbation [14]. This form is also said to be the best for convergence of the Born series in the Weinberg sense [10], whatever that may imply. But the whole question of the relative computational efficiency of these methods and their minor variants is quite complicated; all I would say here is that the effort of comparing them is made much more fruitful when we understand the basic algebraic connections.

One further mystery needs clarification. Let us recall that the basic algebraic equations (3) are for the purpose of discovering the coefficients β_g in some expansion of the wave function in the appropriate plane waves. Thus, if we had been using Γ^{APW} in these equations, we should have been writing

$$\psi_{\mathbf{k}} = \Sigma_g \beta_g \phi^{APW}(\mathbf{k}+g)$$

where $\phi^{APW}(\mathbf{k}+\mathrm{g})$ is augmented plane wave having the form $exp\ \{i(\mathbf{k}+\mathrm{g})\cdot\mathbf{r}\}$ outside of the atomic sphere. Now it turns out [13] that the KKR equations also suppose that the wave function has been expanded in augmented plane waves—but since the matrix elements (8) are different in these equations the coefficients β_g will be different. In other words, the Bloch function ψ_k, which is supposed to be a unique solution to our band structure problem, has two entirely different representations in terms of the same set of basic functions.

This is permissible, because in fact we are only combining APW's to satisfy the Schrödinger equation *outside* the spheres; the part within each sphere is automatically determined by its adjustment to the boundary condition [15]. It is well known that a periodic function defined over only part of the unit cell can be

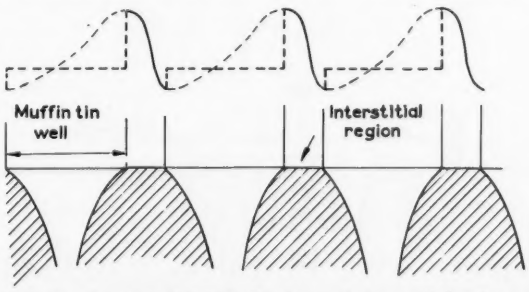

FIGURE 9. *Function defined as Bloch wave in interstitial region may have arbitrary form in muffin-tin well.*

represented by many Fourier expansions, depending on what properties it is allowed to have in the excluded region. The APW and KKR expansions both represent ψ_k correctly—yet they are not made up of exactly the same combinations of simple plane waves in the interstitial regions. This point is perhaps worth emphasizing because in either case we have a very explicit representation of the wave function of the Bloch state, in a form that is quite convenient for calculations of electron-electron interactions, self-consistency of potentials, and optical, x-ray, photoemission, and positron-annihilation matrix elements, *etc.*

It has sometimes been held against the APW & KKR methods that they can only be used for a "muffin-tin potential"—*i.e.* for a periodic lattice of spherically symmetric wells with "empty space" in between. But this is not an absolute restriction. Suppose there really is a significant nonconstant potential $\mathscr{V}_i$ in the interstitial region. Then we can take this into account by adding to $\Gamma_{gg'}$ the corresponding Fourier component $\mathscr{V}_i(\mathbf{g}-\mathbf{g}')$ of this potential—made explicit by being given a constant value across the mouths of the muffin-tin wells [16]. Thus, the level which I call the "muffin-tin zero" [17] cuts across the equipotential surfaces, producing muffin-tin wells with bound states, which are eliminated by a pseudopotential device, and ranges of weak potential hills through which the valence electrons easily tunnel, and which can be represented adequately by their Fourier transforms. If we go further, and suppose that this interstitial potential had been produced by the superposition of screened Coulomb potentials, or charge clouds, carried by the individual atoms, then we can imagine $\mathscr{V}_i$ analysed into these spherically symmetrical constituents arranged in a lattice, and reassign these to the corresponding muffin-tin wells, whose deep potentials have by now been replaced by a model potential or pseudopotential. In other words, we arrive back precisely at the sort of analysis implied by figure 2 or figure 3: the effect of the atoms on the electrons is equivalent to diffraction by an assembly of screened model potentials, whose outer fields may, within reason, be superposed without hindrance. Thus we could use $\Gamma^{KKR}+\mathscr{V}_i$ as the form factor in any calculation where model potentials are employed, *e.g.* resistivity of liquid metals, lattice dynamics, *etc.*

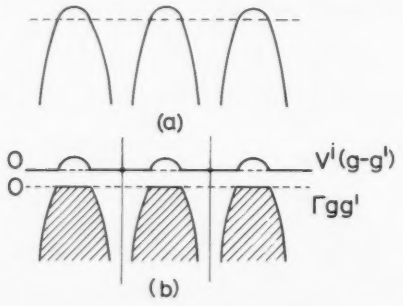

FIGURE 10. *Lattice potential (a) dissected into an interstitial potential and muffin-tin wells.*

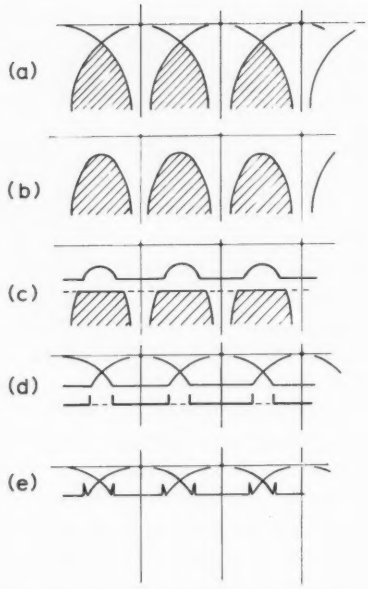

FIGURE 11. *Overlapping potentials (a), summed to make lattice potential (b), dissected into an interstitial potential and muffin-tin wells (c), redefined as pseudopotentials and overlapping external parts (d), and recombined as pseudo-atom potentials (e).*

This final demonstration of the equivalence of all three methods of band structure—OPW, APW and KKR—in the case of simple metals and semiconductors is very satisfactory, but I am now worried about one general point. Suppose we have a very anisotropic lattice—for example, the chain structure of Te, or the layer structure of graphite. The separation of the potential into muffin-tin wells and an interstitial potential must be done at a level below the lowest barriers between the atoms—for example, at the level of the potential half way between neighbors along a chain. But this may leave very high hills in the interstitial potential between the chains or layers—and the unwillingness of the electron to tunnel through such hills may not be well expressed by an expansion in plane waves in this region. Perhaps this is not a serious point after all; but I mention it to show that we are now gaining confidence to attack the electronic structure of more complex molecular crystals, a field which has up to now been dominated by an army of theoretical chemists wielding innumerable linear combinations of atomic orbitals—a

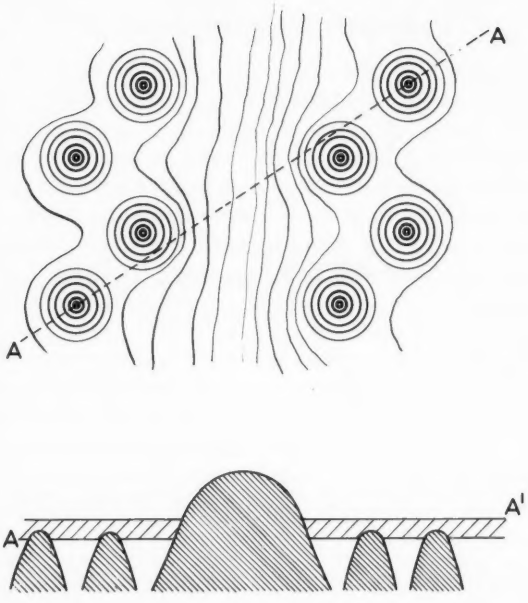

FIGURE 12. *Potentials in a crystal of long chain molecules: electrons occupy the valleys containing muffin-tin wells, separated by high potential hills.*

weapon whose fundamental efficacy I now take leave to doubt.

4. Resonance Bands

What about d-bands, which can be computed numerically by the APW and KKR method, but whose empirical description has usually been handled by the tight binding formula? The answer to this question is perhaps one of the most elegant results of the recent theory. Let us proceed from, say (5), the original KKR equations, which are not unlike the tight-binding equations (4), in that the index L, labelling the unknown coefficients, refers to various spherical harmonics, or components of angular momentum. We might ask, for example, what would happen to the phase shift $\eta_l(\kappa)$ if the energy happened to coincide exactly with a bound state $\mathscr{E}_L$ of the atomic potential. To answer this question in general, we should need to study the theory of scattering in the unphysical regions where $\mathscr{E}$ lies below the muffin-tin zero, making κ pure imaginary; but it turns out that a factor like $\mathscr{E}_L-\mathscr{E}$ then appears in $cot\ \eta_l(\kappa)$ just as we might expect. Now look at our formula (6) for the KKR pseudopotential in the reciprocal lattice representation: if $cot\ \eta'_l$ were to vanish, at any energy, then $tan\ \eta'_l$ would become infinite, and everything would go wrong. Thus, if η'_l should ever go through $\pi/2$ the band structure would be seriously affected.

Now this is a familiar situation in the general theory of scattering by atoms, molecules or nuclei: the phase shift η_l goes through $\pi/2$ in the positive energy region whenever there is a "resonance" of angular momentum. Thus, if the atomic or ionic potential has such a resonance, this will give rise to significant band effects in this neighborhood. There is a standard theory of such phenomena, which tells us that we may write

$$\tan \eta_l \sim \frac{W}{\mathscr{E}-\mathscr{E}_l} \tag{9}$$

for the phase shift of a resonance of width W centered on the energy $\mathscr{E}_l$. It is easy to show, using (6), that this has the effect of introducing a band of states of about this width, at about this energy, in the nearly-free-electron spectrum [11].

This argument can be carried further. Starting from the KKR formulae and making systematic transformations and approximations, Heine [18] showed how one could separate out a particular resonance term, and keep this in the angular momentum representation, with indices m,m' for the different components of l, while reproducing a typical pseudopotential expression in the reciprocal lattice representation $\mathbf{g},\mathbf{g}'$. The matrix of these equations can thus be written in the form

$$\begin{pmatrix} \mathscr{E}-\mathbf{k}^2 & \Gamma_{0\mathbf{g}} & \cdots & \gamma^{\mathbf{g}m} \\ \Gamma_{\mathbf{g}0} & \mathscr{E}-(\mathbf{k}+\mathbf{g})^2 & & \\ \vdots & & \ddots & \\ \hline & & & \mathscr{E}-\mathscr{E}_l \quad V_{mm'} \quad \cdots \\ \gamma^*_{m\mathbf{g}} & & & V_{m'm} \quad \mathscr{E}-\mathscr{E}_l \quad \ddots \\ & & & \vdots \end{pmatrix} \tag{10}$$

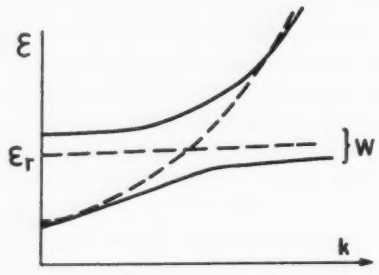

FIGURE 13. *Resonance band crossing nearly free band.*

Without the submatrices γ_{gm} *etc.*, this would factorize into a nearly-free-electron, pseudopotential matrix, such as we might expect to find in a simple metal with an s-p band, together with an ordinary tight binding matrix, corresponding to the overlapping and mixing of the 5 degenerate d-levels of the free atom. The coefficients γ_{gm} *etc.* then describe the hybridization of these two systems of states, which must necessarily occur when these bands cross one another.

As it happens (but not accidentally!) an empirical "model Hamiltonian" of just this form had already been proposed for transition and noble metals [19] before it was deduced directly from the KKR equations. We can now, therefore, justify this type of expression in principle, and even calculate the various coefficients directly from the atomic potential. In fact there are now several different versions of these equations, of varying computability, convergence and analytical simplicity [20] but all essentially equivalent of Heine's formula [5,18].

This reinterpretation of the tight-binding formalism, and its unification with the other band structure methods is very pleasing, but to my mind there is a greater gain. Let us ask how resonances actually arise? For an ordinary one-electron potential, we need to think of the effects of the centrifugal barrier term $l(l+1)/r^2$ in the radial Schrödinger equation, which becomes important for $l=2$. A bound d-state is really constrained to avoid the nucleus by this "potential". Now lower the ordinary potential at the outer edges of the atom: the effect may be to leave a potential dip within the core, where a "virtual", long-lived level could still exist, even though, eventually, it would have to decay as the electron tunnelled out into free space. Thus, the original bound d-state has become a d-resonance; if the potential barrier is sufficiently thick, the resonance will be sharp; it is not surprising that the language of overlapping bound states applies to the bands produced in such cases.

From this picture we can learn a lot about the gross features of the density of states of the metal. We see,

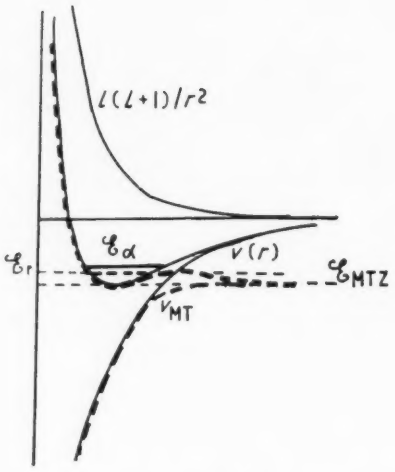

FIGURE 14. *How a bound state of the atom becomes a resonance level of the muffin-tin well (See [17]).*

for example, that although the little peaks and dips of the d-band can be derived from general tight-binding theory, especially when aided by group theory, the width of this complex of bands will depend chiefly on the width of the resonance, which is governed in turn by the potential barrier produced by the centrifugal force in the outer part of each muffin-tin well. Again, the actual position of this band will be determined mainly by the energy of the original d-state from which it derives—and this is fixed on a scale relative to, say, some deep state of the core. On this scale, however, the position of the ordinary conduction band does not depend on any atomic orbitals, but is determined mainly by the muffin-tin zero, which can only be calculated correctly by taking very careful account of screening, correlation energy, overlaps of potential, *etc.* We thus discover the reason for a well-known difficulty in band structure calculations—that the width of the d-band, and its position relative to the Fermi level is very sensitive to the model, and cannot apparently be calculated with the precision we would like.

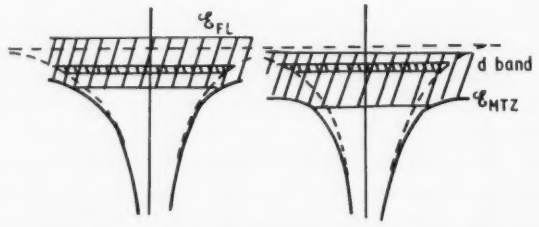

FIGURE 15. *How the position of the d-band within the conduction band depends on the muffin-tin zero (See [17]).*

5. Some Thoughts in Disorder

Now that we understand the electronic structure of crystalline solids so very well, we are tempted to attack disordered materials—liquids, alloys, amorphous and glassy substances. This campaign has been actively waged now for about a decade, but I am not sure that it has yielded many great prizes. The major difficulty, of course, is that we must abandon Bloch's theorem, which reduces the complexity of the problem in the perfect lattice by a divisor of the order of 10^{23}. Without crystal momentum as a good quantum number, we flounder about in a mixture of approximate algebra and incomplete intuition, hoping to find some clearcut concepts that will guide the interpretation of complicated experiments on messy materials.

It is true that the spectrum of the disordered linear array is now well understood [21]—and turns out to be much more spiky than one would have guessed from simple statistical considerations. Some of these features may persist in three-dimensional systems, but unfortunately the mathematical methods used in the one-dimensional case seem ill-adapted to generalization. In particular, real solid systems have two properties that cannot be simulated at all by a linear chain. In three dimensions, a localized defect or impurity can be avoided by a detour, so that it does not present an absolute barrier to an incident particle or excitation. In three dimensions, also we may have "structural disorder", which is no longer topologically equivalent to any regular lattice, whereas in a linear chain the mere succession of atoms prescribes an ordering, however wildly we vary the properties of the individual potential wells.

Let me give two examples of simple cases where our present theory is inadequate. It is obvious enough that a disordered transition metal—*e.g.* liquid iron—should have a d-band arising from the d-resonance, just as in any crystalline phase of about the same atomic volume [22]. The mathematical theory of such a band is still rather uncertain [23], but there is no doubt about the physics. Suppose, however, that we make an alloy—*e.g.* of Ag and Au—whose constituent atoms have their resonance at different energies; how far apart would these energies need to be to give us two distinct d-bands, and how would this depend on the relative concentrations and relative ordering of the constituents? The model can be made extremely elementary—equal numbers of A and B type atoms, with a single bound s-state on each, substituted at random on a regular lattice with a constant overlap integral V between nearest neighbors. Some highly respected statistical theories which rely upon defining an average propagator in such a medium, seem to insist that the bands will be drawn out into a continuous broad spectrum as the two levels move apart; others would allow a split to occur when the spacing is rather larger than the width of either band [24]. I feel sure, myself, that the latter prediction is correct, but we have still a great deal to do before we can calculate the width of each band the shape of the tails into the gap, and the nature of any levels in these regions. How far, for example, do these bands depend upon the possibilities of "percolation", from one atom to another of the same type, through large distances—a property that depends peculiarly on the dimensionality of the lattice and the relative concentrations of the components?

Another contradiction between mathematical theories and physical intuition occurs in the case of

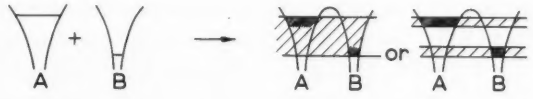

FIGURE 16. *Does a mixed crystal have one bound band or two?*

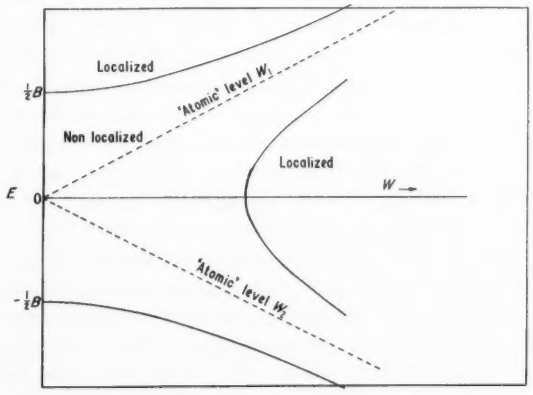

FIGURE 17. *Regions of localized and non-localized states for an "equiconcentration alloy".*

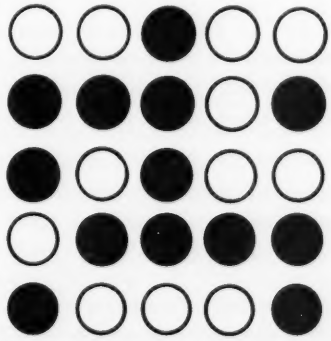

FIGURE 18. *A percolation chain in an equiconcentration alloy.*

amorphous semiconductors. Let it be granted, for the sake of argument, that amorphous Ge and Si are "tetrahedral glasses"; each atom has four neighbors, arranged more or less in the regular tetrahedral orientation, just as in the regular diamond lattice, but the connectivity of the structure has been altered in a random way, so that there is no long-range order. From the point of view of a chemist, this system is a single covalently bonded molecule: the saturation of all the bonds implies that some energy of excitation is required to create a carrier, so we should expect the material to be a semiconductor. The substantial gap in the optical spectrum of amorphous Ge supports this reasonable interpretation. But suppose we were to treat this by the conventional pseudopotential procedure, assigning a model potential to each atom and then calculating the diffraction effect on a free electron gas. In the absence of long-range order, there would be no strong Bragg reflections from well-defined lattice planes, and thus no proper band gaps at the zone boundaries, *etc.*; from the point of view of solid-state theory, this material ought to be a metal. This antinomy needs to be resolved if we are to understand the theory of disordered systems—or even the theory of the chemical bond. There is some evidence—as yet merely qualitative [27]—that the diffraction approach can be made to give a band gap if one takes into account the higher-order particle correlations. Thus, a glass differs from a liquid in that three neighboring atoms may have a strong tendency to be oriented so as to make a good bond angle; this is a form of short-range order, implying a strong constraint on the three-and four-body statistical distributions of atoms. At the same time, the relationship between the localized molecular orbitals of the chemical bonds and the delocalized "Bloch states" of the crystal or amorphous solid needs to be clarified [28]. But these are only two of the numerous unsolved problems in this field.

The above account of the band structure problem is obviously very sketchy and incomplete—especially in the total neglect of all electron-electron effects. We shall obviously learn much more about it as this conference proceeds. But I think it is good to look back and see what progress has been achieved—and even better to look forward to whole Alps of ignorance still to be surmounted.

6. References

[1] **Electrons and Phonons:** (Oxford, Clarendon Press 1960).

[2] **Methods in Computational Physics: Vol. 8: Energy Bands of Solids:** Edited by B. Alder, S. Fernbach, M. Rotenberg (New York: Academic Press 1968).

[3] Ziman, J. M., Advances in Physics, **13,** 89 (1964).

[4] Harrison, W. A., **Pseudopotentials in Metals** (New York: Benjamin 1966).

[5] Heine, V., **The Physics of Metals** (ed. J. M. Ziman: Cambridge, University Press, 1969) Chap. 1.

[6] Herman, F., R. L. Kortum, C. D. Kuglin, J. P. Van Dyke and S. Skillman in Ref. 1, p. 193.

[7] Heine, V. and I. V. Abarenkov, Phil. Mag., **9,** 451, (1964).

[8] Shaw, R. W. and W. A. Harrison, Phys. Rev. **163,** 604 (1967). R. W. Shaw, Phys. Rev. **174,** 769 (1968).

[9] Ashcroft, N. W., J. Phys. C. **1,** 232 (1968).

[10] Rubio, J. and F. Garcia-Moliner, Proc. Phys. Soc. **91,** 739; **92,** 206 (1967). J. B. Pendry, J. Phys. C. **1,** 1065 (1968).

[11] Ziman, J. M., Proc. Phys. Soc. **86,** 337 (1965).

[12] Lloyd, P., Proc. Phys. Soc. **86,** 825 (1965).

[13] Morgan, G. J., Proc. Phys. Soc. **89,** 365 (1966). K. H. Johnson, Phys. Rev. **150,** 429 (1966).

[14] Lawrence, M. J., Thesis, Bristol University (1969).

[15] Slater, J. C., Phys. Rev. **145,** 599 (1966).

[16] Scholsser, H. C. and P. M. Marcus, Phys. Rev. **131,** 2529 (1963). F. Beleznay and M. J. Lawrence, J. Phys. C. **1,** 1288 (1968).

[17] Ziman, J. M., Proc. Phys. Soc. **91,** 701 (1967).

[18] Heine, V., Phys. Rev. **153,** 673 (1967).

[19] Hodges, L. and H. Ehrenreich, Phys. Letters **16,** 203 (1965). F. M. Mueller, Phys. Rev. **153,** 659 (1967).

[20] Hubbard, J., Proc. Phys. Soc. **92,** 921 (1967). R. L. Jacobs, J. Phys. C. **1,** 492 (1968).

[21] See, *e.g.* J. Hori, **Spectral Properties of Disordered Chains and Lattices** (Oxford: Pergamon Press 1968).

[22] Anderson, P. W. and W. L. McMillan, **Teoria del magnetisino nei metalli di transizione**: Verenna Summer School XXXVII (1967).

[23] Lloyd, P., Proc. Phys. Soc. **90,** 207, 217 (1967). G. J. Morgan, J. Phys. C. **2,** 1446, 1454 (1969).

[24] Ziman, J. M., J. Phys. C. **2,** 1230 (1969) (II).

[25] Ziman, J. M., J. Phys. C. **2,** 1532 (1968) (I). D. F. Holcomb and J. J. Rehr (to be published).

[26] Tauc, J., R. Grigorivici and A. Vancu, Phys. Stat. Solid **15,** 627 (1966).

[27] Fletcher, N. H., Proc. Phys. Soc. **91,** 724; **92,** 265 (1967). J. M. Ziman, J. Phys. C. (1969) (III).

[28] Anderson, P. W., Phys. Rev. Letters **21,** 13, (1968).

(Paper 74A2-596)

JOURNAL OF RESEARCH of the National Bureau of Standards—A. Physics and Chemistry
Vol. 74A, No. 2, March–April 1970

Optical Properties and Electronic Density of States*[1]

Manuel Cardona[2]

Brown University, Providence, Rhode Island and DESY, Hamburg, Germany

(October 10, 1969)

The fundamental absorption spectrum of a solid yields information about critical points in the optical density of states. This information can be used to adjust parameters of the band structure. Once the adjusted band structure is known, the optical properties and the density of states can be generated by numerical integration. We review in this paper the parametrization techniques used for obtaining band structures suitable for density of states calculations. The calculated optical constants are compared with experimental results. The energy derivative of these optical constants is discussed in connection with results of modulated reflectance measurements. It is also shown that information about density of empty states can be obtained from optical experiments involving excitation from deep core levels to the conduction band.

A detailed comparison of the calculated one-electron optical line shapes with experiment reveals deviations which can be interpreted as exciton effects. The accumulating experimental evidence pointing in this direction is reviewed together with the existing theory of these effects.

A number of simple models for the complicated interband density of states of an insulator have been proposed. We review in particular the Penn model, which can be used to account for response functions at zero frequency, and the parabolic model, which can be used to account for the dispersion of response functions in the immediate vicinity of the fundamental absorption edge.

Key words: Critical points; density of states; dielectric constant; modulated reflectance; optical absorption.

1. Optical Properties and One-Electron Density of States

The optical behavior of semiconductors and insulators in the near infrared, visible, and ultraviolet is determined by electronic interband transitions. An additional intraband or free electron contribution to the optical properties has to be considered for metals. We shall discuss here the relationship between the interband contribution and the density of states. The interband contribution to the imaginary part of the dielectric constant can be written as (in atomic units, $\hbar = 1$, $m = 1$, $e = 1$):

$$\epsilon_i(\omega) = \frac{1}{4\pi\omega} \iint_{\omega_{ef}=\omega} \frac{\mathbf{F}^{ef}}{|\nabla_{\mathbf{k}}\omega_{ef}|}\, dS_k \qquad (1)$$

where $\omega_{ef} = \omega_e - \omega_f$ is the difference in energy between the empty bands (e) and the filled bands (f). The spin multiplicity must be included explicitly in eq (1). The oscillator strength tensor $\mathbf{F}^{ef}$ is related to the matrix elements of $\mathbf{p}$ through $\mathbf{F}^{ef} = 2 < f|\mathbf{p}|e > < e|\mathbf{p}|f > \omega_{ef}^{-1}$. The Bloch functions are normalized over unit volume. Degenerate statistics has been assumed in eq (1) and spatial dispersion effects have been neglected.

It is customary to take the slowly varying oscillator strength out of the integral sign in eq (1) and thus write:

$$\epsilon_i(\omega) = \frac{2\pi^2}{\omega} \bar{F} N_d(\omega) \qquad (2)$$

where $\bar{F}$ is an average oscillator strength and N_d the combined optical density of states.

Structure in $\epsilon_i(\omega)$ (eq (1)) appears in the neighborhood of critical points, where $\nabla_{\mathbf{k}}\omega_{ef} = 0$. Such critical points can be localized in a small region of $\mathbf{k}$ space or can extend over large portions of the Brillouin zone over which filled and empty bands are parallel (sometimes only nearly parallel). Once the critical points which correspond to observed optical structure are identified in terms of the band structure through various devious and sometimes dubious arguments, their energies can

*An invited paper presented at the 3d Materials Research Symposium, *Electronic Density of States*, November 3–6, 1969, Gaithersburg, Md.

[1]Supported by the National Science Foundation and the Army Research Office, Durham.

[2] John Simon Guggenheim Foundation Fellow.

372-505 O - 70 - 8

be used to adjust parameters of semiempirical band structure calculations.

Four different parametric techniques of calculating band structures have been used for this purpose: the empirical pseudopotential method (EPM) [1], the $\mathbf{k}\cdot\mathbf{p}$ method [2], the Fourier expansion technique (FE) [3], and the adjustable orthogonalized plane waves method (AOPW) [4].

Once reasonably reliable band structures are known it is important to calculate from them the imaginary part of the dielectric constant $\epsilon_i(\omega)$ and to compare it with experimental results so as to confirm or disprove the initial tentative assignment of critical points and thus the accuracy of the band structures. Rich structure is obtained in both experimental and calculated spectra and hence a rather stringent test of the accuracy of the available theoretical band structure is in principle possible.

In order to calculate numerically the integral of eq (1) it is necessary to sample eigenvalues and eigenfunctions at a large number of points in the Brillouin zone. The amount of computer time required for solving the band structure problem with first-principles methods (OPW, APW, KKR) at a general point of the Brillouin zone makes such methods impractical for evaluating eq (1). The parametric methods (EPM, $\mathbf{k}\cdot\mathbf{p}$, FE, but not AOPW) require only the diagonalization of a small matrix (typically 30×30) and hence it is possible to sample the band structure at about 1000 points with only a few hours of computer time. Cubic materials, in particular those with T_d, O, and O_h point groups, are simple in this respect: symmetry reduces the sampling required for the evaluation of eq (1) to only 1/48 of the Brillouin zone. Hexagonal and tetragonal materials have relatively larger irreducible zones and hence a larger number of sampling points is necessary if the resolution of the calculation is not to suffer. Once the band structure problem has been solved for all points of a reasonably tight regular mesh, the bands and matrix elements at arbitrary points can be obtained by means of linear or quadratic interpolation.

The method of Gilat and coworkers [5] has become rather popular for the numerical evaluation of eq (1) [4,6]. In the case of a cubic material the Brillouin zone is divided into a cubic mesh and the band structure problem solved at the center of these cubes (sometimes a finer mesh is generated by quadratic interpolation from the coarser mesh [6]). Within each cube of the mesh the bands are linearly interpolated and approximated by their tangent planes. The areas of constant energy plane within each cube corresponding to a given ω_{ef} are added after multiplying them by the corresponding oscillator strength and thus the integral of eq (1) is obtained.

The real part of the dielectric constant ϵ_r can be obtained from ϵ_i by using the Kramers-Kronig relations. It is also possible to obtain ϵ_r and ϵ_i simultaneously by calculating the integral:

$$\epsilon(\omega)=1-\frac{1}{2\pi^2}\iiint\frac{\mathbf{F}^{ef}\omega_{ef}}{[\omega_{ef}^2-(\omega+i\eta)^2]}\,dV_{\mathbf{k}} \qquad (3)$$

with η small and positive. For $\eta\to+0$ the imaginary part of eq (3) coincides with eq (1). Equation (3) can be evaluated with a Monte Carlo technique. Points are generated at random in $\mathbf{k}$ space within the Brillouin zone and the average value of the integrand for these points calculated. The process can be interrupted when reasonable convergence as a function of the number of random points is achieved [7,8].

We show in figure 1 the results of a calculation of ϵ_i from the $\mathbf{k}\cdot\mathbf{p}$ band structure of InAs with the method of Gilat and Raubenheimer [6]. The band structure problem, including spin-orbit effects, was solved at about 200 points of the reduced zone (1/48 of the BZ). We have indicated in this figure the symmetry of the critical points (or of the approximate regions of space) where the structure in ϵ_i originates. The experimental ϵ_i spectrum, as obtained from the Kramers-Kronig analysis of the normal incidence reflectivity [9], is also shown. The agreement between calculated and experimental spectra is good, with regards to both position and strength of the observed structure, with the excep-

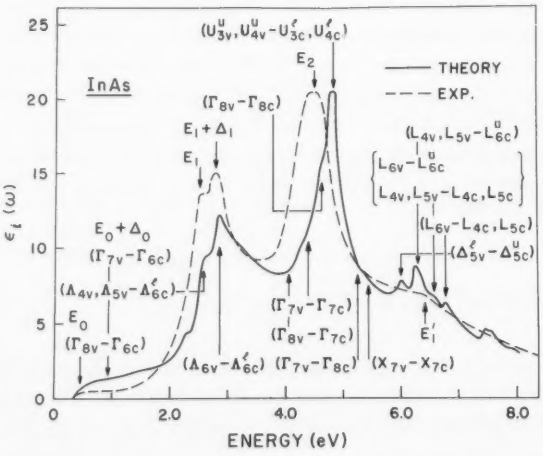

FIGURE 1. *Imaginary part of the dielectric constant of InAs as calculated from the* $\mathbf{k}\cdot\mathbf{p}$ *method* (——) [6] *and as determined experimentally* (----) [9]. *The group theoretical symmetry assignments were made with the help of the calculated isoenergy plots.*

tion of the position of the E_2 peak. This is to be attributed to an improper assignment of the E_2 peak when the 6 adjustable band structure parameters were determined. The E_2 peak had been attributed, following the tradition, to an X critical point while it is actually due to an extended region of **k** space centered around the U points [8]. It should be a simple matter to readjust the band structure parameters to lower the energy of the calculated E_2 peak by about 0.5 eV; in view of the large amount of computer time required to recalculate the energy bands this has not been done. The structure calculated around 6 eV, due mostly to spin-orbit splitting of the L_3 levels, has not yet been observed experimentally.

The conventional experimental determination of ϵ_i from normal incidence reflection data [9] suffers from considerable inaccuracy: to the experimental error produced by possible improper surface treatment and contamination one has to add the uncertainty in the high-energy extrapolation of the experimental data required for the Kramers-Kronig analysis. Some of these difficulties are avoided by comparing the *calculated* reflectivity spectra (obtained from ϵ with Fresnel's equation) with the experimental results. This is done in figure 2 for GaSb: the experimental data [10] have not been Kramers-Kronig analyzed because of the small range of the energy scale. Two calculated spectra have been plotted in this figure: one obtained from the $\mathbf{k} \cdot \mathbf{p}$ band structure [6] and the other obtained from a non-local pseudopotential calculation with 14 adjustable parameters [11]. The discrepancy between experimental and calculated curves at high energy, a common feature of many zincblende-type materials [12], has two origins: the measured reflectivity should be low because of increased diffuse reflectance at small wavelengths while the calculated one should be high because of the finite number of bands included in the calculation. In this region where $\epsilon_r - 1$ is small, the contribution to ϵ_r of transitions not included should lower the calculated reflectivity.

During the past few years a lot of activity has been devoted to the measurement and analysis of differential reflection spectra obtained with modulation techniques [13-15]. The wavelength (or photon energy) derivative spectra [14] should permit an accurate analysis of the line shapes of the spectra of figures 1 and 2. We show in figure 3 the temperature modulated reflection spectrum (thermoreflectance) of GaSb [15]: it has been shown that for the III–V materials [15] this spectrum is very similar to the photon energy derivative spectrum, difficult to obtain experimentally. The corresponding photon energy derivative spectrum obtained from the calculation of figure 2 is also shown in figure 3. The calculated and experimental shapes of the E_1, $E_1 + \Delta_1$ peaks show discrepancies of the type attributed in section 2 to exciton interaction. Derivative spectra for other germanium- and zincblende-type materials have been calculated by Walter and Cohen [12] and by Higginbotham [16].

The methods to calculate band structures from first principles, without or with only a few adjustable parameters (one [17] or three [4]) have recently achieved considerable success. However the calcula-

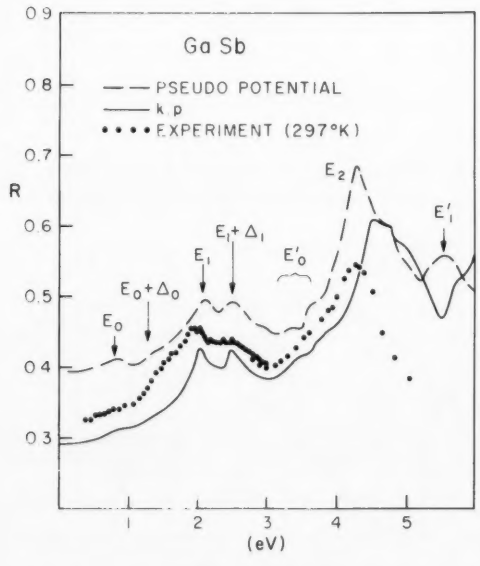

FIGURE 2. *Reflectivity of GaSb calculated from the* $\mathbf{k} \cdot \mathbf{p}$ [6] *and from a pseudopotential band structure* [11]. *Also, experimental reflectivity* [10].

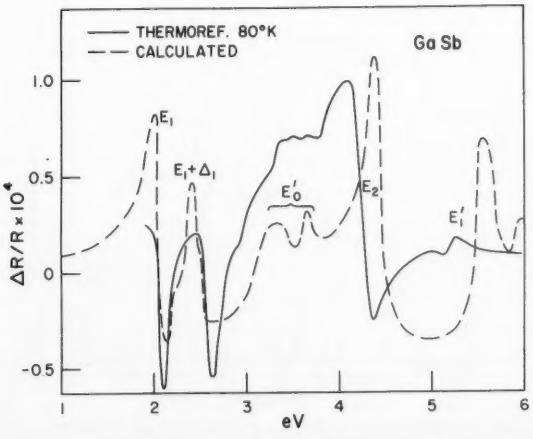

FIGURE 3. *Measured thermoreflectance spectrum of GaSb* [15] *compared with the energy derivative of the spectrum of figure 2* [16].

tion of energy bands at one general point of the BZ requires a lot of time so as to make density of states calculations prohibitive. Moreover, the evaluation of the matrix elements required for eq (1) is difficult with first principles techniques. It is nevertheless possible to use first principles calculations at a few high-symmetry points of the Brillouin zone to adjust the parameters of semiempirical band structures from which the large number of sampling points required for the evaluation of eq (1) can be obtained with relative ease. The $\mathbf{k} \cdot \mathbf{p}$ technique has proved particularly useful in this respect [2,18,19]. Matrix elements of $\mathbf{p}$ can be easily evaluated from the eigenvectors in the $\mathbf{k} \cdot \mathbf{p}$ representation. Spin-orbit interaction can also be easily included. This $\mathbf{k} \cdot \mathbf{p}$ procedure has been applied to the relativistic OPW band structure calculated by Herman and Van Dyke for gray tin [19]. Figure 4 shows the reflectivity of gray tin calculated by this procedure with the method of Gilat and Raubenheimer together with experimental results [20]. Comparison with other experimental results for the germanium family suggests that the high-energy end of the measured spectrum is too low, probably due to surface imperfections in the delicate crystals, grown from mercury solution, which were used for this experiment.

The $\mathbf{k} \cdot \mathbf{p}$ fitting procedure has also been applied to a first principles relativistic APW calculation of the band structure of PbTe by Buss and Parada [7]. Figure 5 shows the reflectivity of PbTe obtained by this method with a Monte Carlo sampling technique and figure 6 the absorption coefficient, both compared with experimental data [7,21,22]. In both cases the semiquantitative agreement between experimental and calculated data is remarkably good in view of the absence of the adjustable parameters. The calculated reflectivity is, at high energies, considerably higher than the experimental one, as discussed earlier for other materials. The E_1 peak of the experimental reflectivity spectrum appears split in the calculated spectrum, possibly because of inaccuracies in the first-principles band structure. The calculated E_1 structure appears due mostly to transitions along the Σ direction. The experimental E_1 structure has been assigned [23] to the lowest gap along Σ. The calculated E_2 peak corresponds to an extended region of the BZ without definite symmetry, as inferred from electroreference measurements [23].

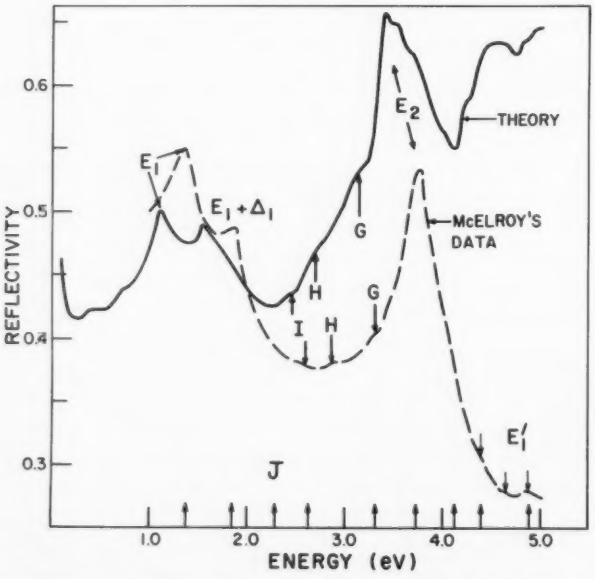

FIGURE 4. *Reflectivity of gray tin calculated from a first principles OPW band structure fitted with the* $\mathbf{k} \cdot \mathbf{p}$ *method [19]. Also experimental results [20].*

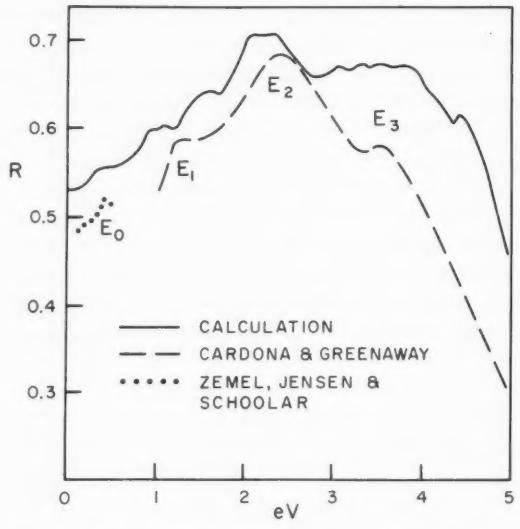

FIGURE 5. *Reflectivity of PbTe calculated from the APW-* $\mathbf{k} \cdot \mathbf{p}$ *band structure [7], compared with experimental results [21].*

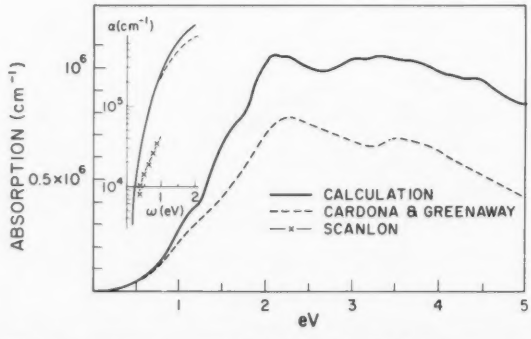

FIGURE 6. *Absorption coefficient PbTe calculated from the APW-* $\mathbf{k} \cdot \mathbf{p}$ *band structure, compared with experimental results [21, 22].*

We have so far discussed optical constants for cubic materials. While calculations for materials with lower symmetry require more computer time, one has the extra reward of being able to predict the experimentally observed anisotropy. Figure 7 shows the two principal components of ϵ_i for trigonal Se as calculated by Sandrock [24] from the pseudopotential band structure. The similarity between calculated and experimental results [25], also shown in figure 7, is especially remarkable in view of the method used to determine the pseudopotential parameters: they were determined from the pseudopotential parameters required to fit the optical structure of ZnSe. Only a small adjustment was performed so as to bring the calculated fundamental gap (1.4 eV) into agreement with the experimental one (2.0 eV). The dielectric constant of antimony (trigonal) for the ordinary and the extraordinary ray has also been calculated by a similar procedure [26].

The reasonable agreement obtained between experimental and calculated optical constants suggests the use of the corresponding band structure to determine the individual density of states $D(\omega)$: the main work, that of diagonalizing the Hamiltonian at a large number of points, has already been done. The programs required to calculate individual density of states are very similar to those used for the evaluation of eq (1): ω_{ef} must be replaced by the single band energies and $\mathbf{F}^{ef}$ must be removed. As an example we show in figure 8 the individual density of states of the 3 highest valence bands (six including spin) and the 3 lowest conduction bands of gray tin [19]. Direct information about the individual density of states can be obtained by a number of methods discussed in this conference. We mention, in particular, optical techniques involving transitions from deep core levels to the conduction band or from the valence band to temporarily empty core levels (soft x-ray emission) [27]. If the sometimes questionable assumption of constant matrix elements is made, the corresponding spectra represent the conduction (for absorption spectra) and the valence (for emission spectra) density of states because of the small width of the core bands. We show in figure 9 the densi-

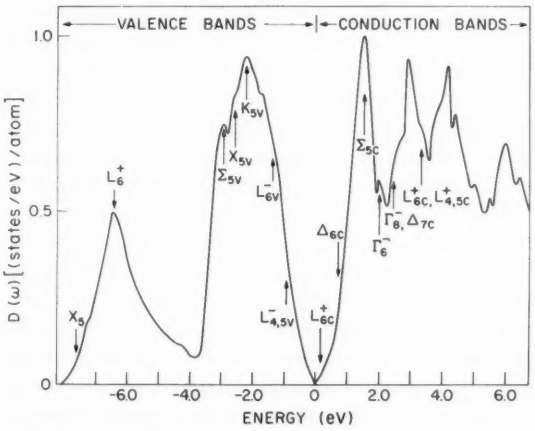

FIGURE 8. *Individual density of states for gray tin, obtained from the OPW-*$\mathbf{k}\cdot\mathbf{p}$ *band structure [19]. The top of the valence band is at 0 eV. The lowest valence band is not included.*

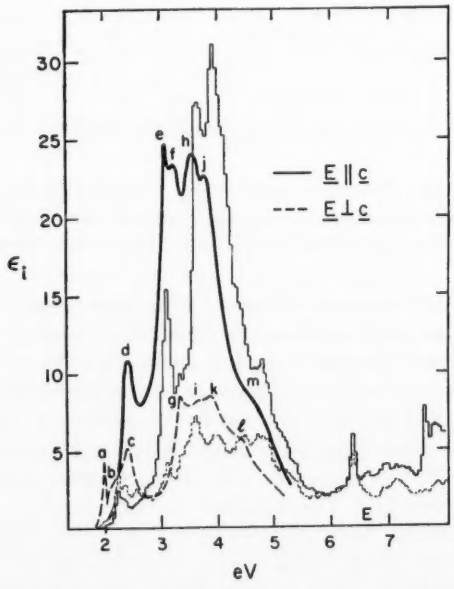

FIGURE 7. *Imaginary part of the dielectric constant of trigonal selenium for both principal directions of polarization of the electric field vector* $\mathbf{E}$ *as calculated from the pseudopotential band structure (histograms) [24] and as determined experimentally [25].*

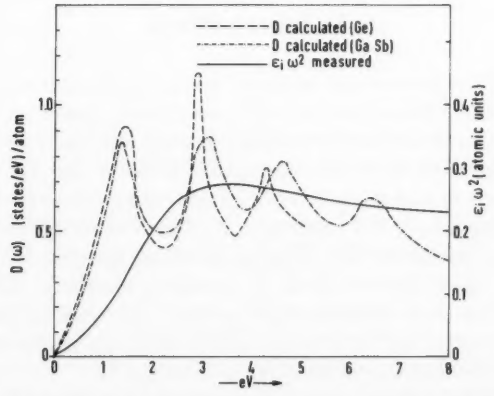

FIGURE 9. *Conduction density of states calculate for Ge [4] and for GaSb [6] together with the function* $\epsilon_i\omega^2$ *obtained from experimental data in the vacuum uv [28] (the horizontal scale for the* $\epsilon_i\omega^2$ *curve has been shifted by 29.5 eV).*

ty of states of the conduction band of Ge calculated by Herman, *et al.* [4] and the corresponding density of states for GaSb as obtained by the $\mathbf{k}\cdot\mathbf{p}$ method [6]. The densities of states for both materials are very similar because of the similarity of their band structures. We also show in figure 9 the quantity $\epsilon_i\omega^2$ obtained by Feuerbacher *et al.* [28] for Ge in the region of the $M_{4,5}$ edge. The origin of energies has been shifted so as to make a comparison with the conduction density of states possible: $\epsilon_i\omega^2$ should be proportional to $D(\omega)$ under the assumption of constant matrix elements of $\mathbf{p}$. While the rich structure of the calculated density of states is not seen in the $\epsilon_i\omega^2$ curve, this curve is reproduced quite well if the density of states is broadened so as to remove the fine structure. The required lifetime broadening of about 1 eV is not unreasonable for the $M_{4,5}$ transitions. Using eq (2) with N_d replaced by the conduction density of states we obtain an average oscillator strength at the maximum of $\epsilon_i\omega^2\mathbf{F}=0.15$. This oscillator strength corresponds to the 20 4d electrons per unit cell and hence it should be divided by 20 to obtain the average oscillator strength per d-band. If one reasons that the transitions from 10 of the 20 d bands to a given conduction band are forbidden because of the spin flip involved while transitions from 5 of these 10 bands are forbidden or nearly forbidden by parity, one finds for the average oscillator strength of each one of the 5 allowed bands $\overline{F}=0.03$, which corresponds to a matrix element of $p = 0.13$ (in atomic units): this value is quite reasonable in view of the fact that the typical valence-conduction matrix element is 0.6. The small value of this matrix element explains why the d core electrons are negligible in the $\mathbf{k}\cdot\mathbf{p}$ analysis of the valence and conduction masses.

2. Exciton Effects

We have devoted section 1 to a comparison of experimental optical spectra with calculations based on the one-electron band structure. Exciton effects, *i.e.* the final state Coulomb interaction between the excited electron and the hole left behind, are known to modify substantially the fundamental edge of semiconductors and insulators [29]. Exciton-modified interband spectra seem also to occur in metals at interband edges which have the final state on the Fermi surface [30]. Experimental evidence for these effects is reported at this conference in the paper by Kunz *et al.*

We shall now discuss the question of exciton effects above the fundamental edge of insulators and semiconductors with special emphasis on the zincblende family. As mentioned in section 1 the gross features of these spectra are explained by the one-electron theory. The exciton interaction is responsible, at most, for small details concerning the observed line shapes. It is generally accepted [31,32] that the exciton interaction suppresses structure in the neighborhood of M_3 critical points: the Coulomb attraction with negative reduced masses is equivalent to a repulsion with positive masses. Such a repulsion smooths out critical point structure: no M_3 critical point has been conclusively identified in the experimental spectra. The E_1 and $E_1+\Delta_1$ critical points of figures 1–3 are of the M_1 variety. Hence the line shape of the corresponding ϵ_i spectrum should be characterized by a steep low-energy side and a broader high-energy side. Figure 10 shows the shape of the E_1 peak observed at low temperature by Marple and Ehrenreich [33] and by Cardona [34]. In order to avoid effects due to the overlap of the E_1 and the $E_1+\Delta_1$ peaks it has been assumed that they have exactly the same shape but shifted by 0.55 eV. The contribution of only E_1 has been extracted from the measured ϵ_i spectrum and displayed in figure 10. It is clear from this figure that the E_1 peak is steeper at high energies than at low energies, against the expectations for an M_1 peak. Also in figure 10 we show the results of a calculation by Kane [32] of the effect of Coulomb interaction on the E_1 line shape for CdTe, using the effective mass approximation. The solution of the effective mass Hamiltonian with non-positive-definite mass is made easier by the fact that the negative mass (along the Λ direction) has a magnitude much larger (about ten times) than the two equal positive masses. It is possible to use the adiabatic approximation [31], *i.e.*, to solve the two-dimensional hydrogen atom problem with the

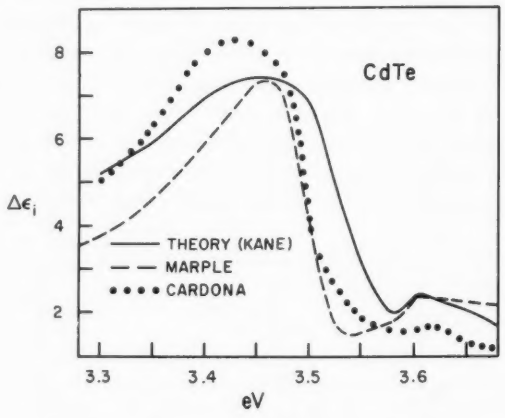

FIGURE 10. *Contribution of the* E_1 *gap to* ϵ_i *in CdTe as measured at low temperatures by Marple and Ehrenreich [33] and by Cardona [34]. Also calculation by Kane [32] using the adiabatic approximation.*

third coordinate as a parameter and then solve the adiabatic equation for the third coordinate. The agreement between the calculated and the experimental line shapes of figure 10 is excellent.

Attempts have been made to calculate the dielectric constant including exciton interactions at an arbitrary point of **k** space, independently of the stringent restrictions of the effective mass approximation [35,36]. Such calculation is possible if one truncates the Coulomb interaction between electron and hole Wannier packets to extend to a finite number of neighboring cells. The extreme and simplest case of a δ-function (Koster-Slater) interaction can be solved by hand [31,35] and gives around an M_1 critical point the shapes of ϵ_r and ϵ_i shown in figure 11: for an M_i critical point the Koster-Slater interaction mixes the M_i one-electron line shape with the M_{i+1}. The high energy side of the ϵ_i peak becomes steeper, in agreement with figure 10. The line shape observed for the $E_1-E_1+\Delta_1$ peaks in the reflectivity spectrum is composed almost additively of the ϵ_i and ϵ_r line shape: at the energies of these peaks $dR/d\epsilon_i$ and $dR/d\epsilon_r$ are almost equal. We also show in figure 11 the line shapes expected for the reflectivity spectra of the $E_1-E_1+\Delta_1$ peaks and for the corresponding differential spectra ($dR/d\omega$). We show in figure 12 the photon energy derivative spectrum of these peaks in HgTe [37]: the observed line shapes disagree with those expected from the one-electron theory (equal positive and negative peaks) but agree with those predicted in the presence of a Koster-Slater interaction (fig. 11). Similar results have been found for other zincblende-type materials [37].

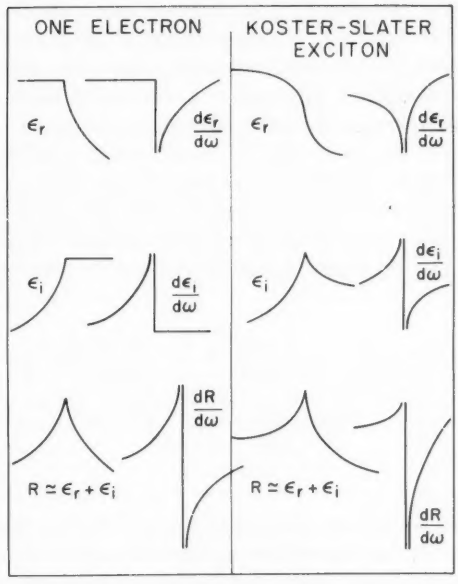

FIGURE 11. *Modification in ϵ_r and ϵ_i introduced by the Koster-Slater exciton interaction in the neighborhood of an M_1 critical point. Also, effect on the reflectivity under the assumption of an equal contribution of $\Delta\epsilon_r$ and $\Delta\epsilon_i$ to the reflectivity line shape.*

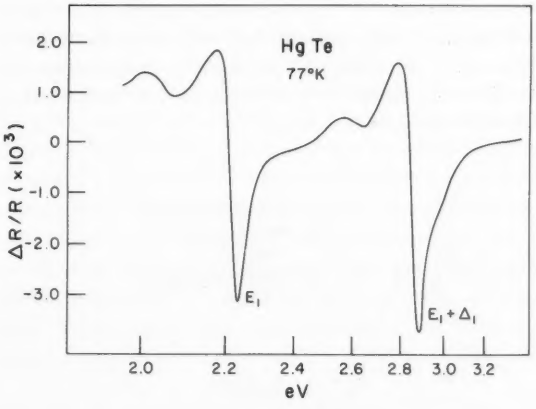

FIGURE 12. *Photon energy derivative spectrum of the reflectivity of HgTe in the neighborhood of the E_1 and $E_1+\Delta_1$ structure* [37].

3. Simplified Models for the Density of States

As seen in section 1 the optical density of states, and thus the dielectric constant, is a complicated function of frequency and its calculation requires lengthy numerical computation. For some purposes, however, it can be approximated by simple functions. In the vicinity of a critical point of the M_i variety, for instance, the singular behavior of the dielectric constant can be approximated by:

$$\epsilon \propto i^{r+1}(\omega-\omega_g)^{1/2}+\text{constant} \qquad (4)$$

if exciton effects are neglected. Exciton interaction can be included, within the Koster-Slater model, by multiplying eq (4) by a phase factor $e^{i\phi}$ with ϕ small and positive.

As shown in figure 1, ϵ_i for the zincblende-type materials has a strong peak (E_2) in the neighborhood of which most of the optical density of states is concentrated. The corresponding transitions occur over a large region of the BZ, close to its boundaries. In order to represent this fact, Penn [38] suggested the model of a non-physical spherical BZ with an isotropic gap at its boundaries. The complex energy bands of the material are then replaced by those of a free electron with an isotropic gas ω_g at the boundary of a spherical BZ. This gap should occur in the vicinity of the E_2 optical structure. While this model represents rather poorly the rich

structure of ϵ_i (fig. 1), it is expected that it should give a good picture of ϵ_r at zero frequency. The reshuffling of density of states involved in the case of the isotropic model should not affect $\epsilon_r(\omega = o)$ very much because of the large energy denominators which appear in eq (3) for $\omega = o$: the lowest gap ω_o, usually much smaller than ω_g, accounts only for a very small fraction of the optical density of states. Penn obtained with this model the static dielectric constant for a finite wavevector $\mathbf{q}$. The result can be approximated by the analytic expression [38]:

$$\epsilon(\omega = o,\ q) = 1 + \left(\frac{\omega_p}{\omega_g}\right)^2 \mathcal{F} \left\{1 + \frac{\omega_F}{\omega_g}\frac{q}{k_F}\mathcal{F}^{1/2}\right\}^{-2} \quad (5)$$

with $$\mathcal{F} = 1 - \frac{\omega_g}{4\omega_F} + \frac{1}{3}\left(\frac{\omega_g}{\omega_F}\right)^2$$

In eq (5) ω_p is the plasma frequency obtained for the density of valence electrons and ω_F and k_F the corresponding free electron Fermi energy and wave number. The dimensionless quantity $\mathcal{F}$ is usually close to one.

Figure 13 shows eq (5) for Si compared with the exact results of the Penn model [39]. These results are obviously independent of the direction of $\mathbf{q}$. A small dependence on this direction is found from a complete pseudopotential calculation by Nara [40] (see also fig. 13). The function $\epsilon(o,\mathbf{q})$ is of interest for the treatment of dielectric screening.

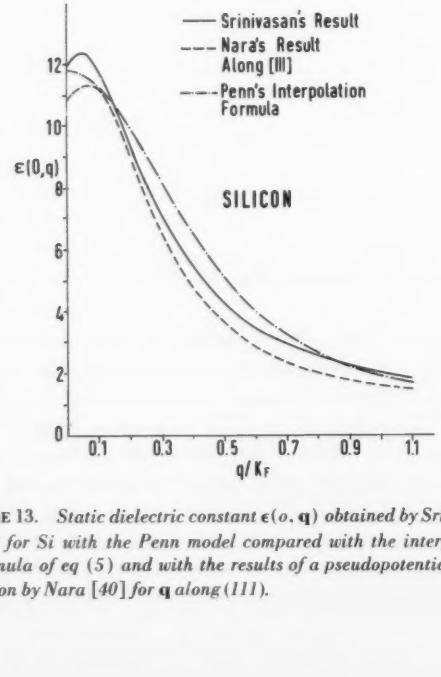

FIGURE 13. *Static dielectric constant $\epsilon(o, \mathbf{q})$ obtained by Srinivasan [39] for Si with the Penn model compared with the interpolation formula of eq (5) and with the results of a pseudopotential calculation by Nara [40] for $\mathbf{q}$ along (111).*

Equation (5) yields for $\mathbf{q} = o$ the electronic contribution to the static dielectric constant:

$$\epsilon_o = 1 + \mathcal{F}\left(\frac{\omega_p}{\omega_g}\right)^2 \simeq 1 + \left(\frac{\omega_p}{\omega_g}\right)^2 \quad (6)$$

The experimental values of ϵ_o agree reasonably well with the results of eq (6) using for ω_g the energy of the E_2 peak [34]. Equation 6 has gained recent interest as the basis of Phillips and Van Vechten's theory of covalent bonding [41,42,43]. These authors use eq (6) and the experimental values of ϵ_o to define the average gap ω_g. With this gap and the corresponding gap of the isoelectronic group IV material they can interpret a wide range of properties such as crystal structure [42], binding energy [43], energies of interband critical points [41], non-linear susceptibilities [44], *etc.* As an example we discuss the hydrostatic pressure (*i.e.* volume) dependence of ϵ_o for germanium and silicon. According to Van Vechten [41], ω_g for C, Ge, Si, and α–Sn is proportional to $(a_o)^{-2.5}$ where a_o is the lattice constant. If one makes the assumption that this law gives also the change in ω_g with lattice constant for a given material when hydrostatic stress is applied one can calculate the volume dependence of ϵ_o [41]. Neglecting the one in eq (6), a valid approximation for Ge and Si, one finds:

$$\frac{1}{\epsilon_o}\frac{d\epsilon_o}{dV} = 2\left(\frac{d\ \ln\ \omega_p}{dV} - \frac{d\ \ln\ \omega_g}{dV}\right)$$

$$= 2[0.83 - 0.50] = 0.66 \quad (7)$$

Equation (7) explains the sign and the small magnitude observed for $(1/\epsilon_o)(d\epsilon_o/dV)$. The experimental values of this quantity are 1.0 for Ge and 0.6 for Si [41,45].

According to eq (6) the average gap ω_g determines the electronic dielectric constant for $\omega = o$. As the lowest gap ω_o is approached ($\omega_o \ll \omega_g$ usually), ϵ_r exhibits strong dispersion. This dispersion is due, in the spirit of eq (3), to the density of states in the vicinity of ω_o. For the purpose of calculating the dispersion of ϵ_r immediately below ω_o, the density of states can be approximated by that of parabolic bands with a reduced mass equal to the reduced mass μ at ω_o. These bands are assumed to extend to infinity in $\mathbf{k}$ space: the unphysical contribution to ϵ_r for $|k| \to \infty$ should be small for $\omega \leqslant \omega_o$, because of the large energy denominators of eq (3). We thus obtain for a cubic material the following contribution of the ω_o gap to the scalar dielectric constant below ω_o (under the assumption of a constant matrix element of $\mathbf{p}$ equal to $\mathbf{P}$) [46]:

$$\Delta\epsilon_r = 2(2\mu)^{3/2}\omega_0^{3/2}|P|^2 f(\omega/\omega_0) = C_0'' f(\omega/\omega_0)$$

with (8)

$$f(x) = 2-(1+x)^{1/2}-(1-x)^{1/2}.$$

Equation (8) represents quite well the behavior of ϵ_r immediately below ω_o for the lead chalcogenides [47] and a number of other semiconductors [48]. As an example we show in figure 14 the observed dispersion of ϵ_r below ω_o at room temperature [49] together with a fit based on eq (8) [48]. For the sake of completeness we have included in the fitting equations not only the effect of ω_o (E_o) but also that of its spin-orbit-split mate $E_o+\Delta_o$ (also represented by an expression similar to eq (8)), the dispersion due to the E_1 and $E_1+\Delta_1$ gaps, and that due to the main ω_g gap assuming $\omega_g \equiv E_2$. Thus the fitting equation with three adjustable parameters C_0'', C_1'', C_2'' is [48]:

$$\epsilon_r(\omega) = 1 + C_o''\left\{f(x_o) + \frac{1}{2}\left(\frac{\omega_o}{\omega_{os}}\right)^{3/2} f(x_{os})\right\} + C_1''\left\{h(x_1) + \left(\frac{\omega_1}{\omega_{1s}}\right) h(x_{1s})\right\} + C_2''(1+2x_2^2) \quad (9)$$

where:

$$\omega_{os} = \omega_o + \Delta_o, \qquad x_{os} = \frac{\omega}{\omega_{os}}, \qquad x_1 = \frac{\omega}{\omega_1}$$

$$\omega_{1s} = \omega_1 + \Delta_1, \qquad x_{1s} = \frac{\omega}{\omega_{1s}}, \qquad x_2 = \frac{\omega}{\omega_g}$$

$$h(x_1) = 1 + \frac{x_1^2}{2}.$$

The fitting values of C_0'' (6.602) and C_1'' (2.791) are in qualitative agreement with those calculated from the band parameters [48].

The parabolic model density of states can also be used to interpret the strong dispersion in the piezobirefringence observed near the lowest direct gap of

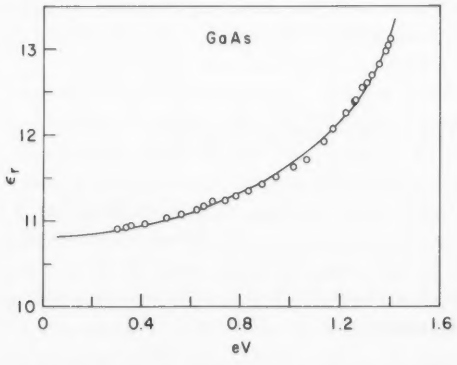

FIGURE 14. *Experimental results for ϵ_r in GaAs below the fundamental edge at room temperature [49] (circles) and fitted curve based on a model density of states.*

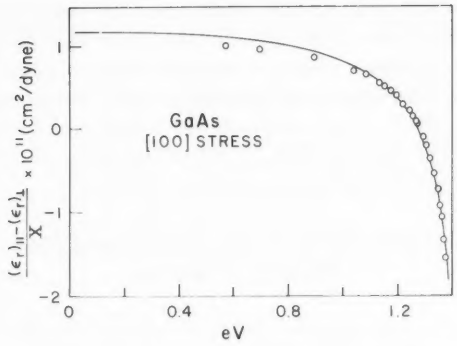

FIGURE 15. *Piezobirefringence in GaAs for an extensive stress along (100) (room temperature). The circles are experimental points. The solid line is a fit based on the model of eq (5) [48].*

Ge, GaAs [48], and other III–V semiconductors [50,51]: uniaxial stress splits the top valence band state (Γ_8) and a birefringence in the contribution of E_o to ϵ_r results because of the selection rules for transitions from the split bands. The main contribution to this piezobirefringence is expected to be proportional to f'(x), which diverges like $(\omega-\omega_0)^{-1/2}$ for $\omega \to \omega_o$. Such behavior can be seen in the experimental results (circles) of figure 15 obtained for GaAs at room temperature. Included in this figure is the corresponding fit based on the model of eq (9) [48].

The long wavelength, non-dispersive contribution to the piezobirefringence of figure 15 can be interpreted, at least qualitatively, in terms of the Penn model of eqs (6) and (7). Equation (7) yields two contributions to the change in ϵ_r one due to the change in plasma frequency (*i.e.* carrier density) with stress and the other due to the change in the isotropic gap. The first contribution should not exist for a pure shear stress. For a hydrostatic stress the second contribution can be written in tensor form as:

$$\frac{1}{\epsilon_0}\Delta\epsilon_0 = 5\mathbf{e} \quad (10)$$

where $\mathbf{e}$ is the strain tensor. We postulate that eq (8) remains valid for pure sheer stress. This crude generalization has a clear physical meaning in terms of the Penn model. The spherical BZ becomes ellipsoidal under a sheer stress and the energy gap at an arbitrary point of the BZ boundary k_F becomes anisotropic. The gap at k_F is assumed to become larger as k_F becomes larger (k_F is the distance between atomic planes per-

pendicular to k_F). Equation (8) gives the right sign for the long wavelength contribution to the piezobirefringence of figure 15 but a magnitude about five times larger. The agreement becomes better if the contribution of the E_o edge to the long wavelength piezobirefringence, of opposite sign to that predicted by eq (10), is subtracted from the experimental results.

4. Third Order Susceptibility and Model Density of States

It has been recently suggested [52] that the third order susceptibility of Ge, Si, and GaAs at long wavelengths is related to the Franz-Keldysh effect (*i.e.* the intraband coupling by the field) of interband critical points [53]. We discuss now the Franz-Keldysh contribution of the ω_g, E_o, and E_1 gaps to $\chi^{(3)}_{1111}$.

4.1. Average Gap ω_g

In the spirit of Penn's model [38] we represent the long-wavelength dielectric constant by eq (6) with $\mathcal{F}=1$. The corresponding imaginary part of the dielectric constant is, for $\omega > \omega_g$ [47]:

$$\epsilon_i = A^{-2}(\omega-\omega_g)^{-1/2} \qquad \text{with} \qquad A=\frac{4}{3}\,\omega_p^2\omega_g^{1/2} \tag{11}$$

The Franz-Keldysh effect for the one-dimensional absorption edge of eq (11) can be expressed in terms of the Airy functions Ai and Bi [54]. One must mention, however, that the isotropic gap problem in the presence of an electric field would only be completely equivalent to the one-dimensional problem if the field experienced by every electron were along the direction of the corresponding **k**. The fact that the field $\boldsymbol{\mathscr{E}}$ is the same for all electrons, regardless of **k**, can be taken into account by using an average field:

$$\langle \mathscr{E}^2 \rangle = \frac{\langle \cos^4\beta\rangle}{\langle \cos^2\beta\rangle}\,\mathscr{E}^2 = \frac{3}{5}\,\mathscr{E}^2 \tag{12}$$

where β is the angle between **k** and $\boldsymbol{\mathscr{E}}$. The long-wavelength expression for $\chi^{(3)}_{1111}$ thus is [54]:

$$\chi^{(3)}_{1111} = \frac{3A}{20\pi\omega^2} \lim_{\substack{\mathscr{E}\to 0\\ \omega\to 0}} \mathscr{E}^{-2}\theta^{-1/2}\left(G_1\left(\frac{\omega_g+\omega}{\theta}\right) + G_1\left(\frac{\omega_g-\omega}{\theta}\right) - G_1\left(\frac{\omega_g}{\theta}\right)\right), \tag{13}$$

where the one-dimensional electro-optic function $G_1(\eta)$ is given by [54]:

$$G_1(\eta) = 2\pi Ai(\eta)Bi(\eta) - H(\eta)\eta^{-1/2} \qquad \theta=\left(\frac{\mathscr{E}^2}{2\mu}\right)^{1/3} \tag{14}$$

In eq (14) H (η) is the unit step function and μ the reduced mass of the Penn model, given by $\mu=\omega_g(2k_F)^{-2}$. The Fermi momentum of the valence electrons is related to the plasma frequency ω_p through $k_F{}^3=(3/4)\pi\omega_p{}^2$.

The limit for $\mathscr{E}\to 0$ in eq (14) is easily found using the asymptotic expansions of Ai (η) and Bi (η) for $\eta\to+\infty$ [55]. By subsequently performing the limit for $\omega\to 0$ one finds:

$$\chi^{(3)}_{1111} = \frac{287}{256\pi}\left(\frac{3}{4}\,\pi\right)^{2/3}(\epsilon_o-1)\,\frac{\omega_p^{4/3}}{\omega_g^4} \tag{15}$$

Or, for ease of evaluation, with $\chi^{(3)}_{1111}$ in e.s.u., and the energies in eV:

$$\chi^{(3)}_{1111} = 1.45\cdot 10^{-11}(\mathscr{E}_o-1)\,\frac{\omega_p^{4/3}}{\omega_g^4} \tag{16}$$

We list in table I the values of ω_g, ω_p and $\epsilon_o - 1$ for Ge, Si and GaAs. The values of $\chi^{(3)}_{1111}$ calculated with eq (16) are then listed in table II. This table shows agreement in sign and magnitude between the values of $\chi^{(3)}_{1111}$ predicted from ω_g and the experimental ones. An increase in the polarizability with field ($\chi^{(3)}_{1111} > 0$) is to be expected for the Franz-Keldysh effect since the intraband coupling by the electric field produces a decrease in the energy gap.

We shall consider now the contribution to $\chi^{(3)}_{1111}$ of the interband coupling by the electric field across the isotropic gap ω_g. This coupling produces an increase in energy gap, and thus its contribution to $\chi^{(3)}_{1111}$ is negative. This contribution to $\chi^{(3)}_{1111}$ is readily found from eq (6):

$$\Delta\chi^{(3)}_{1111} = -\frac{3}{5\pi}(\epsilon_o-1)\frac{1}{\omega_g}\frac{d\omega_g}{d(\mathscr{E}^2)} = -\frac{3(\epsilon_o-1)}{5\pi}\left(\frac{3\pi}{4}\right)^{2/3}\frac{\omega_p^{4/3}}{\omega_g^2} \tag{17}$$

In eq (17) we have made use of the second-order perturbation expression:

$$\frac{d\omega_g}{d(\mathscr{E}^2)} = 2\,\frac{|<v|\mathbf{r}|c>|^2}{\omega_g} = \frac{2k_F^2}{\omega_g^2} \tag{18}$$

Equation (18) is in agreement with the results of ref. [44]. Comparison of this equation with eq (15) shows that the magnitude of the interband contribution to $\chi^{(3)}_{1111}$ differs from that of the intraband contribution by a factor of order $\omega_g{}^2$ (ω_g in atomic units). It is therefore almost two orders of magnitude smaller and hence negligible.

4.2. Lowest Gap E_o

We use for the contribution of an isotropic M_o critical point to the real part of the dielectric constant the result of eq (8). A calculation similar to that performed above yields for an M_o critical point the following Franz-Keldysh contribution to $\chi^{(3)}_{1111}$ [52]:

$$\Delta\chi^{(3)}_{1111} = 0.06\,\frac{p^2\mu_o^{1/2}}{\omega_o^{9/2}}\left(1+1.85\left(\frac{\omega}{\omega_o}\right)^2+\ldots\right) \quad (19)$$

or, transforming $\Delta\chi^{(3)}_{1111}$ to e.s.u. and ω_o to eV (P^2 and μ_o are left in atomic units for ease of computation):

$$\Delta\chi^{(3)}_{1111}(\omega) = 6\cdot 10^{-10}\,\frac{C_0^2\mu_0^{1/2}}{\omega_o^{9/2}} \times\left(1+1.85\left(\frac{\omega}{\omega_o}\right)^2+\ldots\right) \quad (20)$$

We have included in eqs (19) and (20) the first term in the dispersion of $\Delta\chi^{(3)}_{1111}$ since it may be possible to observe it experimentally in small band gap materials. This dispersion is given exactly by the function:

$$\frac{\omega_o^2}{\omega^2}\left(\left(1+\frac{\omega}{\omega_o}\right)^{-2.5}+\left(1-\frac{\omega}{\omega_o}\right)^{-2.5}-2\omega_o^{-2.5}\right) \quad (21)$$

Equation (21) is not immediately valid for the E_o edge because of the degeneracy of the valence band. However, one can apply it to the E_o edge if one neglects the field coupling between degenerate valence bands and uses appropriate average values of P^2 and μ_o. Each one of the three valence bands can be assumed to have a mass equal to three times the conduction band mass and a corresponding matrix element equal to $\frac{1}{3}p^2$ [48]. Hence eq (20) must be used with the matrix element P^2 and $\mu_o = \frac{3}{4}m_e$ if the three valence bands are to be included. The spin-orbit splitting Δ_o of the valence band is taken into account, if $\Delta_o \ll E_o$, by replacing ω_o by its average value $E_o + \frac{\Delta_o}{3}$. Since P^2 is almost the same for all materials of the germanium family, we can replace it by a typical value ≈ 0.4 (in atomic units). The values of μ_o and $\omega_o = E_o + \frac{\Delta_o}{3}$ for Ge, Si and GaAs are listed in table I. Using these numbers, eq (20) yields the values of $\chi^{(3)}_{1111}$ ($\omega = 0$) listed in table II. While this contribution is zero for Si and is not excessive in GaAs (it may, therefore, be assumed as included in the average gap calculation given above), it is dominant in Ge. In first approximation it may be added to the average gap calculation: excellent agreement with the experimental results is then found.

TABLE 1. *Values of the parameters required for the evaluation of the Franz-Keldysh contributions to $\chi^{(3)}_{1111}$. Frequencies in eV, a_0 in Bohr radii, μ_o in units of the free electron mass. p^2 has been taken equal to 0.4 for all materials.*

	Ge	Si	GaAs
ω_g	4.3	4.8	5.2
ω_p	15.5	17.35	15.5
$\epsilon_0 - 1$	11	15	10
μ_o	0.03	0.04	0.05
ω_o	0.9	4	1.5
a_0	10.7	10.3	10.7
ω_1	2.2	3.3	3.0

TABLE II. *Contribution of the various Franz-Keldysh effects discussed here to $\chi^{(3)}_{1111}$ and $\chi^{(3)}_{\xi\xi\xi\xi}$. In units of 10^{-10} e.s.u. Also, experimental values of the bound carrier contributions to $\chi^{(3)}_{1111}$ and $\chi^{(3)}_{\xi\xi\xi\xi}$.*

		E_g contribution	E_0 contribution	E_1 contribution	Experiment[57]
Ge	$\chi^{(3)}_{1111}$	0.26	0.67	0.20	1.0
	$\chi^{(3)}_{\xi\xi\xi\xi}$	0.26	0.67	0.26	1.5
Si	$\chi^{(3)}_{1111}$	0.22	0.00	0.27	0.06
	$\chi^{(3)}_{\xi\xi\xi\xi}$	0.22	0.00	0.36	0.08
GaAs	$\chi^{(3)}_{1111}$	0.12	0.087	0.045	0.12
	$\chi^{(3)}_{\xi\xi\xi\xi}$	0.12	0.087	0.060	0.10

For InAs, with $\omega_o = 0.5$ eV and $\mu = 0.02$, we find from eq (20) $\Delta\chi^{(3)}_{1111}(\omega = 0) = 7\cdot 10^{-10}$, which is of the order of the free-carrier contribution for the samples with the lowest electron concentrations measured ($N = 2\cdot 10^{16}$ cm^{-3}) [57]. This is contrary to the statement found in the literature that for these carrier concentrations in InAs $\chi^{(3)}_{1111}$ is dominated by the free-carrier contribution [56,57,58].

The interband contribution of E_o to $\chi^{(3)}_{1111}$ for $\omega=0$ is easily obtained from the expression (see eq (8)):

$$\Delta\epsilon_r(\omega=0)=\frac{(2\mu_0)^{3/2}p^2}{2}\omega_g^{-3/2} \tag{22}$$

If one assumes that the repulsion produced by the field affects μ_o in the manner predicted by the $\mathbf{k}\cdot\mathbf{p}$ expression with constant matrix elements of $\mathbf{p}(\mu_o \propto \omega_g)$, the corresponding interband contribution to $\chi^{(3)}_{1111}$ vanishes. If, on the other hand, one assumes μ_o to be field independent one also finds a negative contribution to $\chi^{(3)}_{1111}$ about two orders of magnitude smaller than the Franz-Keldysh contribution, and hence negligible.

4.3. E_1 Critical Points

The E_1 optical structure is usually attributed to M_1 critical points along the {111} directions. While M_1 critical points are known to yield no contribution to $\chi^{(3)}_{1111}$ [52], there are M_o critical points of the same symmetry slightly below the M_1 critical points. This combination of M_o and M_1 critical points with a very large longitudinal mass, can actually be approximated by two-dimensional minima [48]. The contribution of one of these two-dimensional minima to the long-wavelength dielectric constant is (we assume four, and not eight equivalent {111} directions):

$$\Delta\epsilon_r=\frac{4\sqrt{3}\mu_\perp p^2}{a_o\omega_1^2} \tag{23}$$

where a_o is the lattice constant and P^2 the appropriate square matrix element. We have tried to calculate the Franz-Keldysh contribution to $\chi^{(3)}_{1111}$ of these two-dimensional critical points in a way similar to that used above, but we have run into difficulties when evaluating the limits of the two-dimensional electro-optic functions for $\eta\rightarrow+\infty$. In view of this we have instead evaluated the effect of the three-dimensional M_o critical points, with the longitudinal effective mass replaced by the value required to give at long wavelengths a contribution to ϵ_r equal to that in eq (23).

Under these conditions, and because of the large longitudinal mass, only fields transverse to the critical point axis contribute to $\chi^{(3)}_{1111}$. When summing the contributions of the four equivalent valleys, it is found that the effect becomes anisotropic: the ratio of the third order susceptibility for $\mathscr{E}$ along {111} ($\chi^{(3)}_{\xi\xi\xi\xi}$), to that for $\mathscr{E}$ along {100} is 4/3. This argument is independent of the specific model chosen for the {111} transitions, provided $\mu_{||}\gg\mu_\perp$. It gives the type of anisotropy ($\chi^{(3)}_{\xi\xi\xi\xi}>\chi^{(3)}_{1111}$) observed for Ge and Si, but not for GaAs [57]. The Franz-Keldysh contribution of E_1 to $\chi^{(3)}_{1111}$ as found by the procedure sketched above, is:

$$\Delta\chi^{(3)}_{1111}=0.52\frac{p^2}{a_o\omega_1^5} \tag{24}$$

or, with ω_1 in eV and $\chi^{(3)}_{1111}$ in e.s.u.:

$$\Delta\chi^{(3)}_{1111}=2.7\cdot10^{-8}\frac{p^2}{a_o\omega_1^5} \tag{25}$$

(a_o in Bohr radii and P^2 in atomic units.)

The matrix element P should have approximately the same value as for the E_o gap. In order to take care of the spin-orbit splitting Δ_1 of E_1 we substitute ω_1 by $E_1+\Delta_1/2$. The approximate values of a_o, and ω_1 for Ge, Si and GaAs are listed in table I. The values calculated for the Franz-Keldysh contribution to E_1 to $\chi^{(3)}_{1111}$ and $\chi^{(3)}_{\xi\xi\xi\xi}$ are listed in table II. While the calculated anisotropy has, for Ge and Si, the sign observed experimentally, its magnitude is far too small to explain the experimental anisotropy, especially after the E_o and the E_g contributions are added. There is a possibility that the E_1 contribution of eq (25) may have been underestimated. Exciton quenching effects [59,60], not included in our calculation, may increase this contribution.

We cannot offer even a qualitative explanation of the sign of the $\chi^{(3)}$ anisotropy observed for GaAs. It would be interesting to determine, through measurements of other III–V or II–VI compounds, whether it is connected with the lack of inversion symmetry in these materials.

The interband contribution of the E_4 edges can be evaluated in a manner analogous to that used for the E_o and the ω_g gaps. We also find that this contribution is negative and, typically, two orders of magnitude below the Franz-Keldysh contribution.

5. Acknowledgments

I am indebted to Drs. Buss, Kane, Phillips, Van Vechten, and Aspnes for sending preprints of their work, prior to publication and to the staff of DESY for their hospitality.

6. References

[1] Cohen, M. L., and Bergstresser, T. K., Phys. Rev. **141**, 789 (1966).
[2] Cardona, M., and Pollak, F. H., Phys. Rev. **142**, 530 (1966).
[3] Dresselhaus, G., and Dresselhaus, M. S., Phys. Rev. **160**, 649 (1967).

[4] Herman, F., Kortum, R. L., Kuglin, C. D., and Shay, J. L., in "II–VI Semiconducting Compounds," D. G. Thomas, ed., (W. A. Benjamin, New York, 1967), p. 503.
[5] Gilat, G., and Dolling, G., Phys. Letters **8,** 304 (1964); Gilat, G., and Raubenheimer, L. J., Phys. Rev. **144,** 390 (1966).
[6] Higginbotham, C. W., Pollak, F. H., and Cardona, M., Proceedings of the IX International Conference on the Physics of Semiconductors, Moscow 1968 (Publishing House Nauka, Leningrad, 1968) p. 57.
[7] Buss, D. D., and Parada, N. J., private communication; see also article by D. D. Buss and V. E. Shirf in these proceedings.
[8] Kane, E. O., Phys. Rev. **146,** 558 (1966).
[9] Philipp, H. R., and Ehrenreich, H., Phys. Rev. **129,** 1550 (1963).
[10] Cardona, M., Z. Physik **161,** 99 (1961).
[11] Zhang, H. I., and Callaway, J., Phys. Rev. **181,** 1163 (1969).
[12] Walter, J. P., and Cohen, M. L., Phys. Rev., to be published.
[13] Seraphin, B. O., and Bottka, N., Phys. Rev. **145,** 628 (1966).
[14] Shaklee, K. L., Rowe, J. E., and Cardona, M., Phys. Rev. **174,** 828 (1968).
[15] Matatagui, E., Thompson, A. G., and Cardona, M., Phys. Rev. **176,** 950 (1968).
[16] Higginbotham, C. W., Ph. D. Thesis, Brown University, 1969.
[17] Eckelt, P., Madelung, O., and Treusch, J., Phys. Rev. Letters **18,** 656 (1967).
[18] Brinkman, W., and Goodman, B., Phys. Rev. **149,** 597 (1966).
[19] Pollak, F. H., Cardona, M., Higginbotham, C. W., Herman, F., and Van Dyke, J. P., Phys. Rev., to be published.
[20] McElroy, P., Ph. D. Thesis, Harvard University, 1968.
[21] Cardona, M., and Greenaway, D. L., Phys. Rev. **133,** A1685 (1964).
[22] Scanlon, W. W., J. Phys. Chem. Solids **8,** 423 (1959).
[23] Aspnes, D. E., and Cardona, M., Phys. Rev. **173,** 714 (1968).
[24] Sandrock, R., Phys. Rev. **169,** 642 (1968).
[25] Tutihasi, S., and Chen, I., Phys. Rev. **158,** 623 (1967).
[26] Lin, P. J., and Phillips, J. C., Phys. Rev. **147,** 469 (1966).
[27] Wiech, G., in "Soft X-Ray Spectra," D. J. Fabian, ed., (Academic Press, New York, 1968) p. 59.
[28] Feuerbacher, B., Skibowski, M., Godwin, R. P., and Sasaki, T., JOSA **58,** 1434 (1968).
[29] See for instance R. S. Knox, "Theory of Excitons," (Academic Press, N.Y., 1963).
[30] Mahan, G. D., Phys. Rev. Letters **18,** 448 (1967).
[31] Velicky, B., and Sak, J., Phys. Status Solidi **16,** 147 (1966).
[32] Kane, E. O., Phys. Rev. **180,** 852 (1969).
[33] Marple, D. T. F., and Ehrenreich, H., Phys. Rev. Letters **8,** 87 (1962).
[34] Cardona, M., J. Appl. Phys. **36,** 2181 (1965).
[35] Inoue, M., Okazaki, M., Toyozawa, Y., Inui, T., and Nanamura, E., Proc. Phys. Soc. Japan **21,** 1850 (1966).
[36] Hermanson, J., Phys. Rev. **150,** 660 (1966).
[37] Shaklee, K. L., Ph. D. Thesis, Brown University, 1969.
[38] Penn, D., Phys. Rev. **128,** 2093 (1962).
[39] Srinivasan, G., Phys. Rev. **178,** 1244 (1969).
[40] Nara, H., J. Phys. Soc. Japan **20,** 778 (1965).
[41] Van Vechten, J. A., Phys. Rev. **182,** 891 (1969). In this reference a correction factor of the order of unity is added to eq (6) so as to take the polarizability of the core d electrons into account.
[42] Phillips, J. C., Phys. Rev. Letters **20,** 550 (1968).
[43] Phillips, J. C., Covalent Bonding in Molecules and Solids (University of Chicago Press, Chicago) to be published.
[44] Phillips, J. C., and Van Vechten, J. A., Phys. Rev. **183,** 709 (1969); Levine, B. F., Phys. Rev. Letters **22,** 787 (1968).
[45] Cardona, M., Paul, W., and Brooks, H., J. Phys. Chem. Solids **8,** 204 (1959).
[46] Korovin, L. I., Soviet Phys. Solid State **1,** 1202 (1959).
[47] Cardona, M. in "High Energy Physics, Nuclear Physics, and Solid State Physics," I. Saavedra, ed., (W. A. Benjamin, New York, 1968).
[48] Higginbotham, C. W., Cardona, M., and Pollak, F. H., Phys. Rev. **184,** 821 (1969).
[49] De Meis, W. M., Technical Report No. HP-15 (ARPA-16), Harvard University (1965).
[50] Shileika, A. Yu., Cardona, M., and Pollak, F. H., Solid State Communications **7,** 1113 (1969).
[51] Yu, P. Y., to be published.
[52] Van Vechten, J. A., and Aspnes, D. E., Phys. Letters, in press.
[53] Aronov, A. G., and Pikus, G. E., Proceedings of the IX International Conference on the Physics of Semiconductors, Moscow, 1968, (Publishing House Nauka, Leningrad, 1968), p. 390.
[54] Cardona, M., "Modulation Spectroscopy," F. Seitz, D. Turnbull, and H. Ehrenreich, eds., (Academic Press Inc., New York, N.Y.).
[55] Antonsiewicz, H. A., in "Handbook of Mathematical Functions," (M. Abramowitz and I. A. Stegun, eds.) (Dover Pub. Inc., New York, N.Y., 1965) p. 448.
[56] Wolff, P. A., and Pearson, G. A., Phys. Rev. Letters **17,** 1015 (1966).
[57] Wynne, J. J., Phys. Rev. **178,** 1295 (1969).
[58] Patel, C. K. N., Slusher, R. F., and Fleury, P. A., Phys. Rev. Letters **17,** 1011 (1966).
[59] Hamakawa, Y., Germano, F. A., and Handler, P., J. Phys. Soc. Japan, Suppl. **21,** 111 (1966).
[60] Shaklee, K. L., Rowe, J. E., and Cardona, M., Phys. Rev. **174,** 828 (1968).

(Paper 74A2-597)

JOURNAL OF RESEARCH of the National Bureau of Standards—A. Physics and Chemistry
Vol. 74A, No. 2, March-April 1970

Excitonic Effects in X-Ray Transitions in Metals*

G. D. Mahan [1]

Institute of Theoretical Science and Department of Physics, University of Oregon, Eugene, Oregon 94703 [2]

and

General Electric Research and Development Center, Schenectady, New York 12301

(October 10, 1969)

In the study of soft x-ray transitions in solids, there has always been some hope that the results provide a direct measure of the density of states. This assumes that (a) matrix element variations over the band and (b) final state interactions are small. Both of these assumptions are now known to be incorrect. To illustrate the possible strength of these effects, two approximate calculations are presented: the one electron oscillator strength of a simple bcc metal as a function of energy; and the strength of the Nozieres—DeDominicis singularity at threshold, with phase shifts estimated from an assumed Yukawa interaction between conduction electrons and core hole.

Key words: Density of states; exciton; many body effects; phase shifts; soft x-ray; transition probability.

I. Introduction

The absorption of a photon can cause an electron to change its state. The traditional viewpoint of this transition assumes that if one knew the electrons initial ψ_i and final ψ_f state, then the oscillator strength was simply proportional to the square of the momentum matrix element.

$$p_{if}=\int d^3r\psi_f^* p\psi_i \tag{1.1}$$

This simple viewpoint is now known to be incorrect. The proper picture is that the optical transition creates an electron and hole, and these two excitations interact with each other, and each separately with their environment. The coulomb scattering between the electron and hole is called the exciton effect, named after the first known example of Frankel excitons in solids. The electron and hole can also emit phonons, suffer electron-electron collisions, *etc.* The sum of all of these processes are called final-state interactions. The rate of optical absorption is affected by these subsequent interactions of the electron and hole.

Upon reviewing our present understanding of the optical properties of solids, one finds that some solids are well understood while others are not. We classify as understood the semiconductors Si and Ge, [1] and simple metals like aluminum [2,3]. It is noteworthy that in these materials the final-state interactions are small: they are small in semiconductors because the large dielectric constant suppresses the exciton effect. Ehrenreich and his co-workers have shown that many body effects are small in aluminum. In these solids the simple one-electron picture implied in (1.1) seems to work quite well.

We classify wide band gap insulators [4], and metals such as copper [5], as solids whose optical properties are not well understood. There is not yet good agreement between theory and experiment in these materials. The dominant optical transitions in these materials create hole states which are heavy, and which are subject to significant final state interactions [3]. We speculate that final state interactions are important in these materials, and explain the difference between theory and experiments.

In the study of x-ray transition in solids, there has always been some hope that the results provide a direct

*An invited paper presented at the 3d Materials Research Symposium, *Electronic Density of States*, November 3-6, 1969, Gaithersburg, Md.

[1] Alfred P. Sloan—Research Fellow.

[2] Research Supported by National Science Foundation Grant.

measure of the density of states [6]. This presumes that (a) matrix element variations over the band are small, and (b) final state interactions are small. Both of these assumptions are now known to be incorrect [7,8,9].

The importance of exciton effects in x-ray transitions was reported in an earlier reference [10]. The effects are large if the hole is highly localized, and if the conduction band of the electron is isotropic. Because the coulomb scattering between the electron and hole occurs in an electron gas, the electron can only scatter into states not already occupied. This Fermi-Dirac exclusion, as well as the exchange interaction among the electrons, causes the problem to resemble the Kondo effect more than the Wannier-exciton case. The hole also has a large interaction with the entire electron gas—this leads to a renormalization effect which inhibits the x-ray transition near threshold [11]. Nozieres and DeDominicis [12] have shown that the exciton and renormalization effects combine to give a threshold behavior for $\epsilon_2(\omega)$

$$\epsilon_2(\omega) \sim \frac{1}{\omega^2}\left(\frac{\xi_0}{\omega-\omega_T}\right)^{\alpha_l}\theta(\omega-\omega_T) \qquad (1.2)$$

where ω_T is the absorption threshold frequency, $\xi_0 \sim E_F$ is a characteristic band energy, and α_l is a function of the phase shifts δ_l of electrons at the Fermi energy scattering from the static potential of the hole.

$$\alpha_l = \frac{2\delta_l}{\pi} - 2\sum_{l=0}^{\infty}(2l+1)\left(\frac{\delta_l}{\pi}\right)^2 \qquad (1.3)$$

The term $2\delta_l/\pi$ is the exciton part which tends to make the threshold singular, while the second term in (1.3) arises from renormalization. The angular momentum l is that of the conduction electron [13]. If the x-ray hole has s-symmetry, the conduction electron must have p-symmetry ($l=1$). If the hole has p-symmetry, the conduction electron can have either s- or d-symmetry; in this case (1.2) has a separate term for each symmetry type.

The x-ray spectra can only be unravelled with a knowledge of the phase shifts δ_l—these are the phase shifts for simple electron-hole scattering. These have been calculated for a free electron gas by Ausman and Glick [13]. They find $\alpha_0 > 0$, and $\alpha_l < 0$ for $l \geq 1$ so that singularities only occur for the $l=0$ case (p-state hole). These results qualitatively agree with the experimental results.

We have independently calculated the phase shifts, and we describe our result in section II. We have concluded that these phase shifts are qualitatively correct but for the wrong reasons. The wrong potential is used in the calculation, but it does not seem to make much difference in this case.

II. Phase Shifts

The present calculations have been performed by assuming that the screened electron-hole interaction has the Yukawa form

$$V(r) = -\frac{e^2}{r}\exp(-k_s r)$$

where the Fermi-Thomas screening length is

$$k_s^2 = 6\pi e^2 n_0/E_F$$

for an electron gas of density n_0 and Fermi energy E_f. This is only a crude approximation to the actual potential the electron feels when scattering from the hole. For example, studies of a point charge impurity in an electron gas show that its potential differs from a Yukawa at long range where Friedel oscillations occur, and at short range where its potential is less steep [14]. In addition, because the hole is part of an atom, there are term due to the exchange and orthogonality with the atomic wave functions [7,8]. In a pseudo-potential formalism these latter effects contribute a short-range repulsive term to the interaction. In spite of these shortcomings of the Yukawa potential, we believe that it predicts phase shifts which are qualitatively correct. The reasons for this will be presented below.

The phase shifts are defined in terms of the eigenvalues E_k and eigen functions $\psi_k(r)$ of the electron in the region of the potential.

$$\left(-\frac{\nabla^2}{2m}+V(r)-E_k\right)\psi_k(r)=0 \qquad (2.1)$$

The wave is decomposed into spherical harmonics

$$\psi_k(r) = \sum_{l=0}^{\infty}(2l+1)i^l P_l(\hat{k}\cdot\hat{r})\phi_l(k,r) \qquad (2.2)$$

In solving for the eigen functions in (2.1), one has the choice of specifying the boundary conditions for states which are plane wave-like outside of the potential region. By choosing standing wave conditions, one is solving for a reaction matrix $K_l(k,k')$ and the phase shifts are defined in terms of the diagonal $k=k'$ component [15].

$$\tan\delta_l(k) = -2mkK_l(k,k)$$
$$= -2mk\int_0^{\infty} r^2 dr j_l(kr)V(r)\phi_l(k,r) \qquad (2.3)$$

Similarly, if one chooses outgoing wave conditions, then one is solving for a T-matrix $t_l(k,k')$ whose diagonal components give the phase shift [15].

$$\sin \delta_l e^{i\delta_l} = -2mkt_l(k,k)$$
$$= -2mk \int_0^\infty r^2 dr j_l(kr) V(r) \phi_l(k,r) \qquad (2.4)$$

We have chosen to use the reaction-matrix formalism (2.3), mostly because it is a real function and this simplifies computation.

The phase shifts $\delta_l(k)$ go to zero as $k \to \infty$. Let us now examine their behavior as $k \to 0$. From (2.3) we have $j_l(kr) \sim (kr)^l$, so

$$\tan \delta_l(k) \sim k^{l+1} \int_0^\infty r^{l+2} dr V(r) \phi_l(0,r) \qquad (2.5)$$

From Levinson's Theorem we know that

$$\delta_l(0) = \pi M_l$$

where M_l is the number of bound states of (2.1) with angular momentum l. For example, if $M_l = 0$ we get $\delta_l \sim k^{l+1}$. Whereas if $M_l = 1$ we get $\delta_l = \pi + ck^{l+1}$ (where c is some constant) for small k. A typical case is shown in figure 1, where $M_0 = 1$, and $M_l = 0$ for $l \geq 1$. So the s-wave phase shift comes into π with a linear slope, while all other $\delta_l \sim k^{l+1}$ at small k.

So in calculating phase shifts, the first thing to decide is the number of bound states M_l. This is determined by examining the radial part of Schrödinger's equation (2.1) which we put into dimensionless form

$$\left[-\frac{\partial^2}{\partial \rho^2} + \frac{l(l+1)}{\rho^2} - \lambda \frac{e^{-\rho}}{p} - \mathscr{E} \right] r\phi_l = 0 \qquad (2.6)$$

$$\rho = k_s r$$
$$\lambda = \frac{2me^2}{\hbar^2 k_s} = \left(\frac{2\pi}{3}\right)^{1/3} \sqrt{r_s}$$
$$\mathscr{E} = 2mE/\hbar^2 k_s^2 \qquad (2.7)$$

The parameter λ determines the strength of the potential. Shey and Schwartz [16] have computed the number of bound states which exist for each value of λ and l. For s-waves ($l = 0$), they find no bound states exist for $\lambda < 1.68$, one bound state for $1.68 < \lambda < 6.45$, two bound states for $6.45 < \lambda < 14.3$, *etc.* For p-waves ($l = 1$) bound states only exist for $\lambda > 9.08$, and d-wave bound states exist for $\lambda > 21.8$.

In (2.7) we have written λ in terms of the density parameter r_s for an electron gas. Since metallic densities vary between $2 < r_s < 6$, then the range of λ values in metals is $1.8 < \lambda < 3.1$. For an electron gas of metallic density, there is one bound state for s-states, and no bound states for any other value of angular momentum l.

These are the predictions of the Yukawa potential. We must decide whether these are reasonable conclusions for the problem of interest. For an actual point charge in an electron gas, *e.g.*, a proton, there is probably a bound state. For an impurity in a host metal, *e.g.*, Al atoms in Mg, there is probably not a real bound state. This is because the atomic core of the impurity cuts off the attractive potential in the region where it is the strongest; for example, see Ashcroft's remarks about the cancellation influence of the atomic cores [8].

In the x-ray problem there is certainly an atomic core. Yet there is also certainly a bound state in the potential. This bound state is the x-ray level itself. That is, if an electron scattering from the potential of the hole did not think a bound state existed in the potential, then it would have no inclination to recombine with the hole in the final emission process. Since the emission can occur, a bound state does exist which must be reflected on the phase shifts.

The cancellation of the potential in atomic core is caused by the necessity of the conduction electron wave function to be orthogonal to all of the core states. In the x-ray problem, one core electron is absent so that the cancellation requirements are less stringent.

The foregoing discussion shows that any phase shifts calculated from a simple Yukawa potential are only going to be qualitatively correct. Yet there is some interest in what this simple model predicts. Our method of calculation proceeds by solving directly the scattering equation for the reaction matrix.

$$K_l(k_1, k_2) = V_l(k_1, k_2)$$
$$+ \frac{4m}{\pi} \int_0^\infty k_3^2 dk_3 \frac{V_l(k_1, k_3) K_l(k_3, k_2)}{k_2^2 - k_3^2} \qquad (2.8)$$

where the l^{th} component of the potential V_l is obtained from the Fourier transform $V(\mathbf{k}_1\text{-}\mathbf{k}_2)$ of $V(r)$

$$V_l(k_1, k_2) = \frac{1}{2} \int_0^\pi d\theta \sin\theta P_l(\cos\theta) V(\mathbf{k}_1 - \mathbf{k}_2)$$
$$= \frac{e^2}{2k_1 k_2} Q_l((k_1^2 + k_2^2 + k_s^2)/2k_1 k_2) \qquad (2.9)$$

372-505 O - 70 - 9

when cos θ is the angle between $\mathbf{k}_1$ and $\mathbf{k}_2$, and Q_l is a Legendre function. We will abbreviate the argument of the Legendre function to write it as $Q_l(k_1, k_2)$. Noyes' method is used to evaluate (2.8). We find

$$K_l(k, k) = V_l(k, k)/(1-\Lambda_l(k)) \tag{2.10}$$

$$\Lambda_l(k) = \frac{-4m}{\pi V_l(k,k)} \int_0^\infty \frac{p^2 dp}{p^2-k^2} V_l(k, p) f_l(k, p) \tag{2.11}$$

$$f_l(k, p) = V_l(k, p) + \frac{4m}{\pi V_l(k,k)} \int_0^\infty \frac{p'^2 dp' f_l(k, p')}{p'^2-k^2} [V_l(p, k)V_l(k, p') - V_l(p, p')V_l(k, k)] \tag{2.12}$$

One obtains $f_l(k,p)$ from (2.12), perhaps by iterating this equation. This is used in (2.11) to obtain $\Lambda_l(k)$, and thus one has the reaction matrix in (2.10). This is an exact result if $f_l(k,p)$ is found exactly. The Born Approximation result is obtained by setting $K_l(k, k) = V_l(k, k)$.

Note that it is natural to write $\Lambda_l(k)$ as a power series in the interaction strength $\lambda = 2/k_s a_B$ in (2.7)

$$\Lambda_l(k) = \sum_{m=1}^{\infty} \lambda^m g_l^{(m)}(k/k_s) \tag{2.13}$$

Each successive power of λ corresponds to another iteration of the equation (2.12) which determines $f_l(k,p)$. For example, the first term is

$$g_l^{(1)}(k) = \frac{k_s}{\pi Q_l(k,k)} \int_0^\infty \frac{dp}{p^2-k^2} Q_l(k, p)^2 \tag{2.14}$$

For $l = 0$ we can evaluate the integral and express the integral as a summation.

$$g_0^{(1)}(k) = \frac{k_s}{2kQ_0(k,k)} \sum_{l=1}^{\infty} \frac{(-)^l}{l^2} [2\rho^l \sin(\varphi l) - \sin(2l\varphi)]$$

$$\rho = [1+4k^2/k_s^2]^{-1/2} \tag{2.15}$$

$$\varphi = \tan^{-1}(2k/k_s)$$

$$Q_0(k,k) = \tfrac{1}{2} \ln (1+4k^2/k_s^2)$$

This form is convenient for numerical computation. In figure 1 is shown the s-wave phase shift calculated by approximating Λ_0 by the first term in (2.13)

$$\tan \delta_0(k) = \frac{Q_0(k,k)}{ka_B[1-\lambda g_0^{(1)}(k)]}$$

Also shown in figure 1 are the phase shifts δ_1 and δ_2. We also calculated the first correction term $g_1^{(1)}(k)$ to the p-wave phase shift, and this correction has been added into the calculation of the curve labeled δ_1. This only changes the Born Approximation result by 10 percent. The $l = 2$ phase shift is the Born Approximation result. The multiple scattering terms are small except for the s-wave.

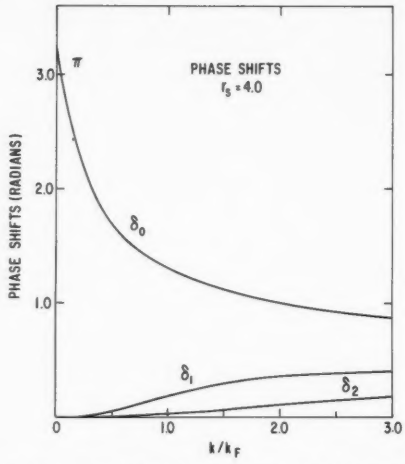

FIGURE 1. *The phase shifts δ_l calculated by a Yukawa potential. This potential represents a coulomb interaction of unit charge, with Fermi-Thomas screening. The phase shift δ_2 is calculated in the Born Approximation, while δ_0 and δ_1 have corrections for multiple scattering.*

In the x-ray transition, the singular effects occur at the Fermi surface, so we are interested in the phase shifts evaluated at k_f. Figure 2 shows the critical ex-

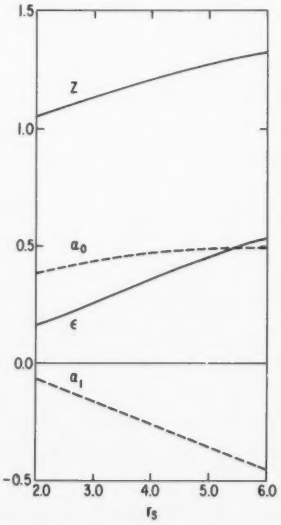

FIGURE 2. *The variation with electron density r_s of the exponents α_0 and α_1. These depend upon the phase shifts evaluated at the Fermi surface. Also shown is the renormalization parameter ϵ and the Friedel sum rate result Z. The value of Z is rigorously unity, and our deviations from that value indicate the errors in the calculation.*

ponents α_0 and α_1, in (1.3) plotted versus electron density r_s. Values of α_l for $l \geq 2$ are essentially equal to $-\epsilon$. Also shown are the values of the Friedel sum Z and the Anderson exponent ϵ, where

$$Z = 2\sum_{l=0}^{\infty} (2l+1)(\delta_l/\pi)$$

$$\epsilon = 2\sum_{l=0}^{\infty} (2l+1)(\delta_l/\pi)^2$$

The Friedel sum rule should rigorously be given by $z = 1$. Our deviation ~20 percent from the exact result of $z = 1$ provides an estimate of the error in the calculation.

Another estimate of the accuracy and convergence of the calculational method is obtained by seeing how well it estimates the position of bound states. As $k \to 0$ we get

$$\lim_{k\to 0} \delta_0(k) = \tan^{-1}\left(\frac{2k/ks}{1-\Lambda_0(0)}\right)$$

A bound state is predicted if $\Lambda_0 > 1$. We find that

$$g_0^{(1)}(0) = 1/2$$

$$g_0^{(2)}(0) = \ln\,(4/3) - 1/4$$

If we just use the first term in the expansion (2.13) so $\Lambda_0(0) = \lambda/2$ then the criteria $\Lambda_0(0) > 1$ means $\lambda > 2$. This is an error of 16 percent from the actual criteria $\lambda > 1.68$. But using two terms gives $\lambda/2 + \lambda^2(\ln 4/3 - 1/4) > 1$ or $\lambda > 1.765$. So a considerable improvement in accuracy is obtained by including the second term in (2.13). So we conclude that the series (2.13) converges rapidly for the range of λ values of interest.

III. Matrix Elements

The change of the matrix element with energy has been discussed before and is known to be a large effect [7,8,9]. We have calculated the change in matrix element near the first critical point in a bcc solid for an x-ray transition from a 1s core level. We used a simple two band model in each 1/12 of the Brillouin Zone [17], so that the energies and eigenstates are

$$E_k^{\pm} = \frac{1}{2}(\mathscr{E}_k + \mathscr{E}_{k-G}) \pm \left[\frac{1}{4}(\mathscr{E}_k - \mathscr{E}_{k-G})^2 + V_G^2\right]^{1/2}$$

$$\psi_k^{\pm}(r) = N_k\left\{|\mathscr{E}_k - E_k^{\mp}|^{1/2} e^{i\mathbf{k}\cdot\mathbf{r}} \pm \frac{V_G}{|V_G|}|\mathscr{E}_k - E_k^{\pm}|^{1/2} e^{ir\cdot(\mathbf{k}-\mathbf{G})}\right\}$$

$$N_k = \frac{1}{2}\left[\frac{1}{4}(\mathscr{E}_k - \mathscr{E}_{k-G})^2 + V_G^2\right]^{-1/2}$$

The matrix elements were calculated assuming that the core was a delta function, and no attempt was made to orthogonalize the conduction states to the core. Thus, after averaging over polarizations, the matrix elements are

$$\langle p_k^2\rangle^{\pm} = \tfrac{1}{3}N_k^2\{k^2|\mathscr{E}_k - E_k^{\mp}| + (\mathbf{k}-\mathbf{G})^2|\mathscr{E}_k - E_k^{\mp}| \pm 2\mathbf{k}\cdot(\mathbf{k}-\mathbf{G})V_G\}$$

In figure 3 we show the density of states $\rho(E)$, and also the absorption strength

$$A(E) = \int \frac{d^3k}{(2\pi)^3}\{\langle p_k^2\rangle^{+}\delta(E-E_k^{+}) + \langle p_k^2\rangle^{-}\delta(E-E_k^{-})\}$$

In this figure, energy has been normalized to $E_0 = \hbar^2G^2/8m$ so that $\mathscr{E} = E/E_0$ and $\nu = V_G/E_0$. The choice $\nu = 0.2$ is close to Ham's value for Li ($\nu = 0.23$). Indeed, the present calculation was done with Li in mind, since the lack of core orthogonalization should not matter here.

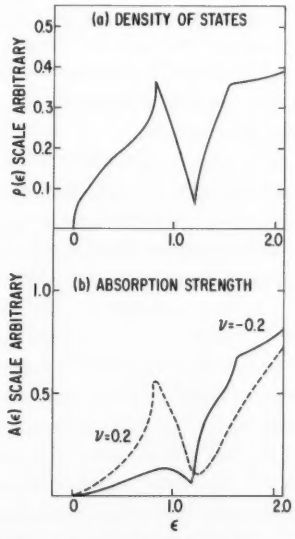

FIGURE 3. *The density of states $\rho(\epsilon)$ and absorption strength $A(\epsilon)$ for a bcc solid such as Li. The energy scale is listed in units $E_0 = \hbar^2G^2_{110}/8m$, and $\nu = V_{110}/E_0$. The absorption strength $A(\epsilon)$ is defined as the integral of the x-ray matrix element $<p^2>$ averaged over the energy band.*

The curve for $\nu = 0.2$ in figure 3(b) has the expected shape for Li [18]. Because the wave function is p-like at the lower critical point $\mathscr{E} = 0.8$, the transition is allowed and the absorption strength has the same shape as the density of states in figure 3a. The density of states structure at $\mathscr{E} = 1.2$ is washed out in $A(\mathscr{E})$ because at the critical point the transition is s-like and largely

forbidden. The curve for $\nu = -0.2$ has the same density of states, but now the upper critical point is p-like and $A(\mathscr{E})$ has the same structure as $\rho(\mathscr{E})$ near 1.2. Neither the curve $\nu = 0.2$ nor $\nu = -0.2$ has any striking resemblance to the density of states [18].

IV. Discussion

Exciton effects should influence nearly all parts of the absorption spectra. The singular behavior at the absorption or emission edge is just one prominent feature. Another result of final state interactions is that oscillator strength is moved from one frequency range to another. Often these shifts are small and can be neglected. Yet in most cases the true magnitude of these effects are unknown, because the relevant theoretical calculations are too complicated to do realistically.

The calculation of exciton effects is a formidable task which has not been performed properly. Of course Wannier excitons have been studied in detail. Some model calculations exist near critical point edges—the hyperbolic excitons [19,20,21]. But the main optical absorption strength comes from states throughout the Brillouin Zone [5], and all of these states are included in the final state interactions.

So before x-ray absorption and emission measurements can be used to provide information on the density of states, two sizable corrections need to be made. One of these is the exciton effect, and the other is the change in the matrix element with energy.

V. Acknowledgments

I wish to thank N. Ashcroft, L. Parrott, and M. Stoneham for informative discussions.

VI. References

[1] Dresselhaus, G., and Dresselhaus, M. S., Phys. Rev. **160**, 649 (1967).
[2] Ehrenreich, H., and Beeferman, L., (private communcation).
[3] Spicer, W. E., Phys. Rev. **154**, 385 (1967).
[4] Fong, C. Y., Saslow, W., and Cohen, M. L., Phys. Rev. **168**, 992 (1968); Park, K., and Stafford, R. G., Phys. Rev. Letters **22**, 1426 (1969).
[5] Dresselhaus, G., Sol. State Comm. **7**, 419 (1969); Mueller, F. M., and Phillips, J. C., Phys. Rev. **157**, 600 (1967).
[6] Tomboulian, D. H., Handbuch der Physik, **Vol. 30**, (Springer-Verlag, Berlin, 1957), 246-304.
[7] Harrison, W. A., Soft X-Ray Band Spectra, edited by D. J. Fabin (Academic Press, New York, 1968), p. 227.
[8] Ashcroft, N. W., ibid, p. 249.
[9] Rooke, G. A., ibid, p. 3.
[10] Mahan, G. D., Phys. Rev. **163**, 612 (1967).
[11] Anderson, P. W., Phys. Rev. Letters **18**, 1049 (1967).
[12] Nozieres, P., and DeDominicis, C. T., Phys. Rev. **178**, 1097 (1969).
[13] Ausman, G. A., and Glick, A., Phys. Rev.
[14] Langer, J. S., and Vosko, S. H., J. Phys. Chem. Solids **12**, 196 (1960).
[15] Goldberger, M. L., and Watson, K. M., Collision Theory (J. Wiley and Sons, New York, 1964), p. 232.
[16] Schey, H. M., and Schwartz, J. L., Phys. Rev. **139**, Bi428 (1965).
[17] Foo, E-Ni, and Hopfield, J. J., Phys. Rev. **173**, 635 (1968).
[18] Shaw, R. W., Smith, K., and Smith, N. V., Phys. Rev. **178**, 985 (1969).
[19] Duke, C. B., and Segall, B., Phys. Rev. Letters **17**, 19 (1966).
[20] Hermanson, J., Phys. Rev. Letters **18**, 170 (1967).
[21] Kane, E. O., Phys. Rev. **180**, 852 (1969).

(Paper 74A2–598)

JOURNAL OF RESEARCH of the National Bureau of Standards — A. Physics and Chemistry
Vol. 74A, No. 2, March-April 1970

Soft X-Ray Band Spectra and Their Relationship to the Density of States *

G. A. Rooke

Metallurgy Department, University of Strathclyde, Glasgow[1]

(October 10, 1969)

The paper concentrates on the similarities and differences between the one-electron spectrum and the density of states; many-body effects, although important, are listed but they are not considered in detail. It is shown that the only reliable information about the density of states that can be obtained from soft x-ray spectroscopy are the energies of the Fermi surface and the van-Hove singularities, although the shape of the density of states can be derived indirectly from the energies of the van-Hove singularities.

It is the differences between the density of states and the one-electron spectra that may prove to be most important. These differences can give information about the symmetry and the local nature of the screening electrons. This is particularly interesting when studying alloys.

The Li K, the Al L_{23} and the Zn L_3 spectra are given as examples which illustrate the above arguments. Finally, a brief discussion on the soft x-ray spectra from the Al-Mg system show how the results may be used to study alloys.

Key words: Alloys; auger transitions; density of states; many-body interactions; plasmons; singularities; soft x rays.

1. Introduction

Before commencing my discussion, I would like to state our objectives in attempting to measure the density of states: they are

(a) to compare experiments that are in some way related to the density of states;
(b) to derive some information about concepts of a more fundamental nature, the band structure, the effective potential, *etc.*, and
(c) to attempt to predict the properties of other metals and alloys.

It is important to bear these in mind, as sometimes our objectives can be achieved more directly by not making use of the density of states.

It will be remembered that when transitions involving atomic core states occur, x-rays may be emitted or absorbed. The x-rays have an energy equal to the energy difference between the two states involved in the transition. If one of the states lies in the valence band or the conduction band, a band spectrum is produced (see fig. 1). Experimentally, better energy resolution is obtained from the band spectra with lower energies; these are called soft x-ray band spectra. Although this paper specifically discusses soft x-ray spectra, the concepts are applicable to all band spectra.

For an introductory review of soft x-ray band emission spectroscopy, I recommend either Skinner [1] or Tomboulian [2]. An excellent bibliography of Yakowitz and Cuthill [3] reviews the literature up to 1961. Some of the most recent work in the field is described in a conference proceedings edited by Fabian [4]. All of these omit very interesting Russian work for which no comprehensive review is known to me.

2. Many-Body Interactions

The many-body interactions are treated in this paper as uninteresting complications that tend to hide the information we are seeking. Each interaction is considered as a perturbation on the one-electron spectrum.

The interactions between individual electrons create two types of perturbations on the spectra, the excited initial and final states, which directly affect the spectra, and exchange and correlation, which affect the spectra

*An invited paper presented at the 3d Materials Research Symposium, *Electronic Density of States*, November 3-6, 1969, Gaithersburg, Md.

[1] Present address: Ferranti Ltd., Western Road, Bracknell, Berks, U.K.

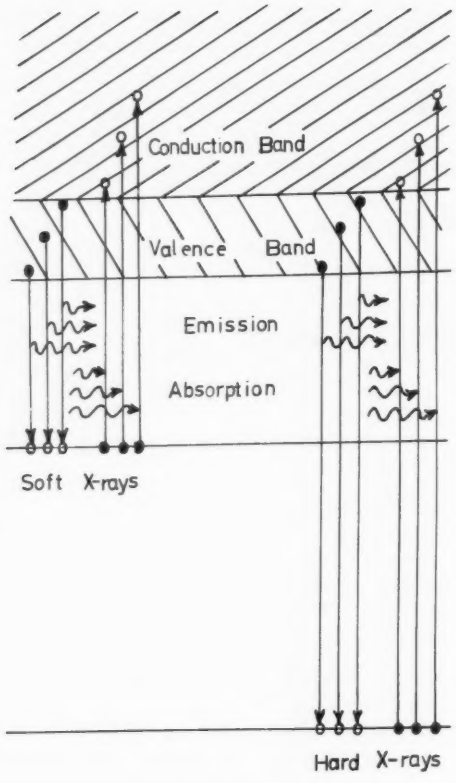

FIGURE 1. *One-electron energy-level diagram showing x-ray transitions.*

through their effects on the band structure. The exchange and correlation only cause trouble when comparing uncorrected one-electron band-structures with experimental results [5]. They are normally allowed for by theoreticians and are only important to experimentalists when they are measuring many-body effects or when they are trying to derive the uncorrected band-structures.

Excited states occur whenever electron transitions occur. For *all* radiating transitions, two single-particle excitations are involved; in emission processes both the initial and the final states are normally excited while in absorption processes the initial state is normally unexcited and the final state contains two single-particle excitations. Each excitation affects the spectrum through its lifetime and through its perturbing effects on the unexcited one-electron spectrum. Three types of one-electron excitation can occur and their effects on the spectra are discussed separately.

First, the hole in the core state perturbs the valence electrons, so that the intensity at the Fermi surface is reduced for K spectra (transitions to 1s-states) and enhanced for L_{23} spectra (transition to 2p-states) [6]. The lifetime of the hole in the core state causes the spectrum to be broadened because of the uncertainty in its energy. If this lifetime is known, it is possible to correct for this broadening [7]. The hole in the core state can only affect spectra that involve x-rays.

Second, a hole in the valence band can be filled by an electron in the same band, provided another valence-band electron is excited into the conduction band, thereby conserving energy; this interaction is called the Auger process. Because of this, there are both holes and excited electrons with energies close to the Fermi energy and this raises the possibility of excitons occurring in the metal. Also, Auger processes shorten the lifetime of the hole and this broadens the spectra considerably. Because many more electrons are capable of filling holes near the bottom of the band than those near the top of the band, the lifetime of a hole near the bottom of the band is shorter and the spectrum is broadened more near the bottom of the band than near the top. It has not yet proved possible to remove the Auger broadening from spectra, because the broadening is not constant throughout the band. Auger broadening is important to any spectroscopy involving the absorption of the ultraviolet light, to x-ray emission spectroscopy and to ion-neutralization spectroscopy.

Third, the scattering of electrons excited into the conduction band is important to any process involving the absorption of radiation. This scattering is very similar to the Auger process; an excited electron falls to an energy level closer to the Fermi energy, giving its energy to another electron which is excited out of the valence band and into the conduction band. The remaining holes and the scattered electrons could form excitons. For any electron emission spectroscopy the scattered electrons can contribute to the spectra and they enhance the spectra near the Fermi edge. In general, the lifetime of the excited states decreases as their energy increases, so that the resultant broadening is not constant throughout the band and is exceedingly difficult to remove.

For each type of optical spectroscopy discussed at this conference, two of these three types of one-electron excitations are involved and for ion-neutralization spectroscopy, four excitations occur.

The first two types of excitations are involved in soft x-ray band emission spectroscopy. The perturbations of the valence band, near the Fermi edge, by the hole in the core state is possibly the cause of the drop in intensity near the Fermi edge in the lithium K spectrum and the cause of the small pip near the Fermi edge in the sodium L_{23} spectrum [6]. It probably contributes more

XUM

to the shape of all light metal spectra than to the heavy metal spectra, because the hole represents a larger proportion of the core electrons in the light metals. The core broadening prevents the detection of spectra resulting from transitions to 2s, 3s, *etc.* core states and it also is important in changing the shape of the spectra from heavy metals; the lifetime of the excited state is considerably reduced because of competing non-radiative transitions. Auger broadening is responsible for the low-energy tails in the spectra from metals and this introduces uncertainty into the measurement of the bandwidths.

For other spectroscopic techniques, these excitations are also highly important, their importance depending on both the technique used and the metal examined.

Besides exciting a single electron state, it is also possible to excite the electrons collectively into plasma oscillations. When this occurs, together with the emission of an x-ray photon, the photon loses enough energy to create the plasmon and a satellite spectrum is formed at lower energies [8,9]. Interactions between individual electrons and the plasmons, which are called plasmarons [10], have a measurable effect on the plasmon satellite [11] but not on the parent band.

3. The Density of States and Band Spectra

In order to discuss the relationship between the density of states and the spectra, it is assumed in the remainder of this paper that the effects of the many-body interactions can be corrected for. The word "spectrum" then implies "one-electron spectrum that would result if such corrections were made"; this spectrum has the same width as the valence band, its shape is related to the density of states but it is affected by the transition probabilities.

The similarities between the density of states, N(E), and the one-electron spectrum divided by the cube of the radiation frequency, $\frac{I(E)}{\nu^3}$, are seen by comparing the following equations:

$$N(E) \propto \int_s d^2\mathbf{k} \frac{1}{\nabla_{\mathbf{k}} E} \tag{1}$$

$$I(E)/\nu^3 \propto \int_s d^2\mathbf{k} \frac{1}{\nabla_{\mathbf{k}} E} \left| \int \psi_{\mathbf{k}} \nabla_x \psi_f d\tau \right|^2 \tag{2}$$

where E is the energy of the state with wave vector **k** and the integral is taken over the surface, s, of constant energy, E. For the density of occupied states and for the emission spectrum, the integral is taken over the region of **k** space that lies inside the Fermi surface, while, for the density of unoccupied states and for the absorption spectrum, the integral is taken over the region of **k** space that lies outside the Fermi surface. The square of the modulus of the matrix element, $\int \psi_{\mathbf{k}} \nabla_x \psi_f d\tau$, is the transition probability, whose properties determine the difference between the two functions; the dipole approximation has been assumed.

A striking similarity between the two functions occurs because the integrations are terminated at the Fermi surface; this produces the Fermi edges in the functions. Unfortunately, for some heavy metals, the core-state broadening and the transition probabilities combine to make the Fermi edge almost impossible to measure.

The Brillouin zone effects are also common to both functions; at certain points of high symmetry on the Brillouin zone boundaries, the gradient, $\nabla_{\mathbf{k}} E$, is zero and van-Hove singularities exist at corresponding points in the two functions. Certain van-Hove singularities are of particular interest; in particular the energy of the bottom of the band can be used to estimate the bandwidth and the energy of the top and bottom of the d-band give the width of this band and its relation to the Fermi energy, both of which are of considerable theoretical interest.

Because the matrix element is **k**-dependent, it is not possible to remove the transition probabilities from inside the integral in eq (2). Hence, it is not possible to write the intensity as a product of the density of states and the average transition probability and, even if the transition probabilities are fully known, it is not possible to remove their effects from the spectra. Rooke [12] has shown that the **k**-dependence of the matrix element is large, sometimes changing it from nearly 1 to nearly 0 on the same constant energy curve, so that errors created by removing the matrix element from the integral can be serious.

From the above considerations it can be seen that the detailed density of states cannot be directly derived by using soft x-ray spectroscopy; or by using any form of spectroscopy, for that matter. Sometimes a spectrum and the density of states will have similar shapes and they will certainly have the Fermi edge and some van-Hove singularities in common. If the spectrum changes under different experimental conditions, such as heat or pressure, it may be possible to assume that the changes will be entirely due to the density of states and to obtain a little more information about the density of states in this way. This technique has been used to find the effect of the Fermi-Dirac statistics on the density of states, by heating the target (1) and to find the effect of

alloying on the density of states. A more sophisticated version of this approach has just been developed by J. H. Willens in Bell Laboratories [13]. In another method for obtaining more information about the density of states, one derives a band structure that fits the measured van-Hove singularities and then uses this to calculate the density of states. However, as Fermi surface techniques are capable of making fine distinctions between band structures, they can also be used to obtain densities of states which are often more accurate than those obtained from soft x-ray spectroscopy. Even though it is only possible to obtain limited information about the density of states, this information is often very interesting. However, it is often even more interesting to examine the information that can be derived by studying the effect of the transition probabilities on the spectra. This information is discussed in the next section.

4. The Transition Probability and the Band Spectra

The differences between the functions defined in eqs (1) and (2) are determined by the matrix element

$$\int \psi_{\mathbf{k}} \nabla_x \psi_f d\tau$$

The integration is taken over all real space and ∇_x is the component of the real-space gradient-operator in the **x** direction.

ψ_f is the wavefunction of the core state and, because of its high symmetry, it is a good approximation to express it as

$$\psi_f(r, \theta, \phi) = R_{n'}(r) Y_{l'}(\theta)\ e^{im'\phi} \tag{3}$$

where $R_{n'}$ (r) is a radical function, $Y_{l'}(\theta)$ is a Legendre polynomial and n′, l′ and m′ are the usual quantum numbers. The radial function has appreciable magnitude only near the center of the atom and the state is localized. Because only one Legendre polynomial is involved, the state can be labeled by atomic notation; 1s, 2p, 3d, *etc*.

$\psi_{\mathbf{k}}$ is the wavefunction of a valence state and it may be expanded as a series of spherical harmonies

$$\psi_{\mathbf{k}} = \sum_{l,\,m} C_l(\mathbf{k}) a_{l,\mathbf{k}}(r)\ Y_l(\theta)^{im\phi} \tag{4}$$

Normally, only the first three values of l are important. The radial terms are roughly constant throughout real space so that the state is shared by all atoms and is not localized like the core states.

Substituting these expansions of the wavefunctions into the matrix elements gives

$$\int \psi_{\mathbf{k}} \nabla_x \psi_f d\tau \propto \sum_{l,\,m} C_l(\mathbf{k}) \times \int R_{n'}(r) a_{l,\mathbf{k}}(r)\, r^3 dr$$

$$\times \int Y_{l'}(\theta)\ Y_l(\theta)\ f\binom{\sin}{\cos}\theta\, d\theta \times \int e^{i(m-m')\phi}\, g\binom{\sin}{\cos}\phi\, d\phi \tag{5}$$

where f and g are functions whose form depends on the polarization. Each of these four terms contributes a distinct characteristic to the transition probability. The **k**-dependence of the first two terms, as shown in the last section, prevents the direct derivation of the density of states from the spectra.

The third term is zero unless

$$l = l' \pm 1 \tag{6}$$

This selection rule is particularly important for x-ray transitions, because the core state involved has a well defined symmetry described by a single spherical harmonic. If the core state is an s-state, only p-like states can make the transition to it. Similarly, only s-like and d-like states can make the transition to a p-state.

This selection rule enables us to describe states in terms of partial densities of states; the density of s-states, the density of p-states and the density of d-states. K spectra (transitions to the s-state) give approximate estimates of the density of p-states, while L_{23} or M_{23} spectra (transitions to the 2p or 3p states respectively) give approximate estimates of the density of s and d states.

Because these partial densities of states only approximate to the shape of the spectra, it is not possible to add them and to derive a meaningful density of states. However, this symmetry dependence of x-ray band spectra makes them unique in the information that they can reveal. This is particularly interesting in the case of alloys, for which this characteristic of x-ray spectra should be fully exploited to determine the nature of the screening charges. Further, it is the authors unsubstantiated view, that the extended fine-structure occurring in absorption spectra can also be attributed to this selection rule.

Besides creating gross features in the spectra, this selection rule modifies the magnitudes of the van-Hove singularities. The symmetry of the crystal dictates that the states associated with points of high symmetry in the Brillouin zone will have high symmetry themselves. Thus, some of these states are almost entirely p-like while others are s-like or s and d like. If a state is entirely s-like, it will not contribute to a K spectrum and, if it

is associated with a van-Hove singularity, that singularity will not be seen in the K spectrum. Similarly, as most states contain a mixture of symmetries, van-Hove singularities associated with states that are entirely p-like will be exaggerated in the K spectra. The reverse situation occurs for L_{23} or M_{23} spectra, for which p-like singularities will not be observed and s and d like singularities will be exaggerated.

The last term in eq (5) is dependent on the polarization of the radiation and it is non-zero if $m = m' \pm 1$, but if the polarization is suitable it may also be non-zero if $m = m'$. We therefore write the second selection rule as

$$m = m' = \pm 1 \text{ or } 0 \qquad (7)$$

This rule implies that not all the transitions described in the second last paragraph are allowed. For any one type of transition, say s to p, only a fraction of transitions are allowed and this fraction may vary throughout the band, thereby distorting the spectrum. However, this distortion may not be serious, as the fraction may be nearly constant throughout the band. Of course, the constant fraction for d to p type transitions will be different from that for s to p type transitions and, in fact, the fraction for these transitions can be shown to be about 2/5 of that for the s to p transitions. This means that the L_{23} or M_{23} spectra give an approximate measure of the density of s-states plus 2/5 density of d-states. This is one reason why the L_{23} and K spectra, when added together, do not give the full density of states.

The second term in eq (5) provides the spectra with some very interesting properties. The integral effectively takes a weighted average of a(r), using a weighting factor of $rR_{n'}(r)$. Because of the localized nature of $R_{n'}(r)$, this integral can be considered to take an average of a(r) in the region near the core state of the emitting atom. This is exceedingly interesting when studying alloys, as the spectra from each component metal will sample the wavefunction in the region of that type of atom. These local properties are of great interest and are only obtainable by the spectroscopies involving x-rays.

Finally, the degree of approximation involved in assuming that spectra are similar to the partial densities of states is discussed. Consider the case of the K spectrum, which samples p-states. Because the wavefunctions are normalized, the term $\int \psi_{\mathbf{k}}^2 \, d\tau$ may be inserted into eq (1) without changing it. This term may be written as

$$\sum_l (2l+1)^2 \, C_l^2(\mathbf{k}) \int a_{l,\mathbf{k}}^2 \, (r) \, r^2 \, dr$$

and the density of p-states may be defined as

$$N_p(E) \propto \int_s^{d^2\mathbf{k}} \frac{1}{\nabla_{\mathbf{k}} E} \, C_l^2(\mathbf{k}) \int a_{l,k}^2(r) \, r^2 dr \qquad (8)$$

By replacing the last two terms in eq (5) by non-zero constants and restricting the summation to $l = 1$, eq (2) may then be written as

$$I_k(E)/v^3 \propto \int^{d^2\mathbf{k}} \frac{1}{\nabla_{\mathbf{k}} E} \, C_l^2(\mathbf{k}) \left| \int_0 a_{l,\mathbf{k}}(r) r^2 dr \right|^2 \qquad (9)$$

where the zero on the radial integral indicates that it is now restricted to the region of the core state of the emitting atom. The final terms in these equations differ, one being the average of the square of a(r) and the other being the square of a local average of a(r). For the densities of s-states and of d-states and the corresponding spectra, the situation is complicated by the factor of 2/5 and by cross terms, but the differences arise in the same way.

5. The Spectra from Pure Metals

It is shown above, that x-ray spectra sample only those wavefunctions that have specific symmetries and that lie near the core of the emitting atom. Apart from these restrictions, they tend to show some of the behavior of the density of states, particularly the Fermi edge and the van-Hove singularities. The spectra are broadened by the experimental resolution and by many-body effects and it is possible that these many-body effects also change the shape of the spectra near the Fermi edge. These ideas are now illustrated by three pure metal spectra; the Li K, the Al L_{23} and the Zn L_3 emission spectra.

The Li K emission spectrum [14] is shown in figure 2. The Auger tail is immediately obvious but the Fermi

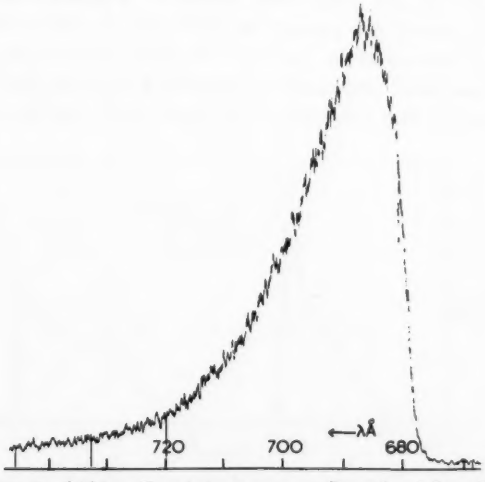

FIGURE 2. *Lithium K emission spectrum. Reproduced from Crisp and Williams [14].*

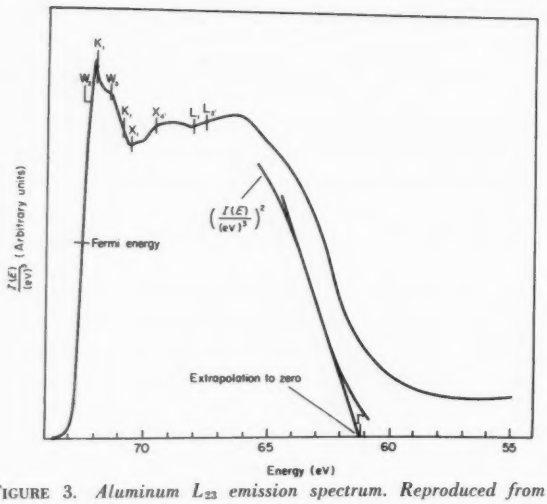

FIGURE 3. *Aluminum L_{23} emission spectrum. Reproduced from Rooke [15].*

edge at eV is not so obvious because of the fall in intensity towards the edge; this fall in intensity is attributed to the effect of the hole in the core state. Because of the low bandwidth, no van-Hove singularities occur below the Fermi edge. The shape of the density of states is almost certainly close to parabolic, but, because of the lack of p-like states near the bottom of the band, the spectrum does not reflect this; its intensity is considerably reduced near the bottom of the band.

The Al L_{23} emission spectrum [15] is shown in figure 3. The Fermi edge and the Auger tail are particularly obvious and the van-Hove singularities appear as discontinuities in the top half of the band. It is seen that the p-like van-Hove singularities, $X_{4'}$ and $L_{2'}$, are much less obvious than the s-like singularities, X_1 and L_1. The bottom of the band rises sharply to a broad hump at about 66 eV; this reflects the parabolic rise of the density of states and the fact that the states near the bottom of the band are nearly all observed because they are mostly s-like. From 66 eV to about 70 eV, the intensity

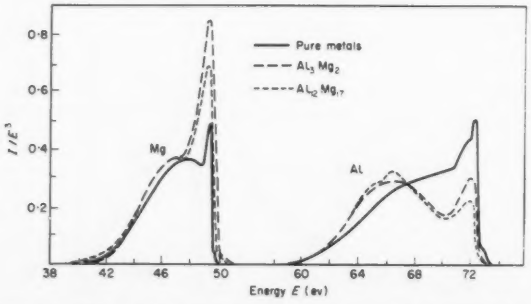

FIGURE 5. *Magnesium L_{23} and Aluminum L_{23} emission spectra from Al-Mg alloys. Reproduced from [17].*

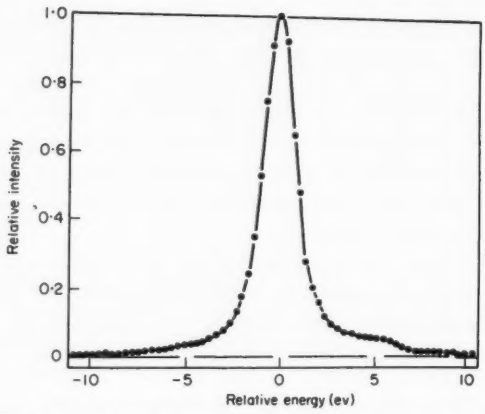

FIGURE 4. *Zinc L_{23} emission spectrum. Reproduced from Liefeld [16].*

falls but then it rises again towards the Fermi edge. This occurs because the states change from being mostly s-like at the bottom of the band to being mostly p-like near the center of the band and then to having both s and d character near the top of the band.

The Zn L_3 emission spectrum [16] is shown in figure 4. This spectrum has been obtained after considerable effort in allowing for the various experimental errors that occur. The tall peak at the center of the spectrum is possibly the d-band while the sharp fall in intensity at about + 7 eV may be the Fermi edge.

6. The Spectra from Alloys

Soft x-ray spectra are proving to be of considerable value for studying alloys and it is for this purpose that soft x-ray spectroscopy will be developed in the next few years. An excellent review of the work done in the West has been given by Curry [17], but the Russians have also done some interesting work, particularly on alloys containing d-band metals.

As an example the very interesting results from the Al-Mg system are discussed. The Mg L_{23} and Al L_{23} emission spectra from two alloys are shown together with the pure metal spectra in figure 5. At first sight, it is seen that the apparent bandwidths of the alloy spectra are not greatly different from those of the pure metal spectra. On alloying, the intensity of the Mg spectrum is relatively enhanced at the top of the band while the intensity of the bottom of the Al spectrum is relatively enhanced. The spectra have been carefully and independently checked by Dimond [18] and it is felt that the results are not due to clustering.

The following analysis produces some very interesting information. First, the width of the density of states must be at least as wide as the bandwidth of the Al spectrum; this fact is in contradiction with most theo-

ries of alloys. Second, either the states at the bottom of the band must be highly localized around the aluminum atoms or they must have mostly s-symmetry in the region of the aluminum ions and mostly p-symmetry in the magnesium ions; the former alternative is the most likely. It is possible that the states are tunneling through a potential barrier in the region of the magnesium ions and can only contribute to the spectra when they are in the vicinity of the aluminum ions. Third, states that are localized near the aluminum ions tend to be relatively more s-like than the states at the same energy in the pure metal. For magnesium, the states near the bottom of the spectrum tend to be relatively more p-like, reflecting the fact that they are now not near the bottom of the band.

This example shows how useful it can be to sample electrons locally and with selected symmetries. Another example involving d-band metals is given later in the conference by Lindsay, Watson and Fabian.

7. Acknowledgments

The author wishes to acknowledge Dr. L. M. Watson, C. A. W. Marshall, and R. K. Dimond for their discussions and help in preparing this paper and also Dr. D. J. Fabian and the Science Research Council for a Research Associateship (at the University of Strathclyde).

8. References

[1] Skinner, H. W. B., Phil. Trans. Roy. Soc. **A239**, 95 (1940).
[2] Tomboulian, D. H., Handbuch der Physik, **XXX**, 246 (1957).
[3] Yakowitz, H. and Cuthill, J. R., National Bureau of Standards (U.S.A.), Monograph **52**, (1962).
[4] Soft X-ray Band Spectra and the Electronic Structure of Metals and Alloys, D. J. Fabian, ed., Academic Press, London (1968).
[5] Pines, D., Solid State Physics **1**, 367 (1955).
[6] Mizuno, Y. and Ishikawa, K., J. Phys. Soc. Japan **25**, 627 (1968).
[7] Liefeld, R. J., p. 133 in [4].
[8] Rooke, G. A., p. 3 in [4].
[9] See part 4 in [4].
[10] Hedin, L., p. 337 in [4].
[11] Cuthill, J. R., McAlister, A. J., Williams, M. L. and Dobbyn, R. C., p. 158 in [4].
[12] Rooke, G. A., J. Phys. Chem. **1**, 767 (1968).
[13] Willens, J. H., Schreiber, H., Buehler, E., and Brasen, D., Phys. Rev. Letters **23**, 413 (1969).
[14] Crisp, R. S. and Williams, S. E., Phil. Mag. (8) **5**, 525 (1960).
[15] Rooke, G. A., J. Phys. Chem. **1**, 776 (1968).
[16] Liefeld, R., p. 149 in [4].
[17] Curry, C., p. 173 in [4].
[18] Dimond, R. K., Ph.D. Thesis, to be submitted to University of Western Australia, (1970).

(Paper 74A2-599)

JOURNAL OF RESEARCH of the National Bureau of Standards — A. Physics and Chemistry
Vol. 74A, No. 2, March-April 1970

The Electronic Structure of Disordered Alloys*

J. L. Beeby

Theoretical Physics Division, Atomic Energy Research Establishment, Harwell, Didcot, Berks., England

(October 10, 1969)

The problem of calculating the electronic density of states in an alloy is considered from first principles. Choosing a suitably simplified model potential a diagrammatic expansion is discussed within which the various existing theories can be compared. Some comments are made on the comparison with experiment.

Key words: Density of states; disordered alloys; one-electron propagator; perturbation expansion; sum rule.

1. Introduction

It has long been appreciated that the information obtainable from experiments on alloys provides a useful supplement to one's knowledge of the pure materials. Much of this information, such as the Hume-Rothery rules, was obtained using binary alloys with similar non-transition-metal constituents. In such an alloy the electron mean free path is long and the alloy can often be regarded as homogeneous. The problem which will be discussed in this paper concerns how to calculate the properties of an alloy in which the constituents are very different. For such an alloy there arises, besides the routine difficulty of choosing an appropriate potential, a major problem involving the order. Perfectly ordered alloys can be handled just as for pure materials, but disordered alloys with strong scattering potentials have needed the development of new theoretical techniques. These methods will be discussed below via a diagrammatic expansion which appears to give improved insight into the whole problem of disorder. No attempt will be made to formally review the literature and no claim is made to completeness. Rather, it is hoped, readers will be better able to judge for themselves the contents of papers in the field.

The paper will begin with a derivation of the alloy potential. The intention here is to clarify, for those not already familiar with the field, what disorder is and how the theorist can describe it by an averaging process. While concepts of this type are already common, as in statistical mechanics for example, it is clear from the current literature that many authors still misunderstand them in the alloy context. The derivation of the potential is then completed by briefly listing the assumptions required with a few comments on their validity. The potential used is of muffin-tin type with invariant potentials for each constituent. The brevity of this section should not be regarded as indicative of the trivial nature of obtaining the potential, which in itself forms a most interesting and difficult task. The heart of the paper is contained in sections 4-6 where the density of states is obtained by considering the imaginary part of the T-matrix for the alloy. The T-matrix can be expanded in a series involving the individual scattering centers (the muffin tins) in the usual way. The procedure adopted in section 5 concerns the way in which the series is to be averaged term by term. Each term requires the knowledge of a probability function and it is these probability functions which must be approximated if the series is to be resumed. A diagrammatic expansion is given which, it is argued, formally converges like Z^{-1} where Z is the number of nearest neighbors. In practice, however, it is the degree of fluctuation which determines the convergence which is anyhow at best asymptotic. Section 6 illustrates these remarks by looking at numerical solutions for different approximations. In the final sections a few examples will be cited of the interrelation between this work and experiment. These are mainly concerned with the transition metals to which the formalism is most appropriate.

*An invited paper presented at the 3d Materials Research Symposium, *Electronic Density of States*, November 3–6, 1969, Gaithersburg, Md.

2. The Meaning of Disorder

When an alloy sample is made there is much information which is available in principle yet is not available in practice. It is normally possible to determine the content of each constituent, the structure and certain ordering parameters. But it is plainly absurd to expect to know the *actual* positions of all the atoms in a disordered sample. Thus while an experiment is performed on a particular sample whose atomic positions may be regarded as fixed during the experiment, a theoretical calculation for this sample must proceed in ignorance of the actual positions. The formal device used to offset this ignorance consists of an averaging procedure about which one might make the following comments.

(i) It is expected that all macroscopically *identically produced* samples will have (within experimental error) identical properties. Systems with large fluctuations in their properties due to unavoidable variations in production need a different approach. Such fluctuations are usually due to variations in some macroscopic parameter not yet controlled in the production process.

(ii) The detailed microscopic order is therefore only important to the extent that certain macroscopic properties (*e.g.*, order parameters) are satisfied.

(iii) Naturally the theoretician is, in these circumstances, at liberty to choose any one microscopic distribution which satisfies the macroscopic restraints. However, since all such distributions are equivalent, it is easier to average over them with a probability function specifying the chance that they occur.

(iv) Such an approach is well known in Statistical Mechanics and works for the same reason: the number of particles involved in the average is very large.

It is most important that any such averaging is made only over observable properties of the sample. As an example consider the density of states which for a given sample might be written $n(E, q_1, q_2, \ldots q_n)$ depending on certain parameters of the sample. If these parameters have a probability of occurence $P(q_1 \ldots q_n)$ within the constraints of the sample production then the *average* density of states is $\int n(E, q_1 \ldots q_n)\, P(q_1 \ldots q_n)\, dq_1 \ldots dq_n$. If the job has been done properly this average value should differ from a typical single alloy value only to the order (1/N) where N is the number of atoms.

Averaging in this way makes things a little simpler algebraically because, like the experimenter, the theorist can ignore all except the macroscopic features of the sample. There are some conceptual difficulties, however, which are worth briefly illustrating. Take first a perfect lattice of one type of atom. Figure 1a shows for a finite number of atoms the energy levels of the system and the singularities which will occur in the complex E-plane for a single particle Green function. A pole will correspond to each energy level. When N becomes infinite the energy levels pack together and can be described by a density of states n(E) as in figure 1b. At the same time the poles merge together to form a branch cut along a portion of the real axis. For an imperfect arrangement the finite system again has poles on the real axis which will turn into branch cuts upon averaging. When approximations are made in the averaging these branch cuts may have been replaced by poles *off* the real axis; the importance of remembering that this is a consequence of the approximations has been particularly stressed by S. F. Edwards. A related point concerns the limit $N \to \infty$. In the perfect lattice case periodic boundary conditions can be used and no difficulty arises. In the disordered case the limit can only be taken *after* the averaging procedure. To see this consider a group of N atoms which is infinitely extended by repetition. The resultant crystal then has N atoms/unit cell and this is well known to yield a band structure with N-1 band gaps in general. As N is increased the band gaps become more numerous and narrower, showing that this is not a sensible treatment.

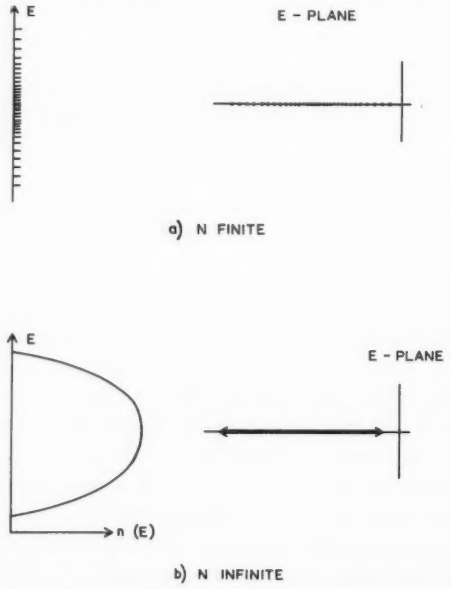

FIGURE 1. *The energy levels and complex plane singularities for (a) a finite, (b) an infinite ordered system.*

3. The Alloy Potential

A correct procedure for obtaining an alloy potential would be as follows.

(i) The positions of the nuclei and core electrons are considered known. (But will in practice be supposed to lie on a perfect lattice).

(ii) The potential throughout the entire lattice is guessed.

(iii) The density of electrons in the system is then obtained.

(iv) A new estimate of the potential is made.

Such an "in principle" self-consistent calculation must be made for a single unaveraged alloy and is plainly an impossible task. Some part of this self-consistency can be achieved in special cases, *e.g.*, where the Friedel sum rule can be used in dilute alloys. Step (iii) to (iv) is, of course, similar to the same step in the perfect lattice except for the lack of order, but even in the perfect lattice case is far from easy to carry out properly. The novelty of alloy theory lies in steps (ii) to (iii), describing the electron density once the potential is known. Since this step is the primary interest of this paper the discussion can be greatly clarified by choosing a suitably simple form for the potential. Only the one-electron approximation will be considered.

For a dilute alloy the best potential to use is the perfect lattice (host) potential with an additional potential at each impurity site representing the difference between the impurity and host potentials. This potential can then be used in perturbation theory or even in more sophisticated schemes. A modified version of this approach will also work quite well for concentrated nearly-free-electron alloys.

For the case where at least one constituent of the alloy has a strong scattering potential with just-bound or nearly-bound states the muffin-tin approximation is best. The muffin-tin assumption is worse in an alloy than in a pure material because the local interstitial energy may vary from place to place through the alloy. It is hard to see how one can readily estimate the effects of such variation. It is customary to make the additional assumption that the muffin-tin potentials for each constituent are independent of the environment. This is not generally correct; there is a spill over of the impurity potential onto neighboring sites. Unfortunately neglecting this change is inevitable at this stage in the development of the theory and, it will be noticed, resembles neglect of positional relaxation about the impurity site in defect calculations. It should be borne in mind, however, that the level of the theory at which such effects would enter is well beyond anything that will be discussed in this paper. Since it is clear that particular features of the band structure may depend critically upon such local effects, the most obvious example being bound states localized near an impurity atom, the defect type theories plainly have important applications here.

The virtue of the nonoverlapping muffin-tin form of the potential is that in the potential free region between the spheres electrons move as in free space. The motion of an electron can thus be seen as a series of scatterings from individual sites with free electron propagation in between. It is this separation of the scattering events which is so important to what follows.

If the alloy constituents are at sites R_i, i = 1, . . . N then the potential just discussed may be written for a particular alloy

$$V(\mathbf{r}) = \sum_i \nu_{\mu_i}(\mathbf{r} - \mathbf{R}_\nu)$$

where μ_i is the type of atom at site R_i and $v_\mu(r)$ is the potential of the μ'th atom type. The nonoverlapping restriction is that

$$\nu_\mu(\mathbf{r}) = 0 \qquad r > r_o$$

where r_o is half the near neighbor distance. There is actually no restriction that $v(r)$ be spherically symmetric though this is often quoted as necessary. With this greatly simplified form for the potential it is possible to proceed with the formal theory of disordered alloys.

4. The T-Matrix

In the discussion of the density of states in an alloy it is necessary to appeal to the concept of a T-matrix and it is therefore worthwhile to demonstrate that it is actually a simple concept. Indeed, while much of the algebra is rather involved, the use of the T-matrix allows almost classical mental pictures to be used and the algebra very largely suppressed.

Consider then a single scattering center of potential V(*r*) with particles incident upon it. It is well known that this problem can be solved in integral equation form as

$$\psi(\mathbf{r}) = \phi(\mathbf{r}) - \frac{1}{4\pi} \int \frac{e^{ik|\mathbf{r}-\mathbf{r}'|}}{|\mathbf{r}-\mathbf{r}'|} V(\mathbf{r}')\psi(\mathbf{r}')d\mathbf{r}'$$

where $\phi(r)$ is the incident beam and the second term gives the wave scattered from the potential. Note that the complete wave function $\psi(r')$ appears in this latter term; if $\phi(r)$ were inserted here the scattering would be given in Born approximation. The T-matrix is formally defined by

$$V(r')\psi(\mathbf{r}') = \int T(\mathbf{r}', \mathbf{r}'')\phi(\mathbf{r}'')d\mathbf{r}''$$

but is best understood in terms of the physical description. The point is that it is very convenient to describe a potential by the scattering it induces among a set of states defined outside the potential and this is what the T-matrix describes. In the crystal these states will be spherical harmonics centered on the atomic position in question. The T-matrix for the potential describes the scattering from one (ingoing) spherical state to another (outgoing) such state.

The infinite crystal potential leads to a T-matrix of different interest. The feature dominant here is that the scattering cross section is infinite for electrons incident on a potential well at an energy at which that well has a bound state. Using this in reverse one may look for the energy levels of the crystal by seeking the poles (or branch cuts) of the T-matrix. Actually the density of states is directly proportional to the imaginary part of the T-matrix and this is the link which will be adopted below. One can now utilize the fact that the total alloy potential is made up of individual scattering sites with their own T-matrices t_i. All scattering processes from the alloy can be described in terms of the sequence of scatterings from these sites. Thus

$$T=\sum_i t_i+\sum_{i\neq j} t_iG_{ij}t_j+\ldots \qquad (1)$$

where the nth term describes those scatterings from the alloy in which n individual site scatterings occur. G_{ij} describes formally the way in which the electron moves between the scatterings at i and j and it is to be noted that two consecutive scatterings cannot be from the same site.

5. The Alloy Formalism

The aim of this section is to introduce a diagrammatic technique which carries considerable insight into the nature of the disorder problem. The algebra required to set up the diagrams is given mainly because of its intrinsic interest. This algebra may otherwise largely be skipped since the meaning of the diagrams is fairly readily understood.

For a single alloy the series (1) can be cast in an entirely real form and the imaginary part corresponding to the density of states ($n(E)\sim\Sigma\delta(E-E_i)$ for this alloy) will only emerge after the infinite series has been summed. In other words the bound states occur at the points where the series diverges. Since the averaging plainly cannot be carried out on the summed T-matrix it is necessary to resort to a term by term averaging followed by the infinite summation. To be specific consider a binary alloy specified by writing at the site i

$$t_i=\sum_{\nu=\alpha,\,\beta} t_\nu c_i^\nu$$

where t_α, t_β are the t-matrices for potential wells of type A and B respectively. Also the c_i^ν are defined by

$$\begin{aligned} c_i^\alpha &= 1 && \text{if the atom at site } i \text{ is of type A}\\ &= 0 && \text{otherwise}\\ c_i^\beta &= 1-c_i^\alpha = 1 && \text{if the atom at site } i \text{ is of type B}\\ &= 0 && \text{otherwise}\end{aligned}$$

In the average system these c_i^ν are given by certain distribution functions appropriate to the alloy composition in question. It is convenient to introduce dummy variables $c^\nu, c^\nu=0,\ 1$ so that $c_i^\nu=\sum_{c^\nu} c^\nu\delta_{c^\nu,\,c_i^\nu}$. Then the T-matrix becomes

$$T=\sum_{i,\,c^\nu\nu} t_\nu c^\nu\delta_{c^\nu,\,c_i^\nu}+\sum_{\substack{i\neq j\\ c^\nu,\,c^\mu\\ \nu,\,\mu}} t_\mu c^\mu G_{ij}t_\nu c^\nu\delta_{c^\mu,\,c_i^\mu}\delta_{c^\nu,\,c_j^\nu}+\ldots \qquad (2)$$

and the averaging which must be performed has been entirely concentrated into the Kronecker-delta functions.

Consider these averages. What one requires to know are probability distributions such as

$$P\begin{pmatrix} c^1, & c^2, & c^3, & c^4\\ i & j & k & l\end{pmatrix}=\langle\,\delta_{c^1,\,c_i^\mu}\,\delta_{c^2,\,c_j^\nu}\,,\,\delta_{c^3,\,c_k^\mu}\,,\,\delta_{c^4,\,c_l^\lambda}\,\rangle \qquad (3)$$

For example, take a completely disordered binary system in which the concentration of the constituent A is c. Then the probability distribution of the c_i^ν's is

$$\prod_{\substack{\text{all}\\ \text{sites}}}\{c\delta_{c_i^\mu,\,c_i^\alpha}+(1-c)\delta_{c_i^\mu,\,c_i^\beta}\} \qquad (4)$$

Since the probability of finding atom A is independently c on every site. When this probability function is used to evaluate the average on the right-hand side of (3) the factor in braces in (4) only occurs once for each independent site in (3). This means there is not necessarily one such factor for each Kronecker delta in (3) but rather only one for each independent site. Thus one obtains

$$P\begin{pmatrix} c^1, & c^2, & c^3, & c^4\\ i & j & k & l\end{pmatrix}=\sum_{c_i^\mu,\,c_j^\nu\,\text{etc.}}{}'\,\Pi'\{c\delta_{c_i^\mu,\,c_i^\alpha}+(1-c)\delta_{c_i^\mu,\,c_i^\beta}\}$$

$$\delta_{c^1,\,c_i^\mu}\ldots\delta_{c,\,c_q^\lambda} \qquad (5)$$

where the prime on the product denotes the restriction that *only independent sites* among the i, j, k, l are included. It is this restriction which is at the heart of the disordered alloy problem. It states that when the same atom appears more than once in a term of the series (2) the average cannot be taken as though each appearance is independent of the others. It is to be

emphasized that this restriction is geometrical; it is a sort of counting problem. Obviously the magnitude of any counting error will depend on the relative size of the various terms and the precise determination of the physical parameters determining these sizes is the essential problem to be faced. The partial progress in this direction will later be illustrated by example but much remains to be done.

A common first step in dealing with a restriction is to first ignore it and then make successively more accurate corrections. This procedure is readily adopted here. Consider the product over independent sites of some factor f_i:

$$\prod_{\substack{\text{indep.}\\ \text{sites}}} f_i = \prod_{\substack{\text{indep.}\\ \text{sites}}} f_i \prod_{\substack{\text{other}\\ \text{sites}}} [f_i + 1 - f_i]$$

$$= \prod_{\substack{\text{all}\\ \text{sites}}} f_i \{1 + \sum_{\substack{\text{other}\\ \text{sites}}} \frac{(1-f_i)}{f_i} + \sum_{\substack{\text{two other}\\ \text{sites}}}$$

$$\frac{(1-f_i)}{f_i}\frac{(1-f_j)}{f_j} + \ldots \} \qquad (6)$$

where the last line is obtained by expanding the second product. Clearly the correct result will only be regained after all the terms in the sum have been included. This formula allows a simple diagrammatic representation in which all the sites appearing in a term are given as dots on a line as in figure 2a. The dots themselves represent the t-matrices and the lines between the dots represent the propagators G_{ij}. In this series of scatterings the repetition of a given scattering center can be treated by the device of eq (6). The first term in the sum in (6) corresponds to ignoring the restriction in which case the probability distribution will be given by

$$P\begin{pmatrix} c^1 & c^2 & c^3 \\ i, & j, & k, \ldots \end{pmatrix} \simeq P\begin{pmatrix} c^1 \\ i \end{pmatrix} P\begin{pmatrix} c^2 \\ j \end{pmatrix} P\begin{pmatrix} c^3 \\ k \end{pmatrix} \ldots$$

where

$$P\begin{pmatrix} c^1 \\ i \end{pmatrix} = \sum_{c_i^\mu} \delta_{c^1, c_i^\mu} \{c\delta_{c_i^\mu, c_i^\mu} + (1-c)\delta_{c_i^\mu, c_i^\beta}\}$$

This gives at once

$$\sum_{c^\mu, \mu} t_\mu c^\mu P\begin{pmatrix} c^\mu \\ i \end{pmatrix} = ct_\alpha + (1-c)t_\beta = \bar{t} \qquad (7)$$

The independent averaging of a point can be denoted by a cross as in figure 2b. The next term in the sum (6) connects each repeat site with the *previous* occasion on which the site appeared and can be represented by a dotted line as in figure 2c. The third term contains

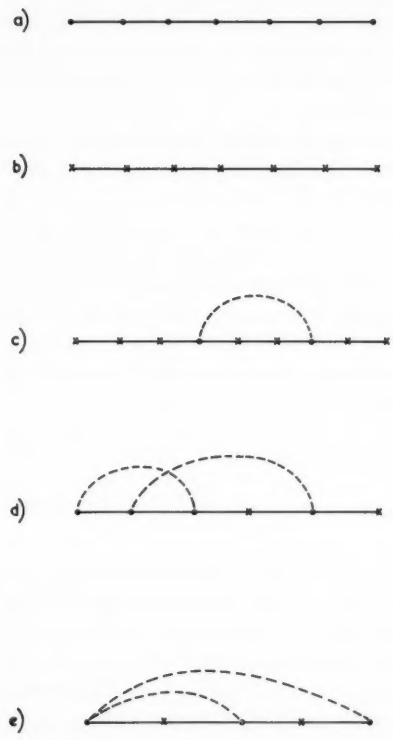

FIGURE 2. *The diagrammatic expansion for the T-matrix showing (a) an unaveraged line, (b) the lowest order approximation, (c) a typical lowest order correction term, (d) a second order correction term, and (e) a forbidden graph.*

two repeats *i.e.* two dashed lines and so on. Indeed, the entire series (2) may be given by the diagrammatic expansion satisfying four simple rules. For each value of n, n = 1, 2, 3, . . . draw all possible diagrams having the following properties

(i) There are n points on a straight line.

(ii) Pairs of these points (but not a consecutive pair) are joined by dashed lines.

(iii) No two dashed lines leave a point in the same direction.

(iv) All points not touched by a dashed line have crosses on them.

The meaning of these diagrams can be readily put into words. For example figure 2c corresponds to a term in which the electron first scatters from 6 different sites then scatters again at the fourth one and finally scatters at two more different sites. Figure 2d represents the electron returning to the first and second sites for its third and fifth scatterings. All such scattering topologies must be drawn and included in the series though it is important to note that diagrams of the type of figure 2e are forbidden by rule (iii). Finally, the dashed line does not represent the actual value of the process it

372-505 O - 70 - 10

describes but the *correction* to the related process in which the restriction is ignored and the two ends of the dashed line replaced by crosses. This is illustrated in the example below.

The evaluation of the contribution of a diagram is complicated by the two separate features involved. First there is the t-average which is given by the procedure outlined between eqs (3) and (6). Secondly the propagator sum must be evaluated for each diagram; it is this which is the limiting difficulty as the diagram becomes more and more complicated. Consider any diagram of the type 2c *i.e.* with only one dashed line. The average corresponding to the dashed line may be written

$$\sum_{c^\alpha,\,c^\nu} t_\mu t_\nu \delta_{c^\alpha,c_i^\mu}\delta_{c^\nu,c_i^\nu}\{c\delta_{c_j^\alpha,c_i^\mu}+(1-c)\delta_{c_i^\mu,c_i^\mu}\} \qquad (8)$$
$$\times\,[\delta_{ij}-\{c\delta_{c_j^\nu,c_j^\nu}+(1-c)\delta_{c_j^\nu,c_j^\mu}\}]=ct_\alpha^2+(1-c)t_\beta^2-\bar{t}^2$$

δ_{ij} is written here as a reminder that j is exactly the same as i and was only introduced as a dummy variable. This is plainly of the form of the exact term less the zeroth approximation to it. Each cross on the line is replaced by $\bar{t}$ as in eq (7). Propagator lines which do not appear inside the dashed curve occur in the combination $\sum_{j(\neq i)} G_{ij}=G$. (In practice the sum is k-dependent;

$$G(\mathbf{k})=\sum_{j(\neq i)} G(\mathbf{R}_i-\mathbf{R}_j)e^{i\mathbf{k}(\mathbf{R}_i-\mathbf{R}_j)}.$$

Between the ends of the dashed line the propagator must trace a scattering path beginning and ending at the same point so that the sum involved is

$$S=\sum_{j(\neq i),\,k(\neq j)\,\text{etc.}} G_{ij}G_{jk}\ \ldots\ G_{mn}\delta_{ni}.$$

There is an additional restriction that no intermediate site can be that of the end point, otherwise rule (iii) will be violated and the correction terms overcounted. This sum is readily completed by Fourier transformation giving

$$S=I/(1+tI)$$

where

$$I=\tau\int d\mathbf{k}G^2(\mathbf{k})\bar{t}[1-\tau\bar{t}G(\mathbf{k})]^{-1}. \qquad (9)$$

Here the appropriate number of $\bar{t}$ factors has been introduced and the integral in (9) is over the Brillouin zone of volume τ.

The formal derivation above yields a diagrammatic expansion of a very familiar sort on which the usual tricks can be pulled. These will be discussed in the next section but it is appropriate that some feeling for the meaning of the diagrams be obtained. It will readily be seen that the expansion is not necessarily in powers of any small parameter of a physical nature (it might be *e.g.* if t were very small) but is more precisely viewed as an expansion in the disorder of the system. One way of looking at this is to consider the sequence of neighboring sites, i,j,k. Of the possible values of k, one will be i and therefore (1/number of values of k) of the terms will require corrections as discussed above. If G_{ij} is short ranged, as is the tight-binding case, this means that the proportion of correction terms is 1/Z (where Z is the number of near-neighbors) for each dashed line. An alternative is to regard the series as an expansion in the fluctuations of the system. While 1/Z appears to be small the number of terms with n dashed lines inceases something like n! as n becomes large so that the series is at least asymptotically convergent. This is well known to occur in certain statistical mechanical expansions to which the above procedure is naturally related.

6. The Simplest Approximations

It is now possible to classify most of the theories of disordered alloys according to which diagrams they retain. This is useful in two ways. It gives information about the nature of the various approximations and it helps one to understand some of the physical parameters determining the convergence of the resummations. Begin with the simplest possible terms.

6.1. The average t-matrix approximation [1]

Ignoring all the diagrams with dashed curves gives at once the result

$$\langle T(\mathbf{k})\rangle=\frac{N\bar{t}}{1-\bar{t}G(\mathbf{k})}$$
$$=\frac{N}{\bar{t}^{-1}-G(\mathbf{k})}$$

in which the alloy is represented by a perfect lattice with identical scatterers having the average scattering of the alloy constituents. The density of states given by this approximation for a binary tight-binding alloy is shown in figure 3. The tightly bound energy levels are E_A and E_B and the various cases are found by comparing $|E_A\text{-}E_B|$ with the bandwidth. While the gap between

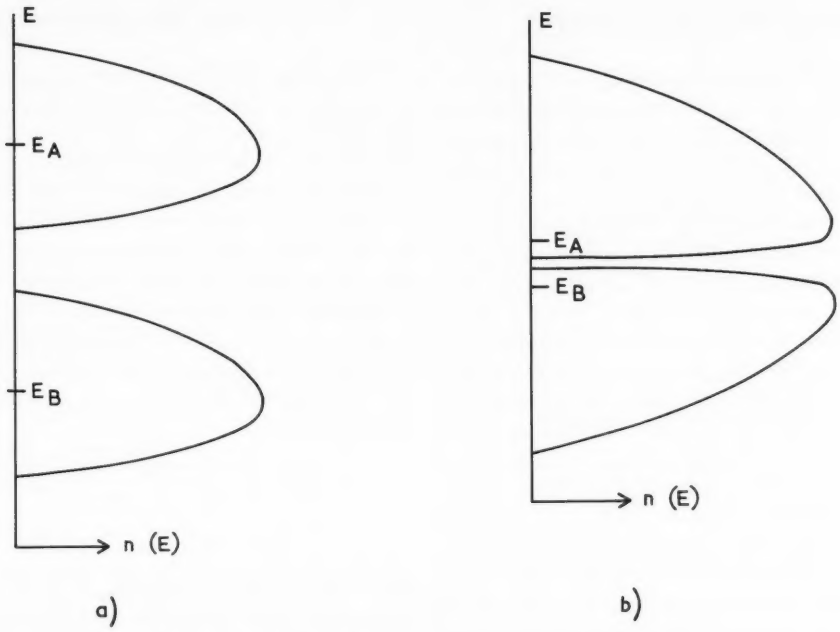

FIGURE 3. *The density of states in the average t-matrix approximation. (a) when* $|E_A\text{-}E_B| >> $ *bandwidth, (b) when* $|E_A\text{-}E_B| <<$ *bandwidth.*

the band halves is reasonable when the bandwidth is much less than the energy splitting (fig. 3a), this approximation incorrectly predicts the gap even when the bandwidth is very large (fig. 3b). At the same time the rest of the band is moderately well described showing that the accuracy of the approximation for a given energy depends on the position of that energy within the band.

6.2. First order approximation

Under the assumption that the 1/Z series converges one might next evaluate the contribution of the terms of the type shown in figure 2c. This contribution must include all possible numbers of intermediate scatterings both inside and outside the dashed loop. But now consider the diagrams in figure 4a. These each have an intermediate denominator which we expect to be nearly singular and all this sequence must be included too. This is simply the usual manipulation to give a self-energy rather than a t-matrix which is absolutely necessary in this context. Now

$$T=\frac{N}{(\bar{t}+\Sigma)^{-1}-G}$$

where Σ is given by the diagram of figure 4b, with all possible numbers of intermediate states and can be evaluated from eqs (8) and (9). The inclusion of this term is an improvement over the average t-matrix approximation but does not resolve all the difficulties.

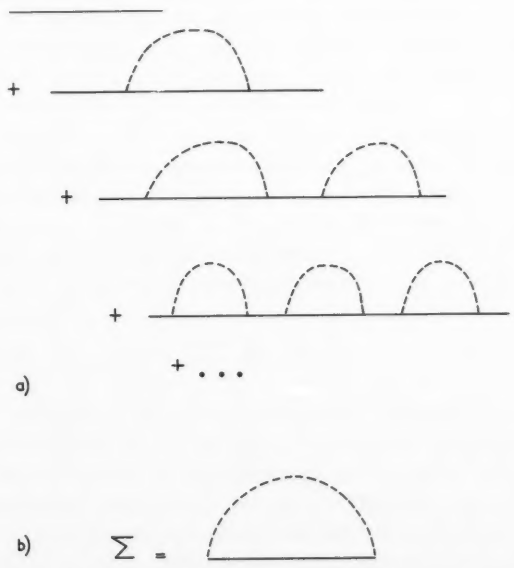

FIGURE 4. *(a) the diagrams summed to give the self energy form, (b) the definition of* Σ.

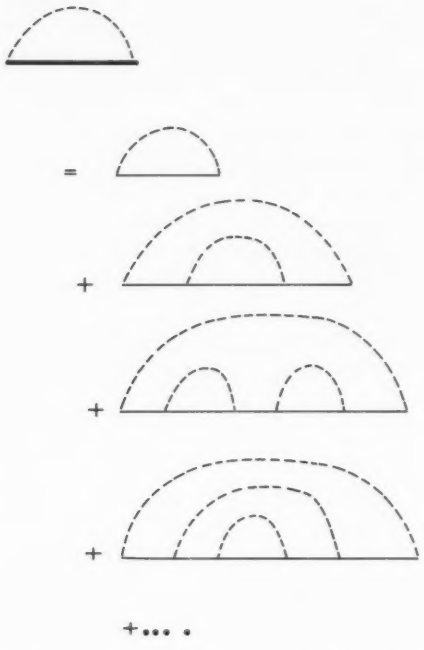

FIGURE 5. *The diagrams summed to give the self-consistent propagator inside the dashed line.*

6.3. Self-consistency

It has long been known that using the unperturbed propagator in the expression for the self-energy is not the best that can be done. The same is true here, where the motion of the electron between successive scatterings can readily be included as if it were being scattered by $(\bar{t}+\Sigma)$ scatterers. This corresponds to including the infinite series of diagrams seen in figure 5. This step is necessary because one really wants to allow scattering of the electron into the *true*, not the unperturbed, density of states. Once this has been done the self-consistent equations obtained can be solved when the unperturbed density of states is given by the expression [2]

$$n_o(E) = \frac{4}{\pi\Delta}\sqrt{1-\left(\frac{E-T_o}{\frac{1}{2}\Delta}\right)^2} \text{ if } |E-T_o| < \tfrac{1}{2}\Delta$$

$$= 0 \quad \text{otherwise.}$$

This self-consistency calculation is an immediate improvement in the sense that the band gap now closes as the splitting $|E_A\text{-}E_B|$ becomes smaller than the bandwidth. Figures 6 and 7 show the alloy density of states in

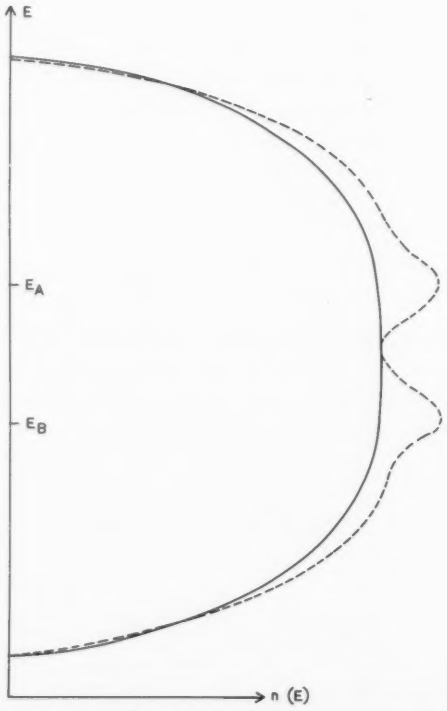

FIGURE 6. *Some density of states curves showing approximations (iii) dashed lines and (iv) full lines for* $c=0.5$ and $|E_A\text{-}E_B| = \Delta/3.9$.

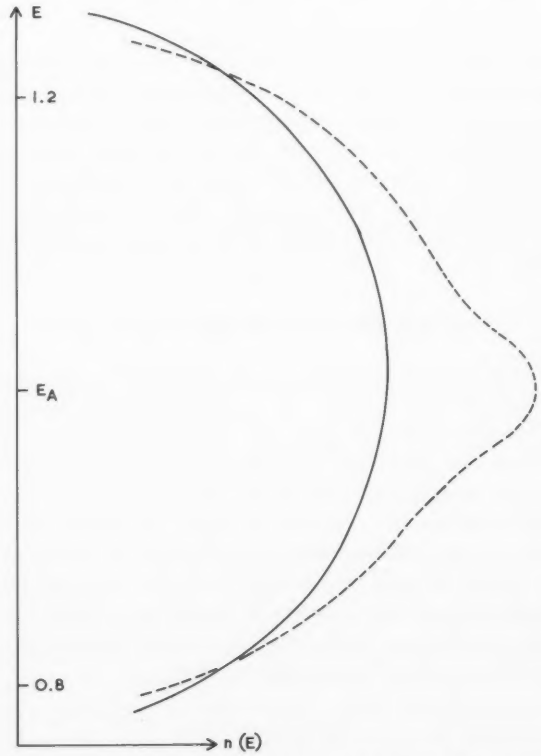

FIGURE 7. *The density of states curves for* $c=0.5$ *and* $|E_A\text{-}E_B|=\Delta/0.7$. *The scale here is such that* $E_A=+1$, $E_B=-1.0$.

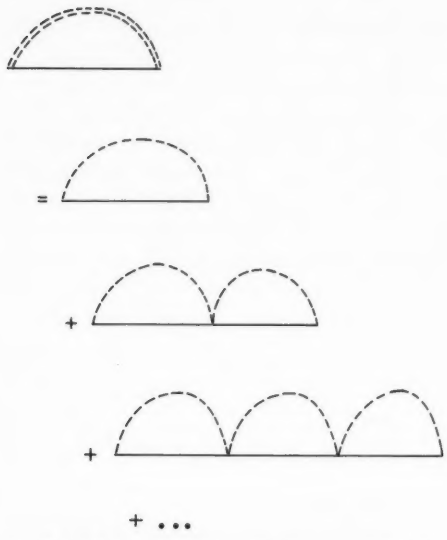

FIGURE 8. *The self-energy graphs required to renormalize the scattering energy levels.*

the approximation as a dashed line. One major error of such a density of states is that it does not satisfy the sum rule on the density of states, a difficulty that can be overcome by a further resummation.

6.4. The renormalized energy levels

The work of Hubbard [2] and later workers [3,4] overcomes the sum rule problem by extending the scattering from any single site to include all possible processes involving only that site. These are the diagrams of figure 8. This has the effect of renormalizing the energy levels and gives the full line density of states in figures 6 and 7. It will also be noticed that the bump in n(E) near E_A and E_B has flattened out. Thus overall this more sophisticated summation gives a smoother density of states. It is interesting to observe that neither the value of the gap width nor the critical ratio $\left|\frac{E_A-E_B}{\Delta}\right|$ at which the gap closes is affected by this last improvement. Within the numerical error approximations (6.3) and (6.4) are identical in this respect.

This last approximation has allowed several alloy density of states calculations to be carried through [3,4] and is probably the best that can be done at the moment. It is rather difficult to see what to do next. There is no general rule for selecting sets of diagrams obeying the density of states sum rule and one has no insight into which of the higher order terms are the most important. Indeed different sets will probably be important in different regions of the energy spectrum.

7. Dimensions and Fluctuations

This section is intended to draw attention to a few of the difficulties associated with the alloy theories just outlined. Rather than dealing directly with the alloy case it is preferable to simplify to the vacancy problem. Here the second alloy species is replaced by vacancies so that only a proportion c of the perfect lattice sites are occupied by type A atoms. In the formalism of the preceding sections it is only necessary to put $t_B \equiv 0$.

The illustrative value of the number of dimensions in this argument arises because the formed procedure just outlined is independent of the dimensionality for fixed unperturbed n(E). The physical nature of the problem, however, depends extremely strongly on the dimension principally through the importance of fluctuations. Obviously the fluctuations in one dimension are very large compared to those in three dimensions since the number of neighbors is so much less. This is reflected in the fact that in one dimension the density of states for the alloy problem has a strongly peaked structure, the peaks being identifiable as local groupings of a few atoms as was first remarked upon by Borland [5]. In particular, for the vacancy tight binding cases, the probability of finding a line of n occupied sites with a vacancy on either end is $c^n(1\text{-}c)^2$ and the density of states for such a group is $\sum_{i=1}^{n} \delta(E\text{-}E_i)$. The total density of states is then effectively a weighted sum over δ-functions and is not continuous. Obviously in two and three dimensions the same is true for sufficiently small concentrations but not in general. Plainly when fluctuations are this important there is no chance that the theory described previously can hold.

Another point which can be readily demonstrated is that in such a vacancy case there exist states outside the bands calculated by any of the models just discussed. Consider a simple square lattice in two dimensions. This has coordination 4. A square of side n fully occupied by atoms will have a mean coordination number

$$\frac{4n^2-4n}{4n^2}=1-\frac{1}{n}$$

since atoms at the sides only have coordination 3. In a tight binding model the mean coordination number is a least estimate for the bandwidth of a group of atoms compared to that for the full lattice. This can be readily seen by a variational calculation with trial function $\Psi = \sum_{i=1}^{n^2} \Psi_i/n$. Now the theories described above give a bandwidth $\propto$ (approx. (6.1)) or $\sqrt{c}$ (approx. (6.4)) so for

the latter case there is a probability $c^{n^2} \simeq c^{(1-\sqrt{c})-2}$ of groups of atoms with energy levels outside the calculated band. Such states of course tail off rapidly but nevertheless exist with positive density of states right out to the full perfect lattice bandwidth. The same applies in three dimensions where the tail is smaller but still there. Figure 9 illustrates this point. Obviously such states are very difficult to spot in the type of theory discussed earlier. They certainly exist at the outside edges of the alloy bands but whether or not they exist inside the band gap is a more difficult question which will undoubtedly be the object of more study.

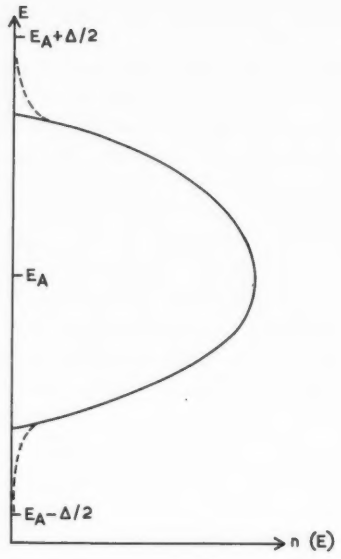

FIGURE 9. *Density of states in the vacancy case showing the limits of the perfect band and the tails extending to those limits.*

9. The Experimental Comparison

It is natural enough that when developing a theory of alloys one begins with the simpler, one-body quantities such as the density of states. Other properties, such as conductivity, Hall effect, *etc.* really require more sophisticated theoretical treatments. The relevant experiments are well dealt with elsewhere in the symposium and so will not be discussed in detail here, but it would be wrong to completely omit commentary on them.

Calculations of the density of states yield a function of energy and a proper experimental comparison would require that function to be observed. Only in the optical type measurements, particularly photoemission and soft x-ray work, is this possible even in principle. In practice there is a good deal of ambiguity in separating out the n(E) curves from other energy dependent variations typically in the matrix elements and many-electron effects. It is clear that for a general comparison with experiment the theoretical work must be pushed to the point of predicting directly the observed data. This is a step which at the moment looks to be just about possible though complicated by the need to take into account local effects through the matrix elements.

Those experiments which measure densities of states at the Fermi surface are complicated by many-body features which, for example, can cause the density of states to be enhanced by quite large factors (~ 1.5 or more). There is the additional difficulty that the pure transition metal band structures lead to density of states curves with a good deal of structure on them so that detailed comparison with experiment requires precise knowledge of potentials and the Fermi energy. Beck and coworkers [6] have overcome some of these objections by using transition metal alloys which seem to conform very closely to the rigid band model and in which the parameters vary only with electron concentration. It is still questionable whether theory can yet predict those cases where Beck's attack will work and in particular where and why it breaks down in the transition metal alloys.

The need for an indirect step in all these experimental analyses has hitherto prevented a satisfactory comparison between the calculated and the measured density of states. It now seems possible that since sophisticated yet fast band structure calculations have been developed and better theoretical understanding of the alloy problem is being rapidly gained the time should soon come when the comparison will become direct.

Finally one might expect some rewards by looking for the gap predicted by the theories when the energy levels are well split as in figure 3a. However, this particular gap is strongly reminiscent of those predicted in the more general disordered system theories and still argued about at length. It is very difficult to observe the difference between a gap and a very low flat minimum even though the distinction is theoretically very important. Perhaps the tunnelling experiments can help here.

10. Conclusions

The theory of disordered alloys is at last coming to the point where it can truly be regarded as a theory rather than being a collection of ad hoc methods. The

problem of a disordered alloy can thus be treated in a parallel fashion to many-body theories and in consequence considerable experience taken over from the many-body theorists. At the same time there remains a real difficulty in producing a satisfactory dialogue with the relevant experiment work. Overall, however, the picture is one holding promise of good developments in the near future which may have a catalyzing effect on the theoretical understanding of disordered systems.

11. References

[1] Beeby, J. L., Phys. Rev. **135**, A130 (1964).

[2] Hubbard, J., Proc. Roy. Soc. **A281**, 401 (1964).

[3] Soven, P., Phys. Rev. **156**, 809 (1967); Onodera, Y. and Toyozawa, Y., J. Phys. Soc. Japan **24**, 341 (1968).

[4] Velicky, B., Kirkpatrick, S., and Ehrenreich, H., Phys. Rev. **175**, 747 (1968).

[5] Borland, R. E. and Agacy, R. L., Proc. Phys. Soc. **84**, 1017 (1964).

[6] See for example, Cheng, C. H., Gupta, K. P., van Reuth, E. C., and Beck, P. A., Phys. Rev. **126**, 2030 (1962).

(Paper 74A2-600)

JOURNAL OF RESEARCH of the National Bureau of Standards—A. Physics and Chemistry
Vol. 74A, No. 2, March-April 1970

Summary of the Conference on Electronic Density of States*[1]

H. Ehrenreich

Division of Engineering and Applied Physics, Harvard University, Cambridge, Massachusetts

(October 10, 1969)

It is very difficult to summarize a conference such as this, involving as it did a many splendored array of topics, both experimental and theoretical, expounded in no less than ninety papers. The organization of a conference of such size is ordinarily impossible without resort to simultaneous sessions. When there are simultaneous sessions, of course, it is easier for a single summarizer because he can only be at one place at one time and therefore can be excused for failing to do justice to half of the papers. It is also easier for the audience because if you permit people to resonate between sessions, you also allow them to become trapped in the halls, advertently or inadvertently as the case may be. However, through the devilish cleverness of the organizers of the present conference, a goodly fraction of the papers were delivered by a rapporteur. Accordingly, the entire audience, including the summarizer were exposed to everything during a period of three and a half hard-working and elaborately organized days. Furthermore, I lose my excuse for having overlooked, as I undoubtedly did, some of the important new developments presented or presaged here.

As it is, in the time of thirty-two minutes that have been allotted to me it is, of course, impossible to mention even a representative fraction of the contributions. Indeed, even the various areas discussed here can only be sketched in broad outlines. Fortunately my task is considerably eased by the various excellent review lectures and rapporteur summaries that punctuated the conference. In order to avoid the risk of offending a few, I have decided instead to offend everybody by not mentioning names in this talk, except when referring to work which was not explicitly reported at this conference which is appropriately referenced.

At the outset, let me thank the organizers on behalf of everyone attending it for providing us with an outstanding scientific program that clearly focussed on the principal questions which those of us who are grappling with the electronic structure of condensed matter are facing. During the time when we were not riding buses or listening to papers, there was also a most pleasant social program, and mercifully, a few hours for sleep.

I would regard the title of the present symposium, "Electronic Density of States" a *leitmotif* rather than an *idée fixe* because the subject matter presented at the conference in fact was far more general than might be implied by the title. Since the density of states is very influential in the determination of many basic physical properties, it provides an excellent focal point for presenting some of the more recent developments in the electronic properties of condensed matter.

More importantly (and to my view this is one of the chief motivations of this conference) the density of states is a convenient central quantity for confronting theory and experiment even though, unfortunately, it never seems to be measured directly by *any* experiment. In the jargon of the modern theorist one might phrase this difficulty in the following way. The density of states is proportional to the imaginary part of the single particle Green's function, whereas many experiments determine a response function, which involves Green's functions of two or more particles. When suitable approximations are made, however, the state density enters in a fairly direct way into the theoretical interpretation of all of the various kinds of measurement described at this conference.

The list of techniques available to the solid state physicist, which was extensively sampled here, is truly impressive and stands in contrast to the much more limited variety available to our colleagues in the elementary particle field. We heard about optical absorp-

*An invited paper presented at the 3d Materials Research Symposium, *Electronic Density of States*, November 3–6, 1969, Gaithersburg, Md.

[1] Supported in part by Grant No. GP-8019 of the National Science Foundation and the Advanced Research Projects Agency.

tion and reflectance, x-ray spectroscopy, photoemission, Fermi surface experiments, tunneling, measurements of the electronic specific heat, magnetic susceptibility, superconducting critical fields, and transport properties, positron annihilation, Compton scattering, ion neutralization spectroscopy among others, and how some of these are influenced by pressure, strain, and temperature.

The preceding list reflects the fact that photons continue to be one of the favorite probes for studying the microscopic properties of matter. It is therefore tempting to use the 1965 Conference in Paris on the Optical Properties and Electronic Structures of Metals and Alloys [1] which dealt with the same class of materials as the present conference and similar ideas concerning the interpretations of experiments as a fiducial mark to give us some indication of what we have learned about metals and alloys during the interim.

Pippard, in his summary of that conference, remarked on the extraordinary number of times the audience was shown the Cu band structure. Since then the variety of band calculations, and, in particular the kinds of materials considered has proliferated greatly. Pd has received a great deal of recent attention largely as a result of excellent high field susceptibility and photoemission measurements. Other examples discussed here involved more exotic materials such as $AuAl_2$, EuO and GeO_2. Evidently the machinery for doing such calculations on ordered alloys containing several atoms per unit cell, some of which are sufficiently heavy that relativistic effects become important, is now available at several laboratories in a readily usable form. However, as in all band calculations, even if one accepts the Hartree-Fock approximation, the result obtained is only as good as the potential that is used as input information. In metallic alloys one might expect some charge transfer among the atoms belonging to a single unit cell. In my view this possibility has not yet received adequate attention.

For example, $AuAl_2$ has the CaF_2 structures and is one of the few metals in which a Raman frequency has been observed [2]. Remarkably, its magnitude is similar to that of CaF_2. One might ask whether the very similar stiffness of the optical frequencies in these materials is purely an accident or whether there could be enough charge transfer among the atoms in the cell to result in appreciable ionic character. I realize that I am undoubtedly not saying anything that is not already familiar to band theorists. However, experimentalists should be warned that the construction of alloy potentials, even for ordered systems, is still a problem that requires attention.

Indeed, the simpler problem of calculating band structures for monatomic metals on the single particle picture is still controversial. As we saw in connection with several of the contributions and much of the spirited discussion that followed them, we still don't understand clearly how, when, or why to localize the exchange interaction. To date no sufficient theoretical reason has been advanced for preferring either the Slater or the Gaspar-Kohn-Sham versions of this potential. Proponents of either point of view, or those favoring intermediate values of the coefficients at present usually support their position by comparison with experiment rather than basic theoretical arguments.

In this same connection we might note the debate following the introductory lecture concerning the relative merits of first principles and pseudo- or model-potential band calculations. The essential point made in that lecture, in my view, is that "pseudism" is important because it provides elementary insight into the meaning of the results of the elaborate machine computations. The two approaches, in fact, are complementary and the proponents of each have a genuine need for, and indeed ideally should merge with the other.

There is no doubt whatsoever that band theory has done sufficiently well that it is worth using its results to calculate the density of states accurately. This is a difficult numerical problem, particularly if one resignedly accepts spending ceilings that curtail the amount of available computer time, for one needs to know the energy at many millions of points in the Brillouin zone in order to construct adequate histograms that yield all the fine detail in the density of states that is often necessary to interpret experimental information reliably. We saw several examples of advances in performing such calculations more economically at this conference. The QUAD scheme is one of these. Another, which I will call the IBM scheme, not after the machine but the workers, is similar to QUAD in its ability to generate very detailed E(k) curves, but it avoids the use of histograms. All these result in very finely grained structure in the state density.

In this same connection, I think the importance of learning how to sum functions of k over constant energy surfaces in the Brillouin zone efficiently and reliably needs emphasis. This is important not only for calculating the state density, but also for computing Green's functions that are central to the solution of alloy band problems, frequency dependent dielectric functions that can be compared with optical data, susceptibilities, and many other quantities. While many theorists may think such problems as insufficiently dignified, I would, nevertheless, stress that their solution is impor-

tant if one ever expects to confront theory and experiment realistically on a more complete basis for more complicated systems.

At the same time let me temper this call to computer and numerical analysis handbooks by reminding you of the obvious fact stressed by many speakers that band calculations are single particle descriptions involving electrons or holes as ideal quasi-particles which interact with a self-consistent field that is in practice determined more or less self-consistently. However, due to electron interactions including those involving phonons, real quasi-particles acquire finite lifetimes, except right at the Fermi surface. Some of the papers presented here reflected the fact that methods of taking quasi-particle effects into account more systematically in band calculations are now being developed. I would look towards greater exploitation of such techniques in the band calculations of the near future. It is important to remember that when we speak of dressing effects, say, due to electron-phonon interactions, we ought to be dressing the right bare object, namely the correctly calculated quasi-particle appropriate to the stationary lattice.

One should again be reminded of the fact that very few if any of the experiments discussed at this meeting correspond to creation of just one quasi-particle near the Fermi surface. This fact was also stressed already at the Paris Conference. Optical experiments, for example, correspond to the creation of two quasi-particles and ion neutralization measurements to three. These may interact with each other as well as with the other particles in the system. This was illustrated in the discussion of the various types of phenomena that can occur in x-ray emission, which lead to the conclusion that the observed spectrum of the valence band may bear less resemblance than one would hope to what is calculated from band theory. In addition to the long familiar Landsberg or Auger tails that smear out the lower valence band edge, there are recently predicted elementary excitations such as the plasmaron and other broad structures that also result from interactions with plasmons. Another effect that was reported on here results from exciton type interactions between electrons near the Fermi surface and the core holes with which they combine in an x-ray emission process. These may strongly affect the transition rate and lead to substantial enhancement or dimunition of the observed intensity near the Fermi surface. As has been pointed out to us, these effects must be quantitatively understood before information concerning band structure can be reliably extracted from such experiments. As a result of particle interaction effects, the information supplied, even what would in a simple minded view correspond to the same theoretical quantity, often differs from experiment to experiment. The Fermi surface effective mass determined from electronic specific heat and Pauli susceptibility measurements is an example of this.

Even within a single particle framework, the state density function is only characteristic of a particular type of experiment. For example, in x-ray emission experiments, optical selection rules pick out only those components of the valence band state density having appropriate symmetries with respect to the core hole. We saw that this fact has particular utility in providing insight into the character of the wave function overlap and hybridization among different components in both ordered and disordered alloys. Since the core hole is localized in a given atomic site, the study of say the Al-$L_{2,3}$ emission spectrum in systems such as $AuAl_2$ and others discussed here, provide an indication of the amount of d wave function in these systems located on the Al sites.

As another example, we might mention the k-conversation rule entering interband optical processes which implies that the state density appearing in theoretical expressions for the optical constants is the so-called "joint density of states." This seemingly innocuous fact has led to a spirited controversy in connection with the interpretation of photoemission experiments which was already in full bloom at the Paris Conference. As you all know by now, there are two schools of thought whose proponents we might call the k-conservationists and the k-nonconservationists. The latter group has maintained, on the basis of a considerable body of experimental evidence, that particularly in materials having narrow bands such as the noble and transition metals, the energy distribution of the photoemitted electrons should directly reflect the structure in the density of states pertaining to these bands. The k-conservationists on the other hand have asked, "Why should this conservation law be violated?" Indeed, one of the papers, which represents the first attempt at the formulation of a systematic theory of the photoelectric effect in solids, points to ways in which this might come about.

Several of the other contributions point to progress towards a reconciliation of these viewpoints. For example, we have heard in connection with Cu that a direct transitions analysis using constant matrix elements accounts quite well for the observed energy distribution. Similar conclusions have been reached on the basis of very detailed calculations for Pd. The essential point, which was emphasized by both camps, is that the strongest peak in the joint density of states coincide with

peaks in the calculated state density, particularly in the case of narrow valence bands.

While in many cases the photoemission technique is a very useful tool, this may not be the case universally. It was suggested, for example, that it is less successful in providing information concerning f states in the Eu chalcogenides and rare earth metals since these states are seen to give rise to abnormally low quantum yield relative to, for example, p states. It is also clear that the variation of optical matrix elements with energy and selection rules, which can also lead to structure in the observed spectra, needs further attention because in many calculations this matrix element is still regarded to be a constant.

Before leaving the subject of optical properties of crystal, two other points are worth making. Despite the fact that one learns only about the joint density of states in such experiments, it is, in fact, possible to derive the conventional state density from optical data by a more circuitous route. The usefulness of differential reflectance techniques is now well established and was illustrated in several of the contributions presented here which even extended to the x-ray case. Information from such measurements can be used as input for pseudopotential band calculations or those based on the $k \cdot p$ approximation. The problem of constructing potentials which plague first principle band calculations is thereby avoided. Since the secular equations for such problems are generally smaller, they can be solved at sufficiently large numbers of points in the Brillouin zone to obtain the state density.

The other point concerns another recent development. A fact that has been distressing to many theorists is that, while in semiconductor calculations of optical coefficients there was always good agreement between theory and experiment in regard to both the position and magnitude of the observed structure, this has not been the case in metals. For the case of Al we saw quite convincing evidence that such discrepancies are on the point of disappearing, largely as a result of better calculations which deal more adequately with the k-dependence of the momentum matrix element. Indeed, other recent investigations have shown that electron-electron scattering effects, which lead to vertex corrections that might be expected to be stronger in metals than semiconductors, are, in fact, very weak in this material [3]. Even though the so-called Mayer-El Naby resonance is probably no longer with us [4], our understanding of the alkali metals is unfortunately still not in as good a shape.

It is regrettable that relatively few papers presented at the conference attempted to provide a detailed comparison between the results obtained by different types of experiments. There was only one noteworthy exception, which was concerned with efforts to confront Knight shift data with those of soft x-ray emission experiments. There is a real need for more such detailed comparisons, even on the basis of band theory alone.

According to a paper count, superconductors and semiconductors received less attention than the simple, transition, and rare earth metals. However, there are good reasons for mentioning them even in this broad summary. As appropriate, superconductivity was not discussed as a phenomenon, but rather as a tool to extract information relevant to the state density. On the positive side, we heard how strong coupling theory can be used together with other measurements to obtain the electron-phonon coupling constants, and how measurements of the critical field at very low temperatures can be made to yield the electronic specific heat as a function of pressure with high accuracy. On the negative side, it was pointed out in connection with a general review of the information provided by tunneling experiments, that such measurements for superconductors do not really tell us all that much about the normal state properties of metals and semiconductors.

It is clear from the exquisitely detailed interpretable information being currently obtained from cyclotron resonance, magneto-optical, and even nonlinear optical data in simple semiconductors and semimetals, that our understanding of these materials is still in a somewhat more mature state than that of most metals. Of course this applies only to the classical and long studied materials like Ge and InSb and not to amorphous semiconductors which were discussed in only a single paper. However, the very beautiful interplay and agreement between theory and experiment must still be regarded as serving as a standard of excellence which solid state physics in general must continue to emulate.

Surfaces also were not discussed extensively here, largely, I think, because the theoretical ideas and techniques for dealing with such problems in realistic systems are only beginning to be developed. However, some very promising experimental techniques, notably ion neutralization spectroscopy and resonance tunneling which shed light on the nature of surfaces and important phenomena like chemisorption were described. This area will surely see a great deal of activity in the near future.

Since the discussion of a large variety of alloy systems occupied so much of the conference, let me conclude this summary with some remarks concerning this subject. We were exposed to a wide variety of data concerning many alloy systems, most of them involving

transition metals. Certainly there are many more than were considered at the Paris Conference. However, this comparison is somewhat unfair since even now, with one or two notable exceptions which were presented here, there is still a dearth of optical information concerning disordered alloys. This is to be contrasted with the situation involving specific heat and transport measurements about which we heard a great deal. Indeed, most of the papers dealing with the electronic specific heat were concerned with alloy systems. A most interesting effect that was described dealt with the recently discovered magnetic clusters in NiCu alloys which can make their own appreciable contribution to the specific heat. This conjecture is quite new and deserves detailed theoretical treatment. There was also an intriguing discussion concerning rare earth metals which raised the question as to whether the *f* electrons could possibly be at least partially itinerant in some of these systems.

One fairly obvious thing that needs emphasis in connection with these papers and that was stressed in a number of them is the need for data of single crystal specimens having known phases, and how crucial it is to avoid samples involving mixture of phases. Without these precautions, the overanxious theorists will, as they did in the case of the Mayer-El Naby anomalies, find themselves in the awkward position of explaining what Pippard already warned in 1965 might be nonfacts.

As we saw, many of the experimental techniques applicable to pure metals are relevant for disordered alloys as well. We have already mentioned optical and x-ray data in this connection. The fruitful and relatively easily interpretable Fermi surface experiments, alas, seem to be much more difficult for many alloy systems. However, measurements such as those involving positron annihilation which also probe the Fermi surface geometry are not restricted by such criteria. They have already been very successfully used to investigate detailed Fermi surface changes in Cu-Al [5] and as we heard here, to brass.

A great deal of progress in this area since the Paris Conference has come along the theoretical front. Until a few years ago the only theoretical models available for describing alloy behavior involved perturbation theory, the virtual crystal, or the rigid band models. However, recently a number of rather effective techniques based on scattering theory have been adapted to this problem and implemented by calculations for both model and realistic systems. These all transcend the earlier, more limited approaches. The first incisive contributions to electronic theory, made by Edwards and Beeby [6], involved the so-called average t-matrix approach which Soven [7] applied to brass. An extension of such calculations was discussed here. Subsequently, Soven [8] formulated a more general self-consistent effective field approach that he termed the coherent potential approximation which is more general than the other. While this was mentioned in several of the papers, it is perhaps worthy of some additional commentary because of its possible applicability to realistic alloy systems.

In this approximation the alloy is replaced by an effective medium described by a single particle non-Hermitian and complex Hamiltonian which, however, is still periodic in the case of substitutional alloys. The self-consistency condition determining this Hamiltonian is simply that an effective electron wave travelling through the crystal which impinges on an atomic site suffers no further scattering due to the random character of the crystal potential. Put another way, the effective wave, just like a Bloch wave in a crystal, is not scattered by the atoms. However, unlike the Bloch wave, the effective wave may be damped as it propagates through the crystal. The present limitation of this description is that it is only applicable to certain classes of Hamiltonians in which the random character is cell localized. The theory has the virtue of correctly reducing to the known results for small impurity concentrations and arbitrary scattering strengths on the one hand, and for arbitrary concentrations but small scattering strengths on the other. It interpolates in a physically reasonable way between these limits, yielding results that are valid for arbitrary alloy concentrations and reasonably strong scattering strengths. It fails in predicting band tailing effects, experimental evidence for which we heard described here in connection with semiconductor tunneling experiments. Also, it does not yield strictly localized states except in the limit of very small impurity concentrations.

We should note parenthetically that while the existence of such states near band edges is generally believed, some questions were raised here as to whether or not such states can exist in the middle of a tight binding band and whether or not the frequently made hypothesis that there exists a sharp demarcation between localized and nonlocalized states is correct. As we were reminded, localized states such as those due to f-electrons, can exist even in periodic systems when the Coulomb interaction is sufficiently strong. As was shown, conventional band descriptions break down under these circumstances.

To obtain the effects omitted by the coherent potential description of disordered alloys it is necessary to

allow for the possibility of statistical clustering effects. This is a much more difficult problem. But as we heard in two of the papers presented here, some very promising progress is beginning to be made in these directions. Indeed, the early work of I. M. Lifshitz [9] has already given us an indication of the sorts of results to be expected.

Because of the previously stated limitations, the coherent potential theory in its present form is strictly speaking applicable only to isoelectronic alloys like GeSi, where the random part of the potential is substantially confined to the core region at each site, or to 3d transition-noble metal alloys in which the d-states that are most affected by the disorder are substantially localized.

To give these remarks a sharper focus, I should like to show you by means of one example the results of an application of this theory to CuNi alloys. Figure 1 exhibits S. Kirkpatrick's calculations [10] for the density of states of these alloys and also the results of photoemission experiments by Seib and Spicer [11], which, for reasons already mentioned, should only be compared qualitatively with the theoretical results. It should be emphasized that these calculations do involve approximations, most of them probably not too serious. Since it would be inappropriate to discuss these in the present context, I would like to confine my remarks to a few brief comments. The first is that the coherent potential approximation is evidently applicable to quite complicated density of states functions

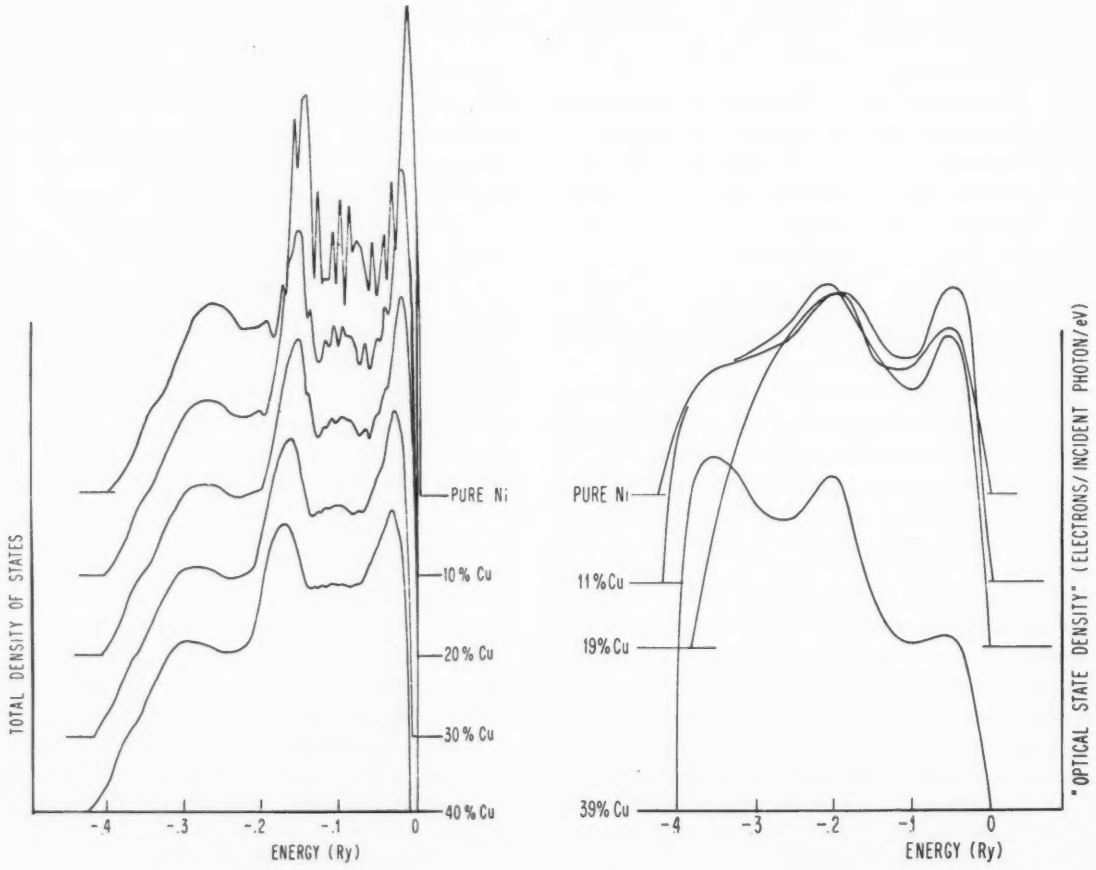

FIGURE 1. *The hybridized d state densities, calculated in the coherent potential approximation, are compared with the optical state density obtained from photoemission experiments [10, 11].*

which include degenerate d-bands and hybridization with conduction bands. Second, the only input information needed for nickel-rich alloys is the hybridized nickel state density, the positions of the resonant Ni and Cu d-levels which give rise to the d-bands, and the concentration. Third, the distortion in the state density curve with increased alloying shows the rigid band model, which has been particularly popular for this alloy system, does not really apply. This is seen even more clearly in the results of calculations of the magnetic properties [12]. Finally, the prominent calculated structures and their behavior is qualitatively in accord with the experimental observations. The principal peaks remain stationary, but they change in intensity and shape in both the calculations as well as the experiment. The contribution of copper to the state density turns out to be broad and relatively structureless and comes principally from the lower regions of the d-band.

While this kind of theory predicts a wealth of detail, its quantitative validity remains an open question that must be explored further. More important, some of its present limitations must be overcome to render it applicable to a wider class of alloys. However, given the improving theoretical and experimental situation that is clearly evidenced from this conference, it seems clear that at the next meeting of this type we will surely hear about further, more extensive developments which will place the theory of alloys on a firmer footing.

After these somewhat discursive concluding remarks, let me close the conference by once again thanking everyone; organizers, speakers, and rapporteurs, questioners, commenters, and listeners for having made it as stimulating as it turned out to be.

References

[1] The Proceedings of that Conference were edited by F. Abeles and published under that title by North-Holland Publishing Company (Amsterdam) in 1966.

[2] Feldman, D. W., Parker, J. H., and Ashkin, M., Phys. Rev. Letters **21**, 607 (1968).

[3] Beeferman, L., and Ehrenreich, H., (Phys. Rev., to be published).

[4] Mayer, H., and El Naby, M. H., Z. Physik **174**, 289 (1963); Smith, N. V., Phys. Rev. Letters **21**, 96 (1968).

[5] Fujiwara, K., Sueoka, O., and Imura, T., J. Phys. Soc. Japan **24**, 467 (1968).

[6] Beeby, J. L., Proc. Roy. Soc. (London) **A279**, 82 (1964) and cited papers.

[7] Soven, P., Phys. Rev. **151**, 539 (1966).

[8] Soven, P., Phys. Rev. **156**, 809 (1967).

[9] Lifshitz, I. M., Soviet Physics—Uspekhi **7**, 549 (1965).

[10] Kirkpatrick, S., Velicky, B., and Ehrenreich, H. (to be published).

[11] Seib, D. H., and Spicer, W. E., Phys. Rev. Letters **22**, 711 (1969).

[12] Kirkpatrick, S., Velicky, B., Lang, N. D., and Ehrenreich, H., J. Appl. Phys. **40**, 1283 (1969).

(Paper 74A2—601)

JOURNAL OF RESEARCH of the National Bureau of Standards—A. Physics and Chemistry
Vol. 74A, No. 2, March–April 1970

Publications of the National Bureau of Standards*

Selected Abstracts

Braun, W., Bass, A. M., Davis, D. D., Simmons, J. D., **Flash photolysis of carbon suboxide: absolute rate constants for reactions of $C(^3P)$ and $C(^1D)$ with H_2, N_2, CO, NO, O_2 and CH_4,** *Proc. Roy. Soc.* **A312,** *417–434 (1969).*

Key words: Absolute rate; carbon suboxide; flash photolysis; primary processes; reactions $C(^3P)$, $C(^1D)$.

The vacuum ultraviolet flash photolysis of C_3O_2 in the 159.0 nm absorption band has been investigated. The major primary products are $C(^1S)$, $C(^1D)$, $C(^3P)$, and CO. The species C_2 and C_3 have also been observed but are of minor importance in the overall reaction scheme. A number of pressure independent reactions involving $C(^3P)$, $C(^1D)$, and $C(^1S)$ with CO, CH_4, N_2, NO, O_2, and H_2 have been observed by means of the kinetic-spectroscopic method. The rate constants measured at room temperature in units of $cm^3\ sec^{-1}\ molec^{-1}$ are summarized here:

(7)	$C(^3P) + CH_4 \rightarrow C_2H_4$ (?);	$k < 5 \times 10^{-15}$
(8)	$C(^1D) + CH_4 \rightarrow C_2H_2 + H_2$;	$k = 3.2 \times 10^{-11}$
(10)	$C(^1D) + N_2 \rightarrow C(^3P) + N_2$;	$k \approx 2.5 \times 10^{-12}$
(12)	$C(^3P) + NO \rightarrow CN + O$;	$k = 1.1 \times 10^{-10}$
(13)	$C(^1D) + NO \rightarrow CN + O$;	$k = 9.2 \times 10^{-11}$
(18)	$C(^1D) + H_2 \rightarrow CH + H$;	$k = 4.15 \times 10^{-11}$
(19)	$C(^1S) + H_2 \rightarrow CH + H$ (?);	$k < 5 \times 10^{-12}$
(20)	$C(^3P) + O_2 \rightarrow CO + O$;	$k = 3.3 \times 10^{-11}$
(22)	$C(^1D) + O_2 \rightarrow CO + O$ (?);	$k < 5 \times 10^{-12}$

The pressure dependent reaction rates of $C(^3P)$ with N_2, CO, and H_2 have been qualitatively measured and are discussed in detail.

Brennan, J. A., Edmonds, D. K., Smith, R. V., **Two-phase (liquid-vapor), mass-limiting flow with hydrogen and nitrogen,** *(Proc. 1968 Cryogenic Engineering Conf., Case Western Reserve Univ., Cleveland, Ohio, Aug. 19–21, 1968), Chapter in Advances in Cryogenic Engineering 14, Paper G-6, 294–298 (Plenum Press, Inc., New York, N.Y., 1969).*

Key words: Choking; critical; hydrogen; nitrogen; two-phase flow.

Experimental data on choked or mass-limiting flow at the exit of a constant area test section are presented. The data are compared to some simple analytical models which have been recommended to indicate upper and lower limits of the flow rates.

Carroll, J. J., Melmed, A. J., **Ellipsometry-LEED study of the adsorption of oxygen on (Oll) tungsten,** *Surface Sci.* **16,** *251–264 (Aug. 1969).*

Key words: Ellipsometry; low-energy-electron-diffraction; optical constants, oxidation of tungsten.

The direct combination of ellipsometry and low-energy-electron-diffraction (LEED) techniques has been extended to a study of room temperature oxygen adsorption on (O11) W. It is shown that, by use of a special continuous data-taking method, ellipsometry is easily capable of detecting small fractions of a monolayer of adsorbed oxygen on this metal crystal face. From the partial correlation of LEED and ellipsometry data, average sticking probability for oxygen adsorption in the first 1/2 monolayer of atoms is deduced to be 0.2 or 0.4, depending on the choice of adsorption model. The experimental ellipsometry results are not understandable in detail in terms of existing ellipsometry theory. Consequently, and in view of the LEED results, it is tentatively concluded that the present results support a previously published complicated adsorption model involving oxygen atom-tungsten atom rearrangements.

Cooper, M. J., Vicentini-Missoni, M., Joseph, R. I., **Linear parametrization of the equation of state near the critical point,** *Phys. Rev. Letters* **23,** *No. 2, 70–73 (July 14, 1969).*

Key words: Critical point; equation of state; scaling laws; Schofield parameterization.

A linear parameterization of the equation of state near the critical point proposed by Schofield is tested. We find the available experimental data in the critical regions of a number of magnets ($CrBr_3$, Ni, Gd) and fluids (CO_2, Xe, He^4) is *not* generally consistent with an assumption of linearity. Agreement with such a linear form can be obtained only by locating the critical isochore asymptotically close to the coexistence line.

Dickens, B., Brown, W. E., **The crystal structures of $CaNa_2(CO_3)_2 \cdot 5H_2O$, synthetic gaylussite and $CaNa_2(CO_3)_2 \cdot 2H_2O$, synthetic pirssonite,** *Inorg. Chem.* **8,** *No. 10, 2093–2103 (Oct. 1969).*

Key words: Carbonates; crystal structure; Gaylussite; hydrated carbonates; hydrates; pirrsonite.

The crystal structure of $CaNa_2(CO_3)_2 \cdot 5H_2O$ (synthetic gaylussite) has been determined from 2988 single-crystal X-ray diffraction data collected by a counter method. The unit cell parameters are $a = 14.361 \pm 0.002$ Å, $b = 7.781 \pm 0.001$ Å, $c = 11.209 \pm 0.002$ Å, and $\beta = 127.84 \pm 0.01°$, and the space group is C2/c. There are four formula weights per cell. The calculated density is 1.99 g/ml; the observed density is also 1.99 g/ml. $R_w = (\Sigma(w||F_o|-|F_c||)^2/\Sigma(w|F_o|)^2)^{1/2} = 0.043$; $R = 0.054$. The hydrogen atoms have been located approximately. Two Co_3 anions, at a dihedral angle of 134.3° to one another, are ionically bonded edgewise to a Ca ion to form a $Ca(CO_3)_2$ triplet. The bonded edges of the CO_3 groups are very nearly parallel. Both CO_3 groups in a triplet are further bonded to a pair of Na ions which are also bonded to adjacent triplets. Four of the water molecules are bonded to Ca and form hydrogen bonds to CO_3 groups in neighboring triplets. The fifth water molecule is bonded to two Na ions and is hydrogen bonded to two water molecules. One hydrogen appears to be only 2.2–2.5 Å from the Na. The crystal structure of $CaNa_2(CO_3)_2 \cdot 2H_2O$ (synthetic pirssonite) has also been determined from 1141 single-crystal X-ray diffraction data collected by a counter method. The unit cell parameters are $a = 11.340 \pm 0.004$ Å, $b = 20.096 \pm 0.005$ Å, and $c = 6.034 \pm 0.002$ Å, and the space group is Fdd2. There are eight formula weights per cell. The calculated density is 2.35 g/ml; the observed density is also 2.35 g/ml; $R_w = 0.029$; $R = 0.044$. The hydrogen atoms have been located approximately. As in $CaNa_2(CO_3)_2 \cdot 5H_2O$, two CO_3 anions are bonded edgewise to a Ca ion to form a triplet. In this triplet, the Ca, the two carbons, and the CO_3 oxygens remote from Ca lie nearly on a line, but the CO_3 groups have twisted about this axis so that the bonded edges are nearly at right angles to one another; the dihedral angle is 95.5°. In contrast to $CaNa_2(CO_3)_2 \cdot 5H_2O$, each CO_3 anion is also bonded to a second Ca ion to form a three-dimensional network.

The Na ions and water molecules form an alternating chain along [011]. Each Na ion is coordinated to four oxygens in CO_3 anions and to two water molecules. The water molecules are primarily coordinated to Ca ions and form hydrogen bonds with neighboring CO_3 anions. The $H_2O \cdots Na$ bonding is thought to be weak.

Evenson, K. M., **Microwave magnetic-dipole transitions between excited electronic states of CN,** *Phys. Rev.* **178,** *No. 1, 1–4 (Feb. 5, 1969).*

Key words: CN; double resonance; excited state; magnetic dipole transitions; microwave spectroscopy.

Eleven microwave transitions in the frequency range from 10.5 to 11.5 GHz have been observed between excited electronic states of CN. These correspond to 11 of 13 allowed magnetic dipole transitions, $\Delta F = 0, \pm 1$, in the $K' = 4$ perturbation complex between the three hyperfine levels of the perturbed component of the Λ doublet of the $A^2\Pi_{3/2}^+(v = 10)$ level and the three hyperfine levels in each of the perturbed and the unperturbed components of the spin doublet of the $B^2\Sigma^+$ $(v = 0)$ level. These transitions and the previously measured 13 electric dipole transitions determine all twelve hyperfine energy levels of this perturbation complex. The experiment is the first microwave measurement of magnetic dipole transitions between excited electronic states of a molecule. CN was produced predominantly in the metastable $A^2\Pi$ state by a chemical reaction when methylene chloride was added to a nitrogen afterglow. Resonant microwave pumping from the Π state increased the population of the three hyperfine levels of each Σ state. The population change was detected by measuring an increase in the intensity of the $B^2\Sigma^+ \rightarrow X^2\Sigma^+$ (0, 0) violet band of CN near 3875 Å.

Fenstermaker, C. A., McCrackin, F. L., **Errors arising from surface roughness in ellipsometric measurement of the refractive index of a surface,** *Surface Sci.* **16,** *85–96 (1969).*

Key words: Ellipsometry; index of refraction; light reflection; optical properties; rough surfaces.

The roughness of a surface is generally neglected when the refractive index of a material is calculated from ellipsometer measurements. Errors produced by neglecting the roughness of the surface are evaluated for three models of the topography of the surface (square ridges, triangular ridges, and pyramids). A range of roughness from 0 to 500 Å and six substrate materials (glass, silicon, chrome, mercury, gold, and silver) are considered. Large errors in determination of indices, even for small values of roughness (50 Å), were found.

Gadzuk, J. W., **Many-body tunneling-theory approach to field emission of electrons from solids,** *Surface Sci.* **15,** *466–482 (1969).*

Key words: Electron tunnelling; electrons in solids; field emission; many-body theory; surface physics.

The equation of motion and thermodynamic Green's function method for describing tunnelling processes in normal and Josephson junctions is here adapted to the problem of field emission of electrons from solids. The formal developments lead to an equation for the emission current in terms of both the Fowler-Nordheim quantities and the spectral weight function of the single particle Green's function in the solid. The formal results are examined in detail for three specific examples.
In the case when the spectral function is that of a free, non-interacting electron gas, the formal results obtained here reduce to the usual Fowler-Nordheim result for the current and the energy distribution.
Expressions are then obtained for the current and energy distribution of field emitted electrons from superconductors. The consequences of these results are discussed.
The last example here is probably the most interesting from the experimental point of view. The emission current characteristics from an electron gas in which collisions between electrons and phonons, electrons, impurities, or imperfections occur are analyzed. The damping of the electron energy eigenstates, which is present in all real metals, results in new current characteristics for energies near the Fermi surface. The derived energy distributions are smeared about the Fermi energy. The degree of smearing is a function of the temperature dependent electron-phonon or electron-electron collision time. It is thus shown how to go backwards from the smeared energy distributions to obtain information pertinent to the electron-phonon interaction and the imaginary part of the bare electron self energy in the phonon field.

Gorden, R., Jr., Rebbert, R. E., Ausloos, P., **Rare gas resonance lamps,** *Nat. Bur. Stand. (U.S.), Tech. Note 496, 55 pages (Oct. 1969), 60 cents.*

Key words: Resonance lamps; rare gases; photo-chemistry; photoionization; extinction coefficients; ionization quantum yield; aluminum windows; saturation ion current.

Rare gas resonance lamps having high spectral purity, high intensity, and long lifetimes have successfully been manufactured. The design and filling procedure for these lamps is described in detail. Particular operational characteristics of the xenon, krypton, argon, neon, and helium resonance lamps are also given. Windows suitable for use with each of these lamps are described, with particular emphasis given to the procedure for fabricating thin aluminum windows for use with neon and helium lamps. In addition, a method for determining extinction coefficients and ionization quantum yields based on the measurement of saturation ion currents is described.

Hardy, S. C., Coriell, S. R., **Morphological stability of cylindrical ice crystals,** *J. Crystal Growth* **5,** *329–337 (1969).*

Key words: Crystal growth; cylinder; ice; morphological stability; surface tension; water.

Small, single crystal ice cylinders have been grown into undercooled water. The initially smooth crystals develop sinusoidal perturbations about the circumference and parallel to the axis. The growth rates and wavelengths of these perturbations are in quantitative agreement with the predictions of a Mullins-Sekerka stability analysis. The growth rates of the perturbations along the axis yield a value of .022 J/m² (22 erg/cm²) for the ice-water surface tension.

Hendricks, R. C., Simoneau, R., Smith, R. V., **Heat transfer with a near-critical fluid,** *Nat. Aeronaut. Space Admin. Report TNX 52612 (National Aeronautics and Space Administration, Greenbelt, Maryland, June 16, 1969).*

Key words: Choking; critical; fluid; fluid flow; heat transfer; oscillations.

The three authors have reviewed the field and added some new material. The intent of the paper is to bring the literature together, to provide information for designers, and to suggest needed research.

Herron, J. T., Huie, R. E., **Rates of reaction of atomic oxygen. II. Some C_2 to C_8 alkanes,** *J. Phys. Chem.* **73,** *No. 10, 3327–3337 (Oct. 1969).*

Key words: Alkane; atomic oxygen; chemical kinetics; mass spectrometry; organic compounds; rate constant.

Rate constants have been measured for the reactions of atomic oxygen (O^3P) with eight straight and branched chain alkanes from 250 to 600K, and for six other branched chain alkanes at 307K. The reactions are interpreted on the basis of a hydrogen atom abstraction mechanism, and Arrhenius parameters are derived for abstraction of primary, secondary, and tertiary hydrogen atoms. The activation energies are found to be in the order primary > secondary > tertiary. For abstraction at secondary C—H bonds, the activation energy is observed to decrease with increasing molecular complexity of the alkane.
A method of estimating rate constants is given.

Jennings, D. A., West, E. D., Evenson, K. M., Rasmussen, A. L., Simmons, W. R., **Laser power and energy measurements,**

Nat. Bur. Stand. (U.S.), Tech. Note 382, 64 pages (Oct. 1969), 65 cents.

Key words: Calorimetry; laser; laser calorimetry; laser energy; laser power.

Most laser calorimeters operate in a constant temperature environment. The calorimeters can be used as deflection devices or the data can be analyzed by extrapolation or integration. Consideration of the heat flow problem common to all of these methods points up the underlying assumptions and the possible errors involved.
Calorimeters for measuring the output energy of pulsed ruby and neodymium glass lasers have been built and calibrated. The absorbing medium is an aqueous solution of $CuSO_4$. Calibration of laser energy detectors has an estimated uncertainty of $\pm 2\%$ for input energies of 0.1J to 100J. Comparisons of absorption cell calorimeters with metal plate calorimeters agree within 1%.
Instrumentation is described that is used for the calibration of CW laser power meters. The calibration unit employs an absorption cell calorimeter to calibrate the output of a photovoltaic cell transfer detector. The power meter to be calibrated is then compared to the calibrated output of the transfer detector. The calibrations are within an accuracy of 4%.
A discussion and description is also given of several types of calorimeters that have been used to measure the output of a 100 watt CO_2 laser. The most recent design provides for measurement from 1 watt to 5 kilowatts with a measured accuracy of better than 3%.

Kamper, R. A., Mullen, L. O., Sullivan, D. B., **Some applications of the Josephson effect,** *Nat. Bur. Stand. (U.S.), Tech. Note 381, 63 pages (Oct. 1969), 65 cents.*

Key words: Josephson effect; superconductivity; tunnel junctions; thermometry.

We describe techniques for fabricating permanent Josephson junctions between thin films of niobium and lead, and for absolute noise thermometry at very low temperatures using the Josephson effect. We discuss the possible benefits of applying superconductivity to nuclear magnetic resonance detection, and review other applications of the Josephson effect.

Maki, A. G., Jr., **Vibrational spectroscopy,** *Ann. Rev. Phys. Chem.* **20,** *273–292 (1969).*

Key words: Absorption spectra; infrared; instrumentation; potential functions; spectroscopy; vibration.

A review is given of the recent scientific literature on the subject of vibrational spectroscopy. Topics which are covered include instrumentation, gas phase spectra including band contour calculations, condensed phase spectra, and vibrational potential functions.

Marinenko, G., **On the atomic weight of potassium,** *Talanta* **16,** *1339–1340 (1969).*

Key words: Atomic weight; potassium.

A brief survey of data is made, which indicates the possibility that the internationally accepted value for the atomic weight of potassium (39.109) is too high. Additional experimental evidence is brought to light, which also supports the above conclusion.

Martin, W. G., Sugar, J., **Perturbations and coupling in the d^9sp configurations of Cu I, Zn II, Ag I, Cd II, and Tl III,** *J. Opt. Soc. Am.* **59,** *No. 10, 1266–1280 (Oct. 1969).*

Key words: Atomic spectra; cadmium; copper; energy levels; energy parameters; silver; thallium; zinc.

Application of intermediate coupling theory to $3d^94s4p$ in Cu I and Zn II revealed perturbations which could not be due to configuration types $3d^{10}nl$. The $3d^94s4p$ levels except $4s4p(^1P^\circ)3d^9\,{}^2P^\circ$ were then fitted by including interaction with $3d^84s^24p$. Initial values for the configuration interaction parameters were based on M. Wilson's Hartree-Fock calculations, and energy parameters for $3d^84s^24p$ (not known experimentally) were fixed at values based on related spectra. The results show that this interaction accounts for the major distortions of $3d^94s4p$ in Cu I and Zn II. The resulting interaction parameter values appear consistent with Roth's values for related iron-group spectra. The discrepancies between calculated and experimental positions for $(^1P^\circ)3d^9\,{}^2P^\circ_{1/2,3/2}$ are qualitatively consistent with known $3d^{10}np\,{}^2P^\circ$ series perturbations in Cu I, Zn II. Calculations without interaction for $4d^95s5p$ in Ag I and Cd II indicate interaction with $4d^85s^25p$ weaker than the corresponding interaction in the Cu I sequence. The levels of Tl III $(5d^96s6p + 5d^{10}7p)$ were fitted with configuration interaction. One experimental d^9sp level is rejected in Zn II, Ag I, and Tl III. Corresponding new levels are found for Zn II and Ag I. Leading eigenvector components for the d^9sp levels in the $[sp(S_1L_1),\ d^9]SL$ and $[sp(S_1L_1)J_1,\ (d^9)J_{\rm II}]J$ coupling schemes are given for all five spectra. The Tl III levels are assigned $J_1J_{\rm II}$ names as most appropriate.

Mason, S. T., **Dependence of the phase shift on energy and atomic number for electron scattering by atomic fields,** *Phys. Rev.* **182,** *No. 1, 97–101 (June 5, 1969).*

Key words: Atomic number; central potential; electron scattering; phase shift; Z-dependence.

Phase shifts of *s*-, *p*-, *d*-, and *f*-electrons scattered elastically by a potential appropriate to singly charged positive ions have been calculated for energies ranging up to 2 Rydbergs above threshold and for selected elements throughout the period system. The results are discussed in terms of characteristics of the model potential.

Peiser, H. S., Wachtman, J. B., Jr., **Jump rates for point defects in special positions held by a trapping centre of cubic symmetry,** *Chapter 12 in Physics of the Solid State, S. Balakrishna, M. Krishnamurty, and Rao B. Ramachandra, ed., pp. 207–222 (Academic Press, Inc., New York, N.Y., 1969).*

Key words: Crystal; cubic; jump rate; point defect; relaxation; symmetry; trapping center.

Point defects, held by a trapping center of cubic symmetry in special positions relative to symmetry elements, generally can move between equivalent sites with more than one jump rate. For all possible symmetry groups of trap and point defect all distinct paths are listed using a novel nomenclature. It is shown how such paths can give rise to relaxation phenomena by the action of external influences. For all relevant symmetry combinations we list J_{max}, the maximum, and J_{min}, the minimum number of jump rates for upsetting (or re-equalizing) the population balance between sites that are equivalent in the unstrained crystal. J_{max} often is the number of prime factors in the quotient between the orders of the point groups of the trap and the defect. J_{min} is the minimum number of operators that will raise the defect point group to that of the trap.

Piermarini, G. J., Mighell, A. D., Weir, C. E., Block., **Crystal structure of benzene II at 25 kilobars,** *Science* **165,** *1250–1255 (Sept. 19, 1969).*

Key words: Benzene II; high-pressure; single-crystal; structure determination; twinning.

At elevated temperatures and pressures, crystals of benzene II may be grown in the diamond-anvil high-pressure cell from either the liquidus or the solid I-solid II transition. Depending upon the conditions of growth, crystals were either single or twinned. X-ray precession data were obtained from a single crystal in the high-pressure cell. Benzene II crystallizes in the monoclinic system with $a = 5.417 \pm .005$ Å (standard error), $b = 5.376 \pm .019$ Å, $c = 7.532 \pm .007$ Å, $\beta = 110.00 \pm .08°$, space group $P2_1/c$, $Z = 2$, $\rho_c = 1.26$ g·cm^{-3} for the conditions 21 °C and ~ 25 kbars. As only a limited amount of data were obtained, the structure was solved by generating all physically reasonable molecular packing configurations. For each configuration, structure factors and a reliability factor were calculated. This procedure produced a unique solution for the molecular packing of the benzene molecules. The final R based on 19 unique reflections is 7.6 percent. This structure was confirmed by molecular packing energy calculations.

Reed, R. P., Schramm, R. E., **Lattice parameters of martensite and austenite in Fe–Ni alloys,** *J. Appl. Phys.* **40,** *No. 9, 3453–3458 (Aug. 1969).*

Key words: Fe-Ni alloys; lattice parameters; martensite.

The lattice parameters of the martensitic, body-centered cubic phase and the face-centered cubic phase were determined for a series of Fe-Ni alloys. Compositions ranged from pure Fe to Fe-35 at.% Ni. Careful Debye-Scherer powder techniques and computerized calculations and error analyses were employed. The martensite lattice parameter has been precisely determined for the first time as a function of composition in Fe-Ni alloys. Results indicate that the martensite lattice parameter reaches a maximum between 9 and 15 at.% Ni and the room temperature lattice parameter of the face-centered cubic phase has a maximum in alloys having greater than 35 at.% Ni. The face-centered cubic parameter was not measurable in alloys having less than 27 at.% Ni.

Rush, J. J., Melveger, A. J., Lippincott, E. R., Laser-Raman spectra of **PH_4I, PH_4Br, and PH_4Cl,** *J. Chem. Phys.* **51,** *No. 7, 2947–2955 (Oct. 1, 1969).*

Key words: Barrier to rotation; crystal force field; crystal structure; lattice modes; phosphonium halides; raman spectra; torsional frequency; vibration.

Laser-Raman spectra have been measured at 23 °C for PH_4I and PH_4Br and at ~ 5 °C for PH_4Cl. Peaks observed in the spectra of all the halides are assigned to "internal" PH_4^+ modes, $\nu_1(A_{1g})$, $\nu_2(A_{1g}, B_{1g})$, $\nu_3(E_g)$ and $\nu_4(E_g)$ and to torsional $[L_2(E_u)]$ and translational $[T_1(A_{1g})]$ lattice modes. The torsional frequencies are 326, 343 and 363 cm^{-1}, respectively, for PH_4I, PH_4Br, and PH_4Cl, while the translational mode is observed at 55.5, 75 and 112 cm^{-1}, respectively. Barriers to rotation are calculated from the torsional frequencies on the simple but unrealistic assumption of a "4-fold" cosine type potential for the PH_4^+ ions. The barriers obtained are 6.7, 7.4 and 8.2 kcal/mol, respectively, for PH_4I, PH_4Br and PH_4Cl. The spectral results and calculated barriers are compared in some detail with previous optical, NMR and neutron scattering results for both the phosphonium and ammonium halides. Suggested differences in force fields between the ammonium and phosphonium salts are discussed.

Shumaker, J. B., Jr., Popenoe, C. H., **Arc measurement of some Ar II optical transition probabilities,** *J. Opt. Soc. Am.* **59,** *No. 8, 980–985 (Aug. 1969).*

Key words: Ar II; arc; argon; lifetimes; transition probabilities.

Wall-stabilized arc measurements employing the generalized Fowler-Milne diagnostic technique have been carried out in argon at atmospheric pressure. Transition probabilities are reported for all lines of the $4s–4p$ and $3d–4p$ Ar II arrays lying below 7200 Å.

Stair, R., **Measurement of natural ultraviolet radiation; historical and general introduction,** (*Proc. Conf. Fourth International Biometeorological Congress, Rutgers University, New Brunswick, N.J., 1966*), *Chapter in The Biologic Effects of Ultraviolet Radiation, Frederick Urbach, ed., pp. 377–390 (Pergamon Press Inc., New York, N.Y., August 1969).*

Key words: Natural ultraviolet; radiometry; solar irradiance; spectroradiometry; ultraviolet.

The development of methods for the measurement of natural ultraviolet radiations interwoven with many fields of optics and electricity. Three hundred years ago Newton first observed that a crude glass prism would separate white light into colors or conversely combine colors. This was followed by the discoveries of ultraviolet and infrared by Ritter and Herschel. Then followed the work of Fraunhofer, Bunsen and Kirchhoff relating to the spectra. The discovery of the thermoelectric effect and its use in measurement by Nobili and Melloni opened the way for accurate measurements. Next came the discoveries in photography, photoelectricity, and great improvements in instrumentation which led the way for the measurements of solar radiation by Rowland, Langley, Fabry and Buisson, Pettit, Abbot, Nicolet, Allen, Mulders, Johnson, Coblentz, Stair and others.

Tipson, R. S., Brady, R. F., Jr., **Synthesis of the two D-2-pentuloses, New derivatives of D-erythro-pentulose,** *Carbohydrate Res.* **10,** *549–563 (Aug. 1969).*

Key words: Acetonation; D-*erythro*-pentulose; D-*threo*-pentulose; isomerization; partition; pyridine.

The syrupy mixture of eight pentoses obtained by boiling a solution of either D-xylose (**1**) or D-arabinose (**2**) in pyridine for 4.5 hours was freed of the four D-aldopentoses. The resulting mixture of four D-pentuloses was resolved by condensation with acetone, followed by partition between solvents or by distillation. In this way, crystalline 2,3-*O*-isopropylidene-β-D-*threo*-pentulofuranose was readily prepared from **1**, and crystalline 1,2:3,4-di-*O*-isopropylidene-D-*erythro*-pentulofuranose (**14**) from **2**. Each of these isomerizations yielded a small proportion of the epimeric D-2-pentulose, but the proportions of the D-3-pentuloses were much lower. The diacetal **14** was partially hydrolyzed, with dilute acid, to 3,4-*O*-isopropylidene-D-*erythro*-pentulofuranose (**17**), the α-D-anomer of which was obtained in crystalline form. The structure of **17** was proved by oxidation with periodate, to give the known, crystalline 2,3-*O*-isopropylidene-D-erythrono-1,4-lactone. The anomers of the 1,3,4-triacetate and 1,3,4-tribenzoate of methyl D-*erythro*-pentulofuranoside were prepared, and characterized by specific optical rotation and n.m.r. spectroscopic evidence.

Venable, W. H., Jr., Shumaker, J. B., Jr., **Observations of departures from equilibrium in a nitrogen arc,** *J. Quant. Spectra. Radiative Transfer* **9,** *1215–1226 (Sept. 1969).*

Key words: Arc; nitrogen; non-equilibrium; spectral-intensity.

Atmospheric-pressure wall-stabilized arcs in nitrogen are found to exhibit molecular band intensities which are incompatible with the assumption of local thermodynamic equilibrium. Mechanisms to account for the departure from equilibrium are suggested.

Weir, C. E., Piermarini, G. J., Block, S., **Instrumentation for single crystal x-ray diffraction at high pressures,** *Rev. Sci. Instr.* **40,** *No. 9, 1133–1136 (Sept. 1969).*

Key words: High pressure; single crystal; X-ray diffraction.

A diamond-anvil high pressure cell made of beryllium, a special goniometer head and a Buerger-type camera designed for X-ray diffraction by single crystals at high pressures are described in some detail. The most important problems still to be solved are discussed.

Wiederhorn, S. M., **Fracture of sapphire,** *J. Am. Ceram. Soc.* **52,** *No. 9, 485–491 (Sept. 21, 1969).*

Key words: Crack propagation; cracks; double-cantilever-cleavage technique; fracture; fracture surface energy; sapphire.

The fracture of sapphire was studied using the double-cantilever-cleavage technique. Fracture surface energies were 7.3 and 6.0 J/m^2 for the $\{10\bar{1}0\}$ and $\{\bar{1}012\}$ type planes, respectively. Attempts to measure the fracture surface energy on the (0001) plane were unsuccessful. The failure of sapphire to fracture along the basal plane was attributed to the fact that these planes lack electrostatic charge neutrality. The possibility of fracture-induced dislocation motion in sapphire at room temperature was investigated using etch-pit techniques, but no evidence for dislocation motion could be found. Fracture behavior on {1012} planes was erratic, varying from boule to boule. The topology of surfaces formed by crack propagation along this plane is described, but no explanation for the erratic behavior or the observed fracture features is given.

Wiese, W. L., Smith, M. W., Miles, B. M., **Atomic transition probabilities. Volume II. Sodium through calcium, a critical data compilation,** *Nat. Stand. Ref. Data Ser., Nat. Bur. Stand. (U.S.), 22, 306 pages (Oct. 1969), $4.50.*

Key words: Allowed and forbidden transitions; oscillator strengths; transition probabilities; sodium; magnesium; aluminum; silicon; phosphorus; sulfur; chlorine; argon; potassium; calcium.

Atomic transition probabilities for about 5,000 spectral lines of the second ten elements, based on all available literature sources, are

XUM

critically compiled. The data are presented in separate tables for each element and stage of ionization. For each ion the transitions are arranged according to multiplets, supermultiplets, transition arrays, and increasing quantum numbers. Allowed and forbidden transitions are listed separately. For each line the transition probability for spontaneous emission, the absorption oscillator strength, and the line strength are given along with the spectroscopic designation, the wavelength, the statistical weights, and the energy levels of the upper and lower states. In addition, the estimated accuracy and the source are indicated. In short introductions, which precede the tables for each ion, the main justifications for the choice of the adopted data and for the accuracy rating are discussed. A general introduction contains a detailed discussion of the critical factors entering into each major experimental and theoretical method. It also includes a general critical assessment of the widely used Coulomb approximation, and a number of illustrative examples for the exploitation of regularities or systematic trends among oscillator strengths.

Yates, J. T., Jr., Madey, T. E., **Chemisorption on rhenium: N_2 and CO,** *J. Chem. Phys.* **51,** *No. 1, 334–337 (July 1, 1969).*

Key words: Carbon monoxide; chemisorption; flash desorption; isotropic mixing; molybdenum; nitrogen; rhenium; sticking coefficient; tungsten.

The chemisorption of N_2 and CO on polycrystalline Re has been studied using flash desorption. A number of binding states have been identified and their binding energies have been estimated kinetically. Isotopic mixing between chemisorbed species has been observed for the β-N_2 and β-CO states on Re; there appears to be no evidence for dissociation of β-CO. The γ-N_2 and two α-CO states on Re desorb without isotopic mixing.
In general, the distribution and properties of binding states for N_2 and CO on Re are remarkably similar to those found for these adsorbates on W.
An enhancement in nitrogen adsorption on Re occurs upon electron impact (150 eV) on $N_2(g)$. A new set of strongly-bound states are produced which are distinct from the β-N_2 states populated by adsorption of ground state $N_2(g)$.
A comparison of the sticking coefficients for N_2 and CO on Re is made, using two independent methods (uptake and isotopic mixing) over a wide temperature range. The sticking coefficient for N_2 on Re decreases markedly with increasing temperature; for CO on Re, there is little effect of temperature on the sticking coefficient.
A discussion is presented of migration-limited bimolecular kinetics at elevated temperatures in the chemisorbed layer.

Other NBS Publications

Allan, D. W., Guetrot, A, Higbie, L. S., Lavanceau, J. D., An application of statistical smoothing techniques on VLF signals for comparison of time between USNO and NBS, Proc. 23rd Frequency Control Symp., Atlantic City, N.J., May 6–8, 1969, p. 248 (1969).

Angeles, R., Aldridge, M., Freeman, D., Wall, L., Cryodegradation of polyelectrolyte networks, Polymer Letters **7,** No. 8, 609–611 (1969).

Alvarez, R., Paulsen, P. J., Kelleher, D. E., Simultaneous determination of trace elements in platinum by isotope dilution and spark source mass spectrometry, Anal. Chem. **41,** No. 7, 955–958 (June 1969).

Beatty, R. W., Coaxial power, impedance and attenuation calibration at the National Bureau of Standards, Microwave J. **11,** No. 5, 65–75 (May 1968).

Bennett, L. H., "Charge transfer" in intermetallic compounds: example—the sodium thallide structure, Chapter in Structural Developments in Alloy Phases, B. C. Giessen, ed., Discussion I, 41–44 (Plenum Press, Inc., New York, N.Y., 1969).

Birmingham, B. W., Flynn, T. W., Cryogenics in United States National Programs, Cryogenics **9,** No. 1, 3–10 (Feb. 1969).

Bullis, W. M., Editor, Methods of measurement for semiconductor materials, process control, and devices, Quarterly Report April 1 to June 30, 1969, Nat. Bur. Stand. (U.S.), Tech. Note 495, 45 pages (Sept. 1969), 50 cents.

Bullis, W. M., Thurber, W. R., Pyke, T. N., Jr., Ulmer, F. H., Koenig, A. L., Use of a time-shared computer system to control a Hall effect experiment, Nat. Bur. Stand. (U.S.), Tech. Note 510, 46 pages (Oct. 1969), 50 cents.

Colwell, J. H., The performance of a mechanical heat switch at low temperatures, Rev. Sci. Instr. **40,** No. 9, 1182–1186 (Sept. 1969).

Coxon, B., Studies of ^{15}N-labeled amino sugars. Synthesis and spectroscopy of derivatives of 6-amino-6-deoxy-D-glucose-6-^{15}N, Carbohydrate Res. **11,** 153–155 (1969).

Crawford, M. L., A new RF–DC substitution calorimeter with automatically controlled reference power, IEEE Trans. Instr. Meas. **IM–17,** No. 4, 378–384 (Dec. 1968).

Daney, D. E., Ludtke, P. E., Sindt, C. F., Slush hydrogen pumping characteristics using a centrifugal-type pump (Proc. 1968 Cryogenic Engineering Conf., Case Western Reserve Univ., Cleveland, Ohio, Aug. 19–21, 1968), Chapter in Advances in Cryogenic Engineering 14, Paper J–2, 438–445 (Plenum Press, Inc., New York, N.Y., 1969).

Davis, H. A., Jr., Hastings, J. R., Waxman, M., An improved tool for refinishing the conical ends of high pressure tubing, Rev. Sci. Instr. **40,** No. 9, 1238 (Sept. 1969).

Dean, J. W., Brennan, J. A., Mann, D. B., Cryogenic flow research facility of the National Bureau of Standards (Proc. 1968 Cryogenic Engineering Conf., Case Western Reserve Univ., Cleveland, Ohio, Aug. 19–21, 1968), Chapter in Advances in Cryogenic Engineering 14, Paper H–1, 299–305 (Plenum Press, Inc., New York, N.Y., 1969).

DeLancey, G. B., Analysis of multicomponent diaphragm cell data, J. Phys. Chem. **73,** No. 5, 1591–1593 (May 1969).

Diamond, J. J., Editor, Bibliography on the high temperature chemistry and physics of materials, July, August, Sept. 1969, Nat. Bur. Stand. (U.S.), Spec. Publ. 315–3, 90 pages (Oct. 1969), $1.00.

Donovan, R. J., Husain, D., Bass, A. M., Braun, W., Davis, D. D., Kinetic spectroscopic studies of Cl($3p^5 2p$?3/2, 1/2) in the vacuum ultraviolet, J. Chem. Phys. **50,** No. 9, 4115–4116 (May 1, 1969).

Drechsel, D., Maximon, L. C., Warner, R. E., Noncoplanar *p-p* bremsstrahlung calculations at 48 and 30 MeV, Phys. Rev. **181,** No. 4, 1720–1722 (May 20, 1969).

Duerst, R. W., Kokoszka, G. F., Hyperfine fields in dimeric metal ion complexes, J. Chem. Phys. **51,** No. 4, 1673–1674 (Aug. 15, 1969).

Edmonds, D. K., Hork, J., Cavitation in liquid cryogens (Proc. 1968 Cryogenic Engineering Conf., Case Western Reserve Univ., Cleveland, Ohio, Aug. 19–21, 1968), Chapter in Advances in Cryogenic Engineering 14, Paper G–4, 274–282 (Plenum Press, Inc., New York, N.Y., 1969).

Engen, G. F., An introduction to the description and evaluation of microwave systems using terminal invariant parameters, Nat. Bur. Stand. (U.S.), Monogr. **112,** 27 pages (October 1969), 35 cents.

Fatiadi, A. J., Acylation of tetrahydroxy-*p*-benzoquinone, J. Chem. Eng. Data **13,** No. 4, 591–593 (Oct. 1969).

Flynn, T. M., Birmingham, B. W., Cryogenics and national goals (Proc. 1968 Cryogenic Engineering Conf., Case Western Reserve Univ., Cleveland, Ohio, Aug. 19–21, 1968), Chapter in Advances in Cryogenic Engineering 14, Paper A–1, 1–12 (Plenum Press, Inc., New York, N.Y., 1969).

Frederick, N. V., A low loss sliding short of limited travel for precision coaxial transmission lines, Proc. IEEE **56,** No. 12, p. 2188 (Dec. 1968).

Gadzuk, J. W., Band-structure effects in the field-induced tunneling of electrons from metals, Phys. Rev. **182,** No. 2, 416–426 (June 10, 1969).

Garvin, D., Suggestion: the minireview, Phys. Today **22,** No. 10, 13–15 (Oct. 1969).

Gatterer, L. E., Clock synchronization experiments at VHF utilizing the ATS–1 and ATS–3 transponders, Natl. Aeronaut. Space Admin. Report ATS Tech. Summary (National Aeronautics and Space Administration, Greenbelt, Md., Feb. 16, 1968).

Geller, S. B., Mantek, P. A., Cleveland, N. G., Standard reference materials: Calibration of NBS secondary standard magnetic tape (computer amplitude reference) using the reference tape amplitude measurement "Process A", Nat. Bur. Stand. (U.S.), Spec. Publ. 260–18, 41 pages (Nov. 1969), 50 cents.

Greenfeld, S. H., Natural weathering of mineral stabilized asphalt coatings on organic felt, Nat. Bur. Stand. (U.S.), Bldg. Sci. Ser. **24,** 17 pages (Oct. 1969), 30 cents.

Gugeler, A. L., Ballard, D. B., The aluminum-porcelain enamel interface as observed by electron microscopy, Am. Ceramic Soc. Bull. **48,** No. 9, 842–845 (Sept. 1969).

Halldane, J. F., Visual responses of travelers in urban environments, (Proc. Symp. Man-Machine Systems, Cambridge, England, Sept. 8–12, 1969), Chapter in Transport Systems Vehicle Control 2, Paper No. 8, 17 pages (1969).

Hiza, M. J., Duncan, A. G., Equilibrium gas-phase compositions of ethane and ethylene in binary mixtures with helium and neon below 150 °K and a correlation for deviations from the geometric mean combining rule (Proc. 1968 Cryogenic Engineering Conf., Case Western Reserve Univ., Cleveland, Ohio, Aug. 19–21, 1968), Chapter in Advances in Cryogenic Engineering 14, Paper B–1, 30–40 (Plenum Press, Inc., New York, N.Y., 1969).

Hudson, G. E., Allan, D. W., Barnes, J. A., Hall, R. G., Lavanceau, J. D., Winkler, G. M. R., A coordinate frequency and time system, Proc. 23rd Frequency Control Symp., Atlantic City, N.J., May 6–8, 1969, p. 249 (1969).

Hudson, G. E., Barnes, J. A., Clock error statistics as a renewal process, Proc. 22nd Frequency Control Annual Symp., Atlantic City, N.J., Apr. 22–24, 1968, pp. 384–413 (1968).

Isbell, H. S., Fatiadi, A. J., Phenylhydrazone-phenylazo tautomerism. Part III. Reactions of phenylformazans and certain bis(phenylhydrazones) with strong acids, Carbohydrate Res. 11, 303–311 (1969).

Isbell, H. S., Frush, H. L., Wade, C. W. R., Hunter, C. E., Transformations of sugars in alkaline solution, Carbohydrate Res. 9, 163–175 (1969).

Jellison, J. C., Collier, R. S., Fluid phase and temperature measurement with a single sensor (Proc. 1968 Cryogenic Engineering Conf., Case Western Reserve Univ., Cleveland, Ohio, Aug. 19–21, 1968), Chapter in, Advances in Cryogenic Engineering 14, Paper H–5, 322–330 (Plenum Press, Inc., New York, N.Y., 1969).

Johnson, V. J., A memoir of Russell B. Scott (Proc. CRYO/68 Conf., Chicago, Illinois, June 9–12, 1968), Chapter in Applications of Cryogenic Technology, R. W. Vance and H. Weinstock, ed., Introduction, pp. 1–11 (Tinnon-Brown, Inc., Los Angeles, California, 1969).

Joiner, B. L., The median significance level and other small sample measures of test efficacy, J. Am. Statist. Assoc. **64,** 971–985 (Sept. 1969).

Kamperer, R. A., Possible contribution of superconducting devices to nuclear magnetic resonance detection, J. Appl. Phys. **40,** No. 5, 2163 (Apr. 1969).

Kieffer, L. J., The reliability of property data, or, whose guess shall we use?, J. Chem. Doc. **9,** No. 3, 167–168 (Aug. 1969).

Kidnay, A. J., Hiza, M. J., Dickson, P. F., The kinetics of adsorption of methane and nitrogen from hydrogen gas (Proc. 1968 Cryogenic Engineering Conf., Case Western Reserve Univ., Cleveland, Ohio, Aug. 19–21, 1968), Chapter in Advances in Cryogenic Engineering 14, Paper B–2, 41–48 (Plenum Press, Inc., New York, N.Y., 1969).

Kropschot, R. H., Thermal diffusivity of powder insulation (Proc. 1968 Cryogenic Engineering Conf., Case Western Reserve Univ., Cleveland, Ohio, Aug. 19–21, 1968), Chapter in Advances in Cryogenic Engineering 14, Paper F–4, 224–229 (Plenum Press, Inc., New York, N.Y., 1969).

LaFleur, P. D., Determination of molybdenum in steels and biological materials by activation analysis, Radiochem. Radioanal. Letters **1,** No. 3, 225–229 (July 1969).

LaVilla, R. E., Mendlowitz, H., Optical properties of germanium, J. Appl. Phys. **40,** No. 8, 3297–3300 (July 1969).

Logan, H. L., Studies of hot salt cracking of the titanium 8%-Al-1% Mo=1% V alloy (Proc. Ohio State Stress Corrosion Symp., Ohio State University, Columbus, Ohio, September 11–15, 1967), pp. 662–672 (National Association of Corrosion Engineers, Houston, Texas, 1969).

McBee, C. L., Kruger, J., Ellipsometric-spectroscopy of films formed on metals in solution, Surface Sci. **16,** 340–352 (1969).

McCaa, W. D., Jr., Nahman, N. S., Frequency and time domain analysis of a superconductive coaxial line using the BCS theory, J. Appl. Phys. **40,** No. 5, 2098–2100 (April 1969).

Madey, T. E., Yates, J. T., Jr., Temperature effects in desorption by electron impact: molecular vibrations in the chemisorbed layer, J. Chem. Phys. **51,** No. 3, 1264–1265 (Aug. 1, 1969).

Mahler, R. J., Interaction of Gunn domains with the Ga^{71} nuclei in GaAs, Appl. Phys. Letters **14,** No. 9, 277–279 (May 1, 1969).

Mandel, J., A method for fitting empirical surfaces to physical or chemical data, Technometrics **11,** No. 3, 411–429 (Aug. 1969).

Margoshes, M., Remarks on linearization of characteristic curves in photographic photometry, Appl. Opt. **8,** No. 4, 818 (April 1969).

Marinenko, G., On the atomic weight of potassium, Talanta **16,** 1339–1340 (1969).

Maximon, L. C., Comments on radiative corrections, Rev. Mod. Phys. **41,** No. 1, 193–204 (Jan. 1969).

Melmed, A. J., Surface characterization by ellipsometry low-energy electron diffraction, and field-electron microscopy (Proc. Conf. Third Battelle Memorial Institute Materials Science Colloquium, Kronberg, Germany, May 6–11, 1968), Chapter in Molecular Processes on Solid Surfaces, pp. 105–127 (McGraw-Hill Book Co., Inc., New York, N.Y., 1969).

Mendlowitz, H., Calculated transition array for the configurations $3d^2-3d4p$ in Ti III, Astrophys. J. 158, 385–388 (Oct. 1969).

Menis, O., Analytical Coordination Chemistry Section: Summary of activities July 1968 to June 1969, Nat. Bur. Stand. (U.S.), Tech. Note 504, 120 pages (Oct. 1969), $1.00.

Mies, F. H., Resonant scattering theory of association reactions and unimolecular decomposition. I. A united theory of radiative and collisional recombination, J. Chem. Phys. **51,** No. 2, 787–797 (July 1969).

Miller, R. C., Prausnitz, J. M., Statistical thermodynamics of simple liquid mixtures. Henry's constants, Ind. Eng. Chem. Fundamentals **8,** No. 3, 449–452 (Aug. 1969).

Milligan, D. E., Jacox, M. E., Matrix-isolation study of the infrared and ultraviolet spectra of the free radical HCO. The hydrocarbon flame bands, J. Chem. Phys. **51,** No. 1, 277–288 (July 1, 1969).

Moore, C. E., Bibliography on the analyses of optical atomic spectra Section 4. $^{57}La-^{71}Lu$ and $^{89}Ac-^{99}Es$, Nat. Bur. Stand. (U.S.), Spec. Publ. 306, Section 4, 55 pages (Aug. 1969), 55 cents.

Nahman, N. S., Superconducting transmission lines—communication and power, Proc. 1968 Summer Study on Superconducting Devices and Accelerators, Brookhaven National Laboratory, Upton, L. I., New York, June 10–July 19, 1968, BNL–50155, pp. 622–627 (1968).

Nemoto, T., Beatty, R. W., Fentress, G. H., A two-channel off-null teachnique for measuring small changes of attenuation, IEEE Trans. Microwave Theory Tech. **MTT–17,** No. 7, 396–397 (July 1969).

Paabo, M., Bates, R. G., Dissociation of deuteriocarbonate ion in deuterium oxide from 5 to 50°, J. Phys. Chem. **73,** No. 9, 3014–3017 (Sept. 1969).

Pfrang, E. O., Yokel, F. Y., Structural performance evaluation of a building system, Nat. Bur. Stand. (U.S.), Bldg. Sci. Ser. 25, 127 pages (Nov. 1969), $1.25.

Reader, J., Optimizing Czerny-Turner spectrographs: A comparison between analytic theory and ray tracing, J. Opt. Soc. Am. **59,** No. 9, 1189–1196 (Sept. 1969).

Reed, R. P., Low-temperature mechanical properties of welded and brazed copper (Proc. 1968 Cryogenic Engineering Conf., Case Western Reserve Univ., Cleveland, Ohio, Aug. 19–21, 1968), Chapter in Advances in Cryogenic Engineering 14, Paper C–3, 83–87 (Plenum Press, Inc., New York, N.Y., 1969).

Richardson, A. C. B., Multiple scattering corrections for the associated-particle neutron time-of-flight technique, Nat. Bur. Stand. (U.S.), Tech Note 499, 68 pages (Oct. 1969), 65 cents.

Robinson, R. A., An osopiestic vapor pressure study of the system potassium chloride-sodium chloride in deuterium oxide solution at 25°, J. Phys. Chem. **73,** No. 9, 3165–3166 (Sept. 1969).

Rockett, J. A., Planned operation of the National Bureau of Standards Fire Research and Safety Office, Fire J. 63, No. 6, 41–43 (Nov. 1969).

Ruthberg, S., Calibration to high precision in the medium vacuum range with stable environments and micromanometer, J. Vacuum Sci. Technol. 6, No. 3, 401–412 (May/June 1969).

Rybicki, G. B., Hummer, D. G., Non-coherent scattering—V. Thermalization distances and their distribution function, Monthly Notices Roy. Astron. Soc. **144,** 313–323 (1969).

Schaffer, R., Editor, Organic Chemistry Section: Summary of activities July 1968 to June 1969, Nat. Bur. Stand. (U.S.), Tech. Note 507, 145 pages (Oct. 1969), $1.25.

Schwartz, R. B., Schrack, R. A., Heaton, H. T., A search for structure in the n-p scattering cross section, Physics Letters **30B,** No. 1, 36–38 (Sept. 1, 1969).

Sparks, L. L., Powell, R. L., Hall, W. J., Progress on cryogenic thermocouples (Proc. 1968 Cryogenic Engineering Conf., Case Western Reserve Univ., Cleveland, Ohio, Aug. 19–21, 1968),

XUM

Chapter in Advances in Cryogenic Engineering 14, Paper H-4, 316–321 (Plenum Press, Inc., New York, N.Y., 1969).

Standard Reference Materials, Catalog and price list of standard materials issued by the National Bureau of Standards, Nat. Bur. of Stand. (U.S.), Spec. Publ. 260, 1969 Edition, 44 pages (July 1969) (Supersedes NBS Misc. Publ. 260–1968 edition), 50 cents.

Sukle, D. J., Wells, J. S., Fine structure in EPR of Mn^{2+} in zinc sulfate, Phys. Rev. **180,** No. 2, 445–450 (Apr. 10, 1969).

Taggart, H. E., Field strength and RFI standards at the National Bureau of Standards, Proc. IEEE Electromagnetic Compatibility Conf., Seattle, Washington, July 23–25, 1968, pp. 149–158 (1968).

Taylor, J. K., Editor, Microchemical Analysis Section: Summary of activities July 1968 to June 1969, Nat. Bur. Stand. (U.S.), Tech. Note 505, 140 pages (Oct. 1969), $1.25.

Viezbicke, P. P., Why WWV moved to Colorado, Mark 5, 13, No. 3, 14–16 (June 1968).

West, E. D., Ishihara, S., Experimental evaluations of heater lead error in calorimetry, Rev. Sci. Instr. **40,** No. 10, 1356–1359 (Oct. 1969).

Williams, R., The effects of extended high-temperature storage on the performance characteristics of several strain gage pressure transducers, Nat. Bur. Stand. (U.S.), Tech. Note 497, 22 pages (Oct. 1969), 30 cents.

Wilson, W. K., Hebert, R. L., Evaluation of the stability of record papers, Tappi **52,** No. 8, 1523–1529 (Aug. 1969).

Yates, J. T., Jr., Madey, T. E., Electron impact study of the γ-N_2 state chemisorbed on tungsten (Proc. Fourth International Materials Symp., Berkeley, Calif., June 1968), Chapter in The Structure and Chemistry of Solid Surfaces, Gabor A. Somorjai, ed., pp. 59–1, 59–27 (John Wiley and Sons, Inc., New York, N.Y., 1969).

**Publications for which a price is indicated are available by purchase from the Superintendent of Documents, U.S. Government Printing Office, Washington, D.C. 20402 (foreign postage, one-fourth additional). The NBS non-periodical series are also available from the Clearinghouse for Federal Scientific and Technical Information, Springfield, Va. 22121. Reprints from outside journals and the NBS Journal of Research may often be obtained directly from the authors.*

U.S. GOVERNMENT PRINTING OFFICE : 1970 OL—372–505

UMA OCT 40129
UNIVERSITY MICROFILMS INC
ATTN SERIALS SECTION
300 NORTH ZEEB RD
ANN ARBOR MICH 48106

UNITED STATES
GOVERNMENT PRINTING OFFICE
DIVISION OF PUBLIC DOCUMENTS
WASHINGTON, D.C. 20402

OFFICIAL BUSINESS

POSTAGE AND FEES PAID
U.S. GOVERNMENT PRINTING OFFICE

JOURNAL OF RESEARCH of the National Bureau of Standards
A. Physics and Chemistry

Vol. 74A, No. 2 Mar.–Apr. 1970

Contents

Page

A theoretical investigation of the configurations $(3d+4s)^4 4p$ in neutral vanadium (V I). C. Roth. 141

A theoretical investigation of the configurations $(3d+4s)^5 4p$ in neutral chromium (Cr I). C. Roth. 157

A theoretical investigation of the configurations $(3d+4s)^7 4p$ in neutral iron. C. Roth. 181

The intensity as a function of temperature of the low-angle x-ray diffraction maxima of the *n*-paraffins: hexatriacontane, tetratetracontane, and tetrananonacontane. Peter K. Sullivan and James J. Weeks. 203

Photoelastic constants of ruby. R. M. Waxler and E. N. Farabaugh. 215

Estimation of critical constants T_c, ρ_c from the $\rho(T)$ and $T(\rho)$ relations at coexistence. Robert D. Goodwin. 221

Synthesis and growth of fresnoite ($Ba_2TiSi_2O_8$) from a TiO_2 flux and its relation to the system $BaTiO_3-SiO_2$. C. R. Robbins. 229

Photoionization study of $Fe(CO)_5$ and $Ni(CO)_4$. G. Distefano. 233

Papers presented at the Conference, Electronic Density of States, National Bureau of Standards, Gaithersburg, Maryland November 3–6, 1969

The band structure problem. J. M. Ziman. 241
Optical properties and electronic density of states. Manuel Cardona. 253
Excitonic effects in x-ray transitions in metals. G. D. Mahan. 267
Soft x-ray band spectra and their relationship to the density of states. G. A. Rooke. 273
The electronic structure of disordered alloys. J. L. Beeby. 281
Summary of the conference on electronic density of states. H. Ehrenreich. 293

Publications of the National Bureau of Standards. 301

Library of Congress Catalog Card Number: 62–37059

For sale by the Superintendent of Documents, U.S. Government Printing Office, Washington, D.C. 20402. (Order by SD Catalog No. C 13.22/sec.A:74/2). Single copy price varies. This issue $2. Subscription price: $9.50 a year; $2.25 additional for foreign mailing.

UNITED STATES GOVERNMENT PRINTING OFFICE, WASHINGTON : 1970

XU